Instytut Niskich Temperatur i Badań Strukturalnych
im. Włodzimierza Trzebiatowskiego Polskiej Akademii Nauk

ROZPRAWA DOKTORSKA

Wpływ alkilowych pochodnych hydrazyny na właściwości fizykochemiczne i mechanizmy przemian fazowych w wybranych hybrydowych kryształach organiczno-nieorganicznych perowskitów oraz perowskitoidów

w formie spójnego tematycznie cyklu artykułów opublikowanych w czasopismach naukowych

mgr Jan Albert Zienkiewicz

Rozprawa wykonana pod kierunkiem dr. hab. Macieja Ptaka

Wrocław 2023

Podziękowania

W tym miejscu chciałbym podziękować wszystkim osobom, bez których wsparcia, współpracy oraz pomocy merytorycznej opublikowanie w tak krótkim czasie cyklu publikacji składających się na niniejszą Rozprawę Doktorską nie byłoby możliwe.

Przede wszystkim pragnę wyrazić swoją głęboką wdzięczność mojemu Promotorowi, dr. hab. Maciejowi Ptakowi, za nieustanne mobilizowanie mnie do osiągania coraz lepszych wyników w pracy naukowej, cierpliwość, ciągłą gotowość do udzielania wsparcia merytorycznego oraz wiarę w finalny sukces.

Podziękowania składam również wszystkim współautorom publikacji wchodzących w skład niniejszej rozprawy.

Chciałbym także serdecznie podziękować wszystkim przyjaciołom i znajomym, którzy nie zostali wymienieni tutaj z nazwiska, za niezliczone inspirujące rozmowy, które napędzały moje działania.

Wreszcie, pragnę z głębi serca podziękować moim rodzicom, Barbarze i Andrzejowi, oraz mojej narzeczonej, Luizie, za ich bezcenne wsparcie i wiarę we mnie.

Składam również podziękowania Narodowemu Centrum Nauki za sfinansowanie części badań wchodzących w skład niniejszej Rozprawy Doktorskiej w ramach grantu Preludium 19 *„Synteza i charakterystyka fizykochemiczna nowych warstwowych i perowskitowych hybrydowych organiczno-nieorganicznych halogenków ołowiu z protonowanymi alkilopochodnymi hydrazyny”* nr UMO-2020/37/N/ST5/02257.

Spis treści

1. Wprowadzenie

1.1. Streszczenie w języku polskim

Niniejszą rozprawę doktorską stanowi spójny tematycznie cykl pięciu publikacji naukowych, które łączy tematyka wpływu kationów amoniowych, będących metylowymi pochodnymi hydrazyny, na właściwości fizykochemiczne materiałów hybrydowych zaliczanych do grup perowskitów i perowskitoidów. Teksty publikacji opatrzono komentarzem wprowadzającym w ich tematykę, przedyskutowano najważniejsze wyniki, a także zestawiono wnioski wyciągnięte z ich analizy.

W ramach badań zsyntezowano siedem nowych, nieopisanych wcześniej w literaturze związków hybrydowych. Następnie dokonano charakterystyki ich właściwości strukturalnych, termicznych, dielektrycznych, magnetycznych, fononowych oraz spektroskopowych. Duży nacisk położono na badanie ich właściwości optycznych w zakresie UV-Vis, a także charakterystykę ich właściwości fononowych metodami spektroskopii w podczerwieni (IR) oraz ramanowskiej. Dla większości kryształów wykonano analizę grupy faktorowej (ang. *factor group analysis*), dokonano przypisania pasm IR i Ramana oraz przedyskutowano zmiany widm w funkcji temperatury i/lub ciśnienia. Szczególną uwagę zwrócono na badanie mechanizmów przejść fazowych otrzymanych związków z wykorzystaniem metod dyfraktometrycznych oraz spektroskopii oscylacyjnej. Ponadto dla cząsteczki 1,1-dimetylohydrazyny oraz kationu 1,1-dimetylohydrazyniowego ($DMHy^+$) wykonano optymalizację geometrii oraz symulację widm IR i Ramana metodami DFT (ang. *density funcional theory*).

Właściwości fizykochemiczne otrzymanych związków zestawiano pomiędzy sobą oraz z opisanymi wcześniej podobnymi materiałami różniącymi się parametrami takimi jak rozmiar i rodzaj jonów amoniowych, ze szczególnym uwzględnieniem alkilowych pochodnych hydrazyny, a także rozmiar i rodzaj pozostałych jonów tworzących strukturę materiału. Na tej podstawie przeanalizowano wpływ ilości grup metylowych w kationach będącymi metylowymi pochodnymi hydrazyny na właściwości fizykochemiczne perowskitowych i perowskitoidowych materiałów hybrydowych z grup mrówczanów metali przejściowych, halogenków ołowiu oraz metali przejściowych.

Poznanie właściwości nowych związków oraz przeanalizowanie wpływu zawady przestrzennej kationu na właściwości otrzymanych materiałów stanowi przyczynek do lepszego zrozumienia fizykochemii materiałów perowskitowych w kontekście potencjalnych zastosowań w optoelektronice.

1.2. Streszczenie w języku angielskim

This doctoral thesis consists of a thematically consistent series of five scientific publications connected by the subject of the influence of ammonium cations, that are methyl derivatives of hydrazinium, on the physicochemical properties of hybrid materials classified as perovskites and perovskitoids. The texts of the publications have been provided with an introductory commentary on their subject, the most important results have been discussed, and the conclusions drawn from their analysis have been put together.

During the research, seven novel hybrid compounds were synthesized that had not been published before. Therefore, characterizations of their structural, thermal, dielectric, magnetic, phonon, and spectroscopic properties have been performed. Huge attention has been paid to the investigation of optical properties in the UV-Vis range, as well as characteristics of their phonon properties using infrared (IR) and Raman spectroscopy. For the majority of crystals, factor group analysis has been performed. IR and Raman bands have been assigned, and changes in the spectra as a function of temperature and/or pressure have been discussed. Special attention has been devoted to the study of phase transition mechanisms utilizing X-ray diffraction (XRD) and vibrational spectroscopy methods. Moreover, geometry optimization and simulation of IR and Raman spectra using DFT (density functional theory) methods have been carried out for the 1,1-dimethylhydrazine molecule and the 1,1-dimethylhydrazinium cation ($DMHy^+$).

The physicochemical properties of obtained compounds have been compared with each other and with similar materials described before, varying in parameters such as size and type of ammonium cation, with particular emphasis on alkyl hydrazinium derivatives, and size and type of other ions creating the structure of the material. Based on that, the influence of the number of methyl groups in hydrazinium derivatives on the physicochemical properties of hybrid materials from the group of transition metal formates and lead and transition metal halides has been analyzed.

Studies on the properties of novel compounds together with a thorough analysis of the influence of steric hindrance of the ammonium cation on the properties of obtained materials contribute to a better understanding of the physical chemistry of perovskite-type materials in the context of further optoelectronic applications.

1.3. Motywacje i cele pracy

Celem niniejszej pracy doktorskiej jest zrozumienie wpływu stopnia metylowania kationu hydrazyniowego na właściwości fizykochemiczne i mechanizmy przemian fazowych w wybranych hybrydowych organiczno-nieorganicznych perowskitach oraz perowskitoidach, ze szczególnym uwzględnieniem mrówczanów metali przejściowych, halogenków ołowiu oraz halogenków metali przejściowych, których wartości współczynnika tolerancji przekraczają lub zbliżają się do wartości granicznych dla trójwymiarowych materiałów typu perowskitu.

Motywacją do podjęcia tematu pracy była chęć lepszego zrozumienia właściwości tych związków oraz poszukiwanie nowych materiałów z grupy hybrydowych organiczno-nieorganicznych perowskitów, które w ostatnich latach zdobywają rosnącą popularność jako obiecujące materiały do zastosowania w szeroko rozumianej optoelektronice. w związku z niewielką ilością znanych materiałów trójwymiarowych tworzących struktury typu perowskitu, uwaga środowiska naukowego skupia się silnie na materiałach o niższej wymiarowości. Związki warstwowe i łańcuchowe, pomimo nieco gorszych parametrów optoelektronicznych, charakteryzują się większą odpornością chemiczną na wilgoć i trwałością, co zwiększa ich potencjał aplikacyjny.

Kation hydrazyniowy oraz jego pochodne zostały wybrane jako cząsteczki modelowe ze względu na fakt, że tworzą kilka metylowych pochodnych różniących się zawadą przestrzenną, rozmiarem i promieniem jonowym. w związku z tym podjęto próbę zsyntezowania wybranych materiałów z grupy organiczno-nieorganicznych hybryd i scharakteryzowania ich właściwości strukturalnych, dielektrycznych, fononowych, luminescencyjnych oraz magnetycznych. Duży nacisk, ze względu na specjalizację Doktoranta, położono na analizę widm IR oraz Ramana w funkcji temperatury dla większości z materiałów oraz ciśnienia dla jednego z badanych związków. Analiza zmian widm oscylacyjnych została wykorzystana do określania mechanizmów zachodzących przemian fazowych.

Dodatkowo w ostatnich latach ukazało się kilka interesujących prac dotyczących niezwykłych właściwości materiałów perowskitowych opartych na pochodnych hydrazyny oraz ich potencjalnego zastosowania w optoelektronice. Dokładne zrozumienie właściwości oraz przeanalizowanie ich zależności strukturalnych pozwoli na wypełnienie luk w dotychczasowej wiedzy.

Na materiał badawczy wybrano **[DMHy]Mn(HCOO)$_3$** – mrówczan manganu z kationem 1,1-dimetylohydrazyniowym ($DMHy^+$), gdyż znane są podobne analogi zawierające kation hydrazyny (Hy^+) oraz metylohydrazyny (MHy^+). Ponieważ opisane dotychczas w literaturze związki posiadają właściwości ferroelektryczne lub multiferroiczne, podjęto próbę określenia

właściwości strukturalnych, dielektrycznych, fononowych, luminescencyjnych oraz magnetycznych zmienianych w wyniku zmiany liczby grup metylowych.

Drugą grupę badanych związków stanowią chlorki metali przejściowych opisanych ogólnym wzorem **[MHy]$M^{II}Cl_3$** (M^{II} = Mn^{2+}, Co^{2+}, Ni^{2+}, Cu^{2+} oraz Cd^{2+}), których właściwości fizykochemiczne nigdy wcześniej nie zostały opisane. Zastępowanie metali ciężkich w związkach hybrydowych mniej szkodliwymi metalami jest zabiegiem zmniejszającym ich toksyczność, dlatego poszukiwanie hybrydowych halogenków metali przejściowych jest tak ważne.

Ostatnim związkiem, który został zsyntezowany na potrzeby niniejszej pracy jest perowskitoid – jodek ołowiu z kationem 1,1,1-trimetylohydrazyniowym (Me_3Hy^+) o wzorze **[Me_3Hy]PbI_3**. Badania nad tym kryształem zostały podjęte ze względu na niezwykłe właściwości optyczne i elektryczne znanych ferroelektryków [MHy]PbX_3 (X = Cl^-, Br^-), bardzo nielicznych przedstawicieli trójwymiarowych perowskitów hybrydowych, oraz ich dwuwymiarowych analogów o ogólnym wzorze $[MHy]_2PbX_4$ (X = Br^-, I^-).

Przeprowadzone badania oraz ich wyniki opisano w następujących publikacjach:

[**D1**] J.A. Zienkiewicz*, D.A. Kowalska, K. Fedoruk, M. Stefański, A. Pikul, M. Ptak, *Unusual isosymmetric order–disorder phase transition in a new perovskite-type dimethylhydrazinium manganese formate exhibiting weak ferromagnetism and photoluminescence properties*, J. Mat. Chem. C **2021**, 9 (21), 6841-6851, doi: 10.1039/d1tc01014j.

[**D2**] J.A. Zienkiewicz, E. Kucharska, M. Ptak*, *Mechanism of unusual isosymmetric order-disorder phase transition in [dimethylhydrazinium]Mn(HCOO)$_3$ hybrid perovskite probed by vibrational spectroscopy*, Materials **2021**, 14 (14), 3984, doi: 10.3390/ma14143984.

[**D3**] J.A. Zienkiewicz*, M. Ptak, D. Drozdowski, K. Fedoruk, M. Stefański, A. Pikul, *Hybrid organic-inorganic crystals of [methylhydrazinium]$M^{II}Cl_3$ (M^{II} = Co, Ni, Mn)*, J. Phys. Chem. C **2022**, 126 (37), 15809-15818, doi: 10.1021/acs.jpcc.2c04893.

[**D4**] J.A. Zienkiewicz*, D.A. Kowalska, D. Drozdowski, A. Pikul, M. Ptak*, *Hybrid chlorides with methylhydrazinium cation:[$CH_3NH_2NH_2$]$CdCl_3$ and Jahn-Teller distorted [$CH_3NH_2NH_2$]$CuCl_3$*, Molecules **2023**, 28 (2), 473, doi: 10.3390/molecules28020473.

[**D5**] J.A. Zienkiewicz*, K. Kałduńska, K. Fedoruk, A.J. Barros dos Santos, M. Stefański, W. Paraguassu, T.M. Muzioł, M. Ptak, *Luminescence and dielectric switchable properties of a 1D (1,1,1-trimethylhydrazinium)PbI_3 hybrid perovskitoid*, Inorg. Chem. **2022**, 61 (51), 20886-20895, doi: 10.1021/acs.inorgchem.2c03287.

1.4. Perowskity

1.4.1. Pochodzenie nazwy

Historia badań perowskitów zaczyna się w roku 1839, kiedy niemiecki mineralog Gustav Rose w górach Ural odkrył minerał będący tytanianem(IV) wapnia, $CaTiO_3$. Nazwa tego minerału – perowskit – upamiętnia Lwa Aleksiejewicza Perowskiego, rosyjskiego arystokratę i mineraloga, który w latach 1841-1852 pełnił funkcję ministra spraw wewnętrznych w administracji cara Mikołaja I.

Struktura perowskitu została po raz pierwszy zaproponowana w roku 1926 przez norweskiego mineraloga, Viktora Moritza Godschmidta [1]. Dokładna struktura analogicznego związku $BaTiO_3$, wyznaczona na podstawie pomiarów dyfrakcyjnych, została następnie opublikowana w roku 1945 przez irlandzką krystalograf Helen Megaw [2].

Pomimo, że termin „perowskit" odnosi się w ścisłym znaczeniu do opisanego powyżej związku, powszechnie jest on także stosowany do nazywania związków o podobnej budowie, które poprawnie powinny być nazywane „związkami o budowie typu perowskitu". Biorąc pod uwagę powszechność tego uproszczenia w literaturze naukowej, w dalszych rozdziałach oba te terminy traktowano zamiennie.

1.4.2. Rodzaje perowskitów

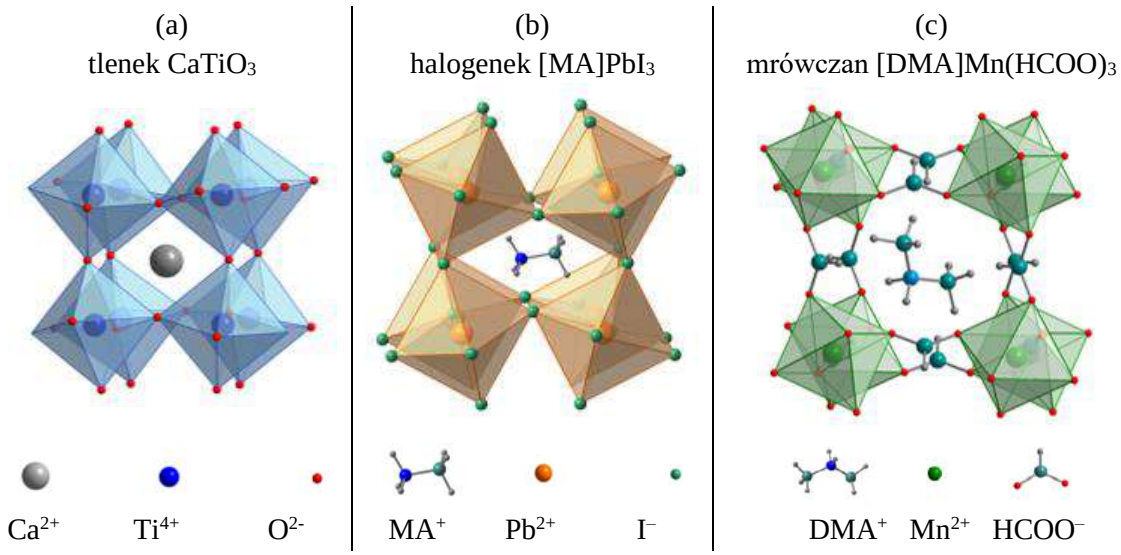

Rysunek 1. Porównanie schematycznej struktury trójwymiarowych perowskitów – tlenkowego $CaTiO_3$ (a), hybrydowego halogenkowego $[MA]PbI_3$ (MA^+ = kation metyloamoniowy) (b) oraz hybrydowego mrówczanowego $[DMA]Mn(HCOO)_3$ (DMA^+ = kation dimetyloamoniowy) (c).

Struktura nieorganicznego tlenkowego perowskitu o wzorze ogólnym ABO_3, gdzie A i B są kationami, przy czym A jest większy od B, składa się z trójwymiarowej sieci oktaedrów BO_6 połączonych wierzchołkami. Kationy A, które kompensują ładunek ujemny sieci, zajmują luki o sześciennym kształcie powstałe w podsieci BO_6 (Rysunek 1a). Idealna struktura perowskitu jest strukturą regularną ($Pm\overline{3}m$), której każda deformacja wynikająca z niedopasowania kationów A oraz B, powoduje obniżenie symetrii poprzez zniekształcenie lub odchylenie oktaedrów oraz przechylenia lub przesunięcia całych ich kolumn.

Współcześnie mianem perowskitów lub związkami typu perowskitu określa się większą grupę związków chemicznych, opisanych za pomocą wzoru ogólnego ABX_3, gdzie X jest prostym anionem lub większym ligandem, najczęściej jednoujemnym.

Ze względu na skład chemiczny, perowskity można podzielić na dwa główne rodzaje – nieorganiczne oraz hybrydowe organiczno-nieorganiczne HOIP (ang. *hybrid organic-inorganic perovskites*). w przypadku tych drugich, co najmniej jeden z jonów (zazwyczaj a lub X) jest zastąpiony przez jon organiczny w pozycji a znajdują się wówczas zazwyczaj kationy amoniowe (protonowane aminy) związane z podsiecią BX_6 wiązaniami wodorowymi, w pozycji B kationy metalu (zwykle dwuwartościowe), zaś w pozycji X jednoujemne aniony (ligandy), takie jak halogenkowy (Cl^-, Br^-, I^-) (Rysunek 1b), mrówczanowy ($HCOO^-$) (Rysunek 1c), fosforanowy(I) nazywany również zwyczajowo podfosforynowym ($H_2PO_2^-$), cyjankowy (CN^-), rodankowy (SCN^-), itp. [3]. Interesującym jest, że znane są również halogenkowe perowskity nie zawierające w swojej strukturze jonów metalu (ang. *metal-free organic halide perovskites*), które w pozycji B zawierają kation amonowy NH_4^+ [4,5].

Jednym z ważniejszych parametrów charakteryzujących perowskity jest tzw. współczynnik tolerancji TF (ang. *tolerance factor*), zaproponowany przez Goldschmidta w 1926 r. [1]. Określa on wzajemną relację rozmiarów kationów a oraz B i jest wyrażony równaniem (1):

$$\mathrm{TF} = \frac{r_A + r_X}{\sqrt{2}(r_B + r_X)}, \qquad (1)$$

gdzie r_A, r_B oraz r_X oznaczają odpowiednio promienie jonowe jonów obsadzonych w pozycjach A, B oraz X.

Nieregularna geometria kationów i anionów organicznych (A oraz X) wymusiła modyfikację wyrażenia na TF, którą zaproponował Gregor Kieslich w 2014 r. (2):

$$TF = \frac{r_{A,eff} + r_{X,eff}}{\sqrt{2}(r_B + 0{,}5h_{X,eff})}, \qquad (2)$$

gdzie $r_{A,eff}$ i $r_{X,eff}$ oznaczają promienie efektywne jonów znajdujących się w pozycjach a oraz X, zaś $h_{X,eff}$ oznacza efektywną wysokość jonu X definiowaną jako wysokość sztywnego cylindra, w którym ligand się mieści [6,7].

Zazwyczaj uznaje się, że warunkiem koniecznym do uzyskania archetypicznego trójwymiarowego (3D) perowskitu krystalizującego w układzie regularnym konieczne jest, aby wartość TF zawierała się pomiędzy 0,8 a 1,0. w przypadku, kiedy wartość współczynnika nie mieści się w tym zakresie, trójwymiarowe podsieci BX_6 prostych perowskitów nieorganicznych ulegają zniekształceniu, które powoduje obniżenie symetrii. w przypadku HOIP efekt jest zgoła różny, gdyż zbyt wysoka lub zbyt niska wartość TF może również powodować, że związek hybrydowy krystalizuje w układach o niższej rzędowości (0D-2D). Zakresy przykładowych parametrów TF wraz ze składem chemicznym oraz układami krystalograficznymi, w których krystalizują przykładowe związki HOIP o budowie perowskitu, zestawiono w Tabeli 1.

Tabela 1. Zestawienie zmiennych chemicznych, układów krystalograficznych oraz wartości TF dla wybranych HOIP opracowano na podstawie źródła literaturowego [3].

HOIP	**Kation**			**Układ krystalograficzny**	**TF**
	A	**B**	**X**		
Halogenki	MA^+ i FA^+	Pb^{2+}, Sn^{2+}, Ge^{2+}	I^-, Br^-, Cl^-	rombowy trygonalny tetragonalny regularny	~0,912–1,142
	PIP^+, $DABCO^+$	Cs^+, K^+, Rb^+	Cl^-	jednoskośny rombowy trygonalny	~0,922–1,037
Mrówczany	Cs^+, K^+, NH_4^+, MA^+, FA^+, GUA^+, EA^+, DMA^+, AZE^+, IM^+, Hy^+	Mg^{2+}, Mn^{2+}, Fe^{2+}, Co^{2+}, Ni^{2+}, Cu^{2+}, Zn^{2+}, Cd^{2+}	$HCOO^-$	jednoskośny rombowy trygonalny tetragonalny trójskośny trygonalny	~0,784–1,001 ~0,897–1,040
Azydki	MA^+, DMA^+, $TrMA^+$, TMA^+	Mn^{2+}, Cd^{2+}, Ca^{2+}	N_3^-	trójskośny jednoskośny regularny	~0,786–1,023
Dicyjanoamidy	$BTBA^+$, $BTEA^+$, SPh_3^+, $TPrA^+$	Mn^{2+}, Fe^{2+}, Co^{2+}, Ni^{2+}	$[N(CN)_2]^-$	rombowy tetragonalny	~1,142–1,166

Legenda: kation AZE^+, azetydyniowy; $BTBA^+$, benzylotributyloamoniowy; $BTEA^+$, benzylotrietyloamoniowy; $DABCO^+$, 1,4-diazabicyklo[2.2.2.]oktaniowy; DMA^+, dimetyloamoniowy; EA^+, etyloamoniowy; FA^+, formamidyniowy; GUA^+, guanidyniowy; Hy^+, hydrazyniowy; IM^+, imidazoliowy; MA^+, metyloamoniowy; PIP^+, piperazyniowy; SPh_3^+, trifenylosulfoniowy; TMA^+, tetrametyloamoniowy; $TrMA^+$, trimetyloamoniowy.

W trakcie realizacji pracy doktorskiej skupiono się szczególnie na właściwościach związków hybrydowych o wartościach parametrów TF przekraczających graniczną wartość 1 lub bliskich przekroczenia granicznych wartości charakterystycznych dla perowskitów jednowymiarowych, w tym chlorków metali przejściowych (Mn^{2+}, Co^{2+}, Ni^{2+}, Cu^{2+} oraz Cd^{2+})

z kationem metylohydrazyniowym (MHy^+), jodku ołowiu z kationem trimetylohydrazyniowym (Me_3Hy^+) oraz trójwymiarowego mrówczanu manganu z kationem dimetylohydrazyniowym ($DMHy^+$).

1.5. Związki hybrydowe typu perowskitu

Hybrydowe perowskity stanowią interesującą rodzinę związków, gdyż ze względu na swoją unikalną strukturę mogą w nich zachodzić zjawiska prowadzące do pożądanych cech nowoczesnych materiałów. Związki typu HOIP ze względu na rodzaj liganda oraz wymiarowość, posiadają mniej lub silniej elastyczną strukturę zdolną do tworzenia kilku faz pod wpływem temperatury lub ciśnienia [8]. Przemiany fazowe w związkach HOIP mogą mieć różny mechanizm, czasem dotyczą one wyłącznie kationu wewnątrz luki, innym razem wywołują też wpływ na właściwości strukturalne szkieletu. Najciekawsze są takie przemiany, podczas których organizacja trójwymiarowa kationu a i/lub podsieci nieorganicznej lub metal-ligand pozwala na pojawienie się porządku polarnego lub nawet zjawiska ferroelektryczności [9].

W wyniku przemian fazowych w związkach typu HOIP mogą występować przesunięcia kationów A w lukach lub kationów B wewnątrz oktaedrów. Najczęściej jednak obserwuje się przemiany typu porządek-nieporządek kationu a wewnątrz luk, gdyż jest słabo związany siecią wiązań wodorowych ze szkieletem [8,10]. Wiązania tego typu mogą być łatwo zerwane lub kation może po prostu się przekonfigurować i dopasować do dostępnej przestrzeni. Czasem porządkowaniu ulegają również ligandy łączące oktaedry [10].

Na skutek przemian fazowych można również obserwować przesunięcia całych kolumn względem sąsiednich, a także skręcenia oktaedrów lub ich całych kolumn. Wszystkie te zjawiska zmieniają kształt luki dostępnej dla kationu A i modyfikują wzajemne oddziaływania pomiędzy kationami a ligandami [11]. Zachodzące zmiany strukturalne prowadzą do modyfikacji pozostałych właściwości zależnych od struktury, tj. optyczne, dielektryczne, fononowe, itp. Dlatego tak niezbędnym jest zrozumienie mechanizmów przemian fazowych oraz wpływu jak największej ilości parametrów strukturalnych, dzięki czemu w przyszłości można będzie przewidywać charakter przemian oraz projektować materiały o dedykowanych właściwościach. Ponadto tak duża różnorodność składników strukturalnych i motywów architektury chemicznej, a także łatwość ich modyfikacji stanowią, że hybrydowe związki są praktycznie nieograniczonym źródłem nowoczesnych materiałów dla inżynierii molekularnej. Silnym impulsem dla ich doskonalenia są coraz nowsze doniesienia literaturowe o ich coraz lepszych właściwościach i zastosowaniach.

1.5.1. Związki trójwymiarowe (3D)

Mrówczany

Mrówczany metali zawierające w swojej budowie protonowane aminy są bardzo szeroką grupą trójwymiarowych materiałów typu perowskitu (Rysunek 1c). Zaliczane są również do grupy związków typu MOF (ang. *metal-organic framework*) [12]. Większość z nich przyjmuje typową dla perowskitów stechiometrię $AB(HCOO)_3$, w której B oznacza dwuwartościowy kation metalu [3,13,14]. w literaturze jest opisanych wiele mrówczanowych perowskitów hybrydowych wykazujących właściwości ferroelektryczne [15], ferroelastyczne [16], magnetyczne [17], luminescencyjne [18] czy dielektryczne [16]. Bardzo dużą uwagę poświęcono poszukiwaniom nowych materiałów wykazujących właściwości multiferroiczne [13,15,16], ze szczególnym uwzględnieniem tych, dla których uporządkowanie zarówno magnetyczne jak i elektryczne współwystępują w tej samej fazie [19].

Większość z wymienionych właściwości związana jest z występowaniem w tych materiałach przemian fazowych indukowanych temperaturą lub ciśnieniem. Ferroelastyczne i ferroelektryczne przejścia fazowe w mrówczanach są wywoływane głównie przez zmianę stopnia uporządkowania kationu w pozycji a (przejścia typu porządek-nieporządek) [16]. Zmiana uporządkowania jonu amoniowego silnie wpływa również na zmianę właściwości dielektrycznych, co w przypadku odwracalnych przejść fazowych powiązane jest z właściwością nazywaną przełączaniem dielektrycznym (ang. *dielectric switching*) [16].

Pomiary spektroskopowe w podczerwieni oraz ramanowskie są potężnym narzędziem w określaniu mechanizmów przejść fazowych typu porządek-nieporządek ze względu na wysoką czułość na zmiany dynamiki molekularnej, szczególnie fragmentów lub grup funkcyjnych zdolnych tworzyć sieć wiązań wodorowych [20].

Halogenki ołowiu

Hybrydowe perowskity z grupy halogenków ołowiu są szeroko znane z ich zastosowania do produkcji warstw pochłaniających światło w perowskitowych ogniwach słonecznych. Ze względu na konieczność dopasowania do reżimu rozmiarowego opisanego przez TF, istnieje bardzo niewielka grupa kationów amoniowych mogących spełnić warunki strukturalne pozwalające na utworzenie trójwymiarowych struktur perowskitowych HOIP.

Najszerzej znanymi i wykorzystywanymi są kationy metyloamoniowy (MA^+) [3,21–25] oraz formamidyniowy (FA^+) [21,26–30]. Halogenki ołowiu zawierające MA^+ oraz FA^+ przechodzą szereg przemian fazowych związanych z uporządkowaniem kationów w lukach. Ponadto wykazują one pewne właściwości, takie jak wysokie współczynniki absorpcji, niskie wartości przerw

energetycznych i wiązań ekscytonów oraz długie drogi dyfuzji nośników, które są pożądane w technologiach optoelektroniki [31]. Najlepiej zbadanymi perowskitami z tej grupy są $[MA]PbI_3$ [3,21–25] (Rysunek 1b) i $[FA]PbI_3$ [21,26–30]. w ostatnich latach otrzymano również trójwymiarowe analogi zawierające kation metylohydrazyniowy (MHy^+) [32,33] oraz azyrydyniowy (AZ^+) [34–36].

Dużo uwagi poświęcono także wpływowi domieszkowania różnymi kationami w pozycji a oraz różnymi ligandami na właściwości fizykochemiczne, głównie optyczne [37]. Dzięki otrzymywaniu materiałów o mieszanym składzie, możliwe jest sterowanie właściwościami optoelektronicznymi, w szczególności szerokością przerwy energetycznej oraz barwą emisji [38,39].

Trójwymiarowe halogenki ołowiu z kationami AZ^+, MA^+ oraz FA^+ mają jednak pewne wady, które utrudniają lub uniemożliwiają ich aplikacje, są to m. in. niska odporność na wilgoć oraz niska stabilność w przypadku nawet śladowych ilości zanieczyszczeń. Najbardziej stabilne i odporne są halogenki ołowiu z kationem MHy^+, gdyż związek ten zdolny jest tworzyć gęstszą sieć wiązań wodorowych z podsiecią PbX_6 ze względu na obecność dwóch grup aminowych.

1.5.2. Związki o niższej wymiarowości

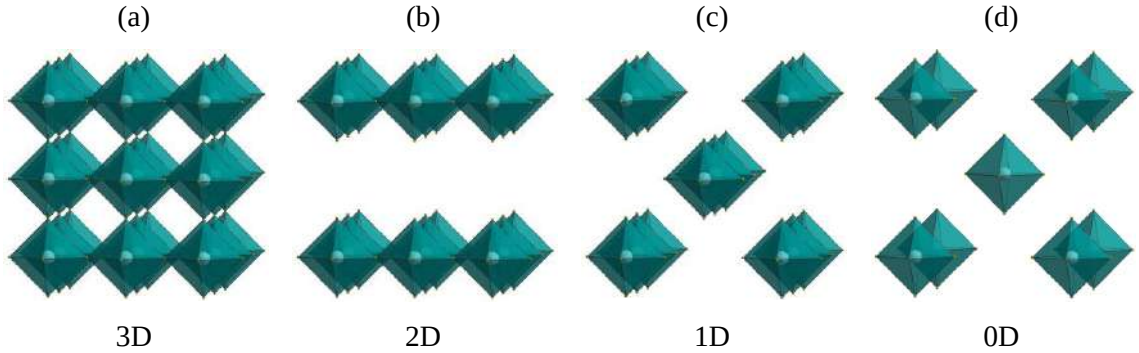

Rysunek 2. Schematyczne porównanie struktury trójwymiarowej 3D (a), dwuwymiarowej (warstwowej) 2D (b), jednowymiarowej (łańcuchowej) 1D (c) oraz zerowymiarowej (d).

Wymiarowość jest kluczowym parametrem opisującym struktury typu HOIP. Pomimo iż termin perowskit powinien być zarezerwowany jedynie dla materiałów trójwymiarowych, jest on powszechnie stosowany do niemalże wszystkich związków hybrydowych.

Zdecydowana większość materiałów HOIP to związki zbudowane z większych kationów A, a tym samym krystalizujące w strukturach o niższej wymiarowości: 2D – materiały głównie warstwowe, 1D – materiały łańcuchowe z pojedynczymi lub podwójnymi łańcuchami oktaedrów BX_6, 0D – materiały, w których oktaedry nie są połączone pomiędzy sobą (Rysunek 2). W materiałach 2D oraz 1D oktaedry mogą się łączyć pomiędzy sobą narożami, krawędziami lub

ścianami, a łańcuchy mogą być pojedyncze, podwójne, zygzakowate, itd. [40]. w każdym z tych przypadków, w dostępnych przestrzeniach podsieci BX_6 znajdują się kationy amoniowe A stabilizujące strukturę za pomocą wiązań wodorowych.

Molekularna wymiarowość materiałów perowskitowych może być łatwo zmodyfikowana poprzez dobór odpowiednich substratów na etapie syntezy. Wykorzystanie większych kationów amoniowych skutkuje zazwyczaj utworzeniem perowskitów o niższej wymiarowości. Warto dodać, że pomiędzy perowskitami trójwymiarowymi a warstwowymi istnieją też materiały o wymiarowości pośredniej (quasi-2D), które składają się ze stosów kilku warstw perowskitowych z wbudowanymi małymi kationami (MA^+, FA^+) odseparowanych od siebie większymi kationami separującymi (z ang. *spacer*). Struktury tego typu można otrzymać modyfikując warunki reakcji oraz skład mieszaniny reakcyjnej. Do najbardziej znanych przedstawicieli należą układy typu Diona-Jacobsona oraz Ruddlesdena-Poppera [41].

Wraz z wymiarowością zmieniają się także właściwości optoelektroniczne otrzymanych materiałów. Szczególne znaczenie ma odwrotna zależność pomiędzy wymiarowością materiału, a szerokością przerwy energetycznej oraz energią wiązania (ang. *binding energy*) [40].

1.5.3. Perowskitoidy

Termin „perowskitoid" (ang. *perovskitoid*) pojawił się w literaturze po raz pierwszy w 2017 roku. Został on wykorzystany do opisania związków o wzorze ogólnym ABX_3 krystalizujących w układzie heksagonalnym, np. $[TMA]SnI_3$ (Rysunek 3) [42].

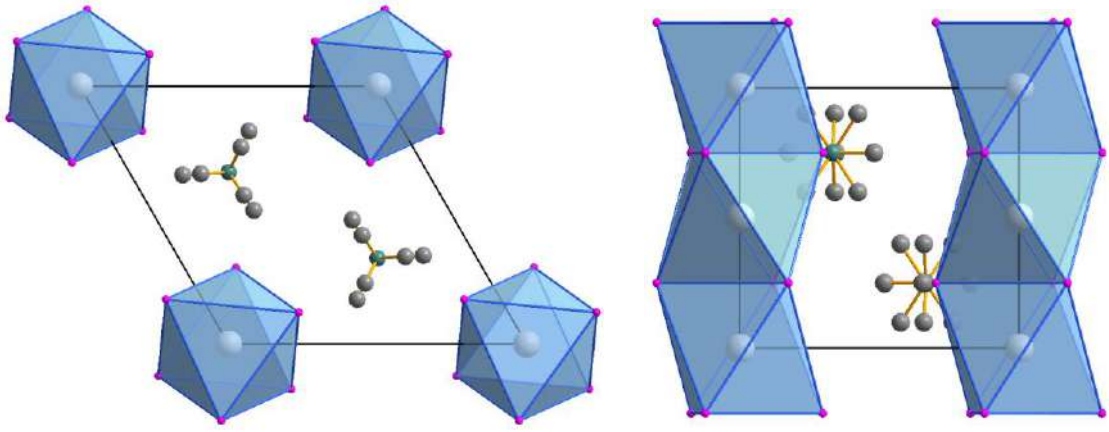

(a) (b)

Rysunek 3. Schemat łańcuchowej heksagonalnej struktury $P6_3/m$ typu perowskitoidu na podstawie danych krystalograficznych związku $[TMA]SnI_3$ zaprezentowany wzdłuż kierunku [001] (a) oraz [010] (b) [42]*; nieuporządkowane kationy tetrametyloamoniowe (TMA^+) narysowano bez atomów H.*

Kryształy perowskitoidów składają się z jednowymiarowych struktur łańcuchowych utworzonych przez połączone krawędziami oktaedry BX_6. Właściwości fizykochemiczne tych związków (w nomenklaturze tlenkowej nazywanych politypem 2H) znacząco różnią się od archetypicznych perowskitów, zbudowanych z oktaedrów połączonych narożami (polityp 3C) [42]. Wraz z popularyzacją pojęcia perowskitoid, terminem tym zaczęto nazywać również inne, podobne do archetypicznych perowskitów związki, zbudowane z łańcuchów oktaedrów BX_6 połączonych ścianami lub krawędziami [43], a same łańcuchy mogą być pojedyncze lub podwójne.

Podobnie jak perowskity trójwymiarowe i ich dwuwymiarowe odpowiedniki, perowskitoidy są związkami o znaczącym potencjalne aplikacyjnym na polu współczesnej optoelektroniki [42–44].

1.5.4. Kation hydrazyniowy i jego metylowe pochodne

Hydrazyna (diazan) jest związkiem nieorganicznym o wzorze ogólnym N_2H_4. Jej cząsteczka zbudowana jest z dwóch grup aminowych połączonych ze sobą pojedynczym wiązaniem N–N. Ma właściwości słabo zasadowe i zdolna jest do przyłączania jednego lub dwóch protonów. Zarówno hydrazyna, jak i jej pochodne, takie jak metylohydrazyna, czy 1,1-dimetylohydrazyna (DMHy), są bezbarwnymi, lotnymi, łatwopalnymi cieczami o zapachu amoniaku. Substancje te są silnymi reduktorami, dlatego znajdują zastosowanie w produkcji paliw rakietowych oraz materiałów wybuchowych.

W Tabeli 2 przedstawione zostały wzory strukturalne oraz rozmiary kationów hydrazyniowego (Hy^+), metylohydrazyniowego (MHy^+), 1,1-dimetylohydrazyniowego ($DMHy^+$) oraz 1,1,1-trimetylohydrazyniowego (Me_3Hy^+), które zostały wykorzystane do syntezy związków opisanych w niniejszej pracy.

Tabela 2. Wzory strukturalne, oznaczenia oraz promienie jonowe metylowych pochodnych kationu hydrazyniowego.

Kation	Hy^+	MHy^+	$DMHy^+$	Me_3Hy^+
Wzór strukturalny	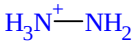	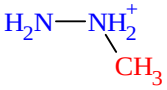	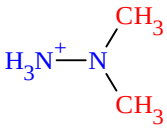	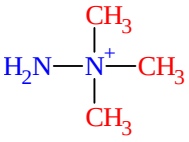
Promień jonowy (pm)	217 [7]	264 [32]	296 [45]	302*

* *rozmiar obliczony na podstawie danych krystalograficznych* [46] *za pomocą metody opisanej wcześniej w literaturze* [7]

Kation hydrazyniowy oraz jego metylowe pochodne są niezwykłą grupą, choć przez długi czas niedocenianą. w porównaniu do najszerzej badanych związków hybrydowych z relatywnie małymi kationami, takimi jak MA^+ czy FA^+, na chwilę obecną liczba znanych analogów materiałów zawierających pochodne hydrazyny pozostaje niewielka.

Ze względu na wiele możliwości podstawiania kationu hydrazyniowego grupami alkilowymi, układy te mogą zostać wykorzystane jako cząsteczki modelowe w badaniach wpływu zmieniających się właściwości strukturalnych, takich jak promień jonowy czy zawada przestrzenna, na właściwości otrzymanych hybrydowych perowskitów i perowskitoidów. Metylowe pochodne Hy^+ wykazują ponadto różną zdolność do tworzenia sieci wiązań wodorowych ze względu na zmienną liczbę donorowych atomów wodoru.

1.5.5. Materiały hybrydowe z pochodnymi kationu hydrazyniowego

Mrówczany metali przejściowych zawierające kationy Hy^+ i MHy^+

W literaturze dostępne są dane dotyczące mrówczanów metali podstawionych kationami Hy^+ o architekturze opartej na kationach Mn^{2+}, Co^{2+}, Zn^{2+}, Mg^{2+} i Fe^{2+} [47–49]. Ze względu na relatywnie niewielki rozmiar kationu hydrazyniowego, związki $[Hy]M^{II}(HCOO)_3$, gdzie M^{II} = Mn^{2+}, Zn^{2+} i Fe^{2+}, mogą występować zarówno w formie trójwymiarowych perowskitów, z sześciennymi przestrzeniami pomiędzy oktaedrami oraz w formie chiralnej, z heksagonalnymi kanałami, w których osadzone są kationy. Analogi zbudowane z kationów Co^{2+} i Mg^{2+} znane są jedynie w formie chiralnej [47–49].

Powyższe związki typu perowskitu w temperaturze ok. 350 K ulegają przejściu fazowemu typu porządek-nieporządek z niskotemperaturowej ferroelektrycznej fazy $Pna2_1$ do wysokotemperaturowej paraelektrycznej i nieuporządkowanej fazy *Pnma*. Analogi posiadające strukturę chiralną przechodzą natomiast z niskotemperaturowej fazy ferroelektrycznej $P2_12_12_1$ do wysokotemperaturowej fazy ferroelektrycznej $P6_3$ w zakresie temperatur 336-380 K. Wyjątkiem jest związek z kationami Mn^{2+}, który w fazie niskotemperaturowej przyjmuje symetrię $P2_1$, a przejście fazowe zachodzi w temperaturze 296 K [47–49].

Obecność grupy metylowej w kationie MHy^+ znacząco wpływa na właściwości strukturalne otrzymanych analogów. w związku z tym, dla związków $[MHy]M^{II}(HCOO)_3$, gdzie M^{II} = Mg^{2+}, Zn^{2+}, Mg^{2+} i Fe^{2+}, preferowana jest wyłącznie architektura perowskitowa [50]. W przypadku wszystkich wymienionych przedstawicieli z wbudowanymi kationami MHy^+ obserwowane są dwa przejścia fazowe związane ze stopniem uporządkowania kationu organicznego [50]. Pierwsze z nich zachodzi w zakresie temperatur 168-243 K, z fazy polarnej o symetrii *P*1 do pośredniej ferroelektrycznej i częściowo nieuporządkowanej fazy o symetrii *R*3*c*, która z kolei w zakresie temperatur ok. 310-327 K przechodzi do nieuporządkowanej wysokotemperaturowej fazy paraelektrycznej $R\bar{3}c$ (Rysunek 4). Wysokotemperaturowe przejście fazowe związane jest z dalszym nieuporządkowaniem kationów MHy^+, natomiast obserwowanej przemianie fazowej w niższych temperaturach towarzyszą również zmiany prowadzące do zniekształcenia szkieletu metalowo-mrówczanowego [50]. Analogi z kationami Mn^{2+} oraz Fe^{2+} wykazują ponadto magnetyczną przemianę fazową prowadzącą do uporządkowania magnetycznego poniżej odpowiednio 9 oraz 21 K [50].

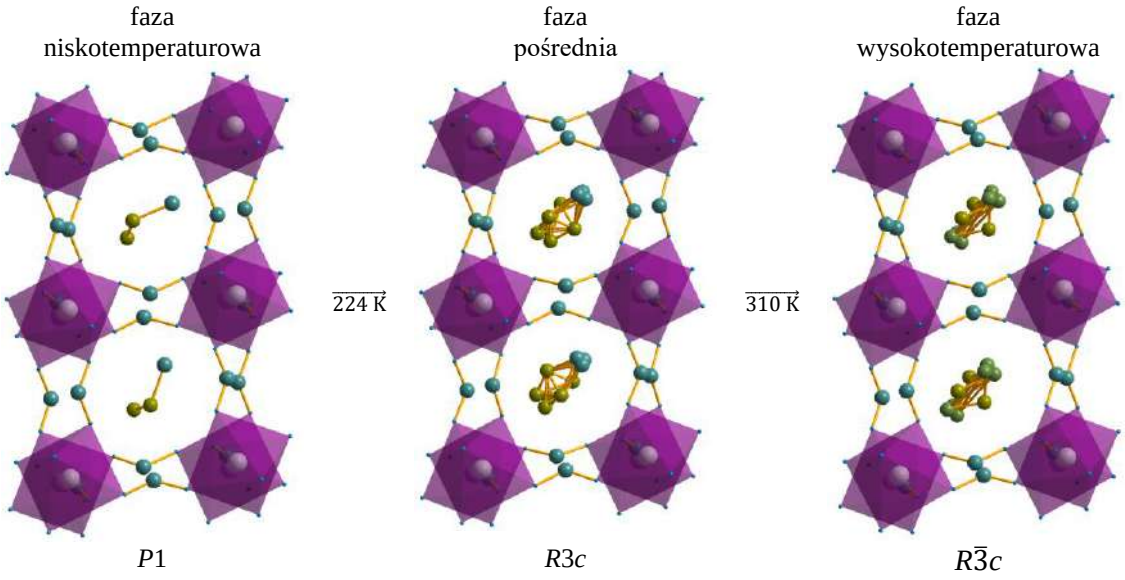

Rysunek 4. Schemat przemian fazowych obserwowanych dla [MHy]Mn(HCOO)$_3$; atomy H zostały pominięte [50].

Halogenki ołowiu zawierające kationy Hy$^+$ i MHy$^+$

Spośród halogenków ołowiu podstawionych wyłącznie kationem Hy$^+$, w literaturze znane są wyłącznie dwa związki jodkowe, prosty o wzorze [Hy]PbI$_3$ (polimorfy α i β) oraz bardziej złożony [Hy]$_{15}$Pb$_3$I$_{21}$ [51]. Pierwszy z nich, pomimo charakterystycznej dla perowskitów stechiometrii ABX$_3$, nie wykazuje archetypicznej struktury trójwymiarowej typu perowskitu. Związek α-HyPbI$_3$ krystalizuje w układzie rombowym, w grupie przestrzennej *Pnma*. Jego struktura krystaliczna zbudowana jest z podwójnych łańcuchów Pb$_2$I$_4$ propagujących w kierunku [001]. Łańcuchy te są otoczone kationami Hy$^+$ [51]. Drugi z polimorfów tego związku – β-[Hy]PbI$_3$ – opisywany jest przez symetrię heksagonalną i grupę przestrzenną *P*6$_3$/*mmc*. Jego jednowymiarowa struktura również składa się z łańcuchów propagujących w tym samym kierunku. Jednak w odróżnieniu od polimorfu α, są to pojedyncze łańcuchy oktaedrów PbI$_6$ połączonych ścianami [51]. Ten typ struktury jest charakterystyczny dla perowskitoidów [42].

Drugi ze związków, [Hy]$_{15}$Pb$_3$I$_{21}$, ma bardziej skomplikowaną budowę, gdyż składa się z dwóch rodzajów łańcuchów – podwójnych oraz pojedynczych. Ponadto część jonów jodkowych wykazuje nieporządek i każdy z nich może zajmować dwie pozycje [51].

Badania optyczne wskazują, że oba związki posiadają relatywnie niską przerwę energetyczną wynoszącą 2,34 eV dla polimorfów α- i β-HyPbI$_3$ oraz 2,70 eV dla [Hy]$_{15}$Pb$_3$I$_{21}$. Ponadto związek o bardziej skomplikowanej budowie wykazuje emisję poniżej 50 K z maksimum energii przy ok. 650 nm w zakresie światła czerwonego [51].

Kation MHy^+ ma niewiele większy promień jonowy (264 pm) od podobnego strukturalnie kationu FA^+ (253 pm) [52], dlatego oczekiwałoby się, że związek [MHy]PbI_3, podobnie do [FA]PbI_3, będzie również tworzyć strukturę trójwymiarową. Przeprowadzone badania wskazują jednak, że stabilny jest wyłącznie związek jednowymiarowy [MHy]PbI_3 krystalizujący w symetrii jednoskośnej, w grupie przestrzennej $P2_1/c$. Podobnie do α-[Hy]PbI_3, składa się on z podwójnych łańcuchów połączonych krawędziami oktaedrów PbI_6, pomiędzy którymi znajdują się kationy MHy^+. w 367 K zachodzi przemiana fazowa do metastabilnej fazy wysokotemperaturowej $P2_1/m$ będącej nadstrukturą fazy $P2_1/c$ w temperaturze pokojowej. Co ciekawe powrót do fazy $P2_1/c$ po ochłodzeniu jest bardzo wolny i trwa ok. 50 minut [53]. Badania optyczne wskazują, że przerwa energetyczna dla metylowanej pochodnej jest wyższa i wynosi 3,11 eV [53].

W przeciwieństwie do [MHy]PbI_3, analogiczne związki zbudowane z mniejszych ligandów [MHy]PbX_3 (X = Cl^-, Br^-) zdolne są wytworzyć stabilne trójwymiarowe fazy o strukturze typu perowskitu [32,33]. Oba związki zsyntezowano w 2020 r., dlatego są one relatywnie nowymi przedstawicielami tej niezwykle rzadkiej grupy trójwymiarowych związków HOIP. Na uwagę zasługuje fakt, że ich właściwości optyczne oraz elektryczne odbiegają od najbardziej dotychczas poznanych analogów z kationami MA^+ oraz FA^+.

[MHy]$PbBr_3$ krystalizuje w temperaturze pokojowej w układzie jednoskośnym, w polarnej grupie przestrzennej $P2_1$ i w 418 K ulega przejściu fazowemu do wysokotemperaturowej fazy regularnej charakterystycznej dla perowskitów ($Pm\bar{3}m$), w której kationy organiczne są silnie nieuporządkowane a oktaedry PbI_6 są mniej zdeformowane (Rysunek 5). Ze względu na rozmiar kationu MHy^+, podsieć nieorganiczna oktaedrów PbI_6 jest w tym materiale ekstremalnie zniekształcona w temperaturze pokojowej, co znacznie wpływa na pozostałe właściwości fizykochemiczne. w przeciwieństwie do analogów zawierających kationy MA^+ i FA^+, [MHy]$PbBr_3$ charakteryzuje się silnie niecentrosymetryczną strukturą już w temperaturze pokojowej, co bezpośrednio potwierdzono generacją drugiej harmonicznej SHG (ang. *second harmonic generation*) [32].

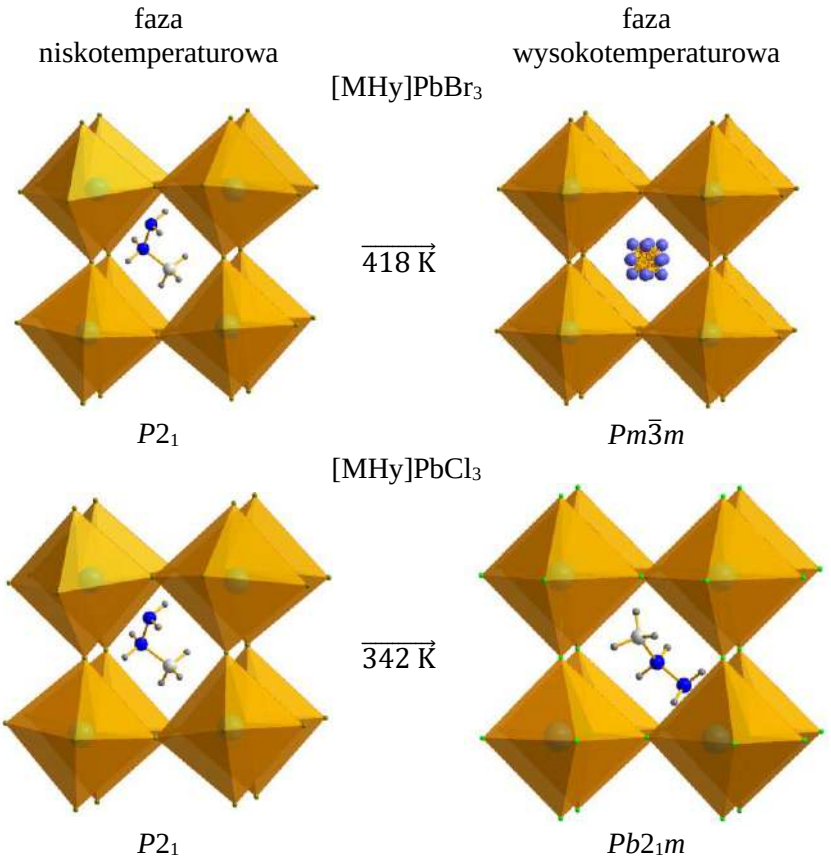

Rysunek 5. Fazy nisko- i wysokotemperaturowe trójwymiarowych perowskitów [MHy]PbX$_3$, gdzie X = Br$^-$, Cl$^-$.

Analog chlorkowy, [MHy]PbCl$_3$, również krystalizuje w temperaturze pokojowej w polarnej jednoskośnej strukturze $P2_1$, jednak w przeciwieństwie do [MHy]PbBr$_3$, w temperaturze 342 K przechodzi do również polarnej fazy rombowej ($Pb2_1m$) z uporządkowanymi kationami organicznymi (Rysunek 5). Ze względu na silną zmianę polarności w obu fazach, związek [MHy]PbCl$_3$ wykazuje zjawisko przełączania optycznego pomiędzy dwoma stanami różniącymi się intensywnością sygnału generacji drugiej harmonicznej [33].

Niezwykle interesujący jest fakt, że we wszystkich fazach [MHy]PbX$_3$ (X = Cl$^-$, Br$^-$) oprócz fazy regularnej $Pm\bar{3}m$, co druga warstwa oktaedrów Pb(2)X$_6$ (X = Cl, Br) jest znacznie silniej zniekształcona niż warstwy Pb(1)X$_6$ (Rysunek 5). Zjawisko to wyjaśniono rozmiarem kationów MHy$^+$ oraz ich asymetrią prowadzącą do powstawania dodatkowego wiązania koordynacyjnego pomiędzy jonami Pb^{2+} a atomem azotu z terminalnej i obojętnej grupy aminowej [32,33]. Tego typu zniekształcenie ma znaczący wpływ na wielkość przerwy energetycznej wynoszącej dla [MHy]PbCl$_3$ oraz [MHy]PbBr$_3$ odpowiednio 3,4 oraz 2,58 eV.

Ze względu na tak znaczne różnice, podjęto również próbę syntezy materiałów mieszanych o składzie [MHy]PbBr$_x$Cl$_{3-x}$ (x = 0,40, 0,58, 0,85, 1,33, 1,95, 2,25 oraz 2,55) [54]. Ustalono że, dla związków o współczynniku $x \leq 1{,}33$ zachodzi jedno przejście fazowe $P2_1 \rightarrow Pb2_1m$, podobnie do

niedomieszkowanego [MHy]$PbCl_3$. Dla $x \geq 1{,}95$ ze wzrostem temperatury zaobserwowano sekwencję dwóch przemian fazowych, $P2_1 \rightarrow Pb2_1m \rightarrow Pm\bar{3}m$ [54]. Wykazano, że wraz ze wzrastającą zawartością ligandów Br^-, przerwa energetyczna się zmniejsza a barwa emisji przesuwa się w kierunku niższych energii.

W literaturze występuje również wzmianka o mieszanym związku trójwymiarowym [MHy]$PbBr_{2,8}I_{0,2}$ [54]. Podobnie do niedomieszkowanego bromku wykazuje on bezpośrednie przejście fazowe pomiędzy polarną fazą $P2_1$ oraz wysokotemperaturową i nieuporządkowaną fazą $Pm\bar{3}m$ [54].

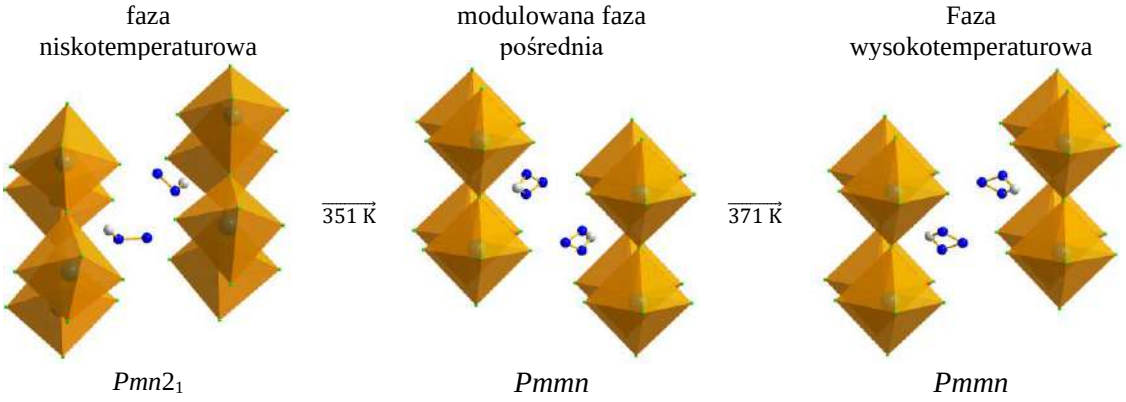

Rysunek 6. Struktury poszczególnych faz 2D perowskitu [MHy]$_2PbCl_4$. Atomy H zostały pominięte.

Poza trójwymiarowymi halogenkami ołowiu z kationami MHy^+, istnieją również halogenki warstwowe o składzie [MHy]$_2PbX_4$ (X = Cl^-, Br^-, I^-) należące do tzw. faz Ruddlesdena-Poppera [55–57]. [MHy]$_2PbCl_4$ w niskich temperaturach posiada polarną symetrię jednoskośna $P2_1$, która przy 224 K transformuje do modulowanej fazy rombowej a następnie powyżej 338 K przechodzi do nieuporządkowanej rombowej fazy *Pmmn*. Faza niskotemperaturowa oraz pośrednia są fazami polarnymi, co potwierdzono pomiarami SHG. Pomiary polaryzacji spontanicznej jednak nie potwierdziły ferroelektrycznego charakteru [MHy]$_2PbCl_4$. Warto dodać, że związek ten posiada rekordowo krótkie odległości pomiędzy warstwami oktaedrów wynoszące 8,79 Å w 350 K, a jego przerwa energetyczna wynosi 3,75 eV [57].

Zmiana liganda chlorkowego na bromkowy powoduje zmianę charakteru strukturalnych przemian fazowych $Pmn2_1$ → faza modulowana → *Pmnm*, które zachodzą przy grzaniu w 351 oraz 371 K. w tym przypadku potwierdzono ferroelektryczny charakter fazy $Pmn2_1$ w temperaturze pokojowej. Wartość wyznaczonej przerwy energetycznej dla [MHy]$_2PbBr_4$ jest niższa niż dla chlorku i wynosi 3,02 eV [56].

Analogiczny jodek, [MHy]$_2PbI_4$, wykazuje najniższą wartość przerwy energetycznej wynoszącą 2,20 eV. w niskich temperaturach posiada strukturę trójskośną $P\bar{1}$, która powyżej 233 K przechodzi do nieuporządkowanej fazy o symetrii rombowej *Pccn*. w trakcie dalszego grzania jodek

ulega transformacji do innej struktury rombowej *Pmmn* w 298 K oraz przechodzi izostrukturalną przemianę fazową w 320 K [55].

Kation MHy^+ został również wykorzystany do syntezy mieszanego dwuwymiarowego związku $[BA]_2[MHy]_2Pb_3Br_{10}$ (BA^+ = kation butyloamoniowy), w którym kationy BA^+ pełnią funkcję separatorów warstw perowskitowych z wbudowanymi kationami MHy^+ w lukach [58].

W literaturze pojawiła się również wzmianka dotycząca kationu Me_3Hy^+, który został wprowadzony do trójwymiarowej struktury $[MA]PbI_3$ użytej do wytworzenia ogniwa słonecznego [59]. Dodatek tego typu o stężeniu 7.5 mol% spowodował wzrost stabilności ogniwa, zmniejszenie ilości defektów, chropowatości powierzchni warstwy oraz wydajności konwersji energii, najbardziej kluczowego parametru charakteryzującego ogniwa. Wyjaśniono to siłą wiązania kationu Me_3Hy^+ z jonami Pb^{2+}, która zapobiega redukcji jonów ołowiu, co przyjęto za początkowe stadium rozpadu $[MA]PbI_3$ [59]. Jakiekolwiek właściwości związku $[Me_3Hy]PbI_3$ pozostają jednak nieznane.

Fosforany(I) manganu(II) zawierające kationy MHy^+

Jedną z nowszych grup hybrydowych perowskitów są fosforany(I) manganu podstawione kationami amoniowymi po raz pierwszy opisane w 2017 r. [11]. Jak do tej pory znane są co najmniej dwa związki należące do tej grupy, które zawierają kation MHy^+. Są to $[MHy]Mn(H_2PO_2)_3$ [60,61] oraz jego analog współdomieszkowany anionami mrówczanowymi, $[MHy]Mn(H_2PO_2)_{2,83}(HCOO)_{0,17}$ [60].

Niedomieszkowany układ krystalizuje w układzie rombowym, w grupie przestrzennej *Pnma*. w przeciwieństwie do analogów mrówczanowych, kationy MHy^+ w sieciach metalowo-fosforanowych pozostają uporządkowane w całym zakresie badanych temperatur i tworzą wiązania wodorowe średniej mocy z atomami tlenu reszt fosforanowych(I). Warto dodać, że w tych oddziaływaniach biorą udział obie grupy aminowe kationów MHy^+, podczas gdy w przypadku mrówczanowego analogu $[MHy]Mn(HCOO)_3$ wiązania wodorowe tworzyły jedynie środkowe grupy aminowe [60].

Cechą wspólną fosforanów(I) są nietypowe przesunięcia kolumnowe w strukturze oraz pochylenia oktaedrów MnO_6 spowodowane większą elastycznością szkieletu w porównaniu do związków mrówczanowych oraz ich silniejszą deformacją (Rysunek 7). Efektem tego zjawiska są rzadko obserwowane przemiany fazowe. $[MHy]Mn(H_2PO_2)_3$ wykazuje uporządkowanie antyferromagnetyczne poniżej 6,5 K [60].

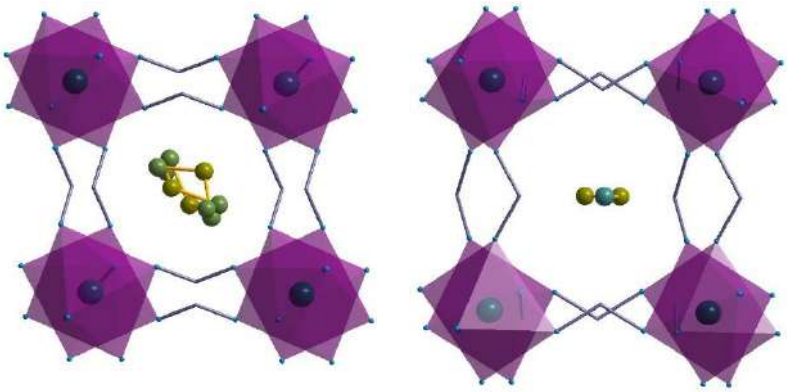

[MHy]Mn(HCOO)$_3$ [MHy]Mn(H_2PO_2)$_3$

Rysunek 7. Porównanie zniekształcenia szkieletu manganowo-mrówczanowgo (a) oraz manganowo-podfosforynowego (b). Atomy H zostały pominięte.

Niewielka domieszka anionu mrówczanowego nie ma znacznego wpływu na strukturę. Sprawia natomiast, że nieznacznie zmniejsza się objętość komórki elementarnej, co ma wpływ na właściwości optyczne, takie jak zmniejszenie czasu zaniku luminescencji w 77 K oraz energii aktywacji luminescencji [60].

1.6. Zastosowanie materiałów hybrydowych typu perowskitu

Wiele związków z rodziny perowskitów hybrydowych są wielofunkcjonalnymi materiałami wykazującymi szereg współwystępujących właściwości optycznych, [18,32,55,60,62,63], przełączalnych dielektrycznych [55,64,65], magnetycznych [17,45,66], ferroicznych [13,15,65,67–72] oraz multiferroicznych [13,15,19,67,73]. Predysponuje je do aplikacji w różnych aspektach przemysłu wysokiej technologii (ang. *high tech*), ze szczególnym uwzględnieniem optoelektroniki [74,75], jako diody LED (ang. *light emitting diode*) [76–80], fotodetektory [81,82], tranzystory [83,84] lub lasery [85,86].

W ostatnich latach sporą popularność zdobyły halogenki ołowiu podstawione kationami MA^+ i FA^+, które znane są ze swoich właściwości fotowoltaicznych [22,87]. Wydajność konwersji energii ciągle wzrasta poprzez doskonalenie ogniw perowskitowych i osiągnęła już 25.7% [88,89].

1.7. Zastosowanie spektroskopii IR oraz Ramana w badaniach przemian fazowych związków hybrydowych

Ponieważ metody spektroskopii oscylacyjnej są głównymi technikami badawczymi wykorzystywanymi do realizacji badań na potrzeby niniejszej pracy doktorskiej i w nich specjalizowałem się w trakcie studiów doktoranckich, warto wyjaśnić znaczenie i umotywować wykorzystanie tychże metod dla badania mechanizmów przemian fazowych w związkach

hybrydowych. Zarówno spektroskopia IR oraz Ramana, pomimo różnych podstaw fizycznych, są metodami dającymi wgląd do dynamiki molekularnej cząsteczek lub ich fragmentów. Obie metody pozwalają na określenie struktury chemicznej i są użyteczne w analizie jakościowej oraz ilościowej.

Metody spektroskopii oscylacyjnej są bardzo czułe na niewielkie zmiany strukturalne w otoczeniu lokalnym atomów lub ich grup, dlatego pozwalają na zaobserwowanie nawet subtelnych zmian strukturalnych wywołanych zmianą temperatury lub ciśnienia. Ponadto w przeciwieństwie do metod dyfrakcyjnych, które obrazują uporządkowanie dalekiego zasięgu, czułość spektroskopii IR i Ramana nie zmniejsza się w przypadku ruchów molekularnych atomów lekkich, takich jak wodór. Pomiary dyfrakcyjne dostarczają uśrednionej informacji, dlatego nie zawsze są tak dobre w określaniu zmian dynamicznych w określonych warunkach termodynamicznych [8,90,91]. w związku z tym metody spektroskopii oscylacyjnej stanowią ważne narzędzie w badaniu na przykład słabych oddziaływań molekularnych takich jak wiązania wodorowe. Metody dyfrakcyjne oraz spektroskopii oscylacyjnej są technikami doskonale się uzupełniającymi. Ponadto pomiary spektroskopowe wymagają mniej przygotowywań próbki oraz są znacznie szybsze. Wysoka czułość na niewielkie zmiany strukturalne pomaga również w określeniu zmian symetrii w wyniku zachodzących przemian fazowych oraz określaniu liczby nierównocennych cząsteczek lub jonów w strukturze, a tym samym siły rozszczepienia Davydova.

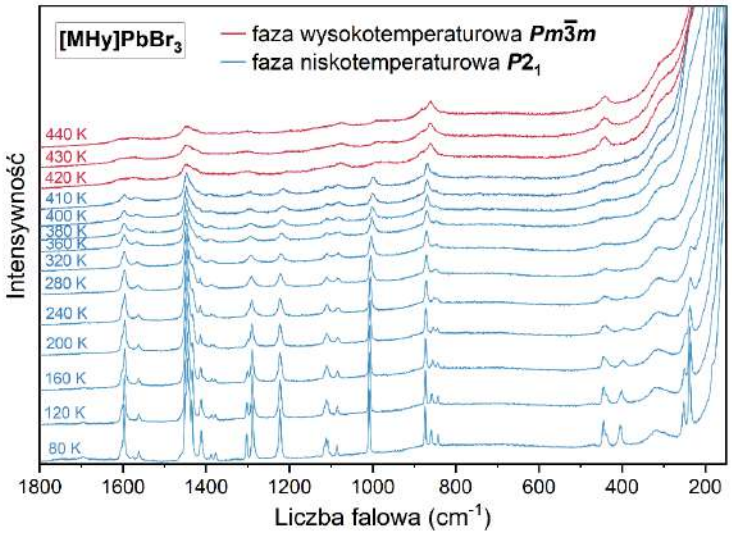

Rysunek 8. Zmiany na widmie Ramana zaobserwowane dla [MHy]PbBr$_3$ w wyniku przemiany fazowej porządek-nieporządek; niebieski kolor oznacza niskotemperaturową fazę uporządkowaną P2$_1$, natomiast czerwony nieuporządkowaną, wysokotemperaturową fazę Pm$\bar{3}$m.

W przypadku związków typu HOIP, za pomocą metod spektroskopii molekularnej najczęściej bada się układy, w których występują przemiany fazowe typu porządek-nieporządek. Zmieniająca się dynamika, najczęściej kationu A, jest doskonale widoczna na widmach IR

i Ramana jako poszerzenia lub zwężenia pasm. Ponadto w efekcie przemian fazowych widać również przesunięcia i/lub rozszczepienia związane ze zmianami symetrii (Rysunek 8). Co więcej obie metody spektroskopowe pozwalają niekiedy na rozróżnienie nieporządku dynamicznego oraz statycznego [8,90,92–96].

Dokładna analiza zmian parametrów pasm, takich jak położenie i szerokość połówkowa w funkcji temperatury lub ciśnienia, pozwala na dokładne zrozumienie mechanizmów przemian fazowych. Do tego niezbędne jest wykonanie jak najdokładniejszego przypisania obserwowanych pasm do odpowiednich drgań molekularnych. Pomocna w tym zakresie jest analiza porównawcza podobnych związków, podstawienia izotopowe oraz obliczenia kwantowo-chemiczne. Do zrozumienia przemian fazowych przydatna się również analiza grupy faktorowej oraz wykonanie diagramów korelacyjnych pozwalających na określenie reguł wyboru dla poszczególnych faz lub zrozumienie rozszczepień pasm o określonych symetriach.

Dla większości spektroskopistów zajmujących się pomiarem widm IR i Ramana, najważniejszy jest zakres drgań wewnętrznych. Dostarczają one cennych informacji na temat drgań poszczególnych grup funkcyjnych w cząsteczkach. Dla spektroskopistów zajmujących się fizykochemią ciała stałego równie ważnym zakresem jest zakres drgań sieciowych (zewnętrznych) – najczęściej poniżej 200-300 cm^{-1}. Zakres ten dostarcza informacji na temat dalekozasięgowego uporządkowania w kryształach. Ponadto próbkuje on dynamikę molekularną drgań związanych z ruchami jonów metali i ich najbliższego otoczenia, co pozwala na określenie zachowania się podsieci metal-ligand. Ogromne znaczenie ma to dla HOIP zbudowanych z oktaedrów halogenków ołowiu (PbX_6, gdzie X = Cl^-, Br^-, I^-), gdyż to właśnie zmiany strukturalne podsieci nieorganicznej (pochylenia, skręcenia i deformacje) są odpowiedzialne za istotne właściwości związane z parametrami optoelektronicznymi [94,95,97,98].

Równie ważną rolę pełnią badania ciśnieniowe, ponieważ są one prostsze do wykonania oraz analizy w porównaniu z eksperymentami dyfrakcyjnymi. Ciśnienie hydrostatyczne ma znaczący wpływ na dynamikę kationów w lukach oraz na zniekształcenie podsieci metal-ligand, dlatego pozwala na poznanie właściwości materiałów w ekstremalnych warunkach. Najczęściej wykonuje się pomiary widm Ramana w podwyższonym ciśnieniu, ale pomiary widm IR są również możliwe [99–103]. Oczywistym jest, że największe zmiany na widmach są otrzymywane dla silnie anizotropowych materiałów jedno- oraz dwuwymiarowych z wyraźnymi kierunkami, w których kompresja struktury jest najsilniejsza [104,105].

2. Materiały i metody

2.1. Synteza materiałów

W tym rozdziale opisane zostaną metody otrzymywania perowskitów wykorzystane podczas syntez związków omawianych w pracy. Bazują one na wykorzystaniu metod chemii mokrej a ogólny przebieg reakcji można przedstawić za pomocą równania (3)

$$A^{+}_{solv} + B^{2+}_{solv} + 3X^{-}_{solv} \rightarrow ABX_3 \downarrow, \qquad (3)$$

gdzie A^{+}_{solv}, B^{2+}_{solv} i X^{-}_{solv} oznaczają odpowiednio solwatowane jony amoniowy, dwuwartościowy jon metalu i anion reszty kwasowej.

Metoda powolnego odparowania z roztworu

W najprostszym ujęciu, metoda powolnego odparowania (ang. *slow evaporation method*) polega na otrzymaniu nasyconego (lub bliskiego nasycenia) roztworu substratów w rozpuszczalniku, a następnie powolnego jego odparowywania aż do pojawienia się odpowiednich rozmiarów kryształów produktu. Proces ten może być przeprowadzany zarówno w warunkach atmosferycznych, atmosferze gazu ochronnego, pod zmniejszonym ciśnieniem lub w podwyższonej temperaturze. Można również zastosować kombinację tych parametrów.

Istnieje również wariant tej metody, w którym zamiast jednego rozpuszczalnika, wykorzystuje się układ dwóch rozpuszczalników różniących się lotnością, polarnością oraz temperaturą wrzenia. Różnice te sprawiają, że występują różnice w rozpuszczalności produktu pomiędzy użytymi rozpuszczalnikami. Rozpuszczalniki należy dobrać tak, żeby oczekiwany produkt lepiej rozpuszczał się w bardziej lotnym z nich. Odparowanie bardziej lotnego rozpuszczalnika spowoduje powstawanie produktu, natomiast zanieczyszczenia (np. nieprzereagowane resztki substratów) pozostaną rozpuszczone w mniej lotnym rozpuszczalniku. Metoda ta daje możliwość dużej kontroli nad procesem wzrostu kryształów poprzez szybkość odparowywania dzięki regulacji temperatury i ciśnienia a także możliwości częściowego zakrycia naczynia, w którym prowadzony jest proces.

Metoda powolnego odparowywania z roztworu została wykorzystana podczas syntezy $[MHy]M^{II}Cl_3$ (M^{II} = Mn^{2+}, Co^{2+}, Ni^{2+}, Cu^{2+} oraz Cd^{2+}).

Metoda przeciwrozpuszczalnikowa

Metoda przeciwrozpuszczalnikowa (ang. *antisolvent method*) bazuje na wykorzystaniu układu dwóch wzajemnie mieszalnych rozpuszczalników, przy czym produkt reakcji rozpuszcza się tylko w jednym z nich. Podczas tej metody substraty rozpuszcza się w niewielkim naczyniu, które pozostaje niecałkowicie zamknięte, aby umożliwić transport par rozpuszczalnika. Naczynie to umieszcza się wewnątrz zamkniętego naczynia z drugim rozpuszczalnikiem (Rysunek 9a). Opary przeciwrozpuszczalnika rozpuszczają się w roztworze substratów, powodując zmniejszenie rozpuszczalności produktu, co prowadzi do wzrostu kryształów. Metoda ta została wykorzystana podczas syntezy $[Me_3Hy]PbI_3$.

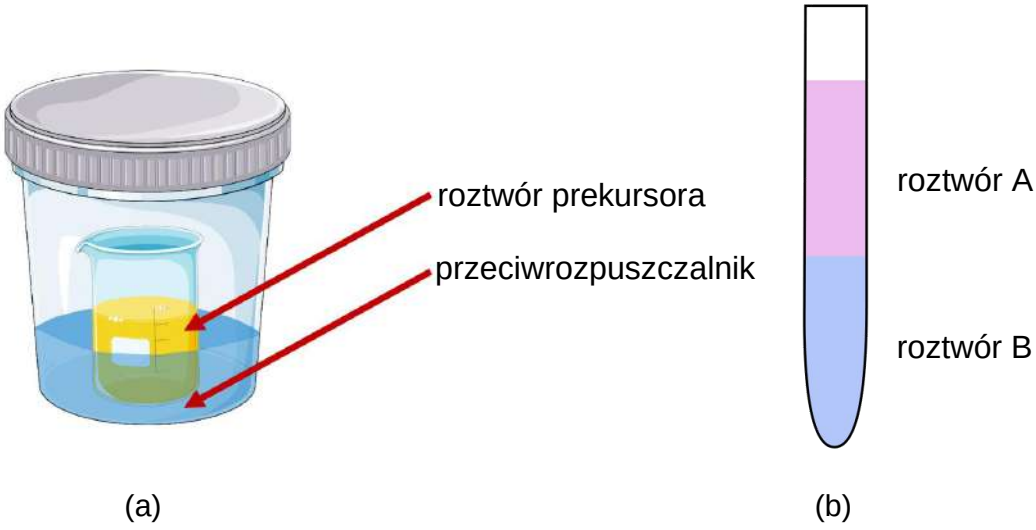

Rysunek 9. Schemat syntezy z wykorzystaniem metody przeciwrozpuszczalnikowej (a) oraz dyfuzyjnej (b).

Metoda strąceniowa

Metoda strąceniowa polega na wytrąceniu z roztworu nierozpuszczalnego produktu. Procedura syntezy polega na zmieszaniu przygotowanych wcześniej dwóch stężonych roztworów w metanolu. Jeden z roztworów (A) zawiera rozpuszczoną sól metalu (zwykle chloran(VII) lub chlorek), natomiast drugi odpowiednią aminę z dodatkiem nadmiaru odpowiedniego kwasu (B). Ze względu na potencjalne wybuchowe właściwości chloranów(VII), wykorzystuje się niewielkie ilości soli metalu. Metoda ta została wykorzystana do syntezy $[DMHy]Mn(HCOO)_3$.

Metoda dyfuzyjna

Metoda dyfuzyjna (ang. *diffusion method*) jest wariacją metody strąceniowej. Polega ona na krystalizacji produktu na granicy dwóch ciekłych faz stanowionych przez roztwory A i B, których przygotowanie opisano powyżej. Reakcję prowadzi się w długich (ok. 50 cm) probówkach o średnicy 8-10 mm umożliwiających wlanie roztworu o większej gęstości (B) na dno probówki, a następnie powolne dodanie po ściankach roztworu o mniejszej gęstości (A) tak, aby roztwory nie uległy zmieszaniu i wytworzyła się granica faz (Rysunek 9b). Metoda ta powoduje powolny wzrost kryształów i prowadzi do małej ilości produktu. Pozwala jednak na otrzymanie większych kryształów w porównaniu do metody strąceniowej.

Metodę dyfuzyjną stosowano równolegle z metodą strąceniową do otrzymania $[DMHy]Mn(HCOO)_3$.

2.2. Metody pomiarowe

Metody dyfrakcyjne

Pomiary dyfraktometrii rentgenowskiej XRD (ang. *X-ray diffraction*) na monokryształach $[MHy]M^{II}Cl_3$ (M^{II} = Mn^{2+}, Co^{2+}, Ni^{2+}, Cu^{2+} oraz Cd^{2+}) oraz $[DMHy]Mn(HCOO)_3$ wykonano przy użyciu dyfraktometru czterokołowego Xcalibur Atlas oraz promieniowania MoKα (λ = 0,71073 Å) (INTiBS PAN). Pomiary dyfrakcyjne na monokryształach $[Me_3Hy]PbI_3$ wykonano na Uniwersytecie im. M. Kopernika (UMK) w Toruniu przy użyciu czterokołowego dyfraktometru XtaLAB Synergy-S oraz promieniowania MoKα.

Proszkowe pomiary dyfraktometryczne związków $[MHy]M^{II}Cl_3$ (M^{II} = Mn^{2+}, Co^{2+}, Ni^{2+}, Cu^{2+} oraz Cd^{2+}) oraz $[DMHy]Mn(HCOO)_3$ wykonano przy użyciu dyfraktometru proszkowego X'Pert PRO oraz promieniowania CuKα1 (λ = 1,54056 Å) (INTiBS PAN). Temperaturowe dyfraktogramy proszkowe dla związku $[Me_3Hy]PbI_3$ zmierzono stosując dyfraktometr Rigaku XtaLAB Synergy-S system również wyposażony w katodę miedziową (UMK).

Metody cieplne

Pomiary skaningowej kalorymetrii różnicowej DSC (ang. *differential scanning calorimetry*) wykonano na Politechnice Wrocławskiej (PWr) stosując kalorymetr Mettler Toledo DSC-1 o rozdzielczości 0,4 μW oraz szybkość grzania/chłodzenia 5 K/min.

Analizę termograwimetryczną TGA (ang. *thermogravimetric analysis*) dla $[Me_3Hy]PbI_3$ wykonano w INTiBS PAN przy użyciu urządzenia PerkinElmer TGA 4000 i zastosowaniu szybkości grzania/chłodzenia równej 5 K/min.

Pomiary dielektryczne

Widma szerokopasmowej spektroskopii dielektrycznej BDS (ang. *broadband dielectric spectroscopy*) wykonano na PWr stosując analizator impedancyjny Novocontrol Alpha oraz napięcie 1 V o częstotliwości w zakresie $1\text{-}10^6$ Hz w zależności od próbki. Temperaturę kontrolowano przy użyciu kriostatu Novocontrol Quattro. Pomiary wykonywano na zorientowanych monokryształach lub pastylkach.

Pomiary magnetyczne

Pomiary magnetyzacji od 2 K do temperatury pokojowej zostały wykonane w INTiBS PAN przy użyciu magnetometru Quantum Design MPMS XL w polu magnetycznym do 70 kOe.

Pomiary optyczne

Pomiary widm rozproszonego odbicia w zakresie UV-Vis-NIR (200-2500 nm) wykonano stosując spektrometr Agilent Cary 5000 oraz przystawkę PryingMantis™.

Pomiary widm emisji wykonano stosując wielokanałowy analizator Hamamatsu PMA-12 oraz źródła wzbudzenia 266, 375, 405 lub 450 nm w zależności od próbki. Temperaturę próbki kontrolowano za pomocą kriostatu THMS600 (Linkam).

Czasy zaniku luminescencji zmierzono przy pomocy cyfrowego oscyloskopu Lecroy ze wzbudzeniem Nd:YAG (1064 nm) lub femtosekundowego lasera Coherent Model Libra. Wszystkie pomiary optyczne wykonano w INTiBS PAN.

Pomiary widm oscylacyjnych

Widma Ramana w zakresie 3500-50 cm^{-1} zmierzono przy użyciu spektrometrów Bruker FT 100/S oraz Bruker FT MultiRAM ze wzbudzeniem Nd:YAG (1064 nm) lub w zakresie 4000-50 cm^{-1} za pomocą spektrometru Renishaw inVia Raman sprzężonego z mikroskopem konfokalnym DM2500 Leica stosując wzbudzenie 488 nm.

Temperaturowe widma Ramana w zakresie 4000-50 cm^{-1} mierzono przy użyciu spektrometru Renishaw inVia Raman stosując wzbudzenie 488 nm. Temperaturę próbki kontrolowano za pomocą kriostatu THMS600 (Linkam).

Pomiary widm Ramana w zakresie 200-50 cm^{-1} w podwyższonym ciśnieniu dla kryształu $[Me_3Hy]PbI_3$ zmierzono na Uniwersytecie Federalnym Para w Belem (Brazylia) stosując spektrometr Horiba Labram Evolution oraz źródło wzbudzenia 514,5 nm. Wykorzystano diamentową komorę ciśnieniową Diacell μScopeDAC-RT(G) Almax easyLab ze stalową

uszczelką. Jako medium ciśnieniowe wykorzystano Nujol (olej mineralny). Wartość ciśnienia oszacowywano na podstawie przesunięć linii emisyjnych R_1 oraz R_2 rubinu.

Widma w zakresie średniej podczerwieni (mid-IR, 4000-400 cm^{-1}) zmierzono w formie pastylek w KBr, pasty w Nujolu lub Fluorolube (fluorowany olej mineralny) stosując spektrometr FTIR (ang. *Fourier-transform infrared*) Nicolet iS50. Dla próbki [DMHy]Mn$(HCOO)_3$ wykonano dodatkowe widma techniką ATR (ang. *attenuated total reflection*) na tym samym spektrometrze z zastosowaniem diamentu jako kryształu, w którym następuje całkowite wewnętrzne odbicie.

Temperaturowe widma w zakresie mid-IR w zakresie 3500-650 cm^{-1} zmierzono stosując mikroskop FT-IR Nicolet iN10. Temperaturę kontrolowano za pomocą kriostatu THMS600 (Linkam).

Pomiary widm w zakresie dalekiej podczerwieni (far-IR, 650-50 cm^{-1}) wykonano w formie pasty w Nujolu przy użyciu spektrometr FT-IR Nicolet iS50. Wszystkie pomiary widm IR oraz Ramana za wyjątkiem pomiarów ciśnieniowych widm Ramana wykonano w INTiBS PAN.

Obliczenia DFT

Optymalizację geometrii cząsteczki dimetylohydrazyny (DMHy) oraz kationu $DMHy^+$ wykonano przy użyciu programu Gaussian 03 [106] z zastosowaniem funkcjonału B3LYP [107–109] oraz bazy 6-311G(2d,2p) [110,111]. Ponadto obliczono teoretyczne widma IR oraz Ramana w przybliżeniu harmonicznym oraz anharmonicznym ze współczynnikami skalowania 0,96 oraz 0,98. Obliczenia wkładów PED (ang. *potential energy distribution*) do drgań obliczono w programie BALGA [112]. Wizualizacje drgań oraz obliczenia intensywności pasm Ramana zostały wykonane przy użyciu programu Chemcraft [113]. Obliczenia zostały wykonane na Uniwersytecie Ekonomicznym we Wrocławiu.

3. Opis najważniejszych wyników

Wyniki zawarte w pracy zawarte zostały w cyklu publikacji [D1]-[D6]. Prace [D1] i [D2] zostały poświęcone wynikom badań nad nowym mrówczanem z kationem $DMHy^+$, $[Me_2Hy]Mn(HCOO)_3$. Motywem przewodnim publikacji [D1] było zbadanie właściwości fizykochemicznych otrzymanego związku, a także określenie, w jaki sposób zmiana zawady przestrzennej kationu amoniowego wpływa na modyfikację właściwości otrzymanego materiału. Wyniki badań przedstawione w pracy [D1] zostały rozszerzone o pracę [D2], która jest poświęcona mechanizmowi izostrukturalnego przejścia fazowego, któremu ulega badany związek. Wyniki zawarte w publikacjach [D3] i [D4] dotyczą serii hybrydowych chlorków metali przejściowych zawierających kationy MHy^+ w swojej budowie. W tej pracy przedyskutowano wpływ kationu metalu na właściwości strukturalne oraz zależne od struktury.

Publikacja [D5] poświęcona została właściwościom fizykochemicznym perowskitoidu $[Me_3Hy]PbI_3$ ze szczególnym uwzględnieniem badania mechanizmów przemian fazowych, którym ulega. Tabela 3 zawiera listę otrzymanych związków wraz ze wskazaniem metody otrzymywania, danymi krystalograficznymi na temat przemian fazowych oraz temperatur, w których zachodzą.

Tabela 3. Zestawienie otrzymanych związków, metod syntezy oraz przemian fazowych, którym ulegają w temperaturach T.

Związek	Metoda syntezy [a]	Fazy [b]	T (K) [c]
$[MHy]MnCl_3$ [**D3**]	MO	$P2_1/n \rightarrow \mathbf{P2_1/m}$	242/243
$[MHy]CoCl_3$ [**D3**]	MO	$P2_1/n \rightarrow \mathbf{P2_1/m}$	227/229
$[MHy]NiCl_3$ [**D3**]	MO	$P2_1/n \rightarrow \mathbf{P2_1/m}$	223/224
$[MHy]CuCl_3$ [**D4**]	MO	$\mathbf{P2_1/c}$	–
$[MHy]CdCl_3$ [**D5**]	MO	$\mathbf{P\bar{1}}$	–
$[DMHy]Mn(HCOO)_3$ [**D1**], [**D2**]	MS/MD	$P2_1/n \rightarrow \mathbf{P2_1/n}$	244,4/283,0
$[Me_3Hy]PbI_3$ [**D5**]	MP	$Pbca \rightarrow \mathbf{P6_3/m} \rightarrow P6_3/mmc$	202/207, 320/322

[a] MO, metoda powolnego odparowywania roztworu; MS, metoda strąceniowa; MD, metoda dyfuzyjna; MP, metoda przeciwrozuszczalnikowa; [b] od niskich do wysokich temperatur, pogrubiona jest faza w temperaturze pokojowej; [c] chłodzenie/grzanie

3.1. Mrówczan manganu(II) z kationem $DMHy^+$

Pierwszy z wybranych do badań układów, związek hybrydowy $[DMHy]Mn(HCOO)_3$, otrzymany metodami strąceniową oraz dyfuzyjną, krystalizuje w układzie jednoskośnym, w grupie przestrzennej $P2_1/n$. Podczas chłodzenia w 244,4 K ulega on nietypowej dla mrówczanów izosymetrycznej przemianie fazowej, jednak ze znaczącymi zmianami strukturalnymi. Faza wysokotemperaturowa jest fazą, w której kationy $DMHy^+$ są nieuporządkowane pomiędzy trzema

stanami (Rysunek 10). Poniżej temperatury przemiany fazowej następuje ich porządkowanie, czemu towarzyszy zniekształcenie szkieletu manganowo-mrówczanowego [D1]. Jest to pierwszy mrówczanowy polimer koordynacyjny, dla którego opisano zjawisko izosymetrycznego przejścia fazowego typu porządek-nieporządek. Ponadto znaleziono ujemny współczynnik rozszerzalności cieplnej w kierunku [001] w fazie uporządkowanej. Warto zaznaczyć, że kation $DMHy^+$ jest do tej pory największym kationem, jaki udało się wykorzystać do otrzymania trójwymiarowych mrówczanów o składzie $[A]M^{II}(HCOO)_3$. Obliczono wielkość promienienia efektywnego kationu $DMHy^+$ (296 pm w 300 K), co pozwoliło stosując wzór (2) wyznaczyć współczynnik TF dla badanego związku wynoszący 1,01 [D1].

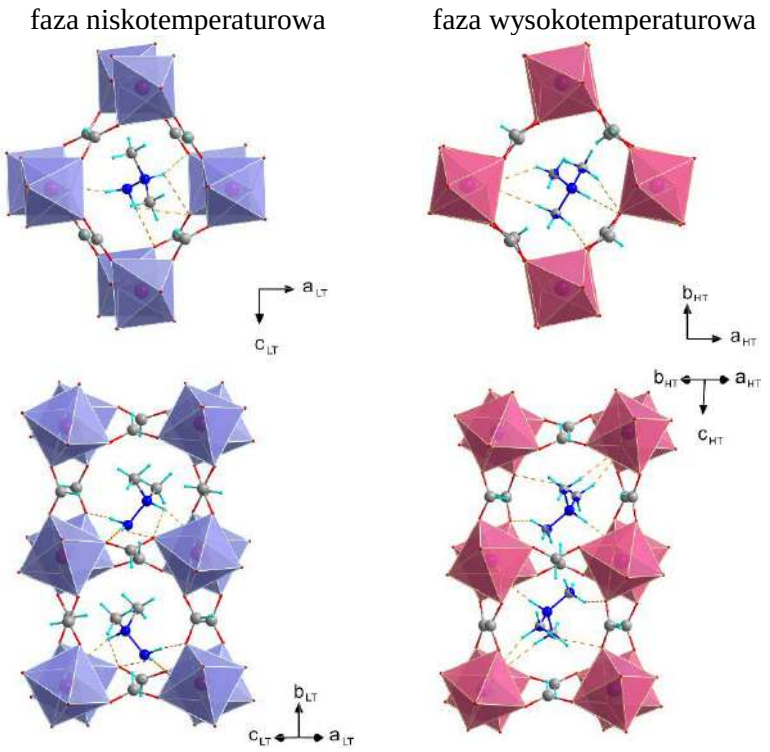

Rysunek 10. Porównanie nieuporządkowanej fazy wysokotemperaturowej oraz uporządkowanej fazy niskotemperaturowej w [DMHy]Mn(HCOO)$_3$ [1]

Badania DSC dowiodły, że przemiana fazowa ma charakter pierwszego rodzaju oraz charakteryzuje się znaczną histerezą termiczną (38,6 K). Oszacowana wartość zmiany entropii jest niższa niż przewidywana, co wskazuje na jej bardziej złożony mechanizm niż przewiduje model Boltzmanna [D1]. Wykonane pomiary dielektryczne wykazały skokowy charakter zmian, co charakteryzuje [DMHy]Mn(HCOO)$_3$ jako tzw. przełącznik dielektryczny.

[1] odtworzono z pracy [62] za zgodą Królewskiego Towarzystwa Chemicznego (Reproduced from Ref. [62] with permission from the Royal Society of Chemistry) [D1]

Praca [D2] stanowi kontynuację publikacji [D1] i koncentruje się na dokładnym zrozumieniu mechanizmu obserwowanej przemiany fazowej. w tym celu wykonano pomiary widm IR oraz Ramana w temperaturze pokojowej, wyznaczono reguły wyboru dla obu faz w oparciu o uzyskane dane krystalograficzne. Dzięki obliczeniom DFT dla cząsteczki DMHy oraz jej kationu zostały zaproponowane dokładne przypisania obserwowanych na widmie pasm do odpowiednich drgań [D2]. Szczególnie istotne było to dla dwóch różnych grup aminowych, kationu MHy^+. Dodatkowo przeprowadzone obliczenia DFT pozwoliły na określenie najsilniejszego wpływu wewnętrznego anharmonizmu dla drgań rozciągających grup metylowych oraz grup aminowych.

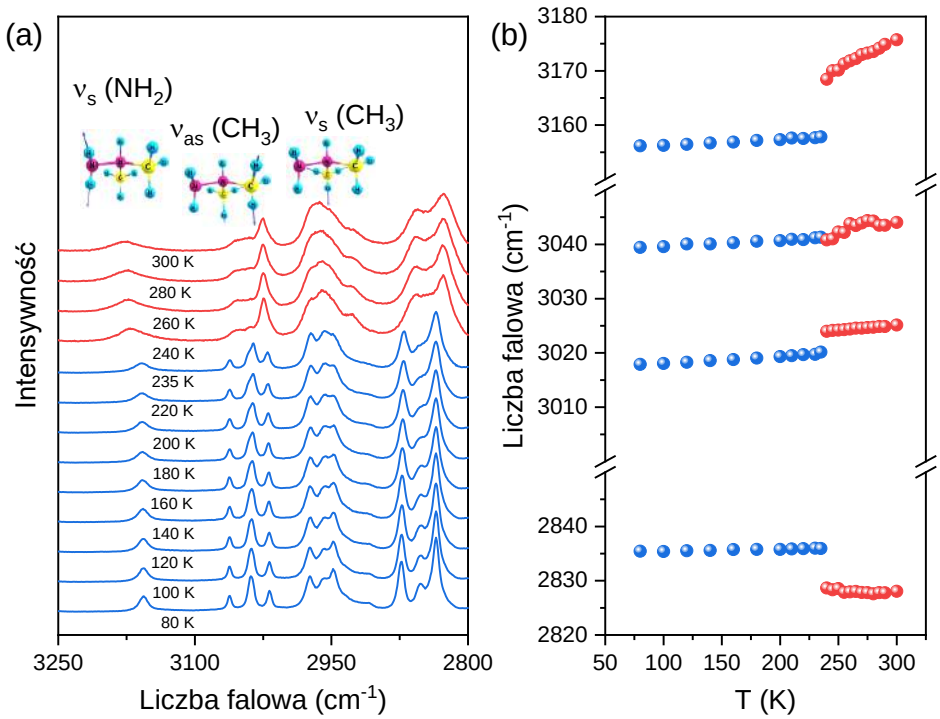

Rysunek 11. Temperaturowo-zależne widma Ramana w zakresie drgań rozciągających C–H oraz N–H (a) oraz zmiany położenia wybranych pasm w funkcji temperatury dla związku [MHy]MnCl$_3$ (b).

Zrozumienie natury powstawania obserwowanych pasm pozwoliło zanalizować ich temperaturowy charakter zmian, dzięki czemu potwierdzono przemianę typu porządek-nieporządek o silnie dynamicznym charakterze (Rysunek 11). Ponadto stwierdzono, że konformacja kationów $DMHy^+$ jest zachowana w obu fazach. Silne rozszczepienie pasm pochodzących od drgań sieciowych dowiodło zniekształcenia szkieletu manganowo-mrówczanowego. Są one wywołane zawadą przestrzenną relatywnie dużego kationu $DMHy^+$. Obserwowane zmiany na widmach wskazały również na zmianę sieci wiązań wodorowych i ich siły w wyniku przemiany fazowej. Oba typy grup aminowych mają znaczącą rolę w mechanizmie zachodzącej przemiany fazowej [D2]. Deformację oktaedrów w fazie niskotemperaturowej potwierdzono również za pomocą

parametrów strukturalnych obliczonych na podstawie danych krystalograficznych w publikacji [D1].

Wykonano również pomiary magnetyczne, które wskazały, że w badanym związku występuje słabe porządkowanie ferromagnetyczne poniżej 8,4 K [D1].

Wyznaczona przerwa energetyczna [DMHy]Mn(HCOO)$_3$ wynosi 4,63 eV. W zakresie temperatur poniżej 200 K, pod wpływem wzbudzenia promieniowaniem o długości fali 266 nm, materiał emituje promieniowanie o różowej barwie z energią termicznego wygaszania równą 62 meV. Wyznaczone czasy zaniku luminescencji wynoszą w 80 K τ_1 = 42,8 μs i τ_2 = 157,6 μs [D1].

W publikacji [D1], dla szeregu związków [A]Mn(HCOO)$_3$ (A = Hy^+, MHy^+, $DMHy^+$), przedyskutowano również zmiany wybranych parametrów strukturalnych oraz termodynamicznych, m.in. TF, parametry zniekształcenia oktaedrów MnO_6, odległości Mn–Mn, siłę wiązań wodorowych, liczbę mikrostanów w fazie nieuporządkowanej *N*, itp. Znaleziono liniową korelację pomiędzy współczynnikiem TF, parametrem nieporządku *N*, promieniem efektywnym kationu w pozycji A, odległością Mn–Mn oraz masą molową kationu w funkcji średniej wartości temperatury przemiany fazowej [D1].

Na podstawie tych parametrów określono, że rosnąca zawada przestrzenna, a tym samym rosnąca liczba grup metylowych, powoduje spadek liczby możliwych mikrostanów *N* oraz wpływa na zmianę entropii układu. Wartości wyznaczonych parametrów dowodzą, że kation Hy^+ jest najluźniej związany ze szkieletem manganowo-mrówczanowym, dlatego przemiana fazowa w [Hy]Mn(HCOO)$_3$ związana jest niemalże jedynie z porządkowaniem kationu. Zwiększenie liczby grup metylowych powoduje wzrost udziału deformacji szkieletu w trakcie przemiany fazowej, aż do jego silnego zniekształcenia w przypadku [DMHy]Mn(HCOO)$_3$, czego następstwem jest niska symetria jednoskośna. Efekt ten jest odpowiedzialny za zanik porządku ferroelektrycznego w badanym mrówczanie.

3.2. Halogenki metali przejściowych z kationem MHy^+

W publikacjach [D3] oraz [D4] skoncentrowano się na serii chlorków metali przejściowych zawierających w strukturze kationy MHy^+, o wzorze ogólnym [MHy]$M^{II}Cl_3$, gdzie M^{II} = Mn^{2+}, Co^{2+} Ni^{2+}, Cu^{2+} oraz Cd^{2+}. w pracy [D3] skoncentrowano się na analogach z kationami Mn^{2+}, Co^{2+} oraz Ni^{2+} wykazującymi przejścia fazowe oraz opisem ich właściwości fizykochemicznych. Natomiast w pracy [D4] opisano analogi zawierające w swoim składzie kationy Cu^{2+} oraz Cd^{2+} i skoncentrowano się na wyjaśnieniu przyczyn braku przemian fazowych.

Wszystkie wymienione w obu pracach związki otrzymane zostały metodą powolnego odparowania. Analogi manganowy, kobaltowy i niklowy krystalizują w temperaturze pokojowej w układzie jednoskośnym, w grupie punktowej $P2_1/m$. Należą do struktur jednowymiarowych i są one zbudowane z łańcuchów oktaedrów $M^{II}Cl_5N$ połączonych krawędziami, w których atom azotu

w pierwszej sferze koordynacyjnej kationu metalu pochodzi z terminalnej grupy NH_2 kationu MHy^+. Po ochłodzeniu poniżej 223-242 K związki te ulegają przemianie fazowej drugiego rodzaju, przechodząc do niskotemperaturowej jednoskośnej fazę o symetrii $P2_1/n$ [D3].

Podobną budową ma też niewykazujący przejść fazowych analog miedziowy, krystalizujący również w strukturze o symetrii jednoskośnej, w grupie punktowej $P2_1/c$. w jego przypadku, oktaedry $CuCl_5N$ budujące łańcuchy są wyraźniej zniekształcone ze względu na efekt Jahna-Tellera przyczyniający się do braku strukturalnych przemian fazowych [D4].

Właściwości strukturalne związku $[MHy]CdCl_3$ zdecydowanie różnią się od opisanych powyżej analogów. w przeciwieństwie do nich, atomy azotu kationów MHy^+ nie wchodzą w skład sfery koordynacyjnej. Ponadto związek ten, w przeciwieństwie do pozostałych badanych chlorków, jest zbudowany z podwójnych, zygzakowatych łańcuchów $[CdCl_3^-]_\infty$. Krystalizuje on w niższej symetrii trójskośnej opisywanej grupą przestrzenną $P\bar{1}$. Pomiędzy łańcuchami znajdują są uporządkowane kationy MHy^+, ustabilizowane siecią wiązań wodorowych [D4]. Typy struktur prezentowanych przez opisane analogi przedstawiono na Rysunku 12.

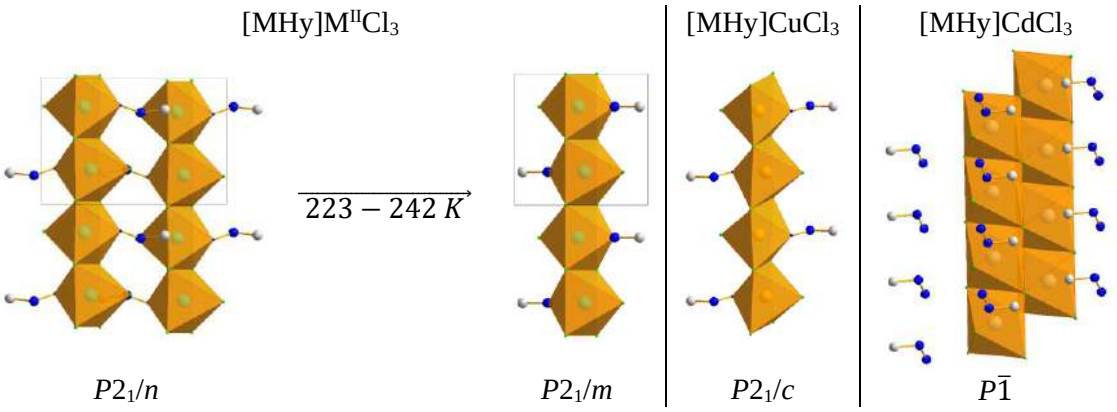

Rysunek 12. Struktury związków $[MHy]M^{II}Cl_3$, gdzie $M^{II} = Mn^{2+}$, Co^{2+} Ni^{2+}, $[MHy]CuCl_3$, oraz $[MHy]CdCl_3$. Atomy H zostały pominięte.

Wsparcie pomiarów krystalograficznych metodami spektroskopii IR i Ramana pozwoliło na uzyskanie szeregu informacji dotyczących struktur otrzymanych związków, co z kolei przyczyniło się do lepszego zrozumienia występowania przemian fazowych oraz ich mechanizmów w badanej serii związków. Dobrze znanym faktem jest, że położenie pasm pochodzących od drgań rozciągających grup NH_2/NH_2^+ jest silne zależne od mocy wiązań wodorowych pomiędzy kationem amoniowym a anionami; im wyżej obserwowane jest dane pasmo, tym słabsze wiązania wodorowe. Na tej podstawie stwierdzono, że spośród czterech analogów o koordynacji $M^{II}Cl_5N$, najsłabsze wiązania wodorowe występują dla analogu Mn^{2+}, zaś najsilniejsze dla Cu^{2+}. Jest to w dobrej zgodności z danymi krystalograficznymi, według których długość kontaktów Cl···H maleje w tej samej kolejności. Widma oscylacyjne analogu $[MHy]CdCl_3$ znacząco różnią się od pozostałych. Ze

względu na to, że atom azotu nie wchodzi w skład pierwszej sfery koordynacyjnej metalu, kation MHy^+ ma więcej swobody wewnątrz podsieci łańcuchów kadmowo-chlorkowych, co prowadzi do utworzenia bezpośrednich, krótkich i silnych wiązań wodorowych N–H···N pomiędzy dwoma sąsiednimi kationami MHy^+. Warto dodać, że tego typu wiązanie dla związków zawierających kationy MHy^+ w swojej budowie zostało zaobserwowane po raz pierwszy.

Obecność silniejszych wiązań wodorowych tłumaczy brak przemian fazowych analogów zawierających kationy Cd^{2+} i Cu^{2+}. Dodatkowo, związek $[MHy]CuCl_3$ wykazuje silny efekt Jahna-Tellera, który powoduje zniekształcenie oktaedrów $CuCl_5N$ tak silne, że na widmie absorpcji w zakresie UV-Vis zamiast pasm typowych dla koordynacji oktaedrycznej (O_h) pojawiają się pasma charakterystyczne dla koordynacji płaskiej kwadratowej $CuCl_4$ (D_{4h}).

Z siłą wiązań wodorowych nie zależy tak mocno temperatura przemian fazowych analogów zawierających jony Mn^{2+}, Co^{2+} i Ni^{2+}, których uszeregowanie pod względem elektroujemności jest odwrotnie proporcjonalne do temperatur przejść fazowych tych związków, a zatem wprost proporcjonalne do udziału wiązania jonowego w układzie M^{II}–Cl. Przejście fazowe w tej serii związków wiąże się z niewielkim zniekształceniem łańcuchów metalowo-chlorkowych, zmianą rozmiaru komórki elementarnej oraz z zanikiem płaszczyzny lustrzanej w fazie niskotemperaturowej. Niewielkie zmiany geometrii oktaedrów $M^{II}Cl_5N$ wpływają na organizację wiązań wodorowych, ich wzmocnienie oraz zwiększenie ich liczby w fazie niskotemperaturowej. Ustalono, że nie wiąże się to jednak ze zmianą konformacji kationów MHy^+.

Warto dodać, że dla analogów Mn^{2+}, Co^{2+} i Ni^{2+} zaobserwowano również wyraźne liniowe zależności pomiędzy promieniem jonowym i elektroujemnością, a parametrami sieci, objętością komórki elementarnej, kątem jednoskośnym β, odległością M^{II}–N, temperaturą przejścia fazowego, współczynnikiem tolerancji, przenikalnością dielektryczną oraz położeniem wybranych pasm IR/Ramana.

Ponadto dla związków z kationami Mn^{2+} i Ni^{2+} zaobserwowano czerwoną oraz żółtozieloną przechodzącą do pomarańczowej luminescencję pod wpływem energii naświetlania odpowiednio 450 oraz 375 nm. Oszacowane na podstawie pomiarów optycznych szerokości pasma wzbronionego wynoszą odpowiednio 5,57, 5,34, 3,96, 3,64 oraz 2,62 eV dla kryształów zbudowanych z kationów Cd^{2+}, Mn^{2+}, Ni^{2+}, Co^{2+} i Cu^{2+}.

Przeprowadzone pomiary magnetyczne wykazały, że analogi zawierające kationy Ni^{2+} i Co^{2+} wykazują uporządkowanie antyferromagnetyczne poniżej temperatury Néela ok. 3,7 K, natomiast analogi zbudowane z kationów Mn^{2+} i Cu^{2+} wykazują rozmyte uporządkowanie antyferromagnetyczne poniżej 5,0 K [D3, D4].

3.3. Jodek ołowiu z kationem Me_3Hy^+

W pracy [D5] skupiono się na syntezie i analizie właściwości fizykochemicznych perowskitoidu $[Me_3Hy]PbI_3$. Wykazuje on typową dla perowskitoidów jednowymiarową budowę, złożoną z połączonych ścianami łańcuchów oktaedrów PbI_6. Związek ten krystalizuje w heksagonalnej fazie o symetrii $P6_3/m$, w której kationy Me_3Hy^+ są nieuporządkowane (Rysunek 13a). Powyżej 321 K transformuje do innej heksagonalnej fazy $P6_3/mmc$, dla której obserwowane zmiany strukturalne są niewielkie, co potwierdza relatywnie niska zmiana entropii. Przemiana ta ma charakter drugiego rodzaju.

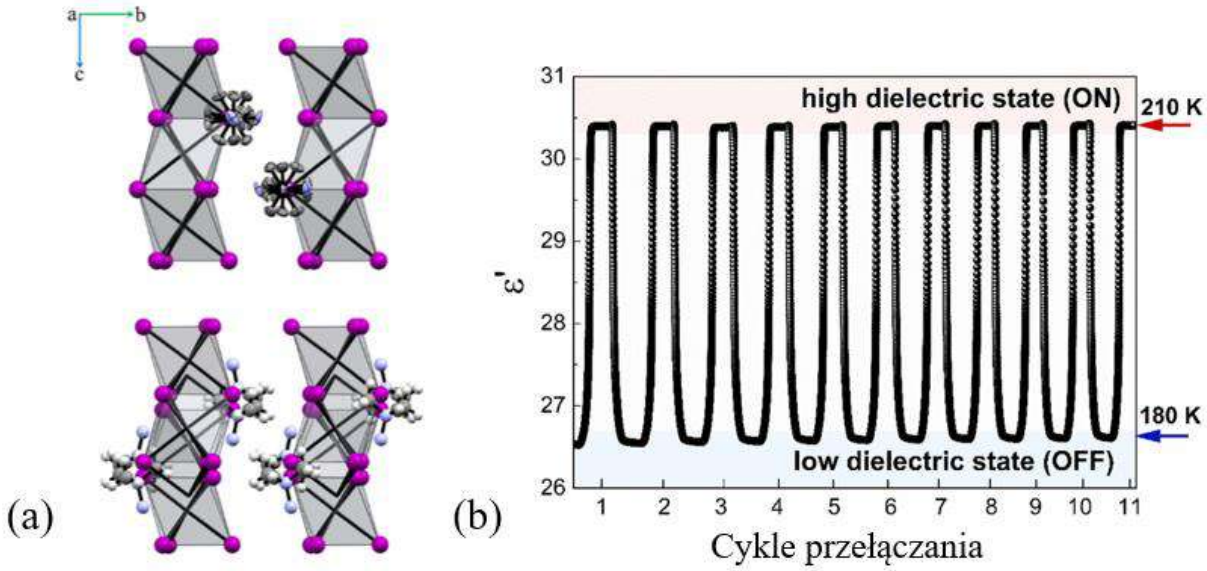

Rysunek 13. Porównanie struktur fazy nieporządkowanej w temperaturze pokojowej i uporządkowanej niskotemperaturowej (a) oraz 10 cykli tzw. przełączania dielektrycznego indukowanego temperaturą; rysunek opracowany na podstawie rysunków 3 i 4 z pracy [D5].

Poniżej 205 K w wyniku przemiany fazowej pierwszego rodzaju następuje porządkowanie kationów Me_3Hy^+, któremu towarzyszy przeorganizowanie wiązań wodorowych oraz niewielkie zniekształcenie łańcuchów oktaedrów. Ponadto przemiana ta jest powiązana ze skokową zmianą przenikalności dielektrycznej, co sprawia, że $[Me_3Hy]PbI_3$ jest potencjalnym przełącznikiem dielektrycznym (Rysunek 13b). Przemiana do rombowej fazy niskotemperaturowej *Pbca* jest powiązana ze zmianą entropii ΔS, która jest dwukrotnie większa niż wynikałoby z prostego modelu porządek-nieporządek, co wskazuje na bardziej złożony charakter tej przemiany.

W celu dokładnego zrozumienia mechanizmów tych przemian wykorzystano komplementarne do XRD metody spektroskopii oscylacyjnej, tj. IR oraz Ramana. Zaproponowano przypisanie pasm na widmach do odpowiednich drgań, a następnie wykonano pomiary temperaturowo-zależne. Widma dopasowywano krzywymi Lorentza, a następnie wykreślono

zależności położenia pasm od temperatury. Tak jak oczekiwano widma IR i Ramana podczas przemiany do fazy wysokotemperaturowej zmieniały się w niewielkim stopniu i znacząco podczas przemiany związanej z uporządkowaniem kationów Me_3Hy^+ oraz zmianą symetrii na rombową (Rysunek 14a).

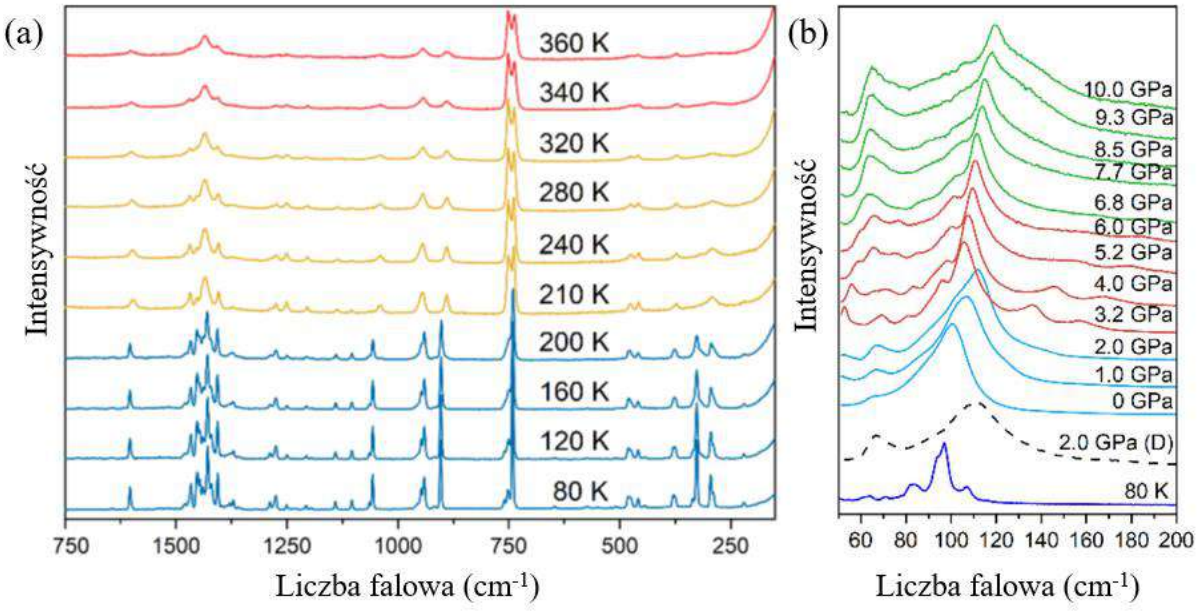

Rysunek 14. Ewolucja widm Ramana związku $[Me_3Hy]PbI_3$ w funkcji temperatury (a) oraz ciśnienia (b); symbol D w części (b) oznacza widmo zmierzone w trakcie dekompresji; rysunek opracowany na podstawie rysunków 8 i S10 z pracy [D5].

Wykazano, że podczas przemiany $P6_3/m \rightarrow P6_3/mmc$ sieć wiązań wodorowych jest zachowana oraz że przemiana jest gównie związana ze zmianami rozmiarów komórki elementarnej i subtelnymi ograniczeniami kationów Me_3Hy^+ w przestrzeniach pomiędzy łańcuchami. W przeciwieństwie do tego, druga z przemian ($Pbca \rightarrow P6_3/m$) ma bardziej dynamiczny charakter, podczas której wzrastająca moc wiązań wodorowych prowadzi do uporządkowania kationów organicznych w fazie niskotemperaturowej. Wykazano obecność nierównocennych wiązań Pb–I, co wskazuje na zniekształcenie łańcuchów oktaedrów.

Dodatkowo wykonano pomiary widm Ramana w podwyższonych ciśnieniach. Ze względu na silną luminescencję, pomiar możliwy był jedynie w zakresie drgań sieciowych. Przeprowadzony eksperyment wykazał obecność dwóch ciśnieniowych strukturalnych przemian fazowych, pierwszej w zakresie 2,8 i 3,2 GPa oraz drugie pomiędzy 6,4 i 6,8 GPa (Rysunek 14b). Wykazano, że przemiana fazowa przy niższych ciśnieniach związana jest z obniżeniem symetrii, porządkowaniem kationów Me_3Hy^+ oraz dystorsją łańcuchów nieorganicznych. Druga z przemian wiąże się najprawdopodobniej z częściową i odwracalną amorfizacją. Ustalono, że obie przemiany są odwracalne do wartości ciśnienia 10 GPa.

Przerwa energetyczna wyznaczona na podstawie pomiarów optycznych wynosi 3,20 eV. Poniżej 250 K związek wykazuje szerokopasmową czerwono-pomarańczową luminescencję związaną z obecnością defektów. Stwierdzono, że emisja pochodzi od ekscytonu spułapkowanego na defektach (ang. *self-trapped exciton*, STE). Wyznaczona energia termicznego wygaszania emisji jest równa 65 meV. Obliczone czasy życia pików emisyjnych przy 520 oraz 700 nm wynoszą odpowiednio 260 ns oraz 725 ns.

Ponadto dla $[Me_3Hy]PbI_3$ wykonano analizę TGA i ustalono prawdopodobną ścieżkę rozkładu termicznego. Wykazano, że związek pozostaje stabilny do relatywnie wysokich temperatur jak na związki hybrydowe, do 300°C.

4. Wnioski

W ramach badań zsyntezowano siedem nowych, nieopisanych wcześniej w literaturze związków hybrydowych. Badania zestawione w publikacjach [D1]-[D5] stanowią wkład w zrozumienie relacji pomiędzy strukturą a właściwościami fizykochemicznymi związków opartych na metylowych pochodnych kationu hydrazyniowego. Materiały tego typu stanowią bardzo interesującą grupę ze względu na możliwość indukowania porządku polarnego. Dlatego hydrazyna i jej związki hybrydowe mają szansę stać się ważnym elementem składowym materiałów dla nowoczesnej optoelektroniki.

Przeprowadzona analiza dotyczyła wybranych trzech typów materiałów, $[DMHy]Mn(HCOO)_3$, $[MHy]M^{II}Cl_3$ (M^{II} = Mn^{2+}, Co^{2+}, Ni^{2+}, Cu^{2+} i Cd^{2+}) oraz $[Me_3Hy]PbI_3$. W oparciu o uzyskane dane eksperymentalne, przeprowadzone analizy oraz dostępne dane literaturowe, dla każdej z grup przeanalizowano wpływ rodzaju i wielkości kationu na właściwości strukturalne, na występowanie i charakter strukturalnych przemian fazowych bądź ich brak, na właściwości fononowe, dielektryczne, luminescencyjne oraz cieplne. Postawione cele pracy doktorskiej zostały zrealizowane a spośród najważniejszych osiągnięć pracy należy wymienić:

- Opracowanie metody syntezy monokryształów $[DMHy]Mn(HCOO)_3$ metodą strąceniową oraz dyfuzyjną umożliwiających wykonanie pomiarów rentgenowskich, dielektrycznych oraz optycznych. $DMHy^+$ jest to największym kationem, jaki do tej pory użyto do syntezy trójwymiarowych mrówczanów o strukturze typu perowskitu.
- Scharakteryzowanie rzadko obserwowanej oraz izosymetrycznej strukturalnej przemiany fazowej typu porządek-nieporządek w związku $[DMHy]Mn(HCOO)_3$, wyznaczenie struktury uporządkowanej fazy niskotemperaturowej oraz nieuporządkowanej fazy wysokotemperaturowej, określenie charakteru nieporządku.
- Wyjaśnienie mechanizmu przemiany fazowej dla związku $[DMHy]Mn(HCOO)_3$ na podstawie danych krystalograficznych oraz uzyskanych za pomocą spektroskopii IR i Ramana. Wykazanie, że porządkowaniu kationów $DMHy^+$ towarzyszy zniekształcenie szkieletu manganowo-mrówcznowego w fazie niskotemperaturowej.
- Wyznaczenie aktywnych drgań dla obu faz $[DMHy]Mn(HCOO)_3$, wykonanie obliczeń DFT dla cząsteczki DMHy oraz jej kationu, wyznaczenie najsilniejszego anharmonizmu dla drgań rozciągających C–H oraz N–H, zaproponowanie przypisania obserwowanych pasm na widmie IR oraz Ramana.
- Określenie wpływu liczby grup metylowych w kationach pochodnych hydrazyny na wybrane parametry i właściwości strukturalne oraz termodynamiczne.
- Znalezienie słabego porządku ferromagnetycznego dla $[DMHy]Mn(HCOO)_3$ poniżej 8,4 K.

- Scharakteryzowanie właściwości optycznych [DMHy]Mn(HCOO)$_3$, określenie przerwy energetycznej (4,63 eV), zarejestrowanie emisji o różowej barwie poniżej 200 K, określenie energii wygaszania termicznego (62 meV).
- Opracowanie metody syntezy monokryształów [MHy]$M^{II}Cl_3$, gdzie $M^{II} = Mn^{2+}$, Co^{2+}, Ni^{2+}, Cu^{2+} oraz Cd^{2+} metodą powolnego odparowania, umożliwiających wykonanie pomiarów rentgenowskich.
- Wyjaśnienie przemiany fazowej zachodzącej w analogach [MHy]$M^{II}Cl_3$, gdzie $M^{II} = Mn^{2+}$, Co^{2+} oraz Ni^{2+}, na podstawie danych krystalograficznych oraz uzyskanych za pomocą spektroskopii IR i Ramana.
- Określenie wpływu kationów $M^{II} = Mn^{2+}$, Co^{2+} oraz Ni^{2+} właściwości strukturalne, termiczne oraz fononowe w [MHy]$M^{II}Cl_3$.
- Wyjaśnienie przyczyn braku przemian fazowych w analogach [MHy]$M^{II}Cl_3$, gdzie $M^{II} = Cu^{2+}$ oraz Cd^{2+}.
- Wyznaczenie reguł wyboru oraz drgań aktywnych na widmie IR i Ramana dla faz [MHy]$M^{II}Cl_3$, gdzie $M^{II} = Mn^{2+}$, Co^{2+}, Ni^{2+} , Cu^{2+} i Cd^{2+}.
- Scharakteryzowanie właściwości optycznych analogów [MHy]$M^{II}Cl_3$, określenie energii przerwy wynoszącej 5,34 (Mn^{2+}), 3,96 (Ni^{2+}), 3,64 (Co^{2+}), 2,62 (Cu^{2+}) oraz 5,57 eV (Cd^{2+}). Opisanie temperaturowo-zależnej czerwonej fotoluminescencji związku zawierającego kationy Mn^{2+} oraz przejścia żółtozielonej fotoluminescencji analogu opartego na jonach Ni^{2+} w pomarańczową pod wpływem temperatury.
- Wykrycie antyferromagnetycznego uporządkowania w związkach [MHy]$CoCl_3$ oraz [MHy]$NiCl_3$ poniżej tej samej temperatury Néela wynoszącej 3,7 K oraz rozmytego uporządkowania antyferromagnetycznego w [MHy]$MnCl_3$ poniżej ok. 5,0 K oraz w [MHy]$CuCl_3$ poniżej ok. 4,8 K.
- Opracowanie metody syntezy monokryształów perowskitoidu [Me_3Hy]PbI_3 metodą przeciwrozpuszczalnikową. Określenie stabilności związku pod wpływem temperatury i ciśnienia.
- Wykrycie oraz scharakteryzowanie właściwości termodynamicznych dwóch przemian fazowych, wyznaczenie struktur wszystkich faz oraz określenie charakteru nieporządku kationu Me_3Hy^+ w dwóch z nich.
- Określenie właściwości dielektrycznych dla [Me_3Hy]PbI_3 jako tzw. przełącznika dielektrycznego podczas przemiany fazowej z uporządkowanej fazy niskotemperaturowej do nieuporządkowanej fazy pośredniej.
- Wyjaśnienie mechanizmów obu strukturalnych przemian fazowych związku [Me_3Hy]PbI_3 indukowanych temperaturą w oparciu o dane rentgenograficzne oraz pomiary widm IR i Ramana w funkcji temperatury.

- Wykonanie pomiarów widm Ramana w zakresie drgań sieciowych w funkcji ciśnienia do 10 GPa, znalezienie dwóch przemian fazowych oraz zaproponowanie ich mechanizmów.
- Scharakteryzowanie właściwości optycznych perowskitoidu $[Me_3Hy]PbI_3$, określenie przerwy energetycznej (3,20 eV) oraz scharakteryzowanie emisji o czerwono-pomarańczowej barwie poniżej 250 K związanej z obecnością defektów, określenie energii wygaszania termicznego (65 meV).

5. Publikacje [D1]-[D5] wchodzące w skład rozprawy doktorskiej

***Publikacja* [D1]**

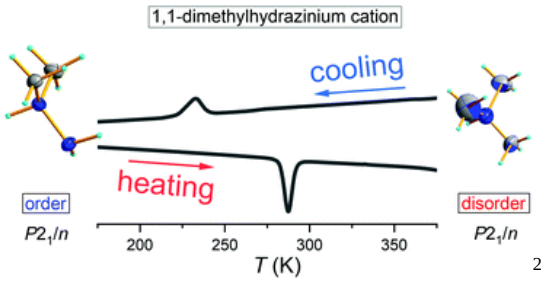

[2]

J.A. Zienkiewicz*, D.A. Kowalska, K. Fedoruk, M. Stefański, A. Pikul, M. Ptak

Unusual isosymmetric order–disorder phase transition in a new perovskite-type dimethylhydrazinium manganese formate exhibiting weak ferromagnetism and photoluminescence properties

J. Mat. Chem. C **2021**, 9 (21), 6841-6851

doi: 10.1039/d1tc01014j IF = 7,059 140 pkt.

Udział Doktoranta w powstanie pracy:

- Synteza monokryształów [DMHy]Mn(HCOO)$_3$ metodą strąceniową i dyfuzyjną;
- Koncepcja badań oraz określenie metodologii;
- Analiza dyfraktogramu proszkowego;
- Analiza widma rozproszonego odbicia;
- Dyskusja wyników oraz określenie wpływu metylowania kationu Hy^+ na właściwości strukturalne, cieplne oraz na mechanizmy przemian fazowych w grupie związków [A]Mn(HCOO)$_3$ (A = Hy^+, MHy^+, $DMHy^+$);
- Analiza izosymetrycznych przemian fazowych w związkach hybrydowych;
- Przygotowywanie manuskryptu, rysunków oraz tabel.

[2] Odtworzono z [62] za zgodą Królewskiego Towarzystwa Chemicznego (Reproduced from Ref. [62] with permission from the Royal Society of Chemistry).

Unusual isosymmetric order–disorder phase transition in a new perovskite-type dimethylhydrazinium manganese formate exhibiting weak ferromagnetism and photoluminescence properties

Article *in* Journal of Materials Chemistry C · May 2021

DOI: 10.1039/D1TC01014J

CITATIONS
5

READS
54

6 authors, including:

Jan Albert Zienkiewicz
Polish Academy of Sciences
10 PUBLICATIONS **32** CITATIONS
SEE PROFILE

Katarzyna Fedoruk
Wroclaw University of Science and Technology
13 PUBLICATIONS **104** CITATIONS
SEE PROFILE

Mariusz Stefanski
Polish Academy of Sciences
36 PUBLICATIONS **538** CITATIONS
SEE PROFILE

Adam Pikul
Institute of Low Temperature and Structure Research Polish Academy of Sciences
134 PUBLICATIONS **2,298** CITATIONS
SEE PROFILE

Journal of Materials Chemistry C

ROYAL SOCIETY OF CHEMISTRY

PAPER

View Article Online
View Journal

Cite this: DOI: 10.1039/d1tc01014j

Unusual isosymmetric order–disorder phase transition in a new perovskite-type dimethylhydrazinium manganese formate exhibiting weak ferromagnetism and photoluminescence properties†

Jan Albert Zienkiewicz, *[a] Dorota Anna Kowalska, [a] Katarzyna Fedoruk, [b] Mariusz Stefanski, [a] Adam Pikul [a] and Maciej Ptak [a]

We report the synthesis and investigation of the physicochemical properties of a novel hybrid organic–inorganic formate perovskite templated by the unsymmetrical 1,1-dimethylhydrazinium ($DMHy^+$) cation, $[DMHy]Mn(HCOO)_3$. This compound undergoes a first-order structural phase transition (PT) at 244.4 K (283.0 K) on cooling (heating) and both phases have the same monoclinic ($P2_1/n$) symmetry. Such isosymmetric PT is very unusual in the family of metal–formate frameworks and the X-ray diffraction and dielectric studies reveal that the PT is associated with ordering of the $DMHy^+$ cations, re-arrangement of hydrogen bonds and strong distortion of the manganese–formate framework. The $DMHy^+$ cation is the largest cation used so far for the synthesis of formate-based 3D perovskites. The comparison with other derivatives of hydrazinium-based analogues reveals that the increased steric hindrance, triggered by an increased number of methyl groups in the hydrazinium cation, affects the temperature and mechanism of the observed order–disorder PTs. We show that the temperature of the order–disorder PTs in this subgroup of compounds depends linearly on the effective ionic radius of organic cations, tolerance factor and number of disordered states. Magnetic studies indicate that $[DMHy]Mn(HCOO)_3$ is a weak ferromagnet with the ordering temperature of 8.4 K. $[DMHy]Mn(HCOO)_3$ exhibits pinkish photoluminescence under 266 nm excitation with the low activation energy of 62 meV. The emission lifetime reaches 157.6 μs at 80 K. The low activation energy and strong temperature-dependent photoluminescence suggest a potential application of $[DMHy]Mn(HCOO)_3$ for non-contact temperature sensing below 200 K.

Received 4th March 2021,
Accepted 24th April 2021

DOI: 10.1039/d1tc01014j

rsc.li/materials-c

Introduction

Metal formates templated by protonated amines are a subclass of metal–organic frameworks (MOFs). Most of them adopt a perovskite-like architecture, described by general formula $AB(HCOO)_3$, where A and B sites are occupied by a protonated amine and metal ion (*e.g.* Mn^{2+}, Co^{2+}, Ni^{2+} or Zn^{2+}), respectively.[1–3] Therefore, they are also classified as hybrid organic–inorganic perovskites (HOIPs).[4] In the literature, there are many described examples of formate HOIPs that exhibit luminescent,[5] ferroelastic,[6,7] ferroelectric,[8] switchable dielectric,[7] magnetic[9] or multiferroic[1,6,8] properties, depending on their composition and crystal symmetry.[10] Most of the reported studies concern metal formates templated by small ammonium cations, such as methylammonium (MA^+),[11] dimethylammonium (DMA^+),[12,13] hydrazinium (Hy^+),[14,15] and methylhydrazinium (MHy^+),[16] among others.

The physicochemical properties of formate MOFs depend on the size and shape of organic cations embedded in the cavities of the framework. Particularly interesting seems to be a series

[a] Institute of Low Temperature and Structure Research, Polish Academy of Sciences, Okólna 2 Str., 50-422 Wrocław, Poland. E-mail: j.zienkiewicz@intibs.pl
[b] Department of Experimental Physics, Wrocław University of Science and Technology, Wybrzeże Wyspiańskiego 27, 50-370 Wrocław, Poland

† Electronic supplementary information (ESI) available: A picture of the asymmetric unit of the LT and HT phase, powder X-ray diffraction pattern, the DSC trace, the temperature dependence of the dielectric loss ε'', relaxation times as a function of $1000/T$, the result of determining the energy band gap (E_g) using the Kubelka–Munk theory, the dependence of activation energy of the thermal quenching as a function of $1/kT$, the luminescence decay profile of crystals excited at 266 nm and monitored at 725 nm recorded at 77 K, hydrogen-bond geometry and selected geometric parameters, and the temperature-dependent isosymmetric PTs reported for single and double 3D hybrid perovskites (pdf). Crystal structures at 100 and 300 K. CCDC 2064864 and 2064865. For ESI and crystallographic data in CIF or other electronic format see DOI: 10.1039/d1tc01014j

of ammonium cations that differ in the number of methyl groups since an increased number of these groups lead to the increased steric hindrance of an organic cation and affects its ability to form hydrogen bonds (HBs) with the metal–formate framework. As a result, the accommodated cations differently fit into the voids and influence the crystal symmetry. For instance, $[MA]Mn(HCOO)_3$ crystallizes in the orthorhombic *Pnma* system,[17] while the $[DMA]Mn(HCOO)_3$] analogue adopts the trigonal $R\bar{3}c$ space group.[17] The former compound does not exhibit any structural PT, whereas the latter one undergoes an order–disorder transformation below 185 K.[18] Both compounds reveal magnetic ordering below 7.8 and 8.6 K, respectively. Moreover, it was reported that $[DMA]Mn(HCOO)_3$ exhibits multiferroic properties.[13]

The Hy^+ cation has nearly the same ionic radius as MA^+ (217 pm)[19] but it creates crystal structures possessing different thermal and ferroic properties. In particular, $[Hy]Mn(HCOO)_3$ crystallizes in the orthorhombic $Pna2_1$ space group, exhibits multiferroic properties and undergoes PT at 355 K to the *Pnma* centrosymmetric phase.[15] Its analogue comprising larger MHy^+ cations (ionic radius of 264 pm),[16] *i.e.* $[MHy]Mn(HCOO)_3$, experiences two PTs at 310 K from the dynamically disordered high-temperature (HT) $R\bar{3}c$ phase to the partially ordered intermediate (IT) $R3c$ phase and at 224 K to the ordered low-temperature (LT) $P1$ phase. The ferroelectric nature of the HT and LT phases was confirmed by pyroelectric measurements.[16]

Recently, it was shown that the MHy^+ cation is an interesting agent that can be used either as a templated cation or spacer cation in the design of novel non-centrosymmetric 3D or 2D lead halide perovskites.[20,21] Taking into account unique properties observed for the Hy^+- and MHy^+-based HOIPs, we decided to employ the unsymmetrical 1,1-dimethylhydrazinium cation ($H_2N–HN^+(CH_3)_2$, $DMHy^+$) for construction of a novel formate-based MOF, namely $[DMHy]Mn(HCOO)_3$. We would like to emphasize that this cation has never been used as a templating agent in any MOF.

The aim of this work is understanding the effect of increased number of methyl groups on the structural, dielectric, thermal, magnetic and luminescence properties of formate-based MOFs. A better understanding of the structural properties that decide/determine whether or not a PT will occur in this class of formate MOFs is of particular interest. Since most of the observed PTs are of an order–disorder type, it is of particular interest to determine how the increased steric hindrance, followed by different ability to create HBs, limits the dynamics of the cation accommodated in the metal–formate voids. For this purpose, a novel tightly-packed $[DMHy]Mn(HCOO)_3$ perovskite was synthesized and subjected to detailed investigations.

Materials and methods

Materials and synthesis

1,1-Dimethylhydrazine (Sigma-Aldrich), formic acid (85%, Avantor Performance Materials), anhydrous methanol (MeOH) (Sigma-Aldrich) and manganese(II) perchlorate hexahydrate (Sigma-Aldrich) were purchased from commercial sources and used without further purification.

In order to grow $[DMHy]Mn(HCOO)_3$, 1,1-dimethylhydrazine (40 mmol, 3.04 ml) was dissolved in 10 ml of MeOH. Then, an excess of formic acid (160 mmol, 7.25 ml) was added to form 1,1-dimethylhydrazinium formate. In the next step, a solution of $Mn(ClO_4)_2{\cdot}6H_2O$ (1 mmol, 0.3619 g) dissolved in 10 ml of methanol was added to the solution of 1,1-dimethylhydrazinium formate. The mixture was sealed in a plastic vessel and left undisturbed for slow crystallization. After three days, cubic shaped transparent crystals were separated from the mother liquid, washed a few times with methanol and air dried. The phase purity of the bulk sample was confirmed by a good match of its powder XRD pattern with the simulated one based on the single crystal structure (Fig. S1, ESI†).

Single-crystal and powder X-ray diffraction

The Oxford X'Calibur four-circle single-crystal diffractometer, equipped with a CCD camera and graphite-monochromated MoKα radiation (λ = 0.71073 Å), was used to examine a single crystal of dimensions 0.45 × 0.37 × 0.25 mm. The data collection and reduction were performed with CrysAlis PRO software (1.171.38.46 (Rigaku OD, 2015)). Absorption was corrected based on Gaussian integration over a multifaceted crystal model. Crystal structures were solved by direct methods and refined at 350, 325, 300 K (HT phase), 280, 260, 240, 220, 200, 180, 160, 140, 120 and 100 K (LT phase) using the SHELX-2014 crystallographic software package (Sheldrick, 2015). The hydrogen atoms were introduced at calculated positions and refined with constrained parameters. All non-hydrogen atoms, except for the disordered atoms in amine in the HT phase, were refined anisotropically. The LT phase was nonmerohedrally twinned and the refinement was performed for the dominated twin domain (94% of separated peaks). Additionally, the pseudo-merohedral twinning occurred and the LT structure was refined from two domains related by [−1 0 0 0 −1 0 0 0 1] rotation.

The powder XRD pattern was measured in reflection mode using an X'Pert PRO X-ray diffraction system equipped with a PIXcel ultrafast line detector and Soller slits for CuKα_1 radiation (λ = 1.54056 Å). The X-ray tube settings were 30 mA and 40 kV.

Differential scanning calorimetry (DSC)

Heat capacity was measured using a Mettler Toledo DSC-1 calorimeter with a high resolution of 0.4 μW. Nitrogen was used as a purging gas. The temperature scanning rate was chosen to be 5 K min^{-1}, and the DSC thermograms were measured for both cooling and heating cycles. The sample weight was 17 mg. The excess heat capacity associated with the phase transition was calculated by subtraction from the data the baseline representing the system variation in the absence of the phase transitions.

Broadband dielectric spectroscopy

The dielectric measurements were performed using the Novocontrol Alpha impedance analyser. Measurements were made on two oriented single-crystal samples (along the [001] direction

and perpendicularly to the [001] direction) with the following dimensions 2.3 × 1.9 × 0.65 and 1.7 × 1.5 × 0.4 mm, respectively. For comparison, additional measurements on a polycrystalline pellet with diameter of 5 mm and thickness of 0.7 mm, were performed. Silver paste was coated on both parallel surfaces of the sample to ensure a good electrical contact. A sinusoidal voltage with amplitude of 1 V and frequency in the range 10^3–10^6 Hz was applied across the sample. The temperature was controlled by the Novocontrol Quattro system by using a nitrogen gas cryostat. The measurements were taken every 1 K in the temperature range of 210–300 K in two cycles (cooling and heating). The temperature stability of the samples was better than 0.1 K.

Magnetic measurements

Magnetization of randomly oriented single crystals of [DMHy]Mn(HCOO)$_3$ (about 50 mg in total) were measured using a commercial magnetometer (Quantum Design MPMS XL) in the temperature range of 2–300 K and in external magnetic fields up to 70 kOe. The background coming from a weakly diamagnetic sample holder (a plastic straw) was found to be negligible in comparison to the signal coming from the sample, and hence its subtraction was omitted.

Optical measurements

The room-temperature absorption spectrum (back-scattering mode) in the UV-VIS range was measured using an Agilent Cary 500 spectrophotometer equipped with a PryingMantis™ diffuse reflectance accessory. The temperature-dependent emission spectra were measured with the Hamamatsu photonic multi-channel analyzer PMA-12 equipped with a BT-CCD linear image sensor. The laser diode operating under 266 nm was applied as an excitation source. The temperature of the samples during emission measurements was controlled by a Linkam THMS600 Heating/Freezing Stage. The low-temperature luminescent decay profile was recorded using a Lecroy digital oscilloscope and the Nd:YAG laser as an excitation source.

Results and discussion

DSC results

The DSC trace revealed a reversible anomaly occurring at 244.4 K and 283.0 K upon cooling and heating, respectively (Fig. S2, ESI†). The change in heat capacity (ΔC_p) and entropy (ΔS) associated with the PT is shown in Fig. 1. The ΔC_p peak has a strongly symmetric shape and ΔS exhibits sharp, step-like change at T_c combined with the large thermal hysteresis indicating the first-order character of PT.

The change in entropy ΔS associated with the observed PT was experimentally estimated to be 7.7 J mol^{-1} K^{-1} on heating and 6.2 J mol^{-1} K^{-1} on cooling. The relatively large values indicate a significant structural order change at T_c. For an order–disorder PT, the change of entropy can be correlated with the number of disordered states N by a simple equation, $\Delta S = R\ln(N)$, where R is the gas constant. For $N = 3$, the theoretically

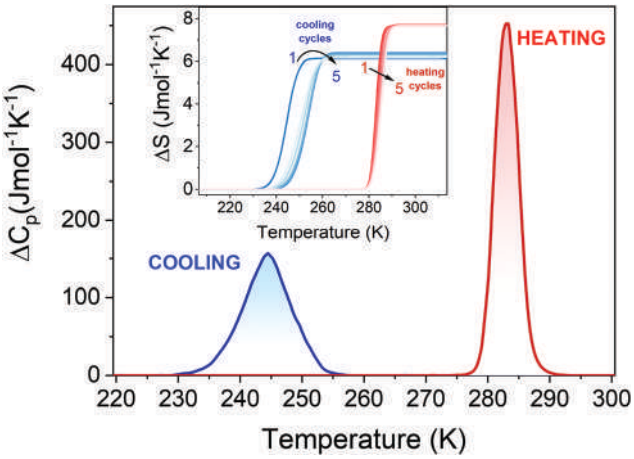

Fig. 1 The change in heat capacity (ΔC_p) of [DMHy]Mn(HCOO)$_3$ measured in heating (red) and cooling (blue) modes. The inset shows the corresponding change of entropy (ΔS) in five cycles.

expected change in entropy should be 9.1 J mol^{-1} K^{-1}. As can be noticed, the experimental value of ΔS for [DMHy]Mn(HCOO)$_3$ is lower than the theoretical one, suggesting that the mechanism of PT has a more complex nature than predicted by an on order–disorder model.

X-Ray diffraction studies

The crystal data together with experimental and refinement details for the two phases are presented in Table 1. HBs and geometric parameters are given in Tables S1 and S2 (ESI†).

[DMHy]Mn(HCOO)$_3$ crystallizes at RT in the monoclinic system, in the $P2_1/n$ space group (HT phase). Upon cooling, a PT occurs to another phase (LT phase) that has the same $P2_1/n$ space group but with the switch of the crystal axes b and c (Table 1). The details of the crystal structures in both phases are presented in Fig. 2. In the HT phase, the inorganic part of the structure consists of two Mn^{2+} ions and three $HCOO^-$ units that connect adjacent metal ions (Mn1 and Mn2 in Fig. 2 and Fig. S3a, ESI†) in the [001], [110] and [1$\bar{1}$0] directions with C–O–Mn1 and C–O–Mn2 angles of 128° and 134°, 137° and 126°, and 132° and 135°, respectively (see Table S2, ESI†). $DMHy^+$ cations, located in the voids of the framework, are disordered over three positions, occurring due to the presence of the pseudo three-fold axis in the $DMHy^+$ cation (Fig. S3a, ESI†). They interact with the inorganic framework by a net of the N–H···O and C–H···O HBs.

The inorganic part of the unit cell of an LT phase contains one symmetry independent metal centre and, similar to the HT phase, three $HCOO^-$ groups creating C–O–Mn angles of 130° and 121°, 127° and 132°, and 134° and 131° in the [010], [101] and [1$\bar{1}$0] direction, respectively. The structure reorganizations leads to ordering of the $DMHy^+$ cations.

The cavities housing the $DMHy^+$ cations change their geometry during the PT: the distance between two opposite Mn^{2+} ions decreases from 8.55 Å to 8.35 Å in the [100] direction and increases from 9.21 Å to 9.39 Å in the [010] ([001] in the LT phase) direction. Especially interesting is the negative thermal expansion along the latter direction (see Fig. 3). The octahedra distortion can

Table 1 Experimental details for [DMHy][Mn(HCOO)$_3$]

	LT phase	HT phase
Crystal data		
Crystal system, space group	Monoclinic, $P2_1/n$	Monoclinic, $P2_1/n$
Temperature (K)	100	300
a, b, c (Å)	8.345 (5), 12.124 (7), 9.387 (5)	8.554 (3), 9.207 (3), 12.387 (4)
β (°)	90.144 (5)	94.432 (3)
V (Å^3)	949.7 (9)	972.6 (6)
Z/calculated density (g cm^{-3})	4/1.756	4/1.715
Absorption coefficient, μ (mm^{-1})	1.40	1.37
Data collection		
Theta range	2.7°–28.5°	2.8°–29.5°
No. of measured, independent and observed $[I > 2\sigma(I)]$ reflections	15 823, 2360, 2188	15 551, 2510, 1861
R_{int}	0.047	0.027
$(\sin\theta/\lambda)_{max}$ (Å^{-1})	0.671	0.693
Refinement		
$R[F^2 > 2\sigma(F^2)]$, $wR(F^2)$, S	0.035, 0.093, 1.07	0.032, 0.085, 1.03
Absorption correction	Gaussian	Gaussian
Data/restraints/parameters	2360/0/131	2510/1/135
$\Delta\rho_{max}$, $\Delta\rho_{min}$ (e Å^{-3})	0.60, −0.91	0.41, −0.33
Extinction coefficient	—	0.0193 (145)
Absolute structure	Twinned by pseudo-merohedry [−1 0 0 0 −1 0 0 0 1]	—
Absolute structure parameter	0.38 (2)	—

For both phases: M_r = 251.11 g mol^{-1}; H atom parameters constrained; crystal size: 0.45 × 0.37 × 0.25 mm.

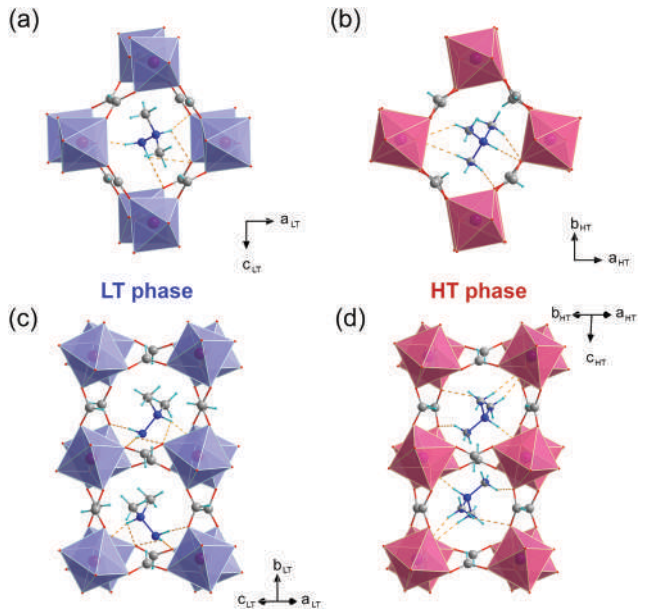

Fig. 2 The details of the crystal structures in the LT phase at 100 K (a and c) and in the HT phase at 300 K (b and d). Dashed lines designate N–H···O HBs. In the HT phase DMHy$^+$ cations have three equivalent positions, and disordered atoms are marked with grey and blue (Mn – magenta, O – red, C – grey, N – blue, H – cyan).

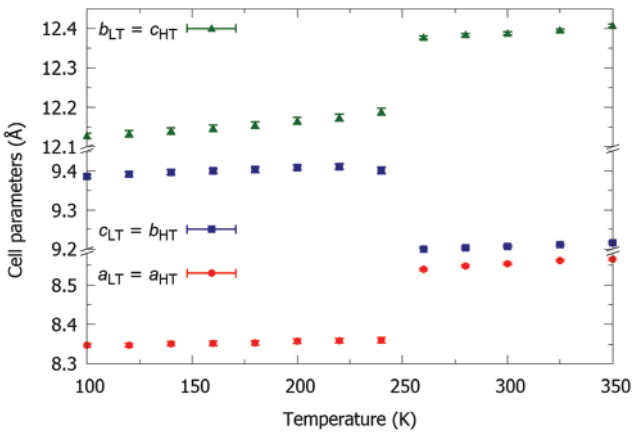

Fig. 3 Changes of the a, b and c lattice parameters as a function of temperature. The subscripts designate the structure phase.

be probed by various parameters, such as bond length distortion (Δd), the distance between the manganese ion and the octahedra centre of gravity (d_G), the Σ^{cis} parameter, representing the sum of deviations from 90° of the 12 cis angles in the coordination sphere of the Mn^{2+} ion, and the octahedral angle variance (σ^2). These parameters, calculated for both phases at different temperatures, are gathered in Table 2. Table 2 shows that all of them exhibit significant changes during PT. In particular, d_G, Σ^{cis} and σ^2 increase in the HT phase with lowering of the temperature, exhibit a sudden and very large increase when going from the HT to the LT phase and increase upon further cooling of the LT phase. Different behaviour is, however, observed for Δd which increases in HT phase with temperature lowering, decreases at the PT temperature and then decreases upon further cooling of the LT phase. The described changes of the framework on cooling lead to increased amine–framework interactions, slowing down of the DMHy$^+$ movements and freezing of these movements associated with distortion of the framework at the PT temperature.

Dielectric properties

In order to check if the observed transition is related to any dielectric permittivity anomaly and reveal the anisotropic

Table 2 Octahedral distortion parameters Δd, d_G, Σ^{cis}, and angle variance σ^2 of [DMHy]Mn(HCOO)$_3$. In the disordered HT phase, the parameter values are given for the more distorted octahedra

T (K)		Δd [$\times 10^{-3}$]	d_G [$\times 10^{-4}$]	Σ^{cis}	σ^2
HT phase	350	5.57	0.017	26.39	7.01
	300	5.81	0.033	28.77	8.01
	260	6.49	0.053	29.96	8.43
LT phase	240[a]	4.52	384.4	43.51	18.87
	210	3.68	384.9	44.42	19.45
	200	3.72	387.4	44.51	19.54
	140	3.42	390.9	45.24	20.21
	100	3.22	392.0	45.52	20.36

[a] The phase transition is still not completed at this temperature.

properties, we performed the proper measurements using broadband impedance spectroscopy. Three samples were measured for comparison sake, *i.e.* a single crystal in the [001] direction, a single crystal in the direction perpendicular to [001], and a polycrystalline pellet. The temperature dependence of the real (ε') and imaginary (ε'') parts of the dielectric permittivity are presented in Fig. 4 and Fig. S4 (ESI†), respectively. The observed spectra are characterized by a characteristic frequency dispersion. Dielectric permittivity ε' increases dynamically with increasing temperature and exhibits frequency dependence with clear anomalies near 250 K and 280 K upon cooling and heating, respectively. The anomalies on heating seem to be observed at slightly lower temperature than in the DSC measurement and this discrepancy can be attributed to the difference in the dynamics of these measurements, characteristic for a first-order phase transition.[22] The step-like anomalies of the real part (ε') of the dielectric permittivity and temperature hysteresis observed around T_c in the heating and cooling modes confirm a first-order character of the PT. The observed frequency dependence of ε' and ε'' implies some relaxation process. The change in dielectric permittivity at T_c for the cooling cycle is equal to 30 for single crystals and 6 for the pellet, while no differences can be seen in the values of the dielectric losses (ε'') (Fig. S4, ESI†). Such behaviour may indicate electrical anisotropy, characteristic for complex structures.[23,24] Moreover, single-crystalline measurements on heating revealed a decrease in value $\Delta\varepsilon'$, most likely due to microcracks of the crystal at T_c. The change in the shape of the dielectric losses in the heating and cooling mode is also affected by this effect, which is confirmed by the measurements on the pellet by reducing the impact of the microcracks. This sharp and large dielectric anomaly at T_c classifies this compound as a switchable dielectric material (see Fig. 4d).[25–27]

The spectra reveal dipolar relaxation processes that can be well approximated by the Havriliak Negami model. A quantitative analysis of the frequency domain dielectric data allowed us to obtain the activation energies E_a. Their values for the observed relaxation in a wide temperature range are estimated upon cooling to 0.15 and 0.32 eV in the LT and HT phases, respectively, and 0.52 eV upon heating (Fig. S5, ESI†). The values obtained for analogues with Hy^+ and MHy^+ are in the same order of magnitude.[15,23,28]

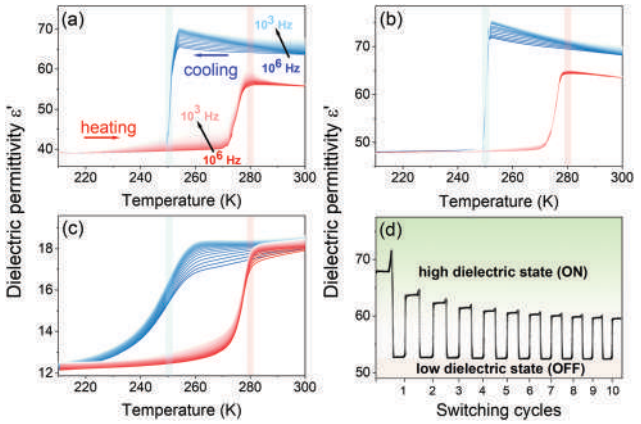

Fig. 4 The dielectric permittivity as a function of temperature upon cooling (blue) and heating (red) in [DMHy]Mn(HCOO)$_3$ performed on the single crystal in the [001] direction (a), the single crystal in the direction perpendicular to [001] (b), and the pellet (c). The representative curves are plotted in frequency decades between 10^3 Hz and 10^6 Hz. The vertical lines correspond to the PT temperatures obtained from the dynamic DSC measurements. Panel (d) shows ten cycles of the temperature-induced dielectric switching measured for a single crystal in the [001] direction at a probing frequency of 0.7 MHz. The high- (ON) and low-dielectric (OFF) states correspond to 240 and 290 K, respectively.

Magnetic measurements

Fig. 5 displays results of magnetic properties measurements performed for [DMHy]Mn(HCOO)$_3$. As can be inferred from panel (a) of that figure, the inverse susceptibility χ^{-1} of the compound is linear in temperature down to about 30 K, being a manifestation of the Curie-like paramagnetism. Least-squares fit of the Curie–Weiss law $\chi(T) = C/(T - \theta_p)$ to the experimental data (see the thick solid line in Fig. 5a, left axis) yielded the Curie constant $C = 4.29(1)$ emu mol^{-1} K and the paramagnetic Curie–Weiss temperature $\theta_p = -12.8(2)$ K. The effective magnetic moment μ_{eff} derived from C as $\mu_{eff} = \sqrt{8C}$ is equal to 5.86(1) μ_B and is very close to the theoretical value of 5.92 μ_B calculated for a free Mn^{2+} ion ($3d^5$ shell) within the Russe–Saunders coupling scheme ($S = 5/2$, $L = 0$, $J = 5/2$, $g_J = 2$; $\mu_{eff} = g_J\sqrt{S(S+1)}\mu_B$). The negative value of θ_p indicates the presence of predominantly antiferromagnetic coupling between the magnetic moments of Mn^{2+} in [DMHy]Mn(HCOO)$_3$. The overall shape of the $\chi T(T)$ curve confirms the above findings. First, the value of χT at 300 K (4.1 emu mol^{-1} K) is very close to the experimental value of C and to the theoretical value of the Curie constant expected for non-interacting Mn^{2+} ions, *i.e.* $C = \frac{1}{8}\mu_{Mn^{2+}}{}^2 = \frac{1}{8}5.92^2 = 4.38$ emu mol^{-1} K. Second, $\chi T(T)$ decreases with increasing temperature (see Fig. 5a, right axis), as expected for systems with antiferromagnetically coupled magnetic moments.

A sudden change of the magnetization of [DMHy]Mn(HCOO)$_3$ below about 8.4 K (Fig. 5b) manifests magnetic ordering of the compound. The shape of the anomaly in H = 20 Oe (which is reminiscent of the Brillouin function at temperatures just below the Curie temperature) and its distinct bifurcation upon measuring $MH^{-1}(T)$ in the zero-field cooling (ZFC)

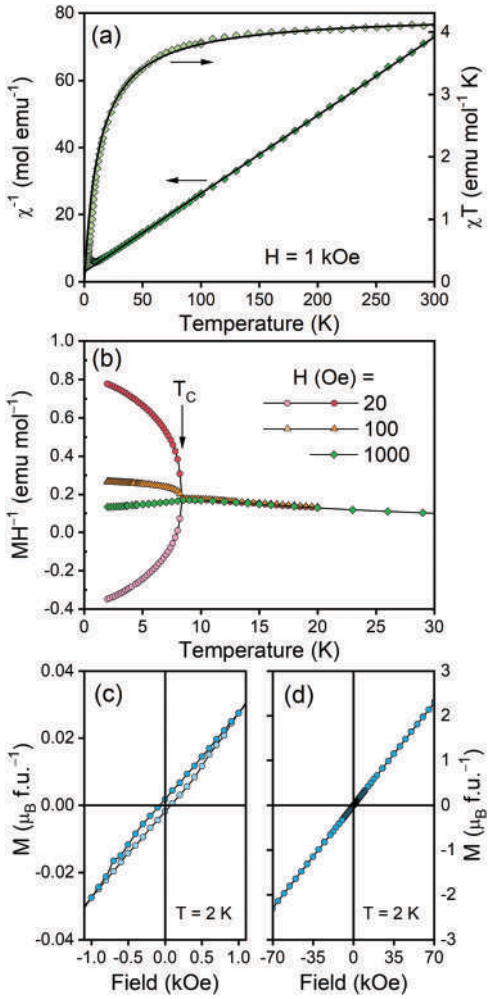

Fig. 5 (a) Temperature dependence of inverse DC magnetic susceptibility χ^{-1} of [DMHy]Mn(HCOO)$_3$ measured in constant external magnetic field H (left axis) and a product χT (right axis). Thick solid lines are a fit of the Curie–Weiss law to the experimental data (for details see the text). (b) Magnetization M divided by H and measured at low temperature at various fields in the ZFC and FC regime (bright and dark symbols, respectively); the arrow marks the Curie temperature T_c, and thin solid lines serve as guides for the eye. (c and d) Magnetization (expressed in units of magnetic moment per formula unit) as a function of increasing and decreasing field (bright and dark symbols, respectively) plotted in two different field ranges.

and field cooling (FC) regime clearly suggests ferromagnetic character of the phase transition. On the other hand, in higher fields the anomaly evolves towards a cusp-like shape without difference between ZFC and FC curves, as expected for antiferromagnets and being in line with the postulated antiferromagnetic coupling of the magnetic moments.

The field dependence of the magnetization of [DMHy]Mn(HCOO)$_3$ is consistent with the above observations. In particular, in low fields (Fig. 5c) the $M(H)$ curve exhibits distinct magnetic hysteresis, which confirms the ferromagnetic character of the phase transition. And above about 0.9 kOe the magnetization increases linearly with H, achieving at the highest field applied (70 kOe) about 2.3 μ_B (Fig. 5d), which is far from a value of the saturated magnetic moment of Mn^{2+} (*i.e.* $M_S = g_J = 5$ μ_B), as expected for antiferromagnets. If we also take into account a very small remnant magnetization M_R of about 0.0018 μ_B and coercivity H_c of about 100 Oe, we can conclude that the magnetic ordering observed in [DMHy]Mn(HCOO)$_3$ below 8.4 K is weak ferromagnetism, *i.e.* of canted antiferromagnetism with a very small ferromagnetic component. The canting angle α estimated from the relationship $\sin\alpha = M_R/M_S$ is as small as about 0.001 degree.

Optical properties

Fig. 6 presents the absorption spectrum of [DMHy]Mn(HCOO)$_3$ measured at RT. It can be observed that it contains a broad, intense band in the 200–300 nm range and the tail above 300 nm ascribed to the overlapping host lattice absorption and charge transfer (CT) transition (O^{2-}–Mn^{2+}), respectively, as well as several less intense bands typical for Mn^{2+} ions in the octahedral crystal field.[29] Their peak maxima are located at 310, 342, 363, 403, 444 and 540 nm corresponding to the spin–forbidden d–d transitions, $^4T_{1g}(^4P)$, $^4E_g(^4D)$, $^4T_{2g}(^4D)$, $^4E_g(^4G)$ and $^4A_{1g}(^4G)$, $^4T_{2g}(^4G)$ and $^4T_{1g}(^4G)$, respectively, from the $^6A_{1g}(^6S)$ ground state.[30] The obtained results were used to determine the energy band gap (E_g) of the [DMHy]Mn(HCOO)$_3$ crystals according to Kubelka–Munk theory using the following equation:[31]

$$F(R) = \frac{(1-R)^2}{2R}, \quad (1)$$

where R represents reflectance. The E_g of the studied compound was calculated to be 4.63 eV (see Fig. S6, ESI†).

The luminescence properties of the [DMHy]Mn(HCOO)$_3$ crystals were investigated in the framework of temperature-dependent (80–200 K) emission measurements under the 266 nm excitation line presented in Fig. 7a. It can be observed that broad emission bands in the visible region with maxima at 725 nm assigned to the spin–forbidden $^4T_{1g}(G) \rightarrow {}^6A_{1g}(S)$ transition of Mn^{2+} ions were registered.[29] The use of a laser diode operating upon 266 nm shows that the [DMHy]Mn(HCOO)$_3$ crystals exhibit

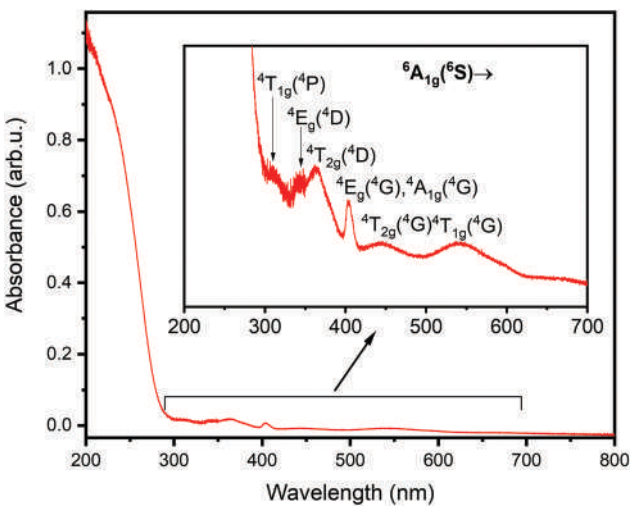

Fig. 6 Absorption spectrum of [DMHy]Mn(HCOO)$_3$.

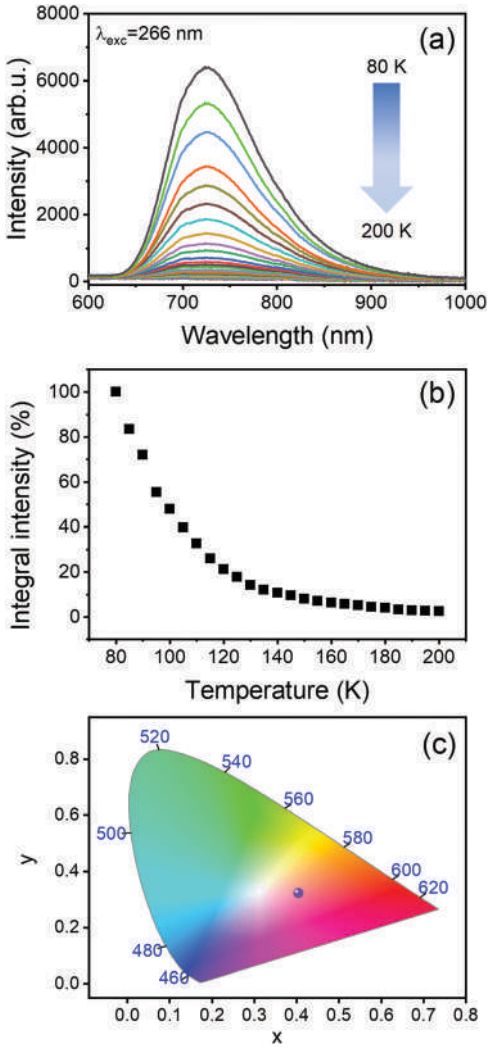

Fig. 7 The temperature-dependent emission spectra of [DMHy]Mn(HCOO)$_3$ crystals recorded upon 266 nm (a) and their integral emission intensities calculated for the 80–200 K range (b) together with the CIE chromaticity diagram of the investigated compound determined for emission measured at 80 K (c).

efficient energy transfer between the host lattice and Mn^{2+} activators at low temperatures. It was found that the investigated compound revealed the most intense emission at 80 K, which was completely quenched at 200 K (Fig. 7b). The presented temperature behaviour can be attributed to the temperature-dependence of the non-radiative process through the electron–phonon interactions.[32] It can be seen that the position of the band maxima did not change during the measurements. In order to visualize the recorded luminescence colour the chromaticity parameters were determined ($x = 0.40, y = 0.32$) and depicted on the CIE diagram presented in Fig. 7c.

The thermal kinetics investigation of the emission presented in Fig. 7a was carried out using the formula shown below:[33]

$$I = \frac{I_0}{1 + \frac{\Gamma_0}{\Gamma_v} e^{-\Delta E/kT}}, \quad (2)$$

where I symbolizes the intensity, I_0 is the initial intensity at low temperature, Γ_0 represents attempt rate for thermal quenching and Γ_v corresponds to the radiative decay rate and ΔE is the activation energy for thermal quenching. After minor mathematical treatments eqn (2) can be written as below, and consequently ΔE can be calculated:[34]

$$\frac{\Delta E}{kT} = -\ln\left(\frac{I_0}{I} - 1\right) + \ln\left(\frac{\Gamma_0}{\Gamma_v}\right), \quad (3)$$

where $\ln\left(\frac{\Gamma_0}{\Gamma_v}\right)$ means a constant and ΔE is the slope of $\ln\left(\frac{I_0}{I} - 1\right)$ as a function of $1/kT$. The absolute value of the ΔE calculated for Mn^{2+} emission upon 266 nm excitation is equal to 62 meV (see Fig. S7, ESI†).

The luminescence decay profile registered for [DMHy]Mn(HCOO)$_3$ crystals in liquid nitrogen temperature is demonstrated in Fig. S8 (ESI†). It was found that it can be well fitted using a double exponential function according to the below formula:

$$I(t) = A_1 \exp\left(-\frac{t}{\tau_1}\right) + A_2 \exp\left(-\frac{t}{\tau_2}\right), \quad (4)$$

where I is the emission intensity, A_1 and A_2 are constants, τ_1, and τ_2 stand for fast and slow decay time components and t means the lifetime. The lifetimes of Mn^{2+} emission at 80 K were determined to be τ_1 = 42.8 μs and τ_2 = 157.6 μs. The presence of the short component may indicate some non-radiative processes.[29]

Recently, Maczka *et al.* showed a possible pathway for energy transfer in hypophosphite-based hybrid perovskites doped with Mn^{2+} ions after excitation into host absorption bands. It was suggested that after irradiation of the material with a 266 nm diode, non-radiative electron transfer from CT to Mn^{2+} states occurred followed by their radiative relaxation from the $^4T_1(G)$ emission level.[29]

Influence of the hydrazinium cation methylation on the structural properties

The comparison of experimental data for [A]Mn(HCOO)$_3$ (A = Hy^+, MHy^+, $DMHy^+$) compounds shows that they exhibit similar interesting features. All three analogues undergo PTs that are not associated with significant symmetry changes.[15,16] However, it should be noted that [MHy]Mn(HCOO)$_3$ undergoes two PTs associated with ordering of MHy^+, *i.e.* a higher-temperature one related to the weak change of symmetry, and a lower-temperature one leading to a large change of crystal symmetry. Table 3 lists a comparison of selected experimentally-determined factors that are crucial for understanding the influence of increased hydrazine methylation on the properties of the final coordination polymer.

Kieslich *et al.* introduced a modified calculation method of the tolerance factor (TF) for HOIPs as follows:[35]

$$TF = \frac{r_{A_{eff}} + r_X}{\sqrt{2}(r_B + 0.5h_{X_{eff}})} \quad (5)$$

where $r_{A_{eff}}$ denotes the effective ionic radius of the protonated amine A, r_X is the ionic radius of the anion X, r_B is the ionic

Table 3 The comparison of the structure-related parameters for [A]Mn(HCOO)$_3$ (A = Hy$^+$, MHy$^+$, DMHy$^+$) compounds

Parameter	Hy$^+$ [13]	MHy$^+$ [14]	DMHy$^+$
T_{c1}^{C}, T_{c1}^{H}, T_{c1}^{av} [a] (K)	353, 357, 355	309, 310, 309.5	244.4, 283.0, 263.7
SG [b]	*Pnma* → *Pna*2$_1$	*R*$\bar{3}$*c* → *R*3*c*	*P*2$_1$/*n* → *P*2$_1$/*n*
PT order	2nd, PE → FE [c]	2nd, PE → FE [c]	1st, PE → PE [c]
T_{c2}^{C}, T_{c2}^{H}, T_{c2}^{av} [a] (K)	—	213, 224, 218.5	—
SG [b]	—	*R*3*c* → *P*1	—
PT order	—	1st, FE → FE [c]	—
$r_{A_{eff}}$ [d] (pm)	217	264	296
TF [e]	0.81	0.92	1.01
Δd [f] ($\times 10^{-3}$)	1.24 (400 K)	0 (330 K)	2.02, 5.65 [g] (300 K)
	2.30 (290 K)	5.62 (290 K)	3.22 (100 K)
	2.34 (110 K)	5.13 (230 K)	
		8.38, 12.55 [g] (100 K)	
Σ^{cis} [h]	25.58 (400 K)	18.51 (330 K)	18.27, 28.77 [g] (300 K)
	27.84 (290 K)	18.98 (290 K)	45.52 (100 K)
	29.27 (100 K)	18.75 (230 K)	
		20.31, 21.68 [g] (100 K)	
Σ^{trans} [i]	0 (400 K)	0.11 (330 K)	0, 0 [g] (300 K)
	6.23 (290 K)	1.58 (290 K)	21.75 (100 K)
	7.63 (110 K)	4.75 (230 K)	
		4.27, 9.04 [g] (100 K)	
Mn–Mn [j] (Å)	5.9392 (400 K)	6.0975 (330 K)	6.1935 (300 K)
	5.9078 (290 K)	6.0908 (290 K)	6.0925 (100 K)
	5.8796 (110 K)	6.0822 (230 K)	
		6.0297 (100 K)	
ΔS^k (J mol^{-1} K^{-1})	10.8	1.99, 3.00 [l]	6.95
N [m]	3.7	1.3, 1.4 [l]	2.11

Key: [a] Temperatures of PTs upon cooling (C), heating (H) and average value (av). [b] Space group. [c] From HT to LT phase, PE, FE denote paraelectric and ferroelectric phase, respectively. [d] The effective ionic radius of the protonated amine. [e] Tolerance factor. [f] Bond length distortion. [g] For Mn1 and Mn2. [h] The sum of deviations from 90° of the 12 *cis* angles in the coordination sphere of the Mn^{2+} ion. [i] The sum of deviations from 180° of the 3 *trans* angles in the coordination sphere of the Mn^{2+} ion. [j] The shortest distances. [k] The average value for heating and cooling runs. [l] For T_{c1} and T_{c2}, respectively. [m] Calculated using the $\Delta S = R\ln(N)$ formula.

radius of the divalent ion B, and $h_{X_{eff}}$ denotes the effective height of the organic anion X.[35] The $r_{A_{eff}}$ of the DMHy$^+$ cation has not yet been reported, however, it can be calculated using the following formula:

$$r_{A_{eff}} = r_{mass} + r_{ion}, \quad (6)$$

where r_{mass} and r_{ion} denote the distance between the center of mass of the molecule and the atom with the largest distance to the center of mass (except of H atoms) and the ionic radius of this ion, respectively.[35] Based on the X-ray data, the $r_{A_{eff}}$ of DMHy$^+$ is estimated to be 296 pm at 300 K and 290 pm at 100 K. It is worth noting that this is the largest cation used so far for the synthesis of formate-based 3D perovskites.

Thus, the corresponding TF for the [DMHy]Mn(HCOO)$_3$ compound is equal to 1.01. According to Kieslich *et al.*,[35] this value is a borderline for hybrids with perovskite-like architecture (0.81–1.01); therefore, the symmetry of [DMHy]Mn(HCOO)$_3$ is lower (monoclinic) compared to more perfectly fitted [MHy]Mn(HCOO)$_3$ with TF = 0.92 being in the middle of that range and adopting trigonal symmetry.[16] The lower (orthorhombic) symmetry of [Hy]Mn(HCOO)$_3$ with reported TF = 0.81 supports the conclusion that Hy$^+$ and DMHy$^+$ cations are too small and too high, respectively, to form high-symmetry perovskite-like phases with the manganese–formate framework. The loosely or tightly filled crystal voids in [Hy]Mn(HCOO)$_3$ and [DMHy]Mn(HCOO)$_3$, respectively, affect the distortion of the manganese–formate framework, as evidenced by the bond distortion (Δd) and $\Sigma^{cis/trans}$ parameters as well as the Mn–Mn distances in different phases (see Table 3). The Δd parameters for [Hy]Mn(HCOO)$_3$ are relatively small (1.24×10^{-3}–2.34×10^{-3}) in both HT and LT phases. The O–Mn–O cis angles in the MnO_6 octahedra deviate moderately from 90° (25.58–29.27) in both phases, while the trans angles are unaffected in the HT phase and distorted in the LT phase (6.23–7.63). In the HT phase of [MHy]Mn(HCOO)$_3$ the MnO_6 units are less distorted compared to the Hy$^+$ analogue. The PT to the IT phase does not involve further significant changes in the manganese–formate framework, however, in the LT phase the Δd parameter increases up to 12.55×10^{-3}, reflecting elongation of the octahedral units. The corresponding $\Sigma^{cis/trans}$ parameters remain similar as calculated for [Hy]Mn(HCOO)$_3$ at 100 K. The DMHy$^+$ cations in the manganese–formate framework do not induce the elongation of the MnO_6 units in both phases. The cis angles are moderately distorted in the HT phase of [DMHy]Mn(HCOO)$_3$, similarly to all phases of [Hy]Mn(HCOO)$_3$ and [MHy]Mn(HCOO)$_3$, but after transformation to the LT phase they reveal the highest observed deviation from the perfect octahedron with Σ^{cis} = 45.52 (100 K). The strongest deformation of the manganese–formate framework is also manifested by the high value of the corresponding Σ^{trans} parameter, which equals 21.75 at 100 K. A very interesting feature, confirming the strongest distortion of the [DMHy]Mn(HCOO)$_3$ framework, is shrinking of the Mn–Mn distances when going from RT to 100 K temperature. This parameter equals 1.00% for [Hy]Mn(HCOO)$_3$ and [MHy]Mn(HCOO)$_3$, while for [DMHy]Mn(HCOO)$_3$ it reaches a higher value of 1.63%.

Table S3 (ESI†) presents a detailed comparison of the HB geometry in all considered analogues. In the HT phase of the Hy^+ analogue, each H atom of the protonated amino group creates one stronger (shorter with angle close to 180°) and one weaker (longer with sharper angle) N–H···O bond, while the second $–NH_2$ group is able to form only weaker HBs. Upon cooling, all HBs become slightly shorter but the pattern of HBs is preserved in the LT phase. The substitution of the H atom by the methyl group in $[MHy]Mn(HCOO)_3$ decreases the number of protons and affects the arrangement of HBs. In the HT phase of $[MHy]Mn(HCOO)_3$ each H atom creates a similar pattern to the Hy^+ analogue, however, the longer N–H···O interactions are clearly weaker. Further methylation leads to disappearance of the longer HBs for the NH^+ group in the HT phase of $[DMHy]Mn(HCOO)_3$. However, due to the tightly fitted $DMHy^+$, the free $–NH_2$ and $–CH_3$ groups create weak HBs and this behaviour was not observed in the HT phase of $[MHy]Mn(HCOO)_3$. In the LT phases of all three compounds the created HB patterns are ordered and have similar arrangement. The strength of HBs follows the order $MHy^+ > Hy^+ > DMHy^+$ and $Hy^+ > DMHy^+ > MHy^+$ for the protonated and not protonated ammonium groups, respectively.

All those effects reflect the fit of ammonium and Mn^{2+} cations in the formate 3D polymers. The Hy^+ cation is small and has the highest freedom in the larger voids of the manganese–formate framework (N = 3.7 and ΔS = 10.8 J mol^{-1} K^{-1}, see Table 3),[13] while the $DMHy^+$ cation is too large to create the ideal perovskite-type architecture, and thus it is more tightly confined (N = 2.11 and ΔS = 6.95 J mol^{-1} K^{-1}).

In general, the increased steric hindrance affects the mechanism of the observed PTs, *i.e.* for the Hy^+ analogue the main driving force of the PT is ordering of Hy^+ cations followed by a weak deformation of the framework, for the MHy^+ analogue there is a subtle interplay of the both effects, while for the $DMHy^+$ analogue both the distortion of the manganese–formate framework and the ordering of $DMHy^+$ contributed strongly to the PT mechanism. Fig. 8a–f presents the dependencies of a few selected factors as a function of the PT temperature. The average temperature of the observed PTs clearly and linearly correlates with the change of the Mn–Mn distance observed near RT and 100 K ($\Delta Mn^{290–300}$–$Mn^{100/110}$), molar mass and $r_{A_{eff}}$ of the cation, TF and N calculated from the experimental value of ΔS. These correlations indicate that the increasing number of methyl groups and subsequent steric hindrance cause a decrease in the number of disordered states and thus change in the corresponding entropy. The deviation from a linear character of ΔS as a function of the PT temperature (Fig. 8f) suggests that vibrational entropy significantly contributes to the mechanisms of the PTs in the studied HOIPs comprising differently fitted hydrazinium cations. Due to the relatively large size of the $DMHy^+$ cation, the crystal symmetry of $[DMHy]Mn(HCOO)_3$ is relatively low (monoclinic) and a ferroelectric order is no longer preferred, in contrast to ferroelectric $[Hy]Mn(HCOO)_3$ and $[MHy]Mn(HCOO)_3$ analogues.[15,16]

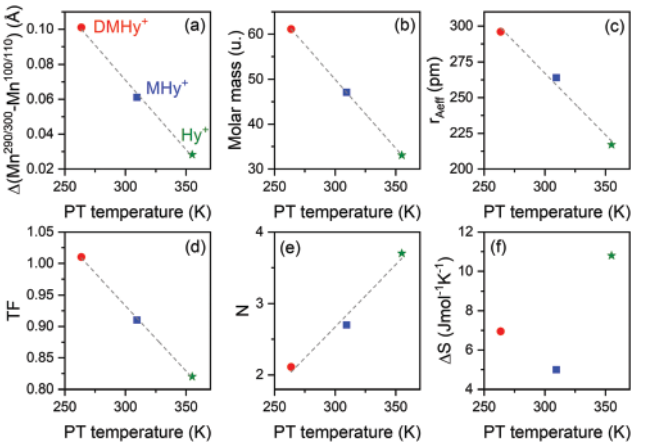

Fig. 8 The dependencies of (a) the change of the Mn–Mn distance observed near room temperature and at 100 K (or 110 K), (b) molar mass, (c) effective ionic radius, (d) tolerance factor, (e) number of disordered states of cation and (f) change of entropy as a function of average PT temperature.

Isosymmetric PTs in 3D hybrid perovskites

According to the phenomenological model, the type 0 PTs with no change of space group or Wyckoff positions are certainly first order.[36] Such PTs are extremely rare among 3D hybrid perovskites, and to the best of our knowledge, they were reported for a few compounds so far (see Table S3, ESI†). Most of them were classified as a first order type, however, for perovskites and double perovskites with imidazolium cations (Im^+) they were recognized as a continuous transformation.[37,38] Almost all compounds exhibit temperature hysteresis of PT, but the value obtained for $[DMHy]Mn(HCOO)_3$ is significantly larger.

PTs listed in Table S3 (ESI†) are mainly driven by ordering of the templated cation; however, for some of them both, the LT and HT, phases are ordered. The distortion of the metal–ligand framework can be either a dominant or an accompanying driving force. Among the listed compounds, the space group and site symmetries are retained for $[DMA]_2KM^{III}(CN)_6$ (M^{III} = Cr^{3+}, Co^{3+} and Fe^{3+})[39–42] and $[Im]_2KM^{III}(CN)_6$ (M^{III} = Co^{3+} and Fe^{3+}) double perovskites.[38,43] For $[DMHy]Mn(HCOO)_3$ and $[MA]Mn(N_3)_3$,[44] the Mn^{2+} ions and middle N atoms in the N_3^- ligands, respectively, change sites during PTs.[44] It should be noted that despite the space group retainment for $[DMHy]Mn(HCOO)_3$, two crystallographic axes, b and c, are switched in the HT phase. Surprisingly, for the second formate listed in Table S3 (ESI†), $[Im]Mg(HCOO)_3$, the unit cell parameter c is halved in the isostructural HT phase.[37]

We also compared TFs for perovskites listed in Table S3 (ESI†). They were calculated for double perovskites using the extended formula presented by Shi *et al.*[45] Most of them are within the expected perovskite-architecture range, except of $[GA]SnCl_3$ (GA^+ = guanidinium cation)[46] and $[Tz]_2KCo(CN)_6$ (Tz^+ = thiazolium cation)[47] with TF = 1.185 and 1.07, respectively.

Since the presented isosymmetric PTs for hybrid perovskites have a unique and complex nature, there is still no clear correlation between observed structural features and their

preference to occur. This subject, however, is worthy to be studied in the future, especially taking into account other structures, measurement techniques and different external stimuli.

Conclusions

We reported the synthesis and properties of a novel perovskite-like manganese–formate framework templated by the $DMHy^+$ cation that, to the best of our knowledge, has not been previously employed in the synthesis of any HOIPs. [DMHy]Mn(HCOO)$_3$ crystallizes in the monoclinic $P2_1/n$ system and undergoes an order–disorder PT to the LT phase possessing the same $P2_1/n$ symmetry but different arrangement of the building blocks. Thus, the PT in [DMHy]Mn(HCOO)$_3$ is the first example of temperature-induced isostructural PT among the large family of hybrid formates. The mechanism of the observed PT is driven by a strong deformation of the metal–formate framework and ordering of the organic cations that leads to re-organization of the HB pattern. The $DMHy^+$ cation is the largest cation used so far for the synthesis of formate-based 3D perovskites. The comparison of the structural features of [DMHy]Mn(HCOO)$_3$ with experimental data reported previously for Hy^+ and MHy^+ analogues indicates that the increased steric hindrance, triggered by the increased number of methyl groups in the hydrazinium cation, suppresses the ferroelectric order. It also affects the PT temperature and the PT mechanism. It has been found that the average PT temperature for the Hy^+, MHy^+ and $DMHy^+$ analogues is linearly correlated with the effective ionic radius of the cation, TF and number of disordered states. We argue that the $DMHy^+$ cations are too large to adopt high symmetry of perovskite-like topology. Thus, our results show that the steric hindrance is another factor that should be taken into account in designing novel hybrid perovskites.

Magnetic studies indicate that [DMHy]Mn(HCOO)$_3$ is a weak ferromagnet with the ordering temperature of 8.4 K. It is also a wide-band gap material with the energy band gap of 4.63 eV. Dielectric studies revealed that the PT is associated with a very pronounced step-like anomaly, suggesting a prospective application of [DMHy]Mn(HCOO)$_3$ as a switchable dielectric material. We have also shown that this perovskite exhibits broadband photoluminescence with a maximum at 725 nm. The intensity of this photoluminescence is strongly temperature-dependent, making [DMHy]Mn(HCOO)$_3$ a potential material for non-contact temperature sensing below 200 K.

Author contributions

J. A. Zienkiewicz – conceptualization, formal analysis, investigation, methodology, visualization, writing – original draft; D. A. Kowalska, K. Fedoruk, M. Stefanski, A. Pikul – investigation, visualization, writing – original draft; M. Ptak – conceptualization, formal analysis, investigation, methodology, supervision, visualization, writing – original draft, writing – review & editing.

Conflicts of interest

There are no conflicts to declare.

References

1 G. P. Nagabhushana, R. Shivaramaiah and A. Navrotsky, *J. Am. Chem. Soc.*, 2015, **137**, 10351–10356.
2 W. Li, A. Stroppa, Z. Wang and S. Gao, *Hybrid Organic–Inorganic Perovskites*, Wiley, 2020.
3 W. Li, Z. Wang, F. Deschler, S. Gao, R. H. Friend and A. K. Cheetham, *Nat. Rev. Mater.*, 2017, **2**, 16099.
4 M. Śanchez-Andujar, S. Presedo, S. Ýnez-Vilar, S. Castro-García, J. Shamir and M. A. Senaris-Rodriguez, *Inorg. Chem.*, 2010, **49**, 1510–1516.
5 M. Mączka, B. Bondzior, P. Dereń, A. Sieradzki, J. Trzmiel, A. Pietraszko and J. Hanuza, *Dalton Trans.*, 2015, **44**, 6871–6879.
6 W. Li, Z. Zhang, E. G. Bithell, A. S. Batsanov, P. T. Barton, P. J. Saines, P. Jain, C. J. Howard, M. A. Carpenter and A. K. Cheetham, *Acta Mater.*, 2013, **61**, 4928–4938.
7 K. Wang, J. B. Xiong, B. Xia, Q. L. Wang, Y. Z. Tong, Y. Ma and X. H. Bu, *Inorg. Chem.*, 2018, **57**, 537–540.
8 M. Mączka, M. Ptak and S. Kojima, *Appl. Phys. Lett.*, 2014, **104**, 222903.
9 Z. Wang, K. Hu, S. Gao and H. Kobayashi, *Adv. Mater.*, 2010, **22**, 1526–1533.
10 H. Schmid, *J. Phys.: Condens. Matter*, 2008, **20**, 434201.
11 L. C. Gómez-Aguirre, B. Pato-Doldán, J. Mira, S. Castro-García, M. A. Señarís-Rodríguez, M. Sánchez-Andújar, J. Singleton and V. S. Zapf, *J. Am. Chem. Soc.*, 2016, **138**, 1122–1125.
12 H. D. Duncan, M. T. Dove, A. Keen and A. E. Phillips, *Dalton Trans.*, 2016, **10**, 4380–4391.
13 P. Jain, V. Ramachandran, R. J. Clark, D. Z. Hai, B. H. Toby, N. S. Dalal, H. W. Kroto and A. K. Cheetham, *J. Am. Chem. Soc.*, 2009, **131**, 13625–13627.
14 M. Mączka, K. Pasińska, M. Ptak, W. Paraguassu, T. A. da Silva, A. Sieradzki and A. Pikul, *Phys. Chem. Chem. Phys.*, 2016, **18**, 31653–31663.
15 S. Chen, R. Shang, K.-L. L. Hu, Z.-M. M. Wang and S. Gao, *Inorg. Chem. Front.*, 2014, **1**, 83–98.
16 M. Mączka, A. Gągor, M. Ptak, W. Paraguassu, T. A. Da Silva, A. Sieradzki and A. Pikul, *Chem. Mater.*, 2017, **29**, 2264–2275.
17 Z. Wang, B. Zhang, T. Otsuka, K. Inoue, H. Kobayashi and M. Kurmoo, *J. Chem. Soc., Dalton Trans.*, 2004, **4**, 2209–2216.
18 R. I. Thomson, P. Jain, A. K. Cheetham and M. A. Carpenter, *Phys. Rev. B: Condens. Matter Mater. Phys.*, 2012, 214304.
19 B. Saparov and D. B. Mitzi, *Chem. Rev.*, 2016, **116**, 4558–4596.
20 M. Mączka, M. Ptak, A. Gągor, D. Stefańska, J. K. Zaręba and A. Sieradzki, *Chem. Mater.*, 2020, **32**, 1667–1673.
21 M. Mączka, A. Gagor, J. K. Zaręba, D. Stefanska, M. Drozd, S. Balciunas, M. Šimėnas, J. Banys and A. Sieradzki, *Chem. Mater.*, 2020, **32**, 4072–4082.

22 A. Z. Szeremeta, A. Nowok, S. Pawlus, K. Fedoruk, M. Trzebiatowska, M. Mączka, J. Symonowicz, M. Paluch and A. Sieradzki, *Appl. Mater. Today*, 2021, **22**, 100957.
23 A. Sieradzki, M. Mączka, M. Simenas, J. K. Zaręba, A. Gągor, S. Balciunas, M. Kinka, A. Ciupa, M. Nyk, V. Samulionis, J. Banys, M. Paluch and S. Pawlus, *J. Mater. Chem. C*, 2018, **6**, 9420–9429.
24 M. Mączka, M. Ptak, S. Pawlus, W. Paraguassu, A. Sieradzki, S. Balciunas, M. Simenas and J. Banys, *Phys. Chem. Chem. Phys.*, 2016, **18**, 27613–27622.
25 W. Zhang, H. Y. Ye, R. Graf, H. W. Spiess, Y. F. Yao, R. Q. Zhu and R. G. Xiong, *J. Am. Chem. Soc.*, 2013, **135**, 5230–5233.
26 M. Trzebiatowska, M. Mączka, A. Gągor and A. Sieradzki, *Inorg. Chem.*, 2020, **59**, 8855–8863.
27 K. Qian, F. Shao, Z. Yan, J. Pang, X. Chen and C. Yang, *CrystEngComm*, 2016, **18**, 7671–7674.
28 M. Šimenas, S. Balčiunas, M. Trzebiatowska, M. Ptak, M. Mączka, G. Völkel, A. Pöppl and J. Banys, *J. Mater. Chem. C*, 2017, **5**, 4526–4536.
29 M. Mączka, A. Gągor, A. Pikul and D. Stefańska, *RSC Adv.*, 2020, **10**, 19020–19026.
30 M. Li, V. Smetana, M. Wilk-Kozubek, Y. Mudryk, T. Alammar, V. K. Pecharsky and A. V. Mudring, *Inorg. Chem.*, 2017, **56**, 11104–11112.
31 P. Kubelka, *J. Opt. Soc. Am.*, 1948, **38**, 448–457.
32 S. Liu, S. Zhang, N. Mao, Z. Song and Q. Liu, *J. Am. Ceram. Soc.*, 2020, **103**, 6793–6800.
33 P. Dorenbos, *J. Phys.: Condens. Matter*, 2005, **17**, 8103–8111.
34 D. Stefańska, B. Bondzior, T. H. Q. Vu, N. Miniajluk-Gaweł and P. J. Dereń, *J. Alloys Compd.*, 2020, **842**, 155742.
35 G. Kieslich, S. Sun and A. K. Cheetham, *Chem. Sci.*, 2014, **5**, 4712–4715.
36 A. G. Christy, *Acta Crystallogr., Sect. B: Struct. Sci.*, 1995, **51**, 753–757.
37 M. Mączka, N. L. Marinho Costa, A. Gągor, W. Paraguassu, A. Sieradzki and J. Hanuza, *Phys. Chem. Chem. Phys.*, 2016, **18**, 13993–14000.
38 W. Zhang, Y. Cai, R.-G. Xiong, H. Yoshikawa and K. Awaga, *Angew. Chem., Int. Ed.*, 2010, **49**, 6608–6610.
39 M. Rok, G. Bator, B. Zarychta, B. Dziuk, J. Repeć, W. Medycki, M. Zamponi, G. Usevičius, M. Šimenas and J. Banys, *Dalton Trans.*, 2019, **48**, 4190–4202.
40 W. Zhang, H.-Y. Ye, R. Graf, H. W. Spiess, Y.-F. Yao, R.-Q. Zhu and R.-G. Xiong, *J. Am. Chem. Soc.*, 2013, **135**, 5230–5233.
41 M. Rok, G. Bator, W. Medycki, M. Zamponi, S. Balčiūnas, M. Šimėnas and J. Banys, *Dalton Trans.*, 2018, **47**, 17329–17341.
42 W.-J. Xu, S.-L. Chen, Z.-T. Hu, R.-B. Lin, Y.-J. Su, W.-X. Zhang and X.-M. Chen, *Dalton Trans.*, 2016, **45**, 4224–4229.
43 X. Zhang, X. D. Shao, S. C. Li, Y. Cai, Y. F. Yao, R. G. Xiong and W. Zhang, *Chem. Commun.*, 2015, **51**, 4568–4571.
44 X. H. Zhao, X. C. Huang, S. L. Zhang, D. Shao, H. Y. Wei and X. Y. Wang, *J. Am. Chem. Soc.*, 2013, **135**, 16006–16009.
45 C. Shi, C. H. Yu and W. Zhang, *Angew. Chem., Int. Ed.*, 2016, **55**, 5798–5802.
46 M. Szafrański and K. Ståhl, *J. Solid State Chem.*, 2007, **180**, 2209–2215.
47 Z. X. Gong, Q. W. Wang, J. J. Ma, J. Y. Jiang, D. Y. E, Z. Q. Li, F. W. Qi and H. Liang, *Mater. Chem. Front.*, 2020, **4**, 918–923.

Electronic Supplementary Material (ESI) for Journal of Materials Chemistry C.

Supporting Information for

Unusual isosymmetric order-disorder phase transition in the new perovskite-type dimethylhydrazinium manganese formate exhibiting weak ferromagnetism and photoluminescent properties

by J.A. Zienkiewicz, D. Kowalska, K. Fedoruk, M. Stefański, A. Pikul, M. Ptak

Content:

Fig. S1. The asymmetric unit at 300 K (HT phase) (a) and at 100 K (LT phase) (b) showing the atom numbering scheme. Displacement ellipsoids are drawn at the 50 % probability level. In the HT phase the $DMHy^+$ cation is disordered over three positions with the same ratio ⅓ (the positions disordered over C and N atoms are presented as octants). [Symmetry codes: ^{i} $-x$, $-y+1$, $-z+2$; ^{ii} $-x+1$, $-y+2$, $-z+2$.]

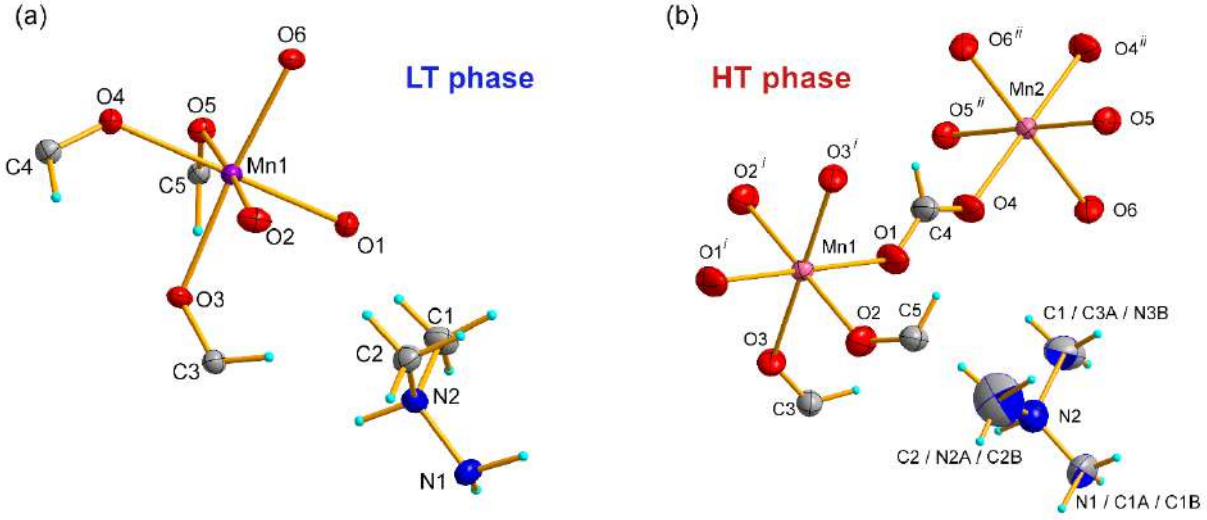

Fig. S2. Powder XRD pattern for the as-prepared bulk sample of [DMHy]Mn(HCOO)$_3$ together with the simulated one based on the single crystal structure refined at 300 K

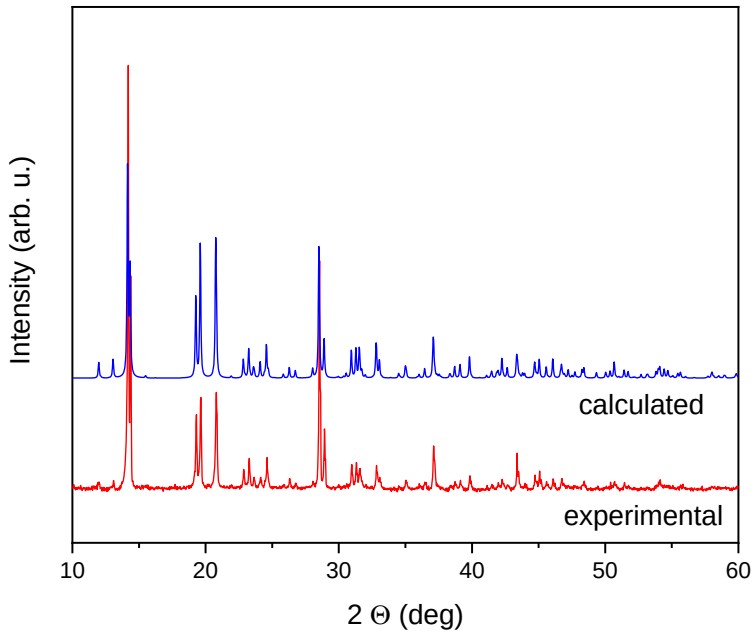

Fig. S3. The DSC traces measured in a cooling and heating runs

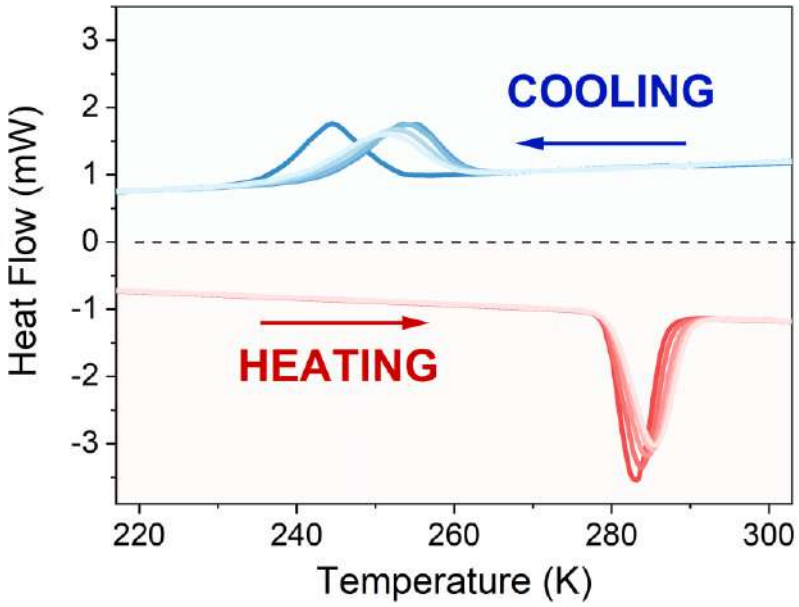

Fig. S4. The temperature dependence of the dielectric loss ε'' of [DMHy]Mn(HCOO)$_3$ measured for (a) single crystal in the [110] directions, (b) single crystal in the perpendicular to [110] direction, (c) a pellet. The representative curves are plotted in frequency decades between 10^3 Hz and 10^6 Hz. The vertical lines correspond to the phase-transition temperatures obtained from the dynamic DSC measurements

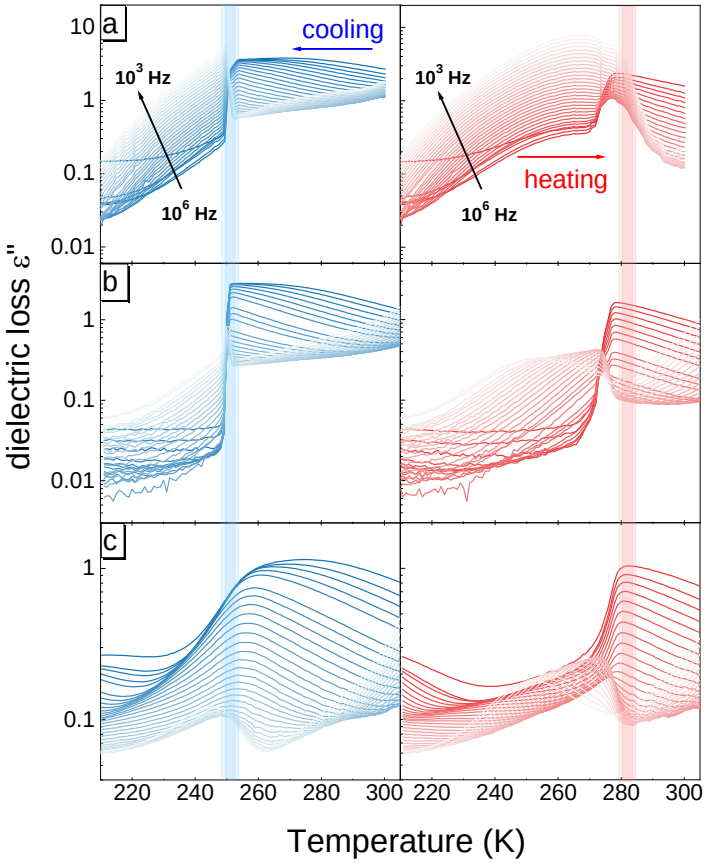

Fig. S5. Relaxation times as a function of 1000/*T*. The blue points correspond to the curves obtained during cooling, and the red points during heating. The inset shows the frequency-dependent dielectric loss measured at 250 K (on cooling) and 275 K (on heating).

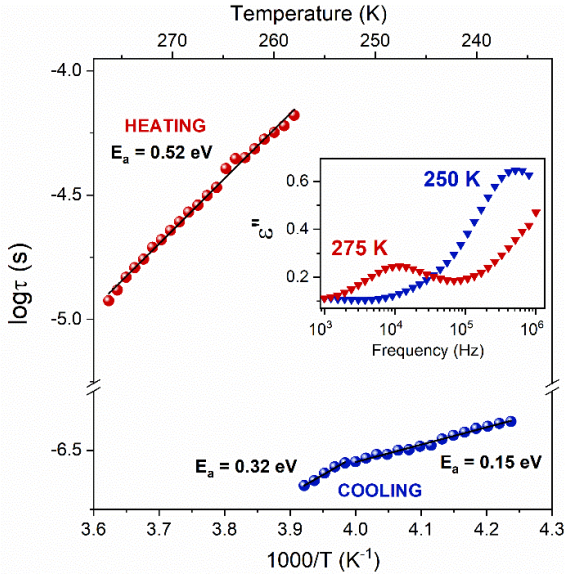

Fig. S6. The result of determining the energy band gap (E_g) using the Kubelka-Munk theory for the [DMHy]Mn(HCOO)$_3$ crystals

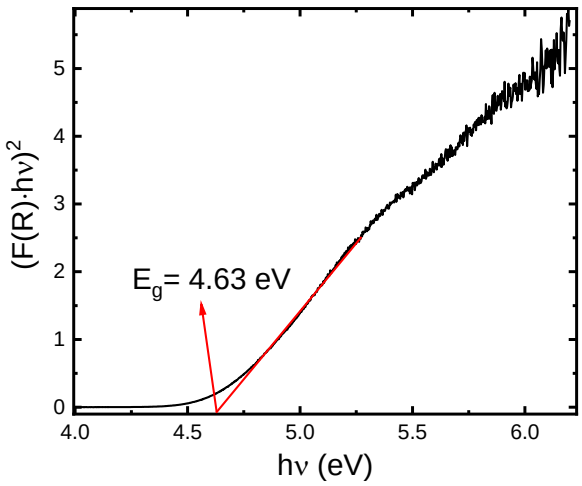

Fig. S7. Activation energy of the thermal quenching of emission bands of [DMHy]Mn(HCOO)$_3$ crystals excited at 266 nm

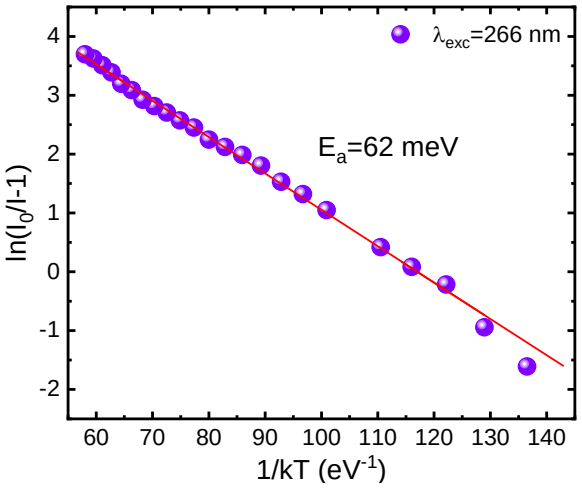

Fig. S8. The luminescence decay profile of [DMHy]Mn(HCOO)$_3$ crystals excited at 266 nm and monitored at 725 nm recorded at 77 K

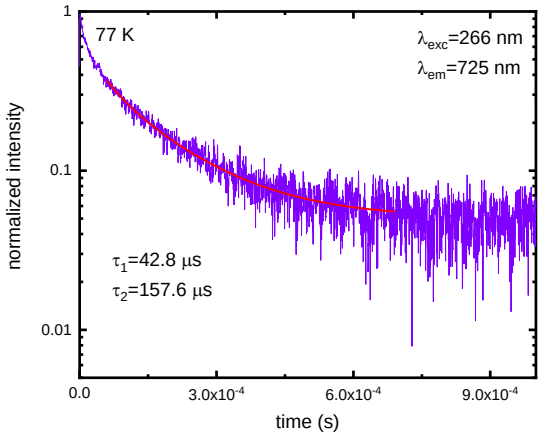

Tab. S1. Hydrogen-bond geometry for [DMHy]Mn(HCOO)$_3$

D—H···*A*	*D*—H (Å)	H···*A* (Å)	*D*···*A* (Å)	*D*—H···*A* (º)
HT phase (300 K)				
N1—H1*A*···O2^{i}	1.03	2.58	3.537 (10)	154
N1—H1*B*···O6^{ii}	1.03	2.16	3.040 (6)	143
N2—H2···O5^{iii}	0.98	1.84	2.811 (3)	173
C1—H1D···O3^{iv}	0.96	2.57	3.432 (10)	149
C1—H1*E*···O4	0.96	2.37	3.265 (10)	154
N1*A*—H1*AB*···O1^{v}	1.03	2.55	3.412 (8)	140
N1*A*—H1*AB*···O2^{vi}	1.03	2.44	3.207 (6)	131
C1*A*—H1*AC*···O3^{iv}	0.96	2.45	3.359 (7)	157
C1*A*—H1*AD*···O4	0.96	2.51	3.428 (8)	161
C2*A*—H2*AC*···O1	0.96	2.38	3.305 (12)	163
LT phase (100 K)				
N1—H1A···O6^{ii}	1.00	1.99	2.961 (3)	163
N1—H1B···O1^{vii}	0.99	2.09	3.072 (3)	177
N1—H1B···O4^{v}	0.99	2.53	3.172 (4)	123
N2—H2···O4^{v}	0.98	2.60	3.133 (3)	115
N2—H2···O5^{v}	0.98	1.94	2.846 (3)	152
C2—H2A···O2^{viii}	0.96	2.52	3.267 (4)	135
C2—H2B···O5^{ix}	0.96	2.37	3.321 (4)	169
C2—H2C···O3^{iv}	0.96	2.55	3.456 (4)	157

Symmetry codes: ^{i} $-x+1/2, y+1/2, -z+3/2$; ^{ii} $-x+3/2, y-1/2, -z+3/2$; ^{iii} $x-1/2, -y+3/2, z-1/2$; ^{iv} $x+1, y, z$; ^{v} $-x+1/2, y-1/2, -z+3/2$; ^{vi} $x+1/2, -y+1/2, z-1/2$; ^{vii} $-x+1, -y+1, -z+1$; ^{viii} $-x+1, -y+1, -z+2$; ^{ix} $x+1/2, -y+3/2, z+1/2$.

All e.s.d.'s (except the e.s.d. in the dihedral angle between two l.s. planes) are estimated using the full covariance matrix. The cell e.s.d.'s are taken into account individually in the estimation of e.s.d.'s in distances, angles and torsion angles; correlations between e.s.d.'s in cell parameters are only used when they are defined by crystal symmetry. An approximate (isotropic) treatment of cell e.s.d.'s is used for estimating e.s.d.'s involving l.s. planes.

Tab. S2. Selected geometric parameters (Å, °) in [DMHy]Mn(HCOO)$_3$

HT phase (300 K)			
Mn1—O1	2.1773 (16)	O1—C4	1.225 (3)
Mn1—O1^{i}	2.1773 (16)	O2—C5	1.224 (3)
Mn1—O2	2.1864 (16)	O3—C3	1.233 (3)
Mn1—O2^{i}	2.1864 (16)	O4—C4	1.229 (3)
Mn1—O3	2.1875 (17)	O5—C5^{iii}	1.256 (3)
Mn1—O3^{i}	2.1875 (17)	O6—C3^{iv}	1.229 (3)

Mn2—O4	2.1681 (16)	N1—N2	1.482 (6)
Mn2—O4^{ii}	2.1681 (16)	N2—C1	1.398 (10)
Mn2—O5	2.2046 (15)	N2—C2	1.476 (10)
Mn2—O5^{ii}	2.2046 (15)	N2—N1A	1.428 (6)
Mn2—O6	2.1873 (16)	N2—C1A	1.538 (8)
Mn2—O6^{ii}	2.1873 (16)	N2—C2A	1.538 (8)

LT phase (100 K)

Mn1—O4	2.173 (2)	O3—C3	1.251 (3)
Mn1—O5	2.199 (2)	O6—C3^{iv}	1.256 (3)
Mn1—O3	2.190 (2)	N1—N2	1.447 (3)
Mn1—O6	2.180 (2)	O2—C5^{vi}	1.252 (4)
Mn1—O2	2.188 (2)	O1—C4^{vii}	1.248 (4)
Mn1—O1	2.181 (2)	N2—C2	1.488 (4)
O4—C4	1.246 (4)	N2—C1	1.490 (4)
O5—C5	1.267 (4)		

HT phase (300 K)

O1—Mn1—O1^{i}	180.0	O6—Mn2—O5	87.93 (6)
O1^{i}—Mn1—O2^{i}	89.44 (7)	O6—Mn2—O5^{ii}	92.07 (6)
O1^{i}—Mn1—O2	90.56 (7)	O6^{ii}—Mn2—O6	180.0
O1—Mn1—O2^{i}	90.56 (7)	C4—O1—Mn1	133.92 (15)
O1—Mn1—O2	89.44 (7)	C5—O2—Mn1	136.81 (15)
O1^{i}—Mn1—O3	90.64 (7)	C3—O3—Mn1	127.76 (16)
O1^{i}—Mn1—O3^{i}	89.36 (7)	C4—O4—Mn2	134.89 (16)
O1—Mn1—O3^{i}	90.64 (7)	C5^{iii}—O5—Mn2	126.38 (14)
O1—Mn1—O3	89.36 (7)	C3^{iv}—O6—Mn2	132.23 (16)
O2^{i}—Mn1—O2	180.0	O6^{v}—C3—O3	128.4 (2)
O2^{i}—Mn1—O3	93.37 (6)	O1—C4—O4	127.6 (2)
O2—Mn1—O3^{i}	93.37 (6)	O2—C5—O5^{iii}	125.5 (2)
O2^{i}—Mn1—O3^{i}	86.63 (6)	N1—N2—C1A	102.7 (4)
O2—Mn1—O3	86.63 (6)	C1—N2—N1	113.7 (5)
O3—Mn1—O3^{i}	180.0	C1—N2—C2	109.2 (6)
O4—Mn2—O4^{ii}	180.0	C1—N2—N1A	120.6 (5)
O4—Mn2—O5^{ii}	85.91 (7)	C1—N2—C1A	12.5 (5)
O4^{ii}—Mn2—O5	85.91 (7)	C1—N2—C2A	98.0 (6)
O4—Mn2—O5	94.09 (7)	C2—N2—N1	113.4 (5)
O4^{ii}—Mn2—O5^{ii}	94.09 (7)	C2—N2—C1A	120.6 (5)
O4—Mn2—O6^{ii}	91.06 (6)	C2—N2—C2A	15.3 (6)
O4^{ii}—Mn2—O6	91.06 (6)	N1A—N2—N1	19.2 (3)
O4—Mn2—O6	88.94 (6)	N1A—N2—C2	94.5 (5)

O4^{ii}—Mn2—O6^{ii}	88.94 (6)	N1A—N2—C1A	112.1 (4)
O5—Mn2—O5^{ii}	180.00 (9)	N1A—N2—C2A	109.5 (5)
O6^{ii}—Mn2—O5^{ii}	87.93 (6)	C2A—N2—N1	128.5 (5)
O6^{ii}—Mn2—O5	92.07 (6)	C2A—N2—C1A	110.2 (5)
LT phase (100 K)			
O4—Mn1—O5	81.16 (8)	O1—Mn1—O2	94.70 (10)
O4—Mn1—O3	92.50 (8)	C4—O4—Mn1	130.7 (2)
O4—Mn1—O6	90.94 (8)	C5—O5—Mn1	126.5 (2)
O4—Mn1—O2	96.20 (9)	C3—O3—Mn1	121.37 (16)
O4—Mn1—O1	168.79 (9)	C3^{iv} —O6—Mn1	129.81 (17)
O3—Mn1—O5	92.58 (8)	C5^{vi}—O2—Mn1	132.2 (2)
O6—Mn1—O5	94.38 (8)	O2^{viii}—C5—O5	125.0 (3)
O6—Mn1—O3	172.64 (7)	C4^{ix}—O1—Mn1	134.1 (2)
O6—Mn1—O2	87.41 (8)	O4—C4—O1^{x}	124.4 (3)
O6—Mn1—O1	92.14 (8)	N1—N2—C2	109.0 (2)
O2—Mn1—O5	176.82 (8)	N1—N2—C1	114.2 (2)
O2—Mn1—O3	85.75 (8)	C2—N2—C1	111.2 (2)
O1—Mn1—O5	87.86 (9)	O3—C3—O6^{v}	125.1 (2)
O1—Mn1—O3	85.72 (8)		
Br3—Pb1—Br1	92.973 (8)		

Symmetry codes: ^{i} $-x, -y+1, -z+2$; ^{ii} $-x+1, -y+2, -z+2$; ^{iii} $-x+1, -y+1, -z+2$; ^{iv} $-x+1/2, y+1/2, -z+3/2$; ^{v} $-x+1/2, y-1/2, -z+3/2$; ^{vi} $x+1/2, -y+3/2, z+1/2$; ^{vii} $x+1/2, -y+3/2, z-1/2$; ^{viii} $x-1/2, -y+3/2, z-1/2$; ^{ix} $x-1, y, z$; ^{x} $x-1/2, -y+3/2, z+1/2$.

Tab. S3. The temperature-dependent isosymmetric PTs reported for single and double 3D hybrid perovskites

Compound	LT → HT	T (K) [a]	Order	TF	Ref.
Perovskites					
[DMHy]Mn(HCOO)$_3$	$P2_1/n \rightarrow P2_1/n$	250.9 / 281.9	1st	1.01	[b]
[Im]Mg(HCOO)$_3$	$P2_1/n \rightarrow P2_1/n$	451 / 448	2nd	0.90	[1,2]
[MA]Mn(N$_3$)$_3$ [c]	$P2_1/c \rightarrow P2_1/c$	280 / 263	1st	0.84	[3,4]
[GA]SnCl$_3$	$Pnma \rightarrow Pnma$	419 / 409	1st	1.185	[5,6]
Double perovskite					
[DMA]$_2$KCo(CN)$_6$	$P4/mnc \rightarrow P4/mnc$	249 / 241	1st	0.96	[7]
[DMA]$_2$KCr(CN)$_6$	$P4/mnc \rightarrow P4/mnc$	218 / 215	1st	0.95	[8]
[DMA]$_2$KFe(CN)$_6$	$P4/mnc \rightarrow P4/mnc$	228 / 227	1st	0.96	[9,10]
[Im]$_2$KCo(CN)$_6$	$R\bar{3}m \rightarrow R\bar{3}m$	198	[d]	0.93	[11]
[Im]$_2$KFe(CN)$_6$	$R\bar{3}m \rightarrow R\bar{3}m$	187	2nd	0.93	[12]
[Tz]$_2$KCo(CN)$_6$	$Cmcm \rightarrow Cmcm$	237	1st	1.07	[13]

Key: [a] on heating/cooling, if given; [b] this work; [c] both (LT and HT) phases are ordered; [d] not given; [e] not calculated; Im$^+$, imidazolium; MA$^+$, methylammonium; GA$^+$, guanidinium, DMA$^+$, dimethylammonium; Tz$^+$, thiazolium

1 M. Mączka, N. L. Marinho Costa, A. Gągor, W. Paraguassu, A. Sieradzki and J. Hanuza, *Phys. Chem.*

Chem. Phys., 2016, **18**, 13993–14000.
2 G. Kieslich, S. Sun and A. K. Cheetham, *Chem. Sci.*, 2014, **5**, 4712–4715.
3 X. H. Zhao, X. C. Huang, S. L. Zhang, D. Shao, H. Y. Wei and X. Y. Wang, *J. Am. Chem. Soc.*, 2013, **135**, 16006–16009.
4 G. Kieslich, S. Sun and A. K. Cheetham, *Chem. Sci.*, 2015, **6**, 3430–3433.
5 M. Szafrański and K. Ståhl, *J. Solid State Chem.*, 2007, **180**, 2209–2215.
6 T. Oku, *Rev. Adv. Mater. Sci.*, 2020, **59**, 264–305.
7 W. Zhang, H.-Y. Ye, R. Graf, H. W. Spiess, Y.-F. Yao, R.-Q. Zhu and R.-G. Xiong, *J. Am. Chem. Soc.*, 2013, **135**, 5230–5233.
8 M. Rok, G. Bator, B. Zarychta, B. Dziuk, J. Repeć, W. Medycki, M. Zamponi, G. Usevičius, M. Šimenas and J. Banys, *Dalt. Trans.*, 2019, **48**, 4190–4202.
9 M. Rok, G. Bator, W. Medycki, M. Zamponi, S. Balčiūnas, M. Šimėnas and J. Banys, *Dalt. Trans.*, 2018, **47**, 17329–17341.
10 W.-J. Xu, S.-L. Chen, Z.-T. Hu, R.-B. Lin, Y.-J. Su, W.-X. Zhang and X.-M. Chen, *Dalt. Trans.*, 2016, **45**, 4224–4229.
11 X. Zhang, X. D. Shao, S. C. Li, Y. Cai, Y. F. Yao, R. G. Xiong and W. Zhang, *Chem. Commun.*, 2015, **51**, 4568–4571.
12 W. Zhang, Y. Cai, R.-G. Xiong, H. Yoshikawa and K. Awaga, *Angew. Chemie Int. Ed.*, 2010, **49**, 6608–6610.
13 Z. X. Gong, Q. W. Wang, J. J. Ma, J. Y. Jiang, D. Y. E, Z. Q. Li, F. W. Qi and H. Liang, *Mater. Chem. Front.*, 2020, **4**, 918–923.

***Publikacja* [D2]**

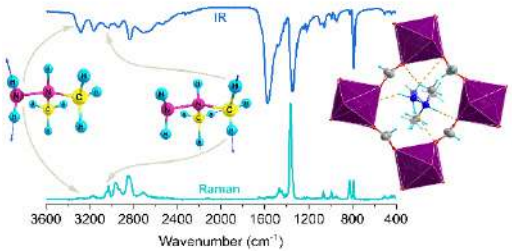

J.A. Zienkiewicz, E. Kucharska, M. Ptak*

Mechanism of unusual isosymmetric order-disorder phase transition in [dimethylhydrazinium]Mn(HCOO)$_3$ hybrid perovskite probed by vibrational spectroscopy

Materials **2021**, 14 (14), 3984

doi: 10.3390/ma14143984 IF = 3,623 140 pkt.

Udział Doktoranta w powstanie pracy:

- Synteza monokryształów [DMHy]Mn(HCOO)$_3$ metodą strąceniową i dyfuzyjną;
- Koncepcja badań oraz określenie metodologii;
- Analiza geometrii zoptymalizowanej cząsteczki DMHy oraz kationu DMHy$^+$ z danymi eksperymentalnymi;
- Wyznaczenie reguł wyboru oraz wykonanie analizy grupy faktorowej;
- Zaproponowanie przypisania pasm IR i Ramana;
- Analiza anharmonizmu na podstawie uzyskanych obliczeń;
- Pomiar widm Ramana oraz IR, również w funkcji temperatury;
- Analiza zachowania pasm IR i Ramana w funkcji temperatury, dekonwolucja widm oraz dopasowywanie krzywych Lorentza do danych eksperymentalnych;
- Dyskusja wyników oraz określenie mechanizmu przemiany fazowej w [DMHy]Mn(HCOO)$_3$
- Przygotowywanie manuskryptu, rysunków oraz tabel.

materials

MDPI

Article

Mechanism of Unusual Isosymmetric Order-Disorder Phase Transition in [Dimethylhydrazinium]Mn(HCOO)$_3$ Hybrid Perovskite Probed by Vibrational Spectroscopy

Jan Albert Zienkiewicz [1], Edyta Kucharska [2] and Maciej Ptak [1,*]

[1] Institute of Low Temperature and Structure Research, Polish Academy of Sciences, Okólna 2 Str., 50-422 Wrocław, Poland; j.zienkiewicz@intibs.pl

[2] Department of Bioorganic Chemistry, Faculty of Production Engineering, Wroclaw University of Economics and Business, Komandorska 118/120 Str., 53-345 Wrocław, Poland; edyta.kucharska@ue.wroc.pl

* Correspondence: m.ptak@intibs.pl

Abstract: [DMHy]Mn(HCOO)$_3$ (DMHy$^+$ = dimethylhydrazinium cation) is an example of an organic–inorganic hybrid adopting perovskite-like architecture with the largest organic cation used so far in the synthesis of formate-based hybrids. This compound undergoes an unusual isosymmetric phase transition at 240 K on heating. The mechanism of this phase transition has a complex nature and is mainly driven by the ordering of DMHy$^+$ cations and accompanied by a significant distortion of the metal–formate framework in the low temperature (LT) phase. In this work, the Density Functional Theory (DFT) calculations and factor group analysis are combined with experimental temperature-dependent IR and Raman studies to unequivocally assign the observed vibrational modes and shed light on the details of the occurring structural changes. The spectroscopic data show that this first-order phase transition has a highly dynamic nature, which is a result of balanced interplay combining re-arrangement of the hydrogen bonds and ordering of DMHy$^+$ cations. The tight confinement of organic cations forces simultaneous steric deformation of formate ions and the MnO_6 octahedra.

Keywords: hybrid perovskite; phase transition; order-disorder; dimethylhydrazinium cation

Citation: Zienkiewicz, J.A.; Kucharska, E.; Ptak, M. Mechanism of Unusual Isosymmetric Order-Disorder Phase Transition in [Dimethylhydrazinium]Mn(HCOO)$_3$ Hybrid Perovskite Probed by Vibrational Spectroscopy. *Materials* **2021**, *14*, 3984. https://doi.org/10.3390/ma14143984

Academic Editor: Franz Saija

Received: 22 June 2021
Accepted: 14 July 2021
Published: 16 July 2021

1. Introduction

3D hybrid metal–formate perovskites, a class of multifunctional materials described by the general formula [A]M^{II}(HCOO)$_3$, where A is an ammonium cation and M^{II} denotes a divalent metal cation, caught the attention of materials scientists in a few recent years because of their unusual luminescent, [1,2] ferroelastic, [3,4] ferroelectric, [5–7] dielectric, [2,4,8] magnetic [2,9,10] or multiferroic [3,11–13] properties. These properties originate from order-disorder phase transitions (PTs) that enable utilizing them as molecular switches [14–16].

Up to date, hydrazine and its derivatives were used only a few times as templating agents in the synthesis of formate-based hybrids. Since the hydrazinium cation (Hy$^+$) has a small size, [Hy]M^{II}(HCOO)$_3$ compounds with M^{II} = Mn^{2+}, Zn^{2+} and Fe^{2+} can adopt two types of structure, namely $4^{12}\cdot6^3$ perovskite-like with cubic cavities or $4^9\cdot6^3$ chiral with hexagonal channels [17–19]. Analogues comprising Co^{2+} and Mg^{2+} ions were found to adopt only chiral architecture. [Hy]M^{II}(HCOO)$_3$ perovskites undergo an order-disorder PT near 350 K from the LT ferroelectric *Pna*2$_1$ to the high-temperature (HT) paraelectric *Pnma* phase. However, chiral analogues transform from the ferroelectric $P2_12_12_1$ LT to the ferroelectric $P6_3$ HT phase in the 336–380 K range. The chiral [Hy]Mn(HCOO)$_3$ adopts exceptionally the $P2_1$ LT symmetry and exhibits lower PT temperature, 296 K [17–19].

The increased size of the methylhydrazinium cation (MHy$^+$) affects the crystal structure, and only perovskite-like architecture is preferred for [MHy]M^{II}(HCOO)$_3$ (M^{II} = Mn^{2+}, Mg^{2+}, Fe^{2+}, Zn^{2+}) [20]. All MHy$^+$ analogues experience two PTs. The first one occurs in

the 168–243 K range from the LT polar phase of $P1$ symmetry to the intermediate polar $R3c$ phase, whereas the second one, near 310–327 K, to the paraelectric HT $R\bar{3}c$ phase [20].

Further increase in the cation size caused by the presence of the second methyl group leads to complete suppression of non-centrosymmetric structures in [DMHy]Mn(HCOO)$_3$, ($DMHy^+$ denotes 1,1-dimethylhydrazinium cation). This crystal, recently synthesized by us, exhibits unusual order-disorder PT among metal–formate hybrids [2]. In fact, [DMHy]Mn(HCOO)$_3$ is the first example of a formate-based perovskite that does not change the space group symmetry as a result of LT ordering. Therefore, it is of great importance to elucidate the mechanism of this PT in detail and focus on the hydrogen bond (HB) interactions. Furthermore, $DMHy^+$ cation is the largest organic cation successfully used in the synthesis of formate-based hybrids. The tolerance factor of [DMHy]Mn(HCOO)$_3$ perovskite is at the theoretically predicted limit by Kieslich et al. [21], making this compound an interesting model for structure-stability considerations.

It is well-known that vibrational spectroscopy, as a support for X-ray diffraction methods, is commonly used to shed some light on the dynamical properties and mechanisms of PTs occurring in hybrid organic–inorganic perovskites. A great advantage of Raman and IR spectroscopy is its high sensitivity to local structural changes involving dynamics of light atoms that are responsible for the formation of HBs. Since the arrangement of HBs is usually strongly affected during PTs, detailed studies of phonon properties can give access to structural information not available using other probing techniques.

IR and Raman studies were used to understand PT mechanisms observed in Hy^+ and MHy^+ analogues [18,20]. Therefore, we have decided to undertake similar studies for [DMHy]Mn(HCOO)$_3$ and compare its phonon properties to former compounds. Detailed temperature-dependent studies with small temperature increments allowed to obtain deeper insight into structural changes occurring in this compound at 244.4 K (283.0 K) on cooling (heating) [2] and to elucidate the main driving force of the PT. It is worth adding that the $P2_1/n$–$P2_1/n$ isosymmetric PT is also interesting from the spectroscopic point of view because weak changes of vibrational selection rules are expected in spite of significant structural changes and the associated high change of entropy [2]. Moreover, the isosymmetric and isostructural PTs occurring in the coordination polymers are still poorly understood [16,22–29].

The main goal of this paper is to analyse the phonon properties of [DMHy]Mn(HCOO)$_3$ as a function of temperature. We propose an assignment of the observed IR and Raman bands based on literature data for Hy^+ and MHy^+ analogues supported by DFT calculations reported in this paper for $DMHy^+$ cation. We show that the presence of an additional methyl group significantly affects the phonon properties of [DMHy]Mn(HCOO)$_3$. In the discussion of temperature-dependent spectra, particular attention is paid to the factor group analysis in order to obtain deep insight into the PT mechanism.

2. Materials and Methods

2.1. Materials and Synthesis

The 1,1-dimethylhydrazine (Sigma-Aldrich, Saint Louis, MO, USA), formic acid (85%, Avantor Performance Materials Poland, Gliwice, Poland), anhydrous methanol (Sigma-Aldrich, Saint Louis, MO, USA) and manganese(II) perchlorate hexahydrate (Sigma-Aldrich, Saint Louis, MO, USA) were purchased from commercial sources and used without further purification.

The cubic transparent crystals of [DMHy]Mn(HCOO)$_3$ were obtained from a sealed and undisturbed mixture of two solutions. The first containing 40 mmol (ca. 3 mL) of 1,1-dimethylhydrazine dissolved in 10 mL of methanol with the addition of 160 mmol (7.25 mL) of HCOOH and the second, composed of 1 mmol (0.3619 g) of $Mn(ClO_4)_2{\cdot}6H_2O$ dissolved in 10 mL of methanol. Further details can be found in [2].

2.2. Raman ad IR Spectroscopy

A room-temperature (RT) Raman spectrum of the polycrystalline sample was measured in the 4000–75 cm^{-1} range using a FT 100/S spectrometer with YAG:Nd laser excitation at 1064 nm (Bruker, Billerica, MA, USA). The temperature-dependent (80–400 K) Raman spectra of a randomly oriented single crystal in the 3500–50 cm^{-1} range were measured using a Renishaw inVia Raman spectrometer (Renishaw, Wotton-under-Edge, UK), equipped with confocal DM2500 Leica optical microscope, a thermoelectrically cooled CCD as a detector and an Ar^+ ion laser operating at 488 nm. The temperature was controlled using a THMS600 stage (Linkam Scientific Instruments Ltd., Epsom, Tadworth, UK).

An RT polycrystalline IR spectrum in the range of 4000–400 cm^{-1} (mid-IR) was measured using a Nicolet iS50 infrared spectrometer (Thermo Fisher Scientific, Waltham, MA, USA) as a suspension in nujol (mineral oil) and Fluorolube (Sigma-Aldrich, Saint Louis, MO, USA). Additional mid-IR spectrum was recorded using an ATR module and diamond crystal. A far-IR spectrum in the range of 650–50 cm^{-1} was measured on a polyethylene plate as a suspension in nujol. The temperature-dependent (80–400 K) IR spectra in the 4000–650 cm^{-1} range were measured using a Nicolet iN10 infrared microscope (Thermo Fisher Scientific, Waltham, MA, USA). The temperature was controlled using a THMS600 stage equipped with ZnSe windows (Linkam Scientific Instruments Ltd., Epsom, Tadworth, UK).

2.3. Quantum Chemical Calculations

The geometry optimization of the molecular structure of dimethylhydrazine molecule (DMHy) and $DMHy^+$ cation was performed using a Gaussian 03 package [30]. All calculations were carried out using density functional three-parameters hybrid (B3LYP) methods [31–33] with the 6-311G(2d,2p) [34,35] basis set starting from the X-ray geometry taken from [2]. The harmonic and anharmonic vibrational wavenumbers were also calculated. The calculated harmonic frequencies were scaled using scaling factors (0.96 and 0.98) to correct the evaluated wavenumbers for vibrational anharmonicity and deficiencies inherent to the used computational level. The potential energy distribution (PED) of the normal modes among the respective internal coordinates was calculated for studied compounds using the BALGA program [36]. The data from DFT calculations were input into the BALGA program. The theoretical Raman intensities were calculated using the Chemcraft program [37] that was also used for the visualization of molecules.

3. Results

3.1. Crystal Structure and Geometry Optimization

Both LT and HT phases of $[DMHy]Mn(HCOO)_3$ are described by the $P2_1/n$ monoclinic symmetry [2]. The crystal structure is built from the manganese–formate 3D framework forming pseudo-cubic voids that accommodate the $DMHy^+$. Organic cations balance the negative charge of the manganese–formate framework and are bonded by medium strength HBs. In the HT phase, $DMHy^+$ cations exhibit a threefold disorder, while in the LT phase, disorder is no longer observed (Figure 1). In the LT phase, the Mn^{2+} centres occupy only one C_1 (4e) site, whereas, in the HT phase, they are distributed equally into two C_s sites (2a and 2d) [2]. All remaining atoms in both phases occupy C_1 sites (4e).

The results of geometry optimisation performed for $DMHy^+$ and DMHy are presented in Table S1. Figure S1 presents the numbering of atoms used for calculations. The calculated skeletal N1–N4, N4–C5 and N4–C10 distances (1.450, 1.504 and 1.503 Å, respectively) for $DMHy^+$ are in good agreement with experimental values obtained using X-ray diffraction methods, i.e., 1.428(6)–1.482(6), 1.398(10)–1.538(8) and 1.476(10)–1.538(8) Å at 300 K and 1.447(3), 1.488(4) and 1.490(4) at 100 K, respectively [2]. The calculated N1–N4–C5, N1–N4–C10 and C5–N4–C10 angles for $DMHy^+$ are equal to 115.46, 108.69 and 112.70°, respectively, and correspond well to ranges of values obtained for crystal structures solved at 100 K (109.0(2)–114.2(2)°) [2]. The calculated lengths of C–H and N–H bonds are higher in comparison to the experimental ones, but this is an expected effect caused by impre-

cise positioning of H atoms by crystallographic methods and by in vacuo character of performing calculations.

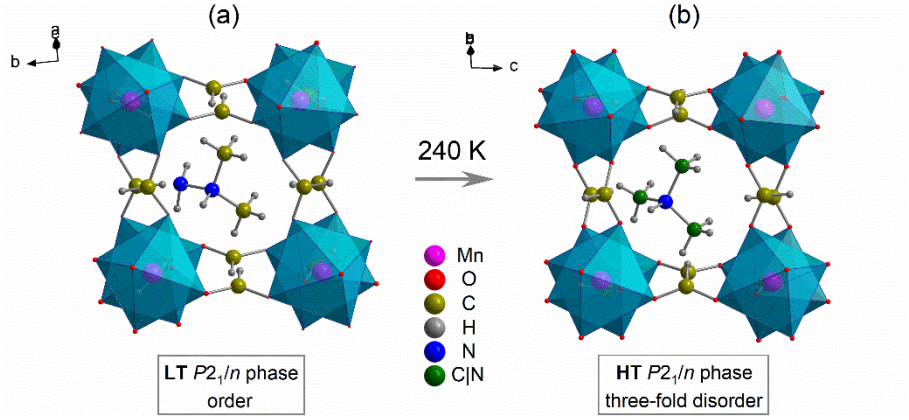

Figure 1. The crystal structure of the LT (**a**) and HT (**b**) phase of [DMHy]Mn(HCOO)$_3$.

The optimised geometry of the DMHy molecule is similar to DMHy$^+$. However, the N–C distances seem to be more sensitive than the N–N one to the presence of proton bonded to N4. The lack of proton causes the shortening of N–C and N–N bonds by 3.2% and 1.3%, respectively.

3.2. Selection Rules and Factor Group Analysis

All 30 vibrational degrees of freedom for DMHy can be subdivided into 11 stretching and 19 bending modes. The stretching (ν) modes can be roughly described as 4 × $\nu_{as}CH_3$ (antisymmetric), 2 × ν_sCH_3 (symmetric), $\nu_{as}NH_2$, ν_sNH_2, ν_{as}CNC, ν_sCNC and νNN. The deformational modes can be described as 4 × $\delta_{as}CH_3$, 2 × δ_sCH_3, 4 × ρCH_3 (rocking) and 2 × τCH_3 (twisting), δNH_2 (bending), ρNH_2, ωNH_2(wagging), τNH_2, 2 × δCNN and δCNC.

The additional proton bonded to the N4 atom in DMHy$^+$ increases the number of vibrational degrees of freedom to 33. Apart from the vibrations mentioned above, there are three additional vibrations involving the N4-H$^+$ group, namely νNH^+, δNH^+ (in-plane) and γNH^+ (out-of-plane bending).

IR and Raman spectra of [DMHy]Mn(HCOO)$_3$ can be understood by subdividing all Brillouin zone-centre vibrations into internal and external (lattice vibrations). The six internal vibrations of free formate ion (see Table S2) are described as νCH (ν_1), ν_sCO (ν_2) (symmetric stretching), $\nu_{as}CO$ (ν_4) (antisymmetric stretching), δOCO (ν_3), δCH (ν_5) and γCH (ν_6) [38]. The 12 formate ions in the primitive cell of [DMHy]Mn(HCOO)$_3$ give rise to 72 internal modes (18A_g + 18A_u + 18B_g + 18B_u) in both the LT and HT phases. The number of expected translational (T′) and librational (L) modes of formate ions is 36 each (9A_g + 9A_u + 9B_g + 9B_u).

A free DMHy$^+$ cation has C_s symmetry similar to isopropylamine [39], and therefore, the symmetries of particular vibrations can be derived (see Table S2). Thus, the 18A′ + 15A″ normal vibrations exhibit factor group splitting to 132 modes (33A_g + 33A_u + 33B_g + 33B_u) in the studied crystal. The translations and librations of DMHy$^+$ give rise to 12 modes each (3A_g + 3A_u + 3B_g + 3B_u). Although the DMHy$^+$ cations are disordered in the HT phase, the total number of their theoretically predicted modes do not change during PT.

The symmetry of Mn^{2+} translations is different for both phases because of occupied sites. In the LT (ordered) phase, the number of expected translations is 12 and distributed into 3A_g + 3A_u + 3B_g + 3B_u. In the HT phase, the total number is unchanged, however, is distributed into 6A_u + 6B_u modes. In both phases, three of these translational modes (A_u + 2B_u) are acoustic, thus cannot be detected using IR and Raman spectroscopy.

To conclude, the total number of expected optical modes is 309 (75A_g + 80A_u + 75B_g + 79B_u) in the HT phase, as well as in the LT phase (78A_g + 77A_u + 78B_g + 76B_u). All

g-symmetry modes are Raman-active, and u-symmetry modes are IR-active. Therefore, the number of expected Raman and IR bands is 150 ($75A_g + 75B_g$) and 159 ($80A_u + 79B_u$) in the HT phase, respectively, and 156 ($78A_g + 78B_g$) and 153 ($77A_u + 76B_u$) in the LT phase, respectively. It should be added that because u-symmetry modes are solely IR-active, the T′(Mn^{2+}) is not detectable in the Raman spectrum of the HT phase.

3.3. DFT Calculations

The calculated wavenumbers, together with PEDs, are listed in Table S3. The theoretical spectra calculated in harmonic and anharmonic approximations are presented in Figure S2. The results of DFT calculations for DMHy showed that 21 vibrational modes have a nearly pure (96% and higher) contribution of a single vibration, 4 modes have the main contribution with PED ranging from 71% to 81%, and the remaining 5 modes have more complex origin. The protonation causes stronger coupling of observed modes, i.e., 15 bands have close to pure contribution (95% or higher), 13 bands have a clearly dominant contribution (63–89%), and 3 bands exhibit stronger coupling. Furthermore, the protonation-induced shifts of some bands are evidenced. For instance, the strongest downshifts in harmonic approximation are observed for the $\nu_s NH_2$ (by 125 cm^{-1}) and $\nu_s CH_3$ (by 163–169 cm^{-1}) modes. This is an interesting behaviour since their antisymmetric counterparts are less sensitive and downshifted only by 24 and 61–106 cm^{-1}.

The largest differences between harmonic and anharmonic wavenumbers are observed for both DMHy and $DMHy^+$ for bands originating from the νNH_2 and νCH_3 vibrations. Interestingly, anharmonicity in DMHy is stronger for $\nu_s CH_3$ (downshifts up to 182 cm^{-1}) than for $\nu_{as} CH_3$ (downshifts in the 125–153 cm^{-1} range) and comparable for $\nu_s NH_2$ (downshifts by 197 cm^{-1}) and $\nu_{as} NH_2$ (downshift by 188 cm^{-1}) counterparts. For $DMHy^+$, the tendency observed for νCH_3 is opposite, namely $\nu_s CH_3$ and $\nu_{as} CH_3$ are downshifted by 100–103 and 143–144 cm^{-1}, respectively. Among νNH_2 vibrations, the stronger anharmonicity is observed for $\nu_{as} NH_2$ (downshift by 167 cm^{-1}) and for $\nu_s NH_2$ (downshift by 107 cm^{-1}). The anharmonicity of νNH^+ is comparable to that observed for $\nu_{as} NH_2$ and reaches a value of 157 cm^{-1}. Furthermore, τNH_2 and τCH_3 vibrations of DMHy exhibit negative anharmonic shifts (from −18 to −40 cm^{-1}). This effect is not evidenced for $DMHy^+$; therefore, the high sensitivity of bands assigned to νNH_2, νCH_3, τNH_2 and τCH_3 to the protonation may be related to their stronger intrinsic anharmonicity.

3.4. Room-Temperature IR and Raman Spectra and Assignment of Bands

RT polycrystalline IR and Raman spectra are presented in Figure 2. The proposed assignment of the observed bands, based on comparative analysis and DFT data, is listed in Table 1. The assignment of the bands corresponding to formate ions is straightforward since internal vibrations of formate ions are commonly observed in narrow spectral ranges for other members of the large [A]$Mn(HCOO)_3$ (A = protonated amine) family. For instance, the ν_1, ν_2, ν_3, ν_4, ν_5 and ν_6 modes were previously observed in the 2827–2888, 1352–1364, 789–805, 1562–1594, 1368–1387 and 1063–1071 cm^{-1} ranges, respectively, for analogues with A = Hy^+ [18], MHy^+ [20] and dimethylammonium cation [40]. Thus, we assign the IR and Raman bands of [DMHy]$Mn(HCOO)_3$ observed in the 2826–2858, 1342–1352, 788–792, 1560–1593, 1363–1365 and 1056–1065 cm^{-1} ranges to ν_1–ν_6 vibrations, respectively. The assignment of the bands corresponding to $DMHy^+$ in [DMHy]$Mn(HCOO)_3$ crystal is based on our DFT calculations and previous ab initio calculations for DMHy molecule performed by Durig et al. [41]. The positions of $\nu_{as} CH_3$, $\nu_s CH_3$, $\nu_{as} NH_2$ and $\nu_s NH_2$ bands for [DMHy]$Mn(HCOO)_3$ are in good agreement with the calculations. Weak bands between 3039 and 3054 cm^{-1}, not present for DMHy, were assigned to νNH^+. They are expected to be observed at lower wavenumbers than $\nu_{as} NH_2$ and $\nu_s NH_2$ bands because the $–NH^+$ group is able to form stronger HBs [2]. The remaining stretching vibrations, ν_{as}CNC, ν_sCNC and νNN, are located in the 990–1002, 820–832 and 1089–1098 cm^{-1} range, respectively. The position of the ν_sCNC bands is in good agreement with previous studies, i.e., this band was observed

at 874 cm^{-1} for [MHy]Mn(HCOO)$_3$ [20], 877 cm^{-1} for [MHy]Mn(H_2POO)$_3$ [42], 868 and 871 cm^{-1} for [MHy]$PbBr_3$ [43] and 881 cm^{-1} for [MHy]$PbCl_3$ [44]. The antisymmetric counterpart was previously observed at 1010 cm^{-1} for [MHy]Mn(H_2POO)$_3$ [42], 1004 cm^{-1} for [MHy]$PbBr_3$ [43] and 1011 cm^{-1} for [MHy]$PbCl_3$ [44]. For the [MHy]Mn(HCOO)$_3$ crystal, this vibration was assigned to bands observed near 1092 cm^{-1} [20], but our DFT and previous ab initio calculations [41] showed that bands observed in the 1089–1098 cm^{-1} range for [DMHy]Mn(HCOO)$_3$ originate from νNN. This mismatch relates to a different division into normal vibrations of the skeleton.

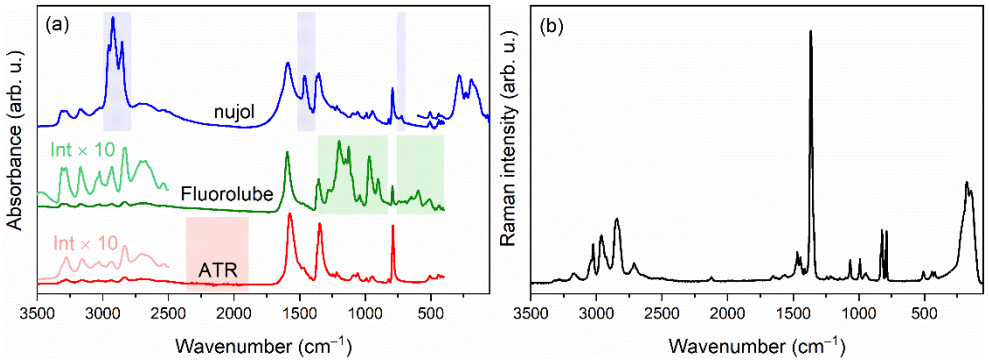

Figure 2. RT polycrystalline IR (**a**) and Raman (**b**) spectra of [DMHy]Mn(HCOO)$_3$. The shaded fields correspond to regions where absorption bands of dielectric media (nujol, Fluorolube) or ATR crystal occur, and therefore, they are not analysed.

Table 1. The tentative assignments of IR and Raman bands observed for polycrystalline [DMHy]Mn(HCOO)$_3$.

Raman	IR (ATR)	IR (Nujol)	IR (Fluorolube)	Assignment
3286vw	3306sh, 3279w	3312w, 3283w	3310w, 3283w	$\nu_{as}NH_2$
3173w	3157w	3171w	3170w	ν_sNH_2
3052sh, 3041w	3054vw, 3040vw	3054vw, 3039vw	3052sh, 3039sh	νNH^+
3025m	3027vw	3025vw	3025w	$\nu_{as}CH_3$
2968sh, 2963m, 2926m	2952sh, 2936vw	*	2953sh, 2931w	ν_sCH_3
2851sh, 2844w, 2831sh	2832w	*	2858w, 2843sh, 2826sh	ν_1
2732sh, 2712w, 2684sh	2710w, 2676sh, 2534vw, 2498vw	2715w, 2674w, 2639sh, 2540vw, 2495vw	2717w, 2675vw, 2639sh, 2540vw, 2494vw	νNH_2 + νNH^+ + o + cb
1654vw	1639sh	1644sh	1642sh	δNH_2
1578vw, 1560vw	1574vw	1591vs	1593vs	ν_4 + δNH^+
1480w, 1469w, 1445w	1478m, 1468m, 1447sh	*	1477w, 1467w, 1446vw	$\delta_{as}CH_3$
1439sh, 1412w	1436vw, 1411vw	*	1436vw, 1411vw	δ_sCH_3 + γNH^+
1365vs	1363sh	*	*	ν_5
1345sh	1347vs	1352s, 1342sh	*	ν_2 + ρNH_2
1243vw, 1217vw, 1202vw, 1145vw	1244w, 1217w, 1202w, 1149vw	1246w, 1217w, 1201vw, 1146sh	*	ρCH_3
1098vw	1089w	1093w	*	ρCH_3 + νNN
1065w	1056w	1058w	*	ν_6
1002vw, 991w	1002w, 991w	1002w, 990vw	*	$\nu_{as}CNC$
957w, 946w, 937vw	957w, 946vw	958w, 946w	*	ωNH_2
832m, 823m	821w	820vw	820vw	ν_sCNN
789m	788vs	792s	792m	ν_3
507vw	506w	504w	*	δCNC
442vw, 421w	442sh, 421w	441w, 419w	*	δCNN
219sh		282s, 233m		τNH_2 + τCH_3 + lm
198sh, 177s, 144s		191s, 161sh		lm

Key: ν, stretching; δ, bending; ρ, rocking; γ, out-of-plane bending; ω, wagging; τ, twisting; vs, very strong; s, strong; m, medium; w, weak; vw, very weak; ν_1–ν_6, internal vibrations of formate ion (see description in text); *, regions of absorption related to the medium; o, overtones; cb, combinational bands; lm, lattice modes.

The assignment of bending vibrations of the skeleton is undoubted since they cover the spectral range free of any other vibrational bands. In this manner, bands in the 419–442 and 504–507 cm^{-1} were ascribed to δCNN and δCNC, respectively. The lack of δCNC bands for MHy^+ analogues and the presence of δCNN ranging from 437–444 cm^{-1} [20,42,43] confirms this assignment.

The bending vibrations of the amino group are expected to be broader than bands corresponding to the methyl group, and therefore, we assign bands observed in the 1639–1654 range to δNH_2. For other formate perovskites, they were observed in similar ranges, i.e., 1589–1654 cm^{-1} [20]. For non-formate analogues, the bending vibrations of protonated amino groups were observed 21–55 cm^{-1} lower than δNH_2 [42,43]. Therefore, in the case of $[MHy]Mn(H_2POO)_3$, the δNH^+ bands are expected to coincide with bands corresponding to the ν_4 vibrations of formate ions. The distinction between the broad ρNH_2, ωNH_2 and τNH_2 bands is more tentative in the literature, but our DFT results and previous ab initio calculations [41] are in good agreement. We found these vibrations in the 1342–1352, 937–958 and 219–282 cm^{-1} ranges, respectively. According to our DFT data, the γNH^+ vibration is expected to contribute to bands at 1374 (1396) cm^{-1} and 1419 (1422) cm^{-1} in an anharmonic (scaled harmonic) model. Therefore, we assign weak and broad bands in the 1411–1439 cm^{-1} range to this vibration.

Vibrations of the methyl groups are expected to be less sensitive to the surroundings than vibrations of the amino groups. The bending modes ($\delta_{as}CH_3$ and δ_sCH_3) can be assigned to the IR and Raman bands observed in the 1445–1480 and 1411–1439 cm^{-1} range, respectively. They were previously observed in similar ranges, i.e., 1454–1478 and 1421–1433 cm^{-1} [20,42]. The ρCH_3 and τCH_3 bands were found between 1098 and 1246 cm^{-1}, as well as between 219–282 cm^{-1}, respectively. These ranges are in a good agreement with reported values for $[MHy]Mn(HCOO)_3$ and $[MHy]Mn(H_2POO)_3$, namely 1092–1234 cm^{-1} (ρCH_3) and 210–237 cm^{-1} (τCH_3) [20,42]. Bands located below 240 cm^{-1} are assigned to lattice modes (Table 1).

3.5. Temperature-Dependent IR and Raman Spectra

The thermal evolution of Raman spectra (measured from single crystal) and polycrystalline IR spectra (measured as a suspension in Fluorolube and nujol) is presented in Figure 3. The observed wavenumbers at 80 and 300 K are listed in Table S4. To obtain more detailed information on the PT mechanism, the fitting of the IR and Raman spectra was conducted through the deconvolution of complex contours to Lorentzian curves.

3.5.1. Internal Modes of Formate Ions

The resulting positions and full widths at half maximum (FWHM) of the IR and Raman bands corresponding to formate linkers are presented as a function of temperature in Figure 4. During the PT (on heating), the IR (Raman) bands above 2840 cm^{-1} corresponding to the ν_1 mode exhibit upshifts by 1.8–6.5 cm^{-1} (3.9 cm^{-1}), while bands below this limit downshift by 2.1 cm^{-1} (8.4 cm^{-1}) (Figure 4a). The sensitivity of bands to the PT is also manifested as a significant broadening by 7.2–7.9 cm^{-1} (Figure 4b). Similar co-occurrence of positive and negative shifts is observed for the ν_5 and ν_6 bending vibrations. The hardening (softening) of the corresponding IR and Raman bands during the PT on heating does not exceed 2.4 cm^{-1} (1.4 cm^{-1}). The corresponding increase in FWHMs for these modes ranges from 2.9 to 6.2 cm^{-1}.

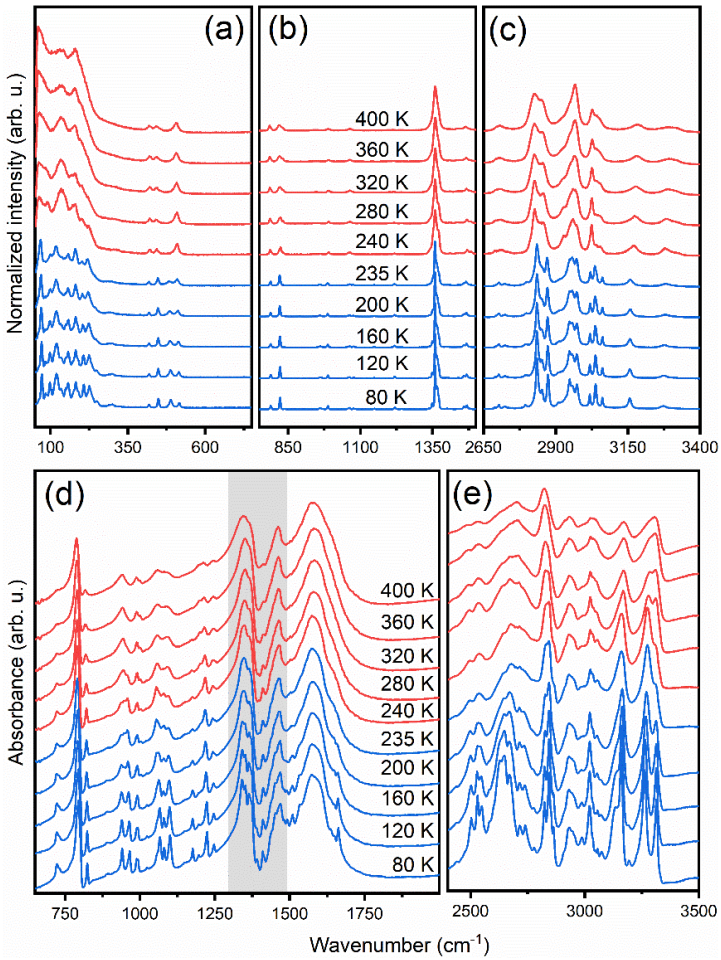

Figure 3. Temperature-dependent Raman spectra measured form single-crystal in the (**a**) 50–750 cm^{-1}, (**b**) 750–1500 cm^{-1} and (**c**) 2650–3400 cm^{-1} ranges compared to temperature-dependent polycrystalline IR spectra measured in nujol (**d**) and Fluorolube (**e**). The grey range in (**d**) was not analysed due to the coexistence of bands corresponding to the nujol and sample.

The ν_2 and ν_4 bands corresponding to stretching modes involving oxygen atoms exhibit downshifts by 1.1–4.2 cm^{-1} and upshift by 4.1 cm^{-1}, respectively, at the PT temperature. The ν_4 and one of the ν_2 Raman bands exhibit strong broadening at the PT temperature upon heating, by 14.7 cm^{-1} and 7.7 cm^{-1}, respectively. Interestingly, the second ν_2 Raman band exhibits unusual narrowing by 3.5 cm^{-1}.

The bending COC modes (ν_3) seem to be less sensitive to the occurring structural transformation. Shifts of IR and Raman bands during the PT are weaker than 0.4 cm^{-1}, and the broadening of the 790 cm^{-1} Raman band (1.6 cm^{-1}) is the lowest among all ν_1–ν_6 bands. Selected detailed ranges of temperature-dependent Raman spectra corresponding to the ν_1–ν_6 formate anion internal modes are presented in Figure S3.

3.5.2. Internal Modes of $DMHy^+$ Cation

The results of fitting of IR and Raman bands corresponding to $DMHy^+$ cation (positions and widths of the bands) are presented as a function of temperature in Figure 5. The details of IR and Raman spectra corresponding to $DMHy^+$ vibrations are presented in Figures S4 and S5.

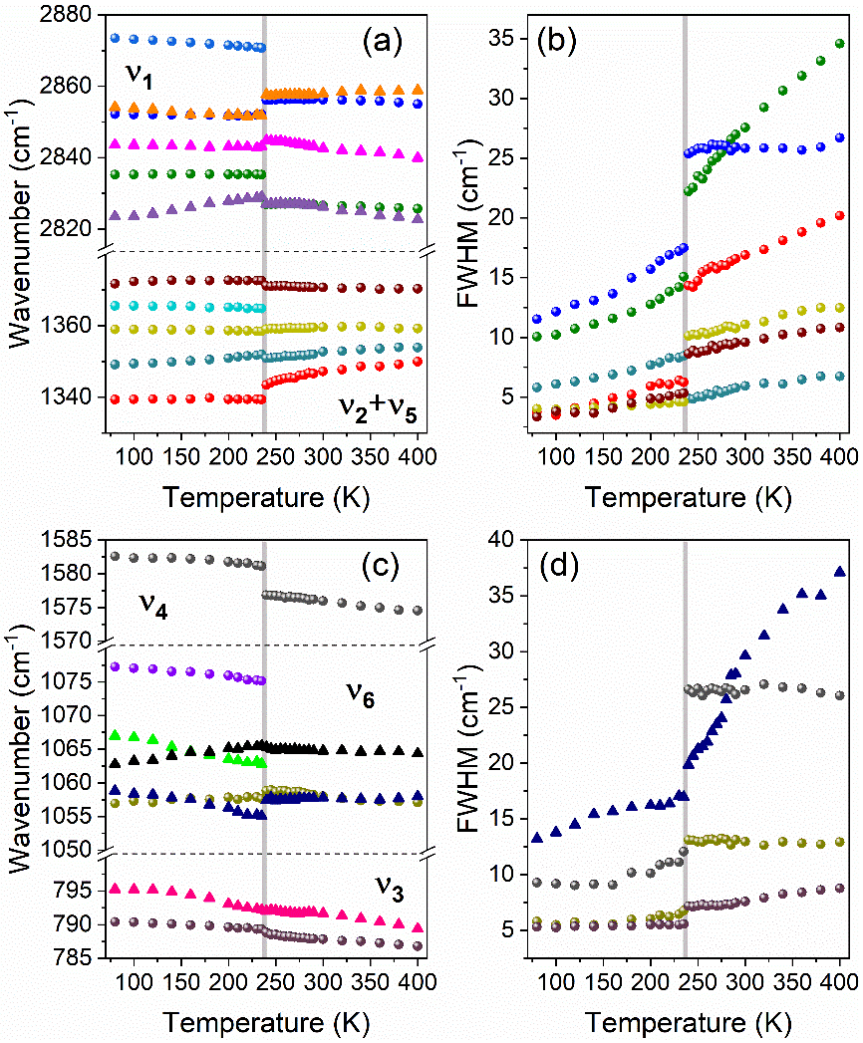

Figure 4. The temperature evolution of selected Raman (circles) and IR (triangles) wavenumbers (**a**,**c**) and bandwidths (**b**,**d**) of bands corresponding to the ν_1, ν_2 + ν_5 (**a**,**b**) as well as to ν_3, ν_4 and ν_6 (**b**,**d**) stretching vibrations of formate linkers. Horizontal dashed lines separate ranges of ν_1–ν_6 modes, vertical grey lines correspond to the PT temperature.

Two Raman bands observed above 3260 cm^{-1}, corresponding to the $\nu_{as}NH_2$ modes, exhibit weak shifts (less than 2.5 cm^{-1}) at the PT temperature (Figure 5a). Almost no changes at the PT temperature are also observed for the IR counterparts. Raman bands corresponding to the ν_sNH_2 and ωNH_2 modes are significantly more sensitive, i.e., they exhibit upshift by 10.8 cm^{-1} and downshift by 8.7 cm^{-1}, respectively. They also disclose significant broadening by ca 14.1 cm^{-1} and 49.5 cm^{-1}, respectively (Figure 5b). The shifts observed for the νNH^+ modes are up to 8.0 cm^{-1}.

Shifts observed for the Raman-active $\nu_{as}CH_3$ and ν_sCH_3 modes are also strong, up to 12 cm^{-1}. The rocking vibrations exhibit weaker changes and seem to be less affected by the PT. The only exception is the 1202 cm^{-1} mode (at 300 K), for which the upshift on heating is equal to 11.5 cm^{-1}. The νCNN skeleton vibrations are weakly affected by the PT.

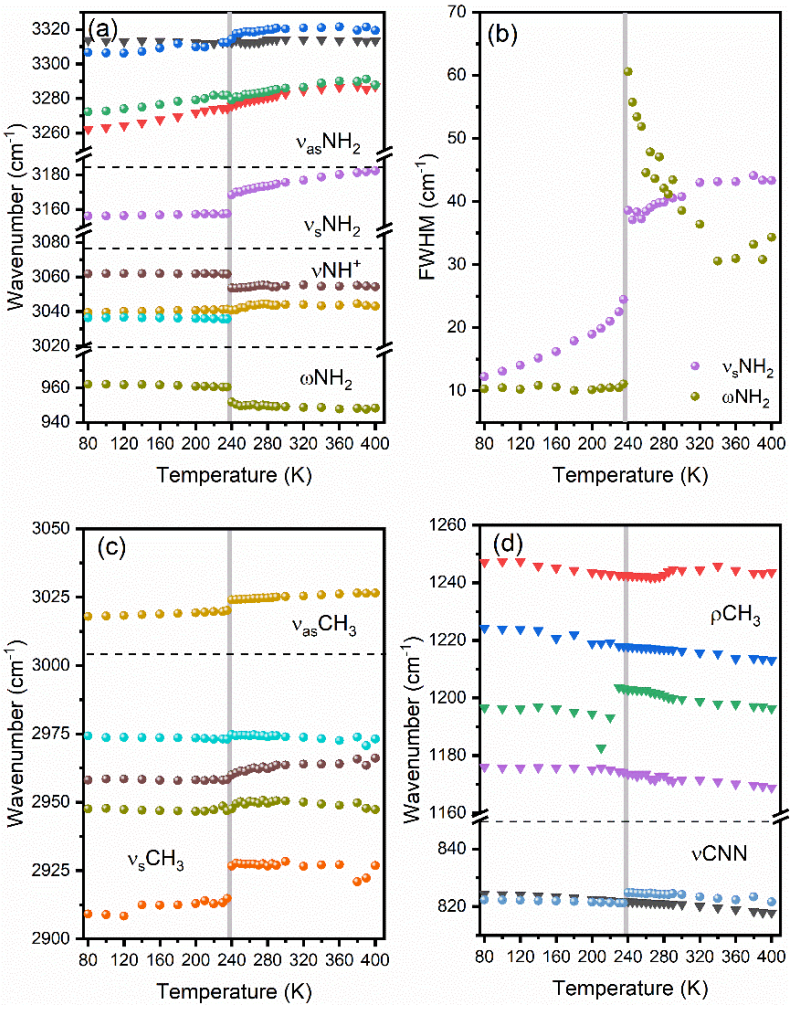

Figure 5. The thermal evolution of positions (**a**,**c**,**d**) and widths (**b**) of selected Raman (circles) and IR (triangles) bands corresponding to stretching and wagging vibrations of NH_2 and NH^+ groups (**a**,**b**), stretching vibrations of CH_3 (**c**) and stretching vibrations of CNN skeleton and rocking vibration of CH_3 group (**d**). Horizontal dashed lines separate ranges of different modes, and vertical grey lines correspond to the temperature of PT.

3.5.3. Lattice Modes

Figure 6 and Figure S6 show the temperature dependence of Raman bands observed in the 50–225 cm^{-1} range corresponding to the lattice modes. They exhibit the most significant changes during the PT. As one can see, after heating to 240 K, a few bands disappear. Furthermore, a large increase in bandwidth is observed (see Figure 6). Similar to the internal modes, they exhibit either up- or down-shifts. The strongest softening during the heating, by 6.7 cm^{-1}, is observed for the lowest wavenumber mode located at 72 cm^{-1} (at 80 K). A weaker decrease in energy at the PT temperature, by 2.3, 0.9 and 0.7 cm^{-1}, is observed for the 86, 136 and 227 cm^{-1} bands. The 180 cm^{-1} band is nearly insensitive to the change of temperature, while that at 208 cm^{-1} slightly hardens at 240 K, by 1.2 cm^{-1}. Details of temperature-dependent Raman spectra corresponding to the range of lattice modes are presented in Figure S6.

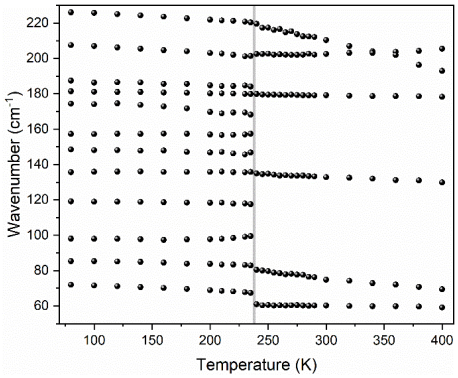

Figure 6. The temperature evolution of Raman lattice modes. The vertical grey line corresponds to the temperature of PT.

4. Discussion

All observed dependencies show clear jumps at 240 K, evidencing the PT. A sudden character of these changes points to the first-order nature of this transformation. According to the selection rules, the $P2_1/n$–$P2_1/n$ isosymmetric PT in [DMHy]Mn(HCOO)$_3$ should not lead to any splitting or appearance of new bands for $DMHy^+$ and $HCOO^-$ ions. Nonetheless, some minor splitting of many internal modes below PT is evidenced. This effect is related to the thermal narrowing of closely lying and superimposed vibrational bands that become well separated at lower temperatures. On the other hand, factor group analysis showed that significant changes are expected for lattice modes with a strong contribution of T′(Mn^{2+}). Indeed, pronounced changes upon cooling are observed for bands located below 225 cm^{-1}. Our experiment shows that 6 of 12 Raman bands in this region disappear upon heating, which is in good agreement with our predictions. All 6 Raman-active T′(Mn^{2+}) modes ($3A_g + 3B_g$) in the LT phase become solely IR-active because of a change of symmetry to A_u and B_u.

Such a strong splitting observed below 225 cm^{-1} confirms a strong deformation of the MnO_6 octahedra in the LT phase. Since lattice modes are strongly coupled and involve librational and translational vibrations of all crystal units, this effect reflects also a strong deformation of the whole manganese–formate framework. This conclusion is further supported by the strong broadening of the ν_4 mode corresponding to the antisymmetric stretching vibration of CO groups and the low sensitivity of the ν_3 bending COC mode. The co-occurrence of up- and down-shits, observed in the same type of vibrational modes corresponding to the formate ion, suggests the presence of a few symmetrically independent formate linkers in the unit cell that have slightly different distortions before and after PT. The crystallographic data reported at 100 and 300 K are consistent with the spectroscopic data [2]. They show three different formate linkers in both LT and HT phases that have different susceptibility to structural distortions. At 300 K, two of them have increased C-O bonds by 1.4–1.8% and the COC angle by 2.6% in comparison to the LT phase, while the third linker has one weakly increased C-O distance (0.8%) and one strongly elongated (2.4%) C-O bond. The corresponding COC angle remains weakly affected by about 0.4% [2]. This phenomenon and co-occurring wide range of changes corresponding to Mn-O distances, from −0.36 to 0.19%, explain well the observed up- or down-shifts of vibrational bands corresponding to lattice modes and formate linkers.

Large broadening observed in the lattice mode region is also caused by the disordering of $DMHy^+$ interplaying with the re-arrangement of HBs. This effect is most clearly visible for bands corresponding to both amino groups. A strong broadening at the PT temperature evidences the highly dynamic nature of this PT. Both IR and Raman bands corresponding to the νNH_2 stretching modes experience shifts and sudden broadening at the PT during heating. In particular, IR and Raman bands corresponding to the $\nu_s NH_2$ and $\nu_{as} NH_2$ vibrations harden when going from the LT to the HT phase. This behaviour is strong evidence that the strength of HBs created by unprotonated amino groups is lower in the

HT phase. In contrast to this behaviour, bands corresponding to the νNH^+ modes soften during the PT on heating. This indicates that the HBs related to the protonated amino group become stronger in the HT phase, in agreement with the crystallographic data [2]. Furthermore, this behaviour proves that both types of amino groups play a crucial role in the PT mechanism. A significant broadening and change of shape of the νCH_3 bands at the PT temperature can also be attributed to their disorder in the HT phase and their ability to form weak HBs.

The X-ray diffraction structural analysis showed that in the HT phase, the amino and methyl groups bonded to the middle N4 atom are disordered; however, one of the N4-(C | N) bonds is slightly shorter [2]. In the LT phase, the N-N bond is shorter compared to two N-C bonds, and the conformation of the skeleton is preserved [2]. We suppose, therefore, that most of the changes observed in the Raman and IR spectra are a consequence of cation ordering. The ordering of cations, along with the re-arrangement of HBs, because of tight confinement in the crystal void, forces the simultaneous deformation of the manganese–formate framework. The order-disorder mechanism is in good agreement with the high change of PT entropy observed for $[DMHy]Mn(HCOO)_3$ [2].

5. Conclusions

We have studied phonon properties of manganese–formate framework templated by $DMHy^+$ cations combining the DFT calculations and the temperature-dependent IR and Raman spectroscopy as a probe. We have presented selection rules and a correlation diagram for the LT and HT monoclinic ($P2_1/n$) phases. We have proposed the assignment of the observed IR and Raman bands to the respective internal and external (lattice) vibrations based on the DFT calculations performed for the DMHy molecule and its single protonated cation and the comparative analysis. We have shown that some bands exhibit stronger anharmonic behaviours and are more sensitive to structural changes.

The detailed analysis of temperature-dependent Raman and IR studies allowed us to obtain deeper insight into the PT mechanism occurring in this hybrid perovskite. We have concluded that the unusual isosymmetric order-disorder phase transformation from one $P2_1/n$ to the second $P2_1/n$ phase occurring near 240 K has a highly dynamic nature because of the ordering of $DMHy^+$ ions and re-arrangement of HBs. We have also proved that this transition has a first-order nature. The observed splitting of lattice modes below 240 K has been explained using selection rules that are slightly different for manganese ions in both phases.

Certainly, the mechanism of the PT involves the ordering of $DMHy^+$ cations as suggested in the previous work. However, the analysis of the thermal evolution of particular bands revealed that the PT mechanism has a more complex nature and is a result of a few contributions. It involves the simultaneous ordering of the organic cations and re-arrangement of the HBs network, but without conformational change of the $DMHy^+$ cations. This ordering and re-orientational motions, because of the tight confinement of the cations and steric hindrance, forces a strong deformation of the manganese–formate framework and MnO_6 octahedra in the LT phase.

Supplementary Materials: The following are available online at https://www.mdpi.com/article/10.3390/ma14143984/s1, Table S1: Calculated and experimental bond angles and lengths of $DMHy^+$ cation and DMHy molecule; Table S2: Optical modes in LT and HT phases; Table S3: Calculated PED and harmonic and anharmonic wavenumbers of $DMHy^+$ and DMHy; Table S4: Experimental IR and Raman bands of LT and HT forms with the assignment; Figure S1: The numbering of atoms in $DMHy^+$ and DMHy; Figure S2: Calculated IR and Raman spectra of $DMHy^+$ and DMHy; Figure S3: Raman bands corresponding to vibrational modes of the formate anion; Figure S4: Details of temperature-dependent Raman spectra, corresponding to vibrational modes of $DMHy^+$ cation; Figure S5: Details of temperature-dependent IR spectra, corresponding to vibrational modes of $DMHy^+$ cation; Figure S6: Raman bands corresponding to lattice modes.

Author Contributions: Conceptualization, J.A.Z. and M.P.; methodology, J.A.Z.; software, E.K.; validation, J.A.Z., E.K. and M.P.; formal analysis, J.A.Z.; investigation, J.A.Z. and E.K.; writing—

original draft preparation, J.A.Z., E.K.; writing—review and editing, M.P.; visualization, J.A.Z. and E.K.; supervision, M.P.; project administration, J.A.Z. All authors have read and agreed to the published version of the manuscript.

Funding: This research received no external funding.

Institutional Review Board Statement: Not applicable.

Informed Consent Statement: Not applicable.

Data Availability Statement: The data presented in this study are available on request from the corresponding author.

Conflicts of Interest: The authors declare no conflict of interest.

References

1. Mączka, M.; Bondzior, B.; Dereń, P.; Sieradzki, A.; Trzmiel, J.; Pietraszko, A.; Hanuza, J. Synthesis and characterization of $[(CH_3)_2NH_2][Na_{0.5}Cr_{0.5}(HCOO)_3]$: A rare example of luminescent metal-organic frameworks based on Cr(III) ions. *Dalt. Trans.* **2015**, *44*, 6871–6879. [CrossRef]
2. Zienkiewicz, J.A.; Kowalska, D.A.; Fedoruk, K.; Stefański, M.; Pikul, A.; Ptak, M. Unusual isosymmetric order-disorder phase transition in the new perovskite-type dimethylhydrazinium manganese formate exhibiting ferrimagnetic and photoluminescent properties. *J. Mater. Chem. C* **2021**, *9*, 6841–6851. [CrossRef]
3. Li, W.; Zhang, Z.; Bithell, E.G.; Batsanov, A.S.; Barton, P.T.; Saines, P.J.; Jain, P.; Howard, C.J.; Carpenter, M.A.; Cheetham, A.K. Ferroelasticity in a metal-organic framework perovskite; Towards a new class of multiferroics. *Acta Mater.* **2013**, *61*, 4928–4938. [CrossRef]
4. Wang, K.; Xiong, J.B.; Xia, B.; Wang, Q.L.; Tong, Y.Z.; Ma, Y.; Bu, X.H. Ferroelastic phase transition and switchable dielectric constant in heterometallic niccolite formate frameworks. *Inorg. Chem.* **2018**, *57*, 537–540. [CrossRef] [PubMed]
5. Jain, P.; Dalal, N.S.; Toby, B.H.; Kroto, H.W.; Cheetham, A.K. Order-disorder antiferroelectric phase transition in a hybrid inorganic-organic framework with the perovskite architecture. *J. Am. Chem. Soc.* **2008**, *130*, 10450–10451. [CrossRef] [PubMed]
6. Abhyankar, N.; Bertaina, S.; Dalal, N.S. On Mn^{2+} EPR probing of the ferroelectric transition and absence of magnetoelectric coupling in dimethylammonium manganese formate $(CH_3)_2NH_2Mn(HCOO)_3$, a metal-organic complex with the Pb-free perovskite framework. *J. Phys. Chem. C* **2015**, *119*, 28143–28147. [CrossRef]
7. Kieslich, G.; Forse, A.C.; Sun, S.; Butler, K.T.; Kumagai, S.; Wu, Y.; Warren, M.R.; Walsh, A.; Grey, C.P.; Cheetham, A.K. Role of amine-cavity interactions in determining the structure and mechanical properties of the ferroelectric hybrid perovskite $[NH_3NH_2]Zn(HCOO)_3$. *Chem. Mater.* **2016**, *28*, 312–317. [CrossRef]
8. Yu, Y.; Shang, R.; Chen, S.; Wang, B.-W.; Wang, Z.-M.; Gao, S. A Series of bimetallic ammonium AlNa formates. *Chem. A Eur. J.* **2017**, *23*, 9857–9871. [CrossRef]
9. Wang, Z.; Hu, K.; Gao, S.; Kobayashi, H. Formate-based magnetic metal-organic frameworks templated by protonated amines. *Adv. Mater.* **2010**, *22*, 1526–1533. [CrossRef] [PubMed]
10. Mączka, M.; Gągor, A.; Hermanowicz, K.; Sieradzki, A.; Macalik, L.; Pikul, A. Structural, magnetic and phonon properties of Cr(III)-doped perovskite metal formate framework $[(CH_3)_2NH_2][Mn(HCOO)_3]$. *J. Solid State Chem.* **2016**, *237*, 150–158. [CrossRef]
11. Nagabhushana, G.P.; Shivaramaiah, R.; Navrotsky, A. Thermochemistry of multiferroic organic-inorganic hybrid perovskites $[(CH_3)_2NH_2][M(HCOO)_3]$ (M = Mn, Co, Ni, and Zn). *J. Am. Chem. Soc.* **2015**, *137*, 10351–10356. [CrossRef]
12. Jain, P.; Ramachandran, V.; Clark, R.J.; Hai, D.Z.; Toby, B.H.; Dalal, N.S.; Kroto, H.W.; Cheetham, A.K. Multiferroic behavior associated with an order-disorder hydrogen bonding transition in metal-organic frameworks (MOFs) with the perovskite ABX_3 architecture. *J. Am. Chem. Soc.* **2009**, *131*, 13625–13627. [CrossRef]
13. Thomson, R.I.; Jain, P.; Cheetham, A.K.; Carpenter, M.A. Elastic relaxation behavior, magnetoelastic coupling and order-disorder processes in multiferroic metal-organic frameworks. *Phys. Rev. B* **2012**, *214304*, 1–7. [CrossRef]
14. Brenes, R.; Eames, C.; Bulović, V.; Islam, M.S.; Stranks, S.D. The impact of atmosphere on the local luminescence properties of metal halide perovskite grains. *Adv. Mater.* **2018**, *30*, 1–8. [CrossRef]
15. Sun, D.-S.; Zhang, Y.-Z.; Gao, J.-X.; Hua, X.-N.; Chen, X.-G.; Mei, G.-Q.; Liao, W.-Q. Reversible high temperature dielectric switching Reversible high temperature dielectric switching in a 2H-perovskite compound: $[Me_3NCH_2CH_3]CdCl_3$. *CrystEngComm* **2019**, *21*, 2669–2674. [CrossRef]
16. Rok, M.; Bator, G.; Zarychta, B.; Dziuk, B.; Medycki, W.; Zamponi, M.; Banys, J. Isostructural phase transition, quasielastic neutron scattering and magnetic resonance studies of a bistable dielectric ion-pair crystal $[(CH_3)_2NH_2]_2KCr(CN)_6$. *Dalt. Trans.* **2019**, *48*, 4190–4202. [CrossRef] [PubMed]
17. Chen, S.; Shang, R.; Hu, K.-L.L.; Wang, Z.-M.M.; Gao, S. $[NH_2NH_3][M(HCOO)_3]$ (M = Mn^{2+}, Zn^{2+}, Co^{2+} and Mg^{2+}): Structural phase transitions, prominent dielectric anomalies and negative thermal expansion, and magnetic ordering. *Inorg. Chem. Front.* **2014**, *1*, 83–98. [CrossRef]

18. Mączka, M.; Pasińska, K.; Ptak, M.; Paraguassu, W.; da Silva, T.A.; Sieradzki, A.; Pikul, A. Effect of solvent, temperature and pressure on the stability of chiral and perovskite metal formate frameworks of $[NH_2NH_3][M(HCOO)_3]$ (M = Mn, Fe, Zn). *Phys. Chem. Chem. Phys.* **2016**, *18*, 31653–31663. [CrossRef] [PubMed]
19. Kieslich, G.; Kumagai, S.; Butler, K.T.; Okamura, T.; Hendon, C.H.; Sun, S.; Yamashita, M.; Walsh, A.; Cheetham, A.K. Role of entropic effects in controlling the polymorphism in formate ABX_3 metal-organic frameworks. *Chem. Commun.* **2015**, *51*, 15538–15541. [CrossRef]
20. Mączka, M.; Gągor, A.; Ptak, M.; Paraguassu, W.; Da Silva, T.A.; Sieradzki, A.; Pikul, A. Phase transitions and coexistence of magnetic and electric orders in the methylhydrazinium metal formate frameworks. *Chem. Mater.* **2017**, *29*, 2264–2275. [CrossRef]
21. Kieslich, G.; Sun, S.; Cheetham, A.K. Solid-state principles applied to organic-inorganic perovskites: New tricks for an old dog. *Chem. Sci.* **2014**, *5*, 4712–4715. [CrossRef]
22. Christy, A.G. Isosymmetric structural phase transitions: Phenomenology and examples. *Acta Crystallogr. Sect. B Struct. Sci.* **1995**, *51*, 753–757. [CrossRef]
23. Zhang, W.; Ye, H.-Y.; Graf, R.; Spiess, H.W.; Yao, Y.-F.; Zhu, R.-Q.; Xiong, R.-G. Tunable and switchable dielectric constant in an mmphidynamic crystal. *J. Am. Chem. Soc.* **2013**, *135*, 5230–5233. [CrossRef]
24. Rok, M.; Bator, G.; Medycki, W.; Zamponi, M.; Balčiūnas, S.; Šimėnas, M.; Banys, J. Reorientational dynamics of organic cations in perovskite-like coordination polymers. *Dalt. Trans.* **2018**, *47*, 17329–17341. [CrossRef]
25. Xu, W.-J.; Chen, S.-L.; Hu, Z.-T.; Lin, R.-B.; Su, Y.-J.; Zhang, W.-X.; Chen, X.-M. The cation-dependent structural phase transition and dielectric response in a family of cyano-bridged perovskite-like coordination polymers. *Dalt. Trans.* **2016**, *45*, 4224–4229. [CrossRef] [PubMed]
26. Zhang, X.; Shao, X.D.; Li, S.C.; Cai, Y.; Yao, Y.F.; Xiong, R.G.; Zhang, W. Dynamics of a caged imidazolium cation-toward understanding the order-disorder phase transition and the switchable dielectric constant. *Chem. Commun.* **2015**, *51*, 4568–4571. [CrossRef] [PubMed]
27. Zhang, W.; Cai, Y.; Xiong, R.-G.; Yoshikawa, H.; Awaga, K. Exceptional dielectric phase transitions in a perovskite-type cage compound. *Angew. Chem. Int. Ed.* **2010**, *49*, 6608–6610. [CrossRef]
28. Zhao, X.H.; Huang, X.C.; Zhang, S.L.; Shao, D.; Wei, H.Y.; Wang, X.Y. Cation-dependent magnetic ordering and room-temperature bistability in azido-bridged perovskite-type compounds. *J. Am. Chem. Soc.* **2013**, *135*, 16006–16009. [CrossRef] [PubMed]
29. Mączka, M.; Marinho Costa, N.L.; Gągor, A.; Paraguassu, W.; Sieradzki, A.; Hanuza, J. Structural, thermal, dielectric and phonon properties of perovskite-like imidazolium magnesium formate. *Phys. Chem. Chem. Phys.* **2016**, *18*, 13993–14000. [CrossRef] [PubMed]
30. Frisch, M.J.; Trucks, G.W.; Schlegel, H.B.; Scuseria, G.E.; Robb, M.A.; Cheeseman, J.R.; Montgomery, J.A.; Vreven, T.; Kudin, K.N.; Burant, J.C.; et al. *Gaussian 03, Revision A.1*; Gaussian, Inc.: Pittsburgh, PA, USA, 2003.
31. Becke, A.D. Density-functional thermochemistry. IV. A new dynamical correlation functional and implications for exact-exchange mixing. *J. Chem. Phys.* **1996**, *104*, 1040–1046. [CrossRef]
32. Lee, C.; Yang, W.; Parr, R.G. Development of the Colic-Salvetti correlation-energy formula into a functional of the electron density. *Phys. Rev. B* **1988**, *37*, 785–789. [CrossRef]
33. Parr, R.G.; Yang, W. *Density-Functional Theory of Atoms and Molecules*; Springer: Dordrecht, The Netherlands, 1989.
34. Mclean, A.D.; Chandler, G.S. Contracted Gaussian basis sets for molecular calculations. I. Second row atoms, Z = 11–18. *J. Chem. Phys.* **1980**, *72*, 5639–5648. [CrossRef]
35. Krishnan, R.; Binkley, J.S.; Seeger, R.; Pople, J.A. Self-consistent molecular orbital methods. XX. A basis set for correlated wave functions. *J. Chem. Phys.* **1980**, *72*, 650–654. [CrossRef]
36. Rostkowska, H.; Lapinski, L.; Nowak, M.J. Analysis of the normal modes of molecules with D_{3h} symmetry: Infrared spectra of monomeric s-triazine and cyanuric acid. *Vib. Spectrosc.* **2009**, *49*, 43–51. [CrossRef]
37. Zhurko, G.A.; Zhurko, D.A. Chemcraft Graphical Program of Visualization of Computed Results. Available online: http://chemcraftprog.com (accessed on 9 March 2021).
38. Ptak, M.; Mączka, M.M.; Gągor, A.; Sieradzki, A.; Stroppa, A.; Di Sante, D.; Perez-Mato, J.M.; Macalik, L. Experimental and theoretical studies of structural phase transition in a novel polar perovskite-like $[C_2H_5NH_3][Na_{0.5}Fe_{0.5}(HCOO)_3]$ formate. *Dalt. Trans.* **2016**, *45*, 2574–2583. [CrossRef] [PubMed]
39. Zeroka, D.; Jensen, J.O.; Samuels, A.C. Infrared spectra of some isotopomers of isopropylamine: A theoretical study. *J. Mol. Struct. Theochem* **1999**, *465*, 119–139. [CrossRef]
40. Mączka, M.; Gągor, A.; Macalik, B.; Pikul, A.; Ptak, M.; Hanuza, J. Order-disorder transition and weak ferromagnetism in the perovskite metal formate frameworks of $[(CH_3)_2NH_2][M(HCOO)_3]$ and $[(CH_3)_2ND_2][M(HCOO)_3]$ (M = Ni, Mn). *Inorg. Chem.* **2014**, *53*, 457–467. [CrossRef]
41. Durig, J.R.; Zheng, C. On the vibrational spectra and conformational stability of 1,1-dimethylhydrazine from temperature dependent FT-IR spectra of krypton solutions and ab initio calculations. *J. Mol. Struct.* **2004**, *690*, 31–44. [CrossRef]
42. Ciupa-Litwa, A.; Ptak, M.; Kucharska, E.; Hanuza, J.; Mączka, M. Vibrational properties and DFT calculations of perovskite-type methylhydrazinium manganese hypophosphite. *Molecules* **2020**, *25*, 5215. [CrossRef]

43. Mączka, M.; Ptak, M.; Gągor, A.; Stefańska, D.; Zaręba, J.K.; Sieradzki, A. Methylhydrazinium lead bromide: Noncentrosymmetric three-dimensional perovskite with exceptionally large framework distortion and green photoluminescence. *Chem. Mater.* **2020**, *32*, 1667–1673. [CrossRef]
44. Mączka, M.; Ptak, M.; Vasconcelos, D.L.M.; Giriunas, L.; Freire, P.T.C.; Bertmer, M.; Banys, J.; Simenas, M. NMR and Raman scattering studies of temperature-and pressure-driven phase transitions in $CH_3NH_2NH_2PbCl_3$ perovskite. *J. Phys. Chem. C* **2020**, *124*, 26999–27008. [CrossRef]

materials

MDPI

Supplementary Material

Mechanism of Unusual Isosymmetric Order-Disorder Phase Transition in [Dimethylhydrazinium]Mn(HCOO)$_3$ Hybrid Perovskite Probed by Vibrational Spectroscopy

Jan Albert Zienkiewicz, Edyta Kucharska and Maciej Ptak

Table S1. Selected calculated and experimental bond lengths (Å) and bond angles (°) of dimethylhydrazinium cation ($DMHy^+$) compared to calculated values obtained for dimethylhydrazine molecule (DMHy).

$DMHy^+$ cation			DMHy molecule	
Bond length / angle	**Calculated**	**Experimental (300 K, 100 K) [1]**	**Bond length / angle**	**Calculated**
N1–N4	1.450	1.4268 (34), 1.4475 (34)	N1–N4	1.431
N1–H2	1.017	0.8899 (35)-0.8903 (27),	N1–H2	1.013
N1–H3	1.017	0.9852 (28)-1.0008 (25)	N1–H3	1.024
N4–C5	1.504	1.4766 (34), 1.4897 (42)	N4–C5	1.456
N4–C10	1.503	1.4722 (44), 1.4878 (40)	N4–C9	1.455
N4–H9	1.021	0.9781 (18), 0.9802 (25)		
C5–H6	1.086	0.9597 (30)-0.9601 (28), 0.9595 (31)-0.9603 (34)	C5–H6	1.090
C5–H7	1.087		C5–H7	1.091
C5–H8	1.086		C5–H8	1.105
C10–H10	1.087	0.9593 (38)-0.9604 (41), 0.9594 (27)-0.9603 (29)	C9–H10	1.103
C10–H11	1.086		C9–H11	1.090
C10–H12	1.085		C9–H12	1.087
N1–N4–C5	115.46	110.966 (218)-112.655 (238), 109.041 (215)-114.215 (227)	N1–N4–C5	112.51
N1–N4–C10	108.69		N1–N4–C9	108.53
C5–N4–C10	112.70	110.984 (219), 111.226 (233)	C5–N4–C9	111.99
N4–N1–H2	107.90	109.445 (311)-109.528 (319), 102.431 (219)-111.051 (226)	N4–N1–H2	107.38
N4–N1–H3	107.29		N4–N1–H3	109.99
N4–C5–H6	108.58	109.453 (246)-109.485 (246), 109.473 (246)-109.510 (322)	N4–C5–H6	109.61
N4–C5–H7	108.85		N4–C5–H7	109.88
N4–C5–H8	108.19		N4–C5–H8	112.49
N4–C10–H10	110.62	109.437 (281)-109.506 (258), 109.447 (258)-109.498 (254)	N4–C9–H10	108.47
N4–C10–H11	108.53		N4–C9–H11	109.42
N4–C10–H12	107.87		N4–C9–H12	108.94
C5–N4–H9	108.22	107.527 (186), 107.334 (236)		
N1–N4–H9	104.41	109.223 (218)-107.363 (227)		

Table S2. The correlation diagram showing the correspondence between the optical modes in the LT (HT) phases of [DMHy]Mn(HCOO)$_3$.

Ion	Vibration	Free ion symmetry	Site symmetry	Factor group symmetry LT (HT)
			C_1=1 ($C_i = \bar{1}$)	C_{2h}=2/*m* (C_{2h}=2/*m*)
Mn^{2+}	T′	-	3A (3A_u)	3A_g + 3A_u + 3B_g + 3B_u (6A_u + 6B_u)
		C_s	C_1=1	C_{2h}=2/*m*
	$\nu_s NH_2$	A′	A	A_g + A_u + B_g + B_u
	$\nu_{as} NH_2$	A″	A	A_g + A_u + B_g + B_u
	δNH_2	A′	A	A_g + A_u + B_g + B_u
	ϱNH_2	A″	A	A_g + A_u + B_g + B_u
	τNH_2	A″	A	A_g + A_u + B_g + B_u
	ωNH_2	A′	A	A_g + A_u + B_g + B_u
	νNH	A′	A	A_g + A_u + B_g + B_u
	δNH	A′	A	A_g + A_u + B_g + B_u
$DMHy^+$	γNH	A″	A	A_g + A_u + B_g + B_u
	$\nu_s CH_3$	A′ + A″	2A	2A_g + 2A_u + 2B_g + 2B_u
	$\nu_{as} CH_3$	2A′ + 2A″	4A	4A_g + 4A_u + 4B_g + 4B_u
	$\delta_s CH_3$	A′ + A″	2A	2A_g + 2A_u + 2B_g + 2B_u
	$\delta_{as} CH_3$	2A′ + 2A″	4A	4A_g + 4A_u + 4B_g + 4B_u
	ϱCH_3	2A′ + 2A″	4A	4A_g + 4A_u + 4B_g + 4B_u
	τCH_3	A′ + A″	2A	2A_g + 2A_u + 2B_g + 2B_u
	νNN	A′	A	A_g + A_u + B_g + B_u
	νCN	A′ + A″	2A	2A_g + 2A_u + 2B_g + 2B_u
	δCNN	A′ + A″	2A	2A_g + 2A_u + 2B_g + 2B_u
	δCNC	A′	A	A_g + A_u + B_g + B_u
	T′	2A′ + A″	3A	3A_g + 3A_u + 3B_g + 3B_u
	L	A′+ 2A″	3A	3A_g + 3A_u + 3B_g + 3B_u
		C_{2v}=*mm*2	C_1=1	C_{2h}=2/*m*
	ν_1	A_1	3A	3A_g + 3A_u + 3B_g + 3B_u
	ν_2	A_1	3A	3A_g + 3A_u + 3B_g + 3B_u
	ν_3	A_1	3A	3A_g + 3A_u + 3B_g + 3B_u
$HCOO^-$	ν_4	B_1	3A	3A_g + 3A_u + 3B_g + 3B_u
	ν_5	B_1	3A	3A_g + 3A_u + 3B_g + 3B_u
	ν_6	B_1	3A	3A_g + 3A_u + 3B_g + 3B_u
	T′	A_1 + B_1 + B_2	9A	9A_g + 9A_u + 9B_g + 9B_u
	L	A_2 + B_1 + B_2	9A	9A_g + 9A_u + 9B_g + 9B_u

Key: red: IR-active modes, blue: Raman-active modes, green: IR- and Raman-active modes.

Table S3. Calculated harmonic (ν_h) and anharmonic (ν_{ah}) wavenumbers for dimethylhydrazinium cation ($DMHy^+$) and dimethylhydrazine molecule (DMHy) as well as potential energy distribution (PED) of the respective predominant modes.

$DMHy^+$ Cation				DMHy Molecule			
ν_h (cm^{-1})	ν_h* (cm^{-1})	ν_{ah} (cm^{-1})	PED (%)	ν_h (cm^{-1})	ν_h* (cm^{-1})	ν_{ah} (cm^{-1})	PED (%)
3556	3414	3389	$\nu_{as}NH_2$-100	3532	3391	3344	$\nu_{as}NH_2$-100
3470	3331	3363	ν_sNH_2-98	3345	3211	3148	ν_sNH_2-100
3445	3307	3288	νNH^+-95				
3190	3062	3047	$\nu_{as}CH_3$-100	3129	3004	2984	$\nu_{as}CH_3$-100
3174	3047	3030	$\nu_{as}CH_3$-99	3099	2975	2946	$\nu_{as}CH_3$-99
3172	3045	3028	$\nu_{as}CH_3$-100	3071	2948	2946	$\nu_{as}CH_3$-100
3165	3038	3022	$\nu_{as}CH_3$-100	3059	2937	2933	$\nu_{as}CH_3$-99
3083	2960	2983	ν_sCH_3-100	2920	2803	2746	ν_sCH_3-99
3074	2951	2971	ν_sCH_3-100	2905	2846	2723	ν_sCH_3-99
1685	1651	1658	δNH_2-99	1670	1637	1612	δNH_2-99
1515	1484	1467	$\delta_{as}CH_3$-70 + ρNH_2-14 + δNH^+-13	1513	1482	1468	$\delta_{as}CH_3$-98
1512	1482	1464	$\delta_{as}CH_3$-85	1497	1467	1462	$\delta_{as}CH_3$-98
1497	1467	1462	$\delta_{as}CH_3$-66 + δNH^+-24				
1492	1462	1442	$\delta_{as}CH_3$-79 + δNH^+-16	1495	1466	1449	$\delta_{as}CH_3$-98
1481	1451	1442	$\delta_{as}CH_3$-79 + δNH^+-16	1483	1453	1448	$\delta_{as}CH_3$-99
1473	1444	1438	δ_sCH_3-96	1463	1434	1422	δ_sCH_3-98
1452	1422	1419	δ_sCH_3-89 + γNH^+-11	1439	1410	1414	δ_sCH_3-100
1424	1396	1374	γNH^+-66 + δ_sCH_3-34				
1359	1332	1321	ρCH_3-43 + ρNH_2-40 + δNH^+-16	1340	1314	1296	ρNH_2-77 + νCN-17
1255	1230	1212	ρCH_3-81 + νNN-10	1284	1258	1245	ρCH_3-71 + ρNH_2-29
1218	1194	1178	ρCH_3-71 + ωNH_2-17	1241	1217	1202	ρCH_3-47 + ωNH_2-47
1138	1116	1112	ρCH_3-74 + ρNH_2-19	1167	1144	1137	ρCH_3-81 + ρNH_2-11
1060	1039	1026	ρCH_3-48 + ωNH_2-45	1115	1093	1087	ρCH_3-98
1050	1029	1025	ρCH_3-67 + ωNH_2-22 + γNH^+-10	1080	1058	1046	ρCH_3-50 + ωNH_2-30 + νNN-20
958	938	923	νCN-95	1029	1008	1005	ρCH_3-53 + ν_{as}CNC-45
915	897	867	νNN-41 + νCN-31 + ωNH_2-26	950	931	898	ωNH_2-49 + ν_{as}CNC-28 + νNN-19
793	777	766	νCN-64 + νNN-30	816	799	788	νNN-44 + ν_sCNC-58
475	466	467	δCNN-89	464	455	454	δCNC-96
426	417	425	δCNN-90	428	420	429	δCNC-99
391	384	364	δCNC-63 + δCNN-27	399	391	371	δCNN-72 + δCNC-27
264	259	231	τCH_3-99	300	294	318	τNH_2-98
262	257	216	τNH_2-99	273	268	299	τCH_3-100
216	212	200	τCH_3-100	247	242	287	τCH_3-98

* scaling factor, 0.9800 (0-2499 cm^{-1}), 0.96 (2500-3600 cm^{-1}); key: ν, stretching; δ, bending; ρ, rocking; γ, out-of-plane bending; ω, wagging; τ, twisting

Table S4. The comparison of IR (polycrystalline) and Raman (single crystal) bands observed at 80 and 300 K for [DMHy]Mn(HCOO)$_3$.

Raman (80 K)	Raman (300 K)	IR (80 K)	IR (300 K)	Assignment
3307sh, 3272vw	3320sh, 3286vw	3352vw, 3314w, 3262m, 3227sh	3312w, 3283w	$\nu_{as}NH_2$
3156w	3176vw	3195vw, 3161m, 3135w	3171w	ν_sNH_2
3062w, 3039sh, 3036m	3055sh, 3044w	3074vw, 3057vw, 3046vw	3054sh, 3039sh	νNH^+
3018m	3025m	3035sh, 3021w	3025w	$\nu_{as}CH_3$
2974m, 2958sh, 2948m, 2909sh	2974sh, 2964m, 2950sh, 2928m	2987w[a], 2947w[a], 2931w[a]	2953sh[a], 2931w[a]	ν_sCH_3
2873s, 2852m, 2835s	2856w, 2827m	2863w[a], 2854sh[a], 2844w, 2824w[a]	2858sh[a], 2843sh[a], 2826w[a]	ν_1
2795w, 2724vw, 2703w, 2690vw	2710vw, 2692vw	2778vw, 2740w, 2716w, 2670w, 2648m, 2628m, 2602sh, 2584sh, 2550w, 2531w, 2504w	2730sh, 2715w, 2674w, 2639sh, 2540vw, 2495vw	$\nu NH_2+\nu NH^++o+cb$
1648vw	1654vw	1661w	1648sh	δNH_2
1583vw	1576vw	1575vs, 1536sh, 1510m	1581vs	$\nu_4+\delta NH^+$
1503vw, 1481sh, 1469w, 1459w	1482sh, 1469vw	*	*	$\delta_{as}CH_3$
1440vw, 1401vw	1434vw, 1410vw	*	*	$\delta_sCH_3+\gamma NH^+$
1372sh, 1366s, 1359vs	1371sh, 1360s,	*	*	ν_5
1349m, 1340vw	1353sh	*	*	$\nu_2+\varrho NH_2$
1243vw, 1220w, 1149w	1243vw, 1217vw, 1143vw	1247w, 1224w, 1197vw, 1176w, 1151vw	1244w, 1216w, 1200w, 1171vw	ϱCH_3
1084sh, 1077w	1097vw	1100w, 1081w	1093w	$\rho CH_3+\nu NN$
1063w, 1057sh	1065w, 1058sh	1067w 1059sh	1058w	ν_6
		994 w, 989 w	1002 w, 990 vw	$\nu_{as}CNC$
962w	949vw	966w, 941w	958w, 946w	ωNH_2
839vw, 822m	833vw, 824w	825w	820vw	ν_sCNN
790w	788wm	800sh, 795s, 767sh	792s	ν_3
516vw, 489vw	507vw			δCNC
449 vw, 419 vw	443 vw, 420 vw			δCNN
301vw, 290vw, 251vw, 226w, 208w	314vw, 210sh, 203sh			$\tau NH_2+\tau CH_3+lm$
187sh, 181w, 174sh, 157w, 148w, 136w, 119w, 98w, 85w, 72w	179w, 133w, 75sh, 60w			lm

Key: ν, stretching; δ, bending; ρ, rocking; γ, out-of-plane bending; ω, wagging; τ, twisting; vs, very strong; s, strong; m, medium; w, weak; vw, very weak; ν_1-ν_6, internal vibrations of formate ion (see description in text); *, regions of absorption related to the medium; o, overtones; cb, combinational bands; lm, lattice modes; [a] in Fluorolube.

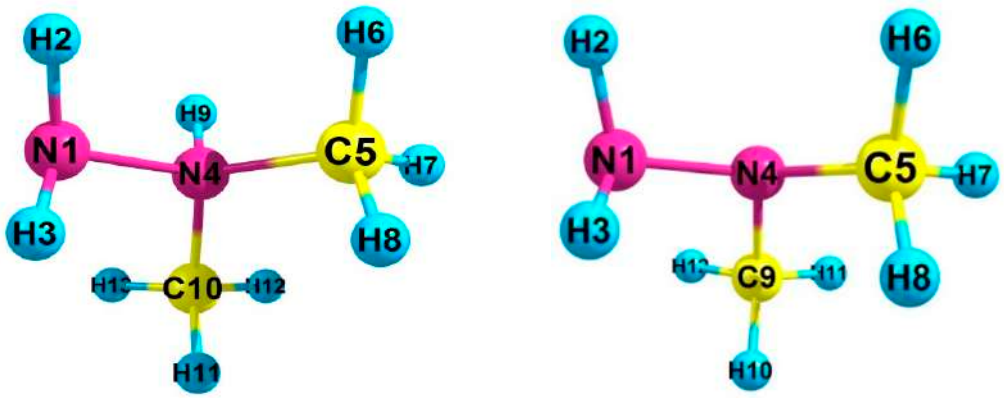

(**a**) (**b**)

Figure S1. The numbering of atoms in the (**a**) dimethylhydrazinium cation ($DMHy^+$) and (**b**) dimethylhydrazine molecule (DMHy).

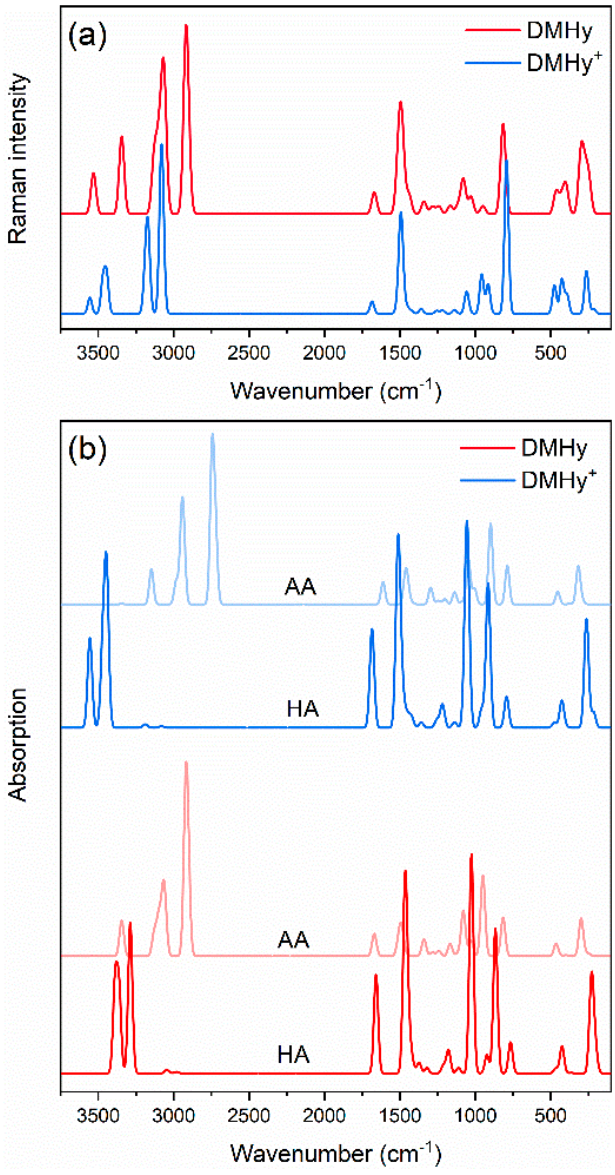

Figure S2. The comparison of calculated Raman spectra (**a**) in harmonic approximation and IR spectra (**b**) of dimethylhydrazinium cation ($DMHy^+$) and dimethylhydrazine molecule (DMHy) in the harmonic (HA) and anharmonic approximation (AA).

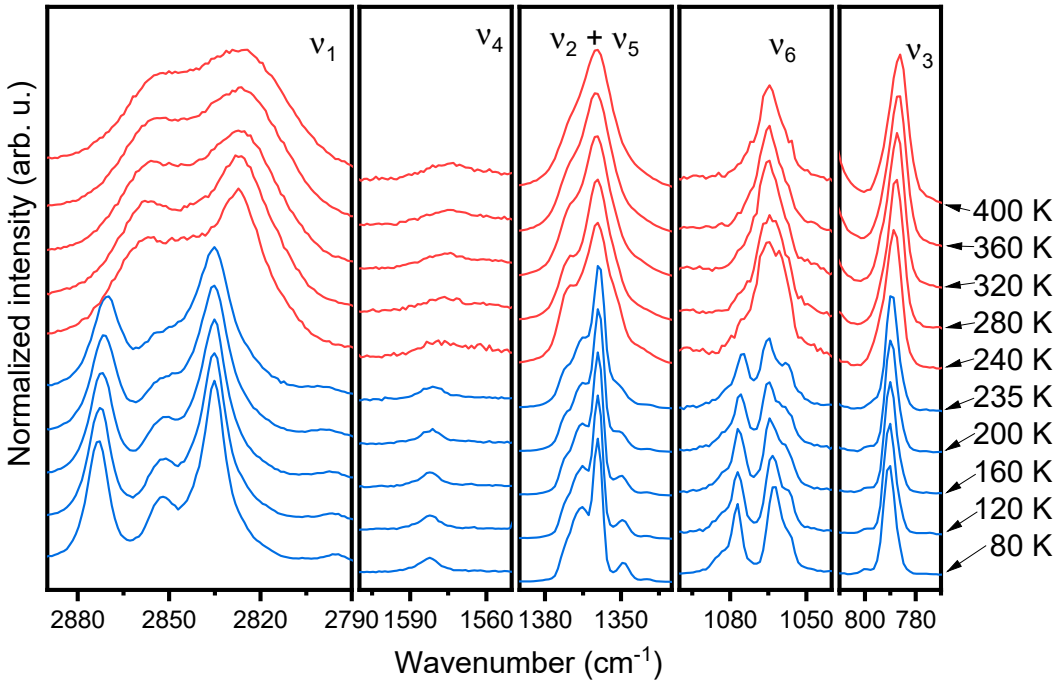

Figure S3. Raman bands corresponding to vibrational modes of the formate anion.

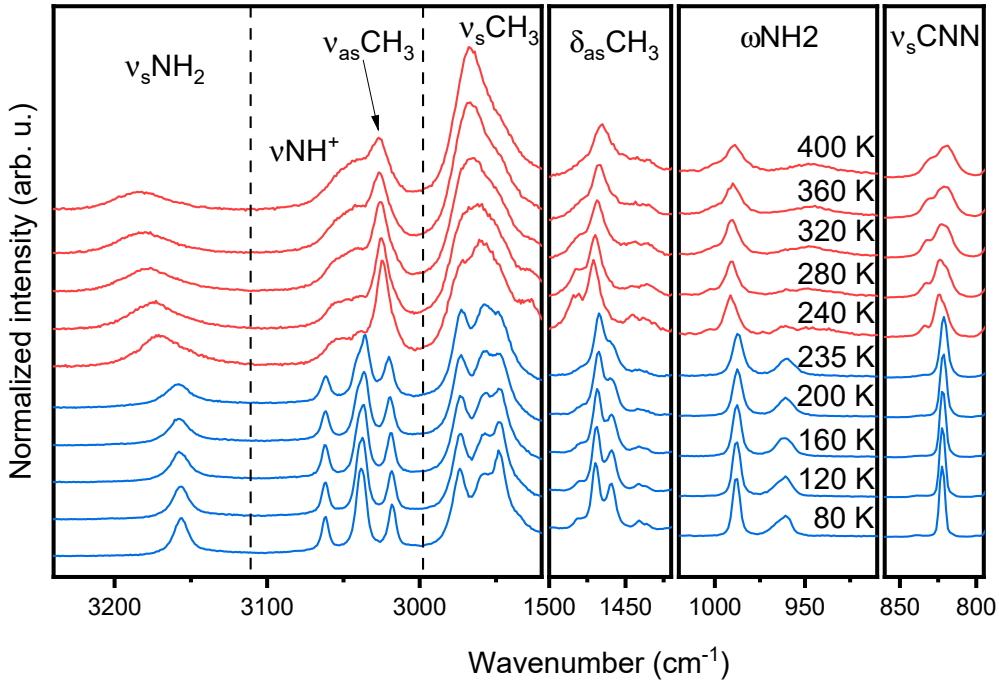

Figure S4. Details of temperature-dependent Raman spectra, corresponding to vibrational modes of $DMHy^+$ cation.

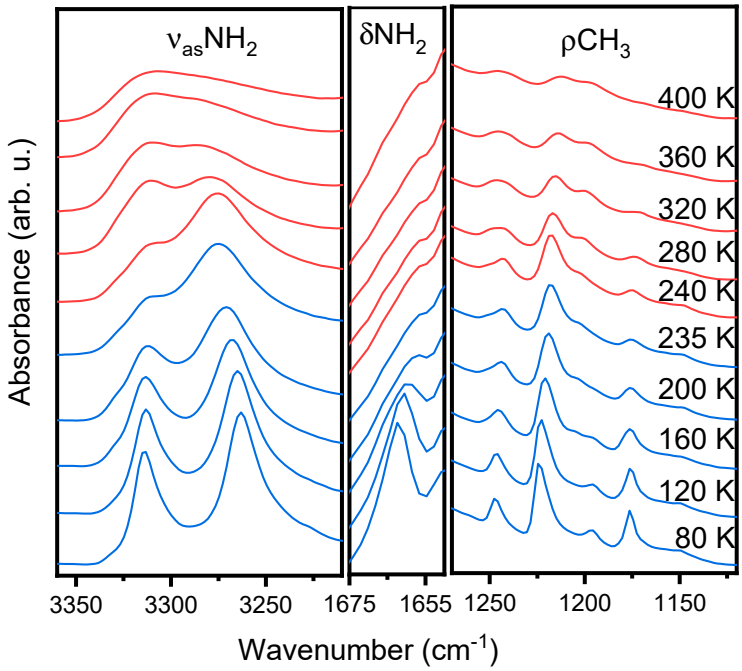

Figure S5. Details of temperature-dependent IR spectra, corresponding to vibrational modes of $DMHy^+$ cation.

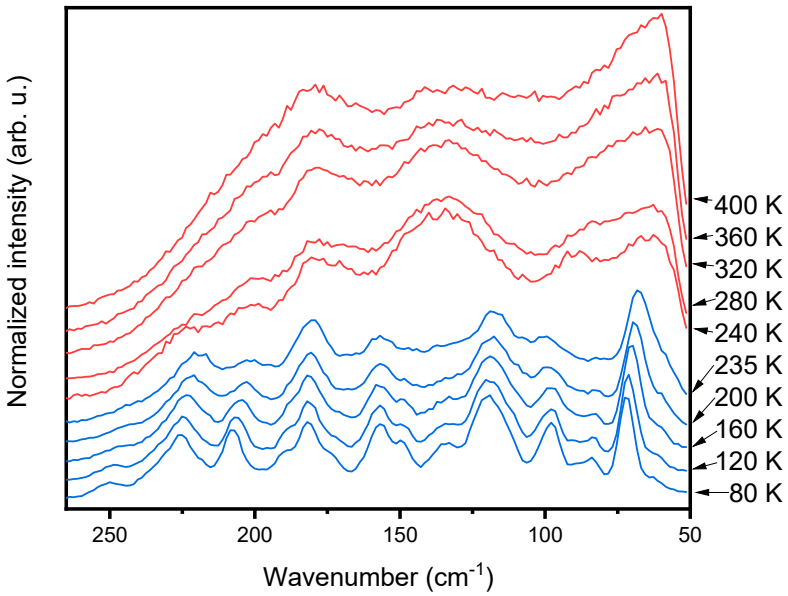

Figure S6. Raman bands corresponding to lattice modes.

Reference

1. Zienkiewicz, J.A.; Kowalska, D.A.; Fedoruk, K.; Stefański, M.; Pikul, A.; Ptak, M. Unusual isosymmetric order-disorder phase transition in the new perovskite-type dimethylhydrazinium manganese formate exhibiting ferrimagnetic and photoluminescent properties. *J. Mater. Chem. C* **2021**, 9, 6841-6851, https://doi.org/10.1039/D1TC01014J

***Publikacja* [D3]**

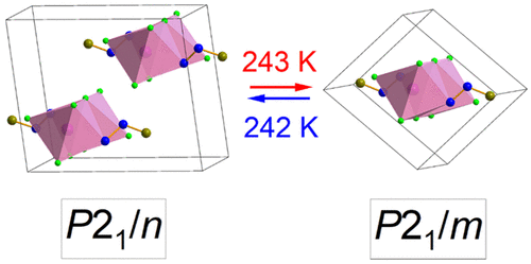

J.A. Zienkiewicz*, M. Ptak, D. Drozdowski, K. Fedoruk, M. Stefański, A. Pikul

Hybrid organic-inorganic crystals of [methylhydrazinium]$M^{II}Cl_3$ (M^{II} = Co, Ni, Mn)

J. Phys. Chem. C **2022**, 126 (37), 15809-15818

doi: 10.1021/acs.jpcc.2c04893 IF = 4,177 140 pkt.

Udział Doktoranta w powstanie pracy:

- Synteza monokryształów [MHy]$M^{II}Cl_3$ (M^{II} = Mn^{2+}, Co^{2+}, Ni^{2+}) metodą powolnego odparowywania z roztworu;
- Koncepcja badań oraz określenie metodologii;
- Wyznaczenie reguł wyboru oraz wykonanie analizy grupy faktorowej;
- Zaproponowanie przypisania pasm IR i Ramana;
- Pomiar widm Ramana oraz IR, również w funkcji temperatury;
- Analiza dyfraktogramów proszkowych;
- Analiza zachowania pasm IR i Ramana w funkcji temperatury, dekonwolucja widm oraz dopasowywanie krzywych Lorentza do danych eksperymentalnych;
- Dyskusja wpływu kationu M^{II} na właściwości strukturalne, cieplne oraz fononowe;
- Określenie mechanizmu przemian fazowych;
- Przygotowywanie manuskryptu, rysunków oraz tabel.

THE JOURNAL OF PHYSICAL CHEMISTRY C
A JOURNAL OF THE AMERICAN CHEMICAL SOCIETY

pubs.acs.org/JPCC

Article

Hybrid Organic–Inorganic Crystals of [Methylhydrazinium]$M^{II}Cl_3$ (M^{II} = Co, Ni, Mn)

Jan A. Zienkiewicz,* Maciej Ptak, Dawid Drozdowski, Katarzyna Fedoruk, Mariusz Stefanski, and Adam Pikul

Cite This: *J. Phys. Chem. C* 2022, 126, 15809–15818

Read Online

ACCESS | Metrics & More | Article Recommendations | Supporting Information

ABSTRACT: We report the synthesis and investigation of the physicochemical properties of novel one-dimensional hybrid organic–inorganic chlorides templated by the methylhydrazinium (MHy^+) cation, $MHyM^{II}Cl_3$ with M^{II} = Mn, Co, and Ni. All crystals exhibit a rare $[M^{II}Cl_5N]$ coordination sphere. They undergo second-order *klassengleiche* structural phase transitions at 242 K (Mn), 227 K (Co), and at 223 K (Ni) upon cooling from the high-temperature $P2_1/m$ to the low-temperature $P2_1/n$ phase. Dielectric studies showed that the transformation has a weak dielectric response. X-ray diffraction data together with Raman and IR spectroscopy showed that the mechanism of phase transitions involves the changes of the metal-chloride framework, rearrangement of hydrogen bonds, and the different confinement of organic cations in the crystal voids. We show that the ionic radius (and electronegativity) of the metal ions correlates with structural factors, temperature of phase transition, dielectric response, hydrogen bond strength, and tolerance factor. The combination of the MHy^+ cation with the small chloride linker does not allow achieving the archetypical perovskite-like architecture. Magnetic measurements revealed that $MHyCoCl_3$ and $MHyNiCl_3$ order antiferromagnetically below the same Néel temperature of about 3.7 K. The noticeable interplay of antiferromagnetic and ferromagnetic correlations leads in both systems to metamagnetic phase transitions in H of about 1 kOe. $MHyMnCl_3$ showed only smeared antiferromagnetic ordering at about 5.0 K, with no trace of ferromagnetic correlations up to the highest field studied. Optical studies showed that all crystals are wide-bandgap materials with bandgaps of 5.34 (Mn), 3.96 (Ni), and 3.64 eV (Co). Moreover, $MHyMnCl_3$ ($MHyNiCl_3$) exhibited red (yellowish-green to orange) photoluminescence under the 450 (375) nm excitation with the activation energies of 299 (49) meV.

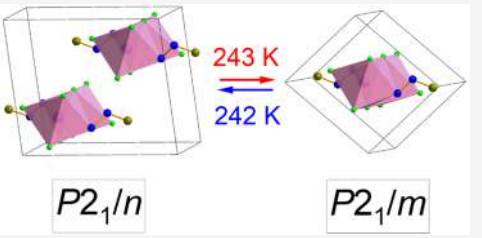

INTRODUCTION

In recent years, due to the dynamical development of the high technology industry, it has become necessary to search for new electronic and optoelectronic materials. A lot of attention has been paid to hybrid organic–inorganic materials, coordination polymers, and metal–organic frameworks (MOFs). Due to their tunable optical,[1,2] electric,[3] ferroic,[4−7] switchable dielectric,[6,8] and magnetic[9] properties, hybrid compounds have garnered increasing attention. Hybrid materials based on Mn^{2+} ions and Cl^- linkers have demonstrated multifunctional properties, such as bright luminescence and dielectric response in $(Hmpy)MnCl_3$ ($Hmpy^+$ = *N*-methylpyrrolidinium cation),[10] or ferroelectricity, a large piezoelectric response, photoluminescence, magnetic ordering, and spin texture in $(TMCM)MnCl_3$ ($TMCM^+$ = trimethylchloromethylammonium cation).[11]

A cation that has lately attracted much attention is MHy^+ because it is capable of fitting into the crystal voids of the lead-halide frameworks with a rare 3D architecture, in $MHyPbX_3$ (X = Cl, Br).[2,12] Both analogues show order–disorder phase transitions (PTs) and the presence of polar orders related to the MHy^+ cations.[2,12,13] The chloride analogue shows quadratic nonlinear optical switching.[12] The bromide analogue exhibits dielectric switching, strong SHG activity, advanced thermochromism, and upconversion.[2] In contrast to Cl and Br, $MHyPbI_3$ adopts a 1D chain structure with edge-sharing octahedra.[14]

Other interesting compounds templated by MHy^+ are $(MHy)_2PbX_4$ (X = Br, I) adopting layered (2D) structures. The Br analogue exhibits a record low separation of the inorganic slabs due to a strong network of hydrogen bonds (HBs). Moreover, the MHy^+ cations are related to the ferroelectric order, red-shifted excitonic absorption, and a small exciton binding energy.[15] The I analogue exhibits unusually small interoctahedral tilting of the octahedral units, a small band gap, and thermochromism.[16] Very recently, MHy^+ was also used to synthesize Ruddlesden–Popper perovskite $(BA)_2(MHy)_2Pb_3Br_{10}$ (BA^+ = butylammonium)

Received: July 11, 2022
Revised: September 1, 2022
Published: September 13, 2022

with 3D stacks intercalated by MHy^+ and spaced by BA^+ cations.[17]

As one can see, there is a large variety of available structural motifs that can be created by the relatively small MHy^+ cation. Due to the limitations of the 3D perovskite architecture, low-dimensional materials are given a lot of consideration. Recently, Stoumpos et al. introduced the term perovskitoids in the field of material science to describe compounds having the ABX_3 stoichiometry and edge-, corner-, or face-sharing connectivity between octahedral units.[18,19] A quite widespread feature of perovskites and perovskitoids is the presence of structural PTs triggered by the collective ordering of molecular cations, a deformation of the framework and reorganization of the HB network.[2,15]

The large perspective of our research is to study the physicochemical behavior of low-dimensional perovskitoids with tolerance factors (TFs) that approach or exceed the boundary conditions for 3D perovskites. In this work, we present a series of transition metal-based hybrid halides described by the general formula $MHyM^{II}Cl_3$. Despite the stoichiometry, combining the MHy^+ cation with relatively small metal cations results in TF values greater than 1, preventing the formation of an archetypical perovskite structure. Instead, 1D chain structures with a rare $[M^{II}Cl_5N]$ coordination sphere are preferred. It provides us a great opportunity to investigate differences between the behavior of MHy^+ inside the coordination sphere of a metal cation and in the voids between metal-halide octahedra described in previous works. It should be noted that for 3D perovskites, $MHyPbCl_3$ and $MHyPbBr_3$, the Pb−N short contact (ca. 3 Å) is also present; however, the N atoms do not enter directly the octahedral coordination sphere $[PbX_6]$ of halides.[2,12] In contrast, the $[M^{II}X_5N]$ type of coordination was reported for hydrazinium[20] (X = Cl, Br) and 1,1,1-trimethylhydrazinium cations (X = Cl).[21]

In this work, we performed a thorough physicochemical analysis of the thermal, structural, dielectric, vibrational, optical, and magnetic behavior of three novel perovskitoids, $MHyM^{II}Cl_3$ (M^{II} = Mn, Co, Ni). DSC measurements provided preliminary information regarding the nature of PTs, which was extended upon by determining the crystal structure using X-ray diffraction (XRD) measurements. Complementary methods of vibrational spectroscopy (temperature-dependent Raman and IR spectroscopy) provided us with a deeper insight into the mechanisms of PTs. This physicochemical investigation was expanded by looking into dielectric, optical, and magnetic properties.

EXPERIMENTAL SECTION

Materials and Synthesis. Methylhydrazine (98%, Sigma-Aldrich), hydrochloric acid (35−38%, Avantor Performance Materials Poland), manganese(II) (96%, Sigma-Aldrich), cobalt(II) (98%, Sigma-Aldrich), and nickel(II) (98%, Sigma-Aldrich) chlorides were obtained commercially and used without further purification.

In order to grow $MHyM^{II}Cl_3$ crystals, 1 mmol of $M^{II}Cl_2$ was digested in hydrochloric acid. Next, methylhydrazine (1.5 mmol, 0.2 mL) was added to this solution dropwise. The obtained mixture was kept undisturbed at RT in order to slowly evaporate the solvent. The pinkish (Mn), blue (Co), and brownish-orange (Ni) crystals were harvested from the mother solution after 7−30 days and dried in the air.

X-ray Diffraction. Single-crystal X-ray diffraction (SC-XRD) experiments were carried out with MoKα radiation using an Xcalibur Atlas diffractometer. Absorption was corrected by multiscan methods, CrysAlis PRO 1.171.39.46 (Rigaku Oxford Diffraction, 2018). Empirical absorption correction using spherical harmonics, implemented in SCALE3 ABSPACK scaling algorithm, was applied. Refinement was on 65 parameters. H atom parameters were constrained. The crystal structure was solved in Olex2 1.3 using SHELXT-2014/4 and refined with SHELXL-2018/3 (see Appendix 1, Supporting Information).[22,23] The experimental details and selected geometric parameters are presented in Tables S1−S4. The CIF files of all structures can be found in the CCDC Database with deposition nos. 2047530, 2047532−2047536.

Powder X-ray diffraction (PXRD) patterns were taken of all samples on an X'Pert PRO X-ray diffraction system equipped with a PIXcel ultrafast line detector and Soller slits for CuKα_1 radiation (λ = 1.54056 Å). The powders were measured in the reflection mode; the X-ray tube settings were 30 mA and 40 kV.

Thermal Properties. Heat capacity was measured using a Mettler Toledo DSC-1 calorimeter. The weights used for measurements were equal to 23.75, 32.19, and 21.71 mg for M^{II} = Mn, Co, and Ni, respectively. Nitrogen was used as the purge gas, and the heating and cooling rate was 5 K min^{-1}.

Dielectric Properties. The complex dielectric permittivity of the pelletized polycrystalline samples was measured as a function of temperature with a parallel plate capacitor coupled to a broadband impedance Novocontrol Alpha analyzer. The samples were dried, and then silver paste was spread on their surfaces to ensure good electrical contact with the electrodes. The AC voltage with an amplitude of 1 V and a frequency in the range of $1-10^6$ Hz was applied across the samples, and the measurements were taken over the temperature range of 170−270 K at every 1 K during the cooling cycle.

Vibrational Properties. Room-temperature (RT) and temperature-dependent (80−400 K) Raman spectra of randomly oriented single crystals were measured in the 3500−50 cm^{-1} range using a Renishaw inVia Raman spectrometer equipped with a confocal DM2500 Leica optical microscope, a thermoelectrically cooled CCD as a detector, and an Ar^+ ion laser operating at 488 nm. A Linkam THMS600 heating/freezing stage was used to control the temperature. The RT IR spectra were measured as a suspension in nujol (mineral oil) in mid-IR (4000−400 cm^{-1}) and far-IR (400−50 cm^{-1}) regions using a Nicolet iS50 infrared spectrometer. The temperature-dependent mid-IR (3500−600 cm^{-1}) spectra were measured using a Nicolet iN10 infrared microscope. The temperature was controlled using a Linkam THMS600 heating/freezing stage equipped with ZnSe windows. The spectral resolution of all IR and Raman measurements was set to 2 cm^{-1}.

Optical Properties. The absorption measurements were performed in the back scattering mode using an Agilent Cary 5000 spectrophotometer. The temperature-dependent emission spectra were measured with the Hamamatsu photonic multichannel analyzer PMA-12 equipped with a BT-CCD linear image sensor. The laser diodes operating at 375 and 450 nm were applied as excitation sources. The luminescent decay profiles were recorded using a femtosecond laser (Coherent Model Libra) generating excitation fluence to be 0.44 $\mu J/mm^2$ and 0.31 $\mu J/mm^2$ for 375 and 450 nm excitation lines,

https://doi.org/10.1021/acs.jpcc.2c04893
J. Phys. Chem. C 2022, 126, 15809−15818

respectively. The temperature of the samples during emission and kinetics measurements was controlled by the Linkam THMS600 heating/freezing stage.

Magnetic Properties. Magnetization of randomly oriented single crystals of $MHyMnCl_3$, $MHyCoCl_3$, and $MHyNiCl_3$ (from 20 to 70 mg in total) was measured using a commercial Quantum Design MPMS XL magnetometer from room temperature down to 2 K and in applied magnetic fields up to 70 kOe. The diamagnetic background coming from a sample holder was found to be weak and negligible in comparison to the signal coming from the samples; hence, its subtraction was omitted. Moreover, no diamagnetization corrections were made to the data reported here.

RESULTS AND DISCUSSION

Thermal Properties. Heat flow measurements carried out at a rate of 5 K min^{-1} show reversible temperature anomalies upon heating and cooling for all investigated samples (Figure S1). The excess specific heat (ΔC_p), calculated from the heat flow data on heating/cooling, shows the presence of anomalies at 243/242 K (Mn), 229/227 K (Co), and 224/223 K (Ni) (Figure 1 and Table 1). All observed ΔC_p peaks related to PTs

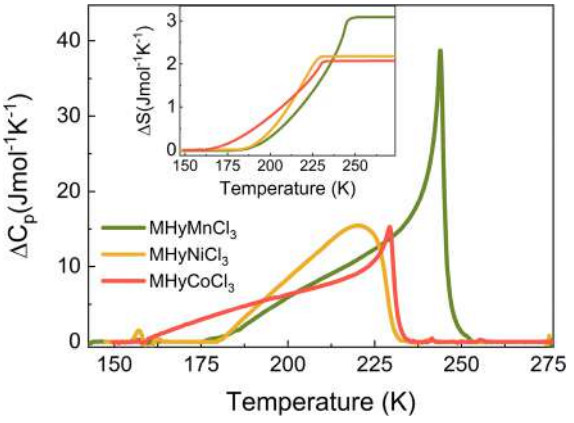

Figure 1. Temperature dependence of excess specific heat (ΔC_p) related to PTs for Mn (green), Co (red), and Ni (yellow) in the heating mode. The inset shows the corresponding changes of entropy (ΔS).

Table 1. Comparison of Selected Parameters for $MHyM^{II}Cl_3$ (M^{II} = Mn, Co, Ni)

	Mn	Co	Ni
T_c[a] (K)	243/242	229/227	224/223
ΔS (J mol^{-1} K^{-1})	3.1	2.1	2.2
M^{II}-NH_2[b] (Å)	2.365	2.194	2.116
MHy-cage mode (cm^{-1})	515	563	595
V_{fu}[b] (Å^3)	171.2	162.1	158.4
E_g (eV)	5.34	3.96	3.64
E_a (meV)	299	-	49
TF	1.16	1.23	1.26

[a]Heating/cooling. [b]In **I**, T_c, temperature of the PT; ΔS, change of entropy; V_{fu}, volume per formula unit; E_g, band gap energy; E_a, activation energy; TF, tolerance factor.

are strongly asymmetric. The corresponding changes in entropy (ΔS) decrease gradually with the temperature, suggesting the second-order nature of PTs (see Appendix 2).

The experimental values of ΔS on heating were estimated to be 3.1 J mol^{-1} K^{-1} (Mn), 2.1 J mol^{-1} K^{-1} (Co), and 2.2 J $mol^{-1}K^{-1}$ (Ni) (see Table 1). These ΔS values inserted into the Boltzmann formula $\Delta S = R \ln(N)$ give a low value of N parameter (1.3−1.4), suggesting that the mechanism of PT is not associated with molecular ordering.

Dielectric Properties. As the thermal data revealed the presence of one PT in each sample, dielectric measurements were performed to elucidate the relationship between PTs and dielectric anomalies. The resulting dielectric permittivity ε' spectra exhibit small inflections for all samples that are most pronounced at higher frequencies (Figure 2). They correspond

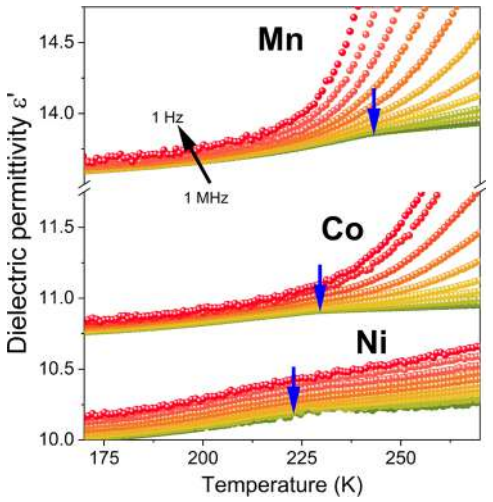

Figure 2. Real part of dielectric permittivity vs temperature at selected frequencies between 1 Hz and 1 MHz. Blue arrows indicate the PT temperatures obtained from DSC traces.

well to the thermal anomalies determined by DSC measurements. The total increase in ε' with increasing temperature is caused by ionic or electronic conductivity. Similar behavior has been previously noted for some hybrid organic−inorganic compounds.[2,12,24]

Single-Crystal X-ray Diffraction. All $MHyM^{II}Cl_3$ (M^{II} = Mn, Co, Ni) structures crystallize at RT in the monoclinic centrosymmetric $P2_1/m$ space group (phase **I**) with $Z = 2$ (see Table S1). The motif of **I** is composed of parallel chains of the edge-sharing $[M^{II}Cl_5N]$ octahedra propagating along the [010] direction (Figures 3a,b). MHy^+ cations are ordered, and the N(1) atoms from the terminal NH_2 groups of MHy^+ cocreate with Cl^- anions the coordination sphere of M^{II}. The N−H···Cl HBs and long-range forces (turquoise dashed lines in Figure 3a) between both NH_2 groups and Cl^- ions stabilize the crystal structure. The M^{II}−NH_2 distances in **I** are 2.365 (Mn), 2.194 (Co), and 2.116 Å (Ni), which are below the maximum limit for the M^{II}−NH_2 coordinate bonds (Figure S2 and Table S2). Considering the alignment of the inorganic part, two types of chlorine positions can be distinguished, namely, bridging and nonbridging ones. The nonbridging ligands lie on the mirror plane m, whereas the bridging ones adopt general symmetry sites (C_1). For all structures, the terminal M^{II}−Cl distances are shorter, i.e., 2.446 (Mn), 2.390 (Co), and 2.397 Å (Ni), while the bridging ones are longer, namely, 2.540 Å (Mn), 2.460 (Co), and 2.418 Å (Ni) (see Table 1). These values are typical for the coordination compounds with the above metal centers and Cl ligands.[25,26]

https://doi.org/10.1021/acs.jpcc.2c04893
J. Phys. Chem. C 2022, 126, 15809−15818

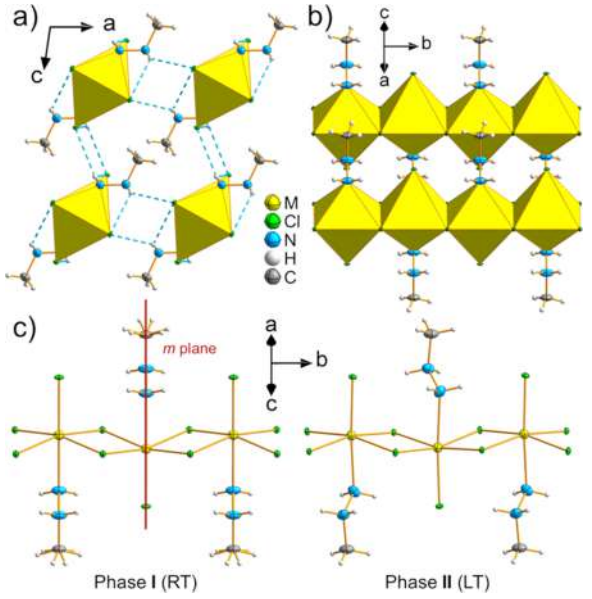

Figure 3. Crystal structure of $MHyM^{II}Cl_3$; (a) Phase **I** with N−H···Cl interactions marked as turquoise dashed lines, (b) $[M^{II}Cl_3N]_\infty$ chains of edge-sharing octahedra propagating along the [010] direction, (c) the distortion of $[M^{II}Cl_3N]_\infty$ chains due to the symmetry reduction.

It is noteworthy that the coordinating nature of MHy^+ favors the edge-sharing connections between mixed octahedral spheres of $[M^{II}Cl_5N]$. The other common cations, A = MA^+ (methylammonium), DMA^+ (dimethylammonium), TMA^+ (tetramethylammonium), GA^+ (guanidinium), or FA^+ (formamidinium), prefer to form face-sharing chains in $AM^{II}Cl_3$ (M^{II} = Mn, Ni) perovskitoids.[27−29]

When lowering the temperature, $MHyM^{II}Cl_3$ undergoes a PT to another monoclinic, centrosymmetric phase of $P2_1/n$ symmetry (phase **II**). The **I** → **II** PT is *klassengleiche*, where $P2_1/n$ is a maximal non-isomorphic subgroup of $P2_1/m$.[30] The mirror plane vanishes (Figure 3c) in **II**, and all atoms adopt a general C_1 site. Thus, the number of inequivalent Cl^- ligands increases from 2 to 3.

One should note that while the general alignment of the motif after the **I** → **II** PT is barely changed, an enhancement of N−H···Cl attracting forces in **II** is observed, due to the shortening of the interatomic distances when lowering the temperature (see the example for (Mn) in Figure S3). The detailed analysis of these forces is devoted to the HB interactions, with respect to the Jeffrey "cut-off" distance criterium (H···A < 2.83 Å for N−H···Cl).[45] For all compounds, the **I** → **II** PT provokes an increase in the number of the HBs, i.e., from 4 to 6 for (Mn, Co) and from 6 to 7 for (Ni) (Tables S5 and S6). Indeed, in **I**, the terminal NH_2 group of MHy^+ is not involved (Mn, Co) or weakly involved (Ni) in the creation of the HBs (Figure S3a), while in **II**, the N−H···Cl hydrogen bonding with both N(1) and N(2) donors occurs (Figure S3b).

Apart from the **I** → **II** PT, the existence of two different (N and Cl) atoms in the M^{II} coordination sphere causes distortion of the octahedral symmetry, which is confirmed by the angle variance (σ^2) and bond length distortion (Δd) parameters (Figure S4).

The powder XRD measurements were performed and followed by Pawley refinement (see Appendix 3 for details) in order to validate the structural model. There were some differences in peak intensities between the experimental and theoretical patterns, which may be caused by the textural effects and/or inadequate grinding of the sample before measurement (Figure S5).

Vibrational Properties. *RT Raman and IR Spectra and Assignment of Bands.* RT Raman and IR spectra are presented in Figure S6. The factor group analysis is presented in Appendix 4 and Table S7. The proposed assignment, presented in Table S8, is based on comparative analysis with literature sources including $MHyPbX_3$ and MHy_2PbX_4 (X = Cl, Br, I),[14−16,31,32] $MHyMn(H_2PO_2)_3$,[33,34] $MHyM^{II}(HCOO)_3$ (M^{II} = Mg, Fe, Mn, Zn),[35] as well as DFT calculations for the MHy^+ ion.[34] Bands corresponding to internal vibrations of MHy^+ are observed in characteristic ranges as reported in the literature.

It is well-known that the position of bands originating from stretching modes of NH_2/NH_2^+ directly correlates with the strength of HBs. Usually, a higher wavenumber of a band indicates weaker HBs.[36] For $MHyMnCl_3$, the highest IR (Raman) bands are observed at 3251 and 3130 (3224 and 3145) cm^{-1} (see Table S8). For Co, IR (Raman) bands are downshifted by 8 and 9 (14 and 15) cm^{-1}, respectively, while for Ni by 12 and 20 (20 and 16) cm^{-1}. One can therefore conclude that the HB strength increases in the order of Mn < Co < Ni. This is in good agreement with X-ray diffraction data showing that the length and number of short H···Cl contacts in **I** increase in the same manner (cf. Table S6).

Crystallographic data also showed that the structural parameters are similar for the Ni and Co compounds but differ significantly for the Mn analogue. As expected, the majority of IR and Raman bands are sensitive to these structural changes. Especially strong dependence of the type of metal cation is, however, observed for the MHy^+-cage mode, which appears in the IR spectra at 595, 563, and 515 cm^{-1} for Ni, Co, and Mn, respectively. Such a large downshift can be attributed to the increased space per formula unit (V_{fu}) able to accommodate MHy^+ cations, i.e., 158.4 $Å^3$ (Ni), 162.1 $Å^3$ (Co), and 171.2 $Å^3$ (Mn) (see Table 1). This observation is in line with the position of this mode and the volume per formula unit reported for other hybrid compounds with the MHy^+ cation. The lower the frequency of the MHy^+-cage mode, the greater the space for the cation in the crystal lattice, i.e., 184.80 $Å^3$ (488 cm^{-1}) for $MHyPbCl_3$, 209.18 $Å^3$ (309 cm^{-1}) for $MHyPbBr_3$, 223.36 $Å^3$ (237 cm^{-1}) for $MHyMn(HCOO)_3$, and 269.38 $Å^3$ (210 cm^{-1}) for $MHyMn(H_2PO_2)_3$.[32] This clear correlation is depicted for hybrids composed of MHy^+ in Figure S7. The value for $MHyMn(H_2PO_2)_3$ deviates from the linear dependence, probably due to the greater flexibility of the frameworks based on the hypophosphite ion.[37]

Temperature-Dependent IR and Raman Studies. To understand the mechanism of the **I** → **II** PT, IR and Raman spectra of $MHyMnCl_3$ were measured as a function of temperature from 80 to 400 K (see Figures S8 and S9). Minor changes upon cooling confirm that this is a second-order PT. It can be noticed, however, that a few bands appear below ca. 240 K. The observed splitting of other bands is rather weak, which is consistent with the PT within the same monoclinic point group C_{2h}.

For certain Raman and IR bands, the intensity increases strongly in phase **II**. Closer inspection reveals that the majority of bands exhibiting this behavior are attributed to the internal vibrations of the NH_2^+ group, i.e., Raman bands at 853 (ρNH_2^+) and 1583 cm^{-1} (δNH_2^+), as well as IR band at 1306

https://doi.org/10.1021/acs.jpcc.2c04893
J. Phys. Chem. C 2022, 126, 15809−15818

cm^{-1} corresponding to τNH_2^+. All these bands are very narrow at 80 K and are practically invisible at RT (see the intensity drop for the rocking mode presented in Figure S10). This suggests that the observed PT is HB-driven and excludes any type of disorder because the corresponding broadening of bands upon heating is weak.[38] Figure S3 demonstrates that in **I** both the amino groups form fewer HBs, and therefore, the MHy^+ cations are more loosely bound in the cage. The thermal evolution of the MHy-cage Raman mode, presented in Figure S11, leads to similar conclusions. The upshift for this band upon cooling is the strongest among other bands (ca. 20 cm^{-1}). This is accompanied by a very strong narrowing of these bands suggesting that the space available for MHy^+ is much lower in **II**, and cations are more tightly confined.

To further analyze the structural changes associated with the occurring PT, the exact parameters, position, and full-width-at-half-maximum (fwhm) of bands determined by spectral fitting were plotted as a function of temperature. The thermal dependencies of IR and Raman bands corresponding to the CNN ($CH_3-NH_2-NH_2$) skeleton are shown in Figure S12. Position and fwhm of Raman bands, assigned to stretching and bending vibrations of the skeleton, are weakly sensitive to PT. This implies that the MHy^+ ions do not experience any pronounced conformational or reorientational changes during PT. Similarly, the results of fitting obtained for internal modes of methyl groups revealed weak changes (see Figure S13).

In contrast to methyl groups, the terminal NH_2 and the middle NH_2^+ groups experience a stronger influence (Figures 4 and S14). A very interesting feature is that Raman bands corresponding to the δNH_2 and δNH_2^+ deformational vibrations exhibit 13.3 cm^{-1} downshift and 30.8 cm^{-1} upshift, respectively, when heated from 80 to 380 K. The corresponding change of fwhm for the δNH_2^+ mode is also very high, from 8.5 cm^{-1} at 80 K to 38.3 cm^{-1} at 380 K. Such a great variation suggests a completely different role in the PT mechanism. Indeed, this is expected since the nitrogen atom of the terminal group is directly coordinated by Mn^{2+} ions.

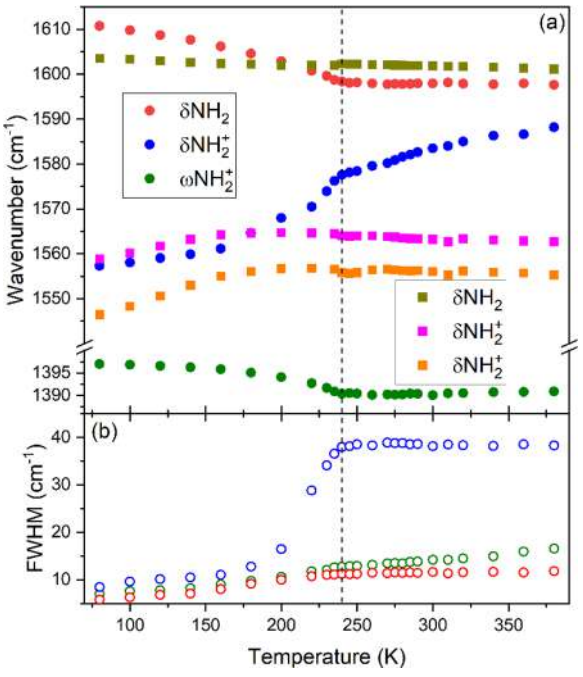

Figure 4. Thermal evolution of selected Raman (circles) and IR (squares) band positions (full symbols, left scale) and fwhms (open symbols, right scale) for $MHyMnCl_3$.

Optical Properties. Figures 5a and S15 present the absorption spectra of $MHyM^{II}Cl_3$ samples measured at 300 K. In the low wavelength range, all compounds reveal a broad intense band attributed to charge transfer. $MHyMnCl_3$ shows less intense absorption bands related to the d−d transitions, i.e., $^4E_g(^4D)$ (332 nm), $^4T_{2g}(^4D)$ (356 nm), $^4E_g(^4G)$, $^4A_{1g}(^4G)$ (422 nm), $^4T_{2g}(^4G)$ (463 nm), and $^4T_{1g}(^4G)$ (540 nm) from the $^6A_{1g}(^6S)$ ground state.[39] Moreover, two additional bands at 239 and 263 nm, probably corresponding to the exciton absorption and the transitions between p orbitals of carbon and chlorine, are observed.[40] The $MHyNiCl_3$ crystals exhibit absorption bands ascribed to the following transitions: $^3T_{1g}(P)$ (447 nm), $^1T_{2g}(D)$ (517 nm) $^3T_{1g}(F)$ (794 nm), and $^3T_{2g}(F)$ (1285 nm) from the $^3A_{2g}(F)$ ground state.[41] The $MHyCoCl_3$ crystals present absorption bands attributed to the transitions: $^2A_{1g}(G)$, $^2T_{1g}(P, H)$ (415 nm), $^4T_{1g}(P)$, $^2T_{2g}$ $^2T_{1g}(G)$, $^4A_{2g}(F)$ (617 nm), $^2E_g(G)$ (762 nm), and $^4T_{2g}(F)$ (1622 nm) from the $^4T_{1g}(F)$ ground state.[41] The first and second overtones of the CH and NH vibrational modes correspond to the weak bands in the 1081−1156 and 1258−1445 nm ranges as well as the medium intensity bands in the 1584−1998 nm range. The strong absorption bands above 2000 nm are related to the combinational modes of the organic cation.

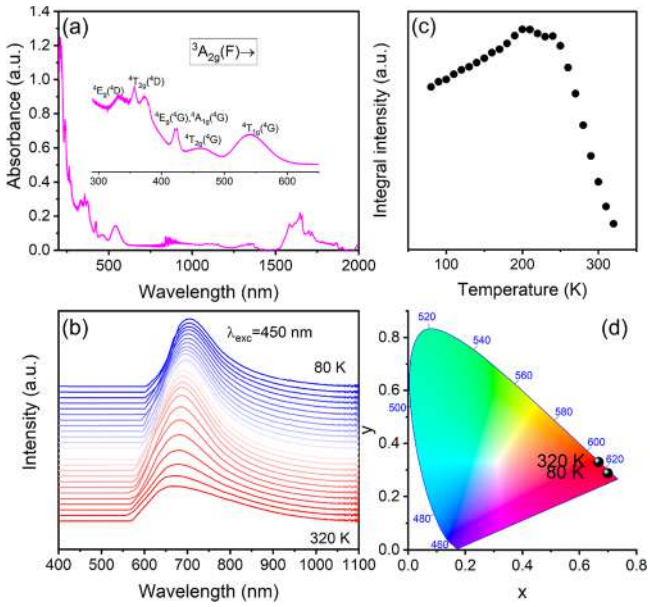

Figure 5. The absorption spectrum of the $MHyMnCl_3$ crystals (a), the temperature-dependent emission spectra (b), the integral emission intensity of the $MHyMnCl_3$ crystals registered under 450 nm excitation (c), and the CIE chromaticity diagram (d).

Based on the above measurements, the values of the energy band gap (E_g) were calculated for all samples using Kubelka−Munk relation:

$$F(R) = \frac{(1-R)^2}{2R}$$

where R symbolizes reflectance. The estimated values of E_g were 5.34 (Mn), 3.96 (Ni), and 3.64 eV (Co) (see Figure S16 and Table 1).

The investigations of the optical properties of the studied materials included measurements of their emission intensity as

https://doi.org/10.1021/acs.jpcc.2c04893
J. Phys. Chem. C 2022, 126, 15809−15818

a function of temperature are presented in Figures 5b (Mn) and S17 (Ni). Unfortunately, no luminescence from the $MHyCoCl_3$ crystals under 532 nm excitation was detected. Figure 5b shows that $MHyMnCl_3$ crystals reveal intense emission at low temperatures in the red spectral region with the maximum at 706 nm under 450 nm excitation ascribed to the $^4T_{1g}(G) \rightarrow {}^6A_{1g}(S)$ transition of Mn^{2+} ions in the octahedral field.[33] It can be noticed that the increase in temperature leads to a blueshift of the band maximum associated with the change of the crystal field strength.[39] Moreover, the heating from 80 to 230 K leads to an initial increase in the emission intensity, followed by the luminescence quenching beyond 230 K (Figure 5c). This behavior is most likely related to the presence of the second-order PT at 243 K. The CIE chromaticity diagram demonstrates pure red color of the $MHyMnCl_3$ crystals under 450 nm excitation (Figure 5d). It was found that the temperature has a negligible impact on the color change. Figure S17a shows that $MHyNiCl_3$ crystals exhibit broadband emission in the visible spectral range with two maxima at 478 and 550 nm upon 375 nm excitation attributed to the $^3T_{1g}(P) \rightarrow {}^3A_{2g}(F)$ and $^1T_{2g}(D) \rightarrow {}^3A_{2g}(F)$ transitions of Ni^{2+} ions with octahedral coordination, respectively.[42,43] In contrast to the Mn analogue, heating from 80 K leads to a redshift of the band maximum, indicating a change in the crystal field strength.[39] Figure S17b,c shows that as the temperature increases, the emission intensity gradually decreases. Furthermore, it can be seen in Figure S17a that the $^3T_{1g}(P) \rightarrow {}^3A_{2g}(F)$ transition weakens, probably due to the PT.

The analysis of the thermal kinetics of the $MHyMnCl_3$ and $MHyNiCl_3$ crystals was performed, taking the following equation:[42]

$$I = \frac{I_0}{1 + \frac{\Gamma_0}{\Gamma_v} e^{-\Delta E/kT}}$$

where I and I_0 present the intensity and the initial intensity at low temperature, respectively. Γ_v and Γ_0 are radiative decay rate and attempt rate for thermal quenching, respectively. Finally, ΔE symbolizes the activation energy for thermal quenching. In order to determine ΔE, the above formula was recalculated as follows:[12]

$$\frac{\Delta E}{kT} = -\ln\left(\frac{I_0}{I} - 1\right) + \ln\left(\frac{\Gamma_0}{\Gamma_v}\right)$$

where ΔE is the slope of $\ln\left(\frac{I_0}{I} - 1\right)$ in the $1/kT$ function and $\ln\left(\frac{\Gamma_0}{\Gamma_v}\right)$ represents a constant. Based on results, the activation energy E_a for the $MHyMnCl_3$ and $MHyNiCl_3$ crystals was calculated to be 299 and 49 meV, respectively (Figure S18 and Table 1).

The luminescence decay profiles recorded for the investigated samples at 80 K are presented in Figure S19. The curve obtained for the $MHyMnCl_3$ crystals can be well fitted by a single exponential function with a lifetime value equal to τ = 124 μs. Because in the emission spectra of the $MHyNiCl_3$ crystals two bands can be distinguished, the photoluminescence decay profiles were recorded for both of them. In both cases, the curves were well fitted by a double exponential function with lifetime values equal to τ_1 = 1.02 ns, τ_2 = 7.15 ns and τ_1 = 0.21 ns, τ_2 = 2.19 ns for λ_{em} = 478 nm and λ_{em} = 550 nm, respectively. The presence of the short component indicates the occurrence of nonradiative processes in the $MHyNiCl_3$ crystals.

The mechanism of energy transfer probably includes a population of higher excited levels of transition metal ions during laser diode irradiation. The electrons are then transported nonradiatively to their emission levels. Subsequently, the electrons relax in a radiative manner to the ground state of the transition metal ions, producing visible luminescence. Further theoretical calculations, however, are required to support this idea.

Magnetic Properties. Results of magnetic properties measurements carried out for $MHyMnCl_3$ are displayed in Figure 6. The inverse magnetic susceptibility χ^{-1} of the compound exhibits linear behavior (characteristic of Curie-like

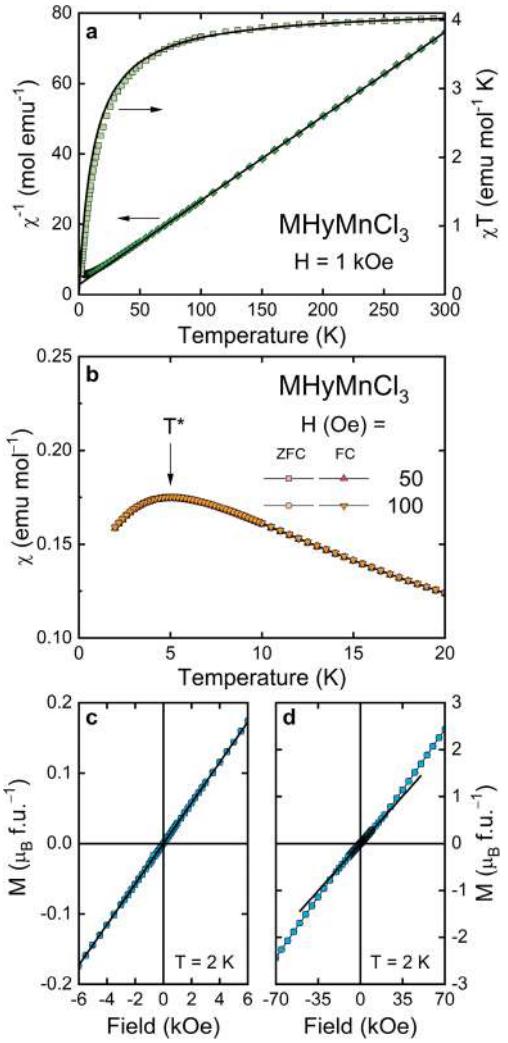

Figure 6. (a) Inverse DC magnetic susceptibility χ^{-1} (left axis) and a product χT (right axis) of $MHyMnCl_3$ measured as a function of temperature in a constant magnetic field H; thick solid lines are a fit of the Curie–Weiss law to the experimental data (for details see the text). (b) Low-temperature susceptibility χ measured in two different magnetic fields in the ZFC and FC; the arrow marks a characteristic temperature T^*. (c, d) Magnetization M (expressed in a unit of a magnetic moment) as a function of increasing and decreasing magnetic field (circle- and square-shaped symbols, respectively) plotted in two different field ranges; solid lines show the linear behavior of the experimental curve in low fields.

https://doi.org/10.1021/acs.jpcc.2c04893
J. Phys. Chem. C 2022, 126, 15809−15818

paramagnets) almost in the entire temperature range studied (Figure 6a, left axis). The least-squares fit of the Curie–Weiss law $\chi(T) = C/(T - \theta_p)$ to the experimental data above about 50 K yielded the parameters $C = 4.18(1)$ emu mol^{-1} K and $\theta_p = -11.7(2)$ K (see the thick solid line in Figure 6a). The effective magnetic moment μ_{eff} derived from the Curie constant C as $\mu_{eff} = \sqrt{8C}$ is equal to 5.78(1) μ_B, which is close to the theoretical value of 5.92 μ_B calculated within the Russel–Saunders coupling scheme for a free Mn^{2+} ion with the electron configuration $3d^5$ ($S = 5/2$, $L = 0$, $J = 5/2$, $g_J = 2$) as $\mu_{eff} = g_J\sqrt{J(J+1)}\ \mu_B$. The negative value of the paramagnetic Curie–Weiss temperature θ_p suggests the presence of predominantly antiferromagnetic coupling between the magnetic moments of Mn^{2+}.

Analysis of temperature variation of the product χT (see Figure 6a, right axis) leads to similar conclusions. First, at RT χT achieves a value of about 4.03 emu mol^{-1} K, which is close to the experimental C given above and to its theoretical value expected for Mn^{2+} ions, i.e., $C = \frac{1}{8}\mu^2_{Mn2+} = \frac{1}{8}5.92^2 = 4.38$ emu mol^{-1} K. Second, upon lowering temperature, the $\chi T(T)$ curve clearly bends toward lower values, which is characteristic of systems exhibiting antiferromagnetic interactions between the magnetic moments.

Figure 6b displays magnetic susceptibility of $MHyMnCl_3$ at low temperatures. As seen, below about 10 K, the curvature of $\chi(T)$ changes, and the susceptibility exhibits a broad maximum located at T^* of about 5 K. The shape and the position of that maximum do not depend in low field on its magnitude, and the ZFC and FC curves do not show any bifurcation, which suggests an occurrence at T^* of an antiferromagnetic ordering in the presence of high crystallographic disorder, rather than a formation of a spin-glass-like state. Field dependence of the magnetization of $MHyMnCl_3$ (Figure 6c,d) is in line with the postulated antiferromagnetic character of the transition observed in $\chi(T)$ at T^*. In particular, M is linear in H up to the highest field studied, exhibiting only a hardly visible change of the slope above about 5 kOe (see the guiding solid line in Figure 6c,d) and achieves at 70 kOe a value of about 2.43 μ_B, being far from a value of the ordered magnetic moment of Mn^{2+} (i.e., $\mu_{ord} = g_J J = 5\ \mu_B$).

Analogous experiments and data analysis were also carried out for the compounds $MHyCoCl_3$ and $MHyNiCl_3$. In contrast to the analogue with Mn, they were found to exhibit very distinct, sharp antiferromagnetic phase transitions at the same Néel temperature of about 3.7 K. In weak magnetic fields, their magnetization is linearly dependent on the magnetic field, as expected for antiferromagnets. In higher fields, it increases sharply and shows a clear tendency to saturation, suggesting the occurrence of a metamagnetic transition from the antiferromagnetic alignment of the moments to a field-induced ferromagnetism (or rather, polarized paramagnetism). A full description of the magnetic properties of $MHyCoCl_3$ and $MHyNiCl_3$ can be found in Appendix 5.

Influence of M^{II} on the Physicochemical Properties and T_c. Despite many similarities, the physicochemical properties of the reported compounds vary from each other. The only factor, which should influence these properties, is M^{II}. According to Shannon, the effective ionic radii of Ni^{2+}, Co^{2+}, and Mn^{2+} in high spin configuration are 69.0, 74.5, and 83.0 pm, respectively.[44] All metals exhibit different values of electronegativity and hence ionic character of M^{II}–Cl and M^{II}–N bonds. In the Allen scale, the electronegativity of Ni, Co, and Mn increases from the left to the right side of the period in the periodic table in opposition to ionic radii.

Even though all $MHyM^{II}Cl_3$ compounds crystallize in the same space group, variations in the geometric parameters are observed (Figures 7a–d and S20a–d). With increasing ionic radius (decreasing electronegativity), and thus the increasing ionic character of M^{II}–Cl and M^{II}–N(1) bonds, the unit cell expands (Figures 7a,b and S20ab) due to the increased distortion of the $[M^{II}Cl_5N]$ inorganic framework (Figure S4) and increase of the β angle (Figures 7c and S20c). Moreover, the distance between the M^{II} cation and N(1) atom increases (Figures 7d and S20d).

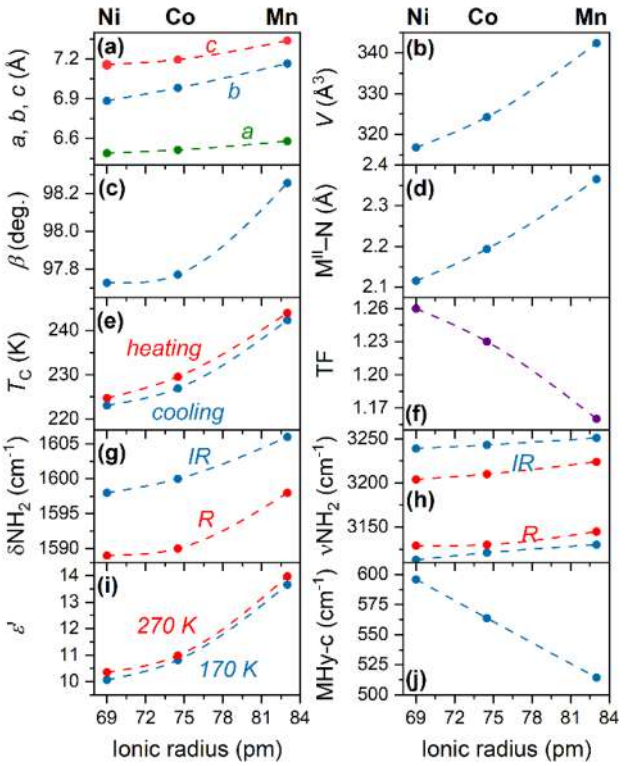

Figure 7. Lattice parameters (a), cell volume (b), beta angle (c), M^{II}–N distance (d), temperature of PT T_c (e), tolerance factor TF (f), δNH_2 band position (g), νNH_2 band position (h), dielectric permittivity ε' (i), and the position of MHy-cage mode (j) as a function of M^{II} ionic radius.

The above differences have a non-negligible influence on the N–H···Cl interactions. With the unit cell expansion, the strength of these interactions weakens. This provides a conclusion that longer D···A distance causes lower stability of HB motifs. This finding is in line with IR and Raman spectroscopic results, which clearly demonstrate a decrease in HB strength as the unit cell expands. The bands related to HB strength shift toward higher wavenumbers for the bigger ions, as can be observed in Figures 7g,h and S20g,h.

Therefore, a crystal with a larger unit cell should experience a PT at higher temperatures, as shown by DSC measurements (Figures 7e and S20e, Table 1), demonstrating that $MHyMnCl_3$ has the highest T_c and $MHyNiCl_3$ has the lowest. In other words, T_c correlates directly with increasing ionic character of M^{II}–Cl and M^{II}–N bonds. It is worth noting that changes in PT temperatures are more linear in the function of electronegativity than in the function of ionic radius. A similar

https://doi.org/10.1021/acs.jpcc.2c04893
J. Phys. Chem. C 2022, 126, 15809–15818

temperature dependence was observed for 3D metal-formate frameworks comprising the MHy^+ cation.[35] In $MHyM^{II}(HCOO)_3$ (M^{II} = Zn, Fe, Mn), the temperature of a PT increases with the ionic radius of these cations.

The presented composition of $MHyM^{II}Cl_3$ differs from the typical hybrid perovskite alignment consisting of an inorganic framework and organic cation rotating inside the voids, as well as from the lead halide counterparts with MHy^+.[2,12] This behavior can be explained by considering TF.[45] A combination of MHy^+ cation with relatively small ionic radius of M^{II} induces TF values much larger than 1 (1.26, 1.23, and 1.16 for Ni, Co, and Mn, respectively), and thus, an archetypical perovskite structure cannot be achieved (see Table 1). Instead, several chain structures with both Cl and N atoms cocreating a metal coordination sphere can be found in the literature.[20,25,26,46] The dependence of TF as a function of ionic radius and the electronegativity is nearly linear (see Figures 7f and S20f).

The analysis of the value of the real part of the dielectric permittivity at 170 and 270 K for a frequency equal to 1 MHz confirmed the tendency that the ε' value increases with the higher ionic radius and ionic character of the M^{II}−Cl and M^{II}−N bonds (Figures 7i and S20i). Furthermore, the position of the MHy-cage mode is also compatible with the higher dielectric response for Mn (Figures 7j and S20j). The more available space the cation has accessible, the lower the energy of the cage mode is observed. The PT is observed at the highest T_c for Mn because the unit cell of $MHyMnCl_3$ has the largest volume and the most ionic coordination bonds, while the MHy^+ cation has the largest accessible volume and is the least tightly bound.

There is no linear dependency between the temperature of magnetic ordering and band gap as a function of ionic radius or electronegativity. According to the literature,[47] the band gap is rather dependent on the structure of energy levels in metal cations and on A-site cations, than on the ionic radius and electronegativity of the used metal.

Mechanism of Phase Transition. The $P2_1/m(\mathbf{I}) \rightarrow P2_1/n(\mathbf{II})$ second-order *klassengleiche* structural PT at T_c is entropy-driven and controlled by variations in the arrangement of HBs. The mechanism of PT includes a minor distortion of the metal-chloride chains, particularly the geometry of M^{II}-Cl bonds, in addition to the doubling of the unit cell in **II** and the removal of the mirror plane *m*. Because the M^{II}−N distances essentially remain unchanged (Figure S21a), the shrinking of the $[M^{II}Cl_5N]$ octahedra, variations of the bond length distortion index (Δd), and decreased bond angle variance (σ^2), presented in Figures S21b−d, apply only to M^{II}−Cl distances, as well as *cis* and *trans* Cl−Mn−Cl angles.

Subtle structural changes of the octahedra are accompanied by a slow increase in the strength of H-bonding and a higher number of HB contacts in **II**. This effect stabilizes the phase II and is responsible for stronger binding of the MHy^+ cation, which was evidenced by the unusually strong upshift of the MHy^+-cage mode. Furthermore, vibrational data showed that PT is associated with rearrangement of HBs without co-occurring conformational changes of the organic cation or molecular ordering. The nitrogen atom coordinating the first sphere of the metal cation in $MHyM^{II}Cl_3$ somewhat restricts the typical cation dynamics observed in hybrid materials.[24]

CONCLUSIONS

We reported the synthesis and properties of a series of novel $MHyNiCl_3$, $MHyCoCl_3$, and $MHyMnCl_3$ perovskitoids. All analogues crystallize in the $P2_1/m$ (HT phase) space group and undergo second-order *klassengleiche* PT to other monoclinic $P2_1/n$ symmetry at 224, 229, and 243 K respectively. All the described compounds are composed of chains of edge-sharing $[MCl_5N]$ octahedra, where the nitrogen atom comes from the terminal NH_2 group of MHy^+. This is a rare and untypical coordination for hybrid materials. The occurring second-order PT is driven by structural changes of the $[MCl_5N]$ chains (vanishing of the mirror plane), rearrangement of HBs, and different confinement of MHy^+ cations. The mechanism of the PT was elucidated using DSC, X-ray diffraction measurements, dielectric, and IR and Raman spectroscopy.

There is a clear relationship between structural properties, like lattice parameters, cell volume, and value of the β angle with electronegativity of the used metal, or ionic character of the M^{II}−Cl and M^{II}−N bonds. Raman spectroscopy revealed that the MHy-cage mode is very sensitive to the space available for the cation and its confinement in the crystal lattice.

The absorption spectra showed that the $MHyM^{II}Cl_3$ crystals exhibit typical bands characteristic for metal centers in octahedral environment. Based on these measurements, the band gap energies were estimated to be 5.34, 3.96, and 3.64 eV for M^{II} = Mn, Ni and Co, respectively. The Mn and Ni analogues exhibit red and yellowish-green to orange emission under the 450 and 375 nm excitation, respectively. From the dependence of the emission intensity on temperature, the activation energy of the nonradiative deactivation through the thermal quenching process was estimated to be 299 meV for $MHyMnCl_3$ and 49 meV for $MHyNiCl_3$. Unfortunately, no luminescence from the $MHyCoCl_3$ crystals was detected.

Magnetic measurements showed that $MHyCoCl_3$ and $MHyNiCl_3$ order antiferromagnetically below the same Néel temperature of about 3.7 K. The noticeable interplay of antiferromagnetic and ferromagnetic correlations leads in both systems to metamagnetic PTs in H of about 1 kOe. In turn, the compound with Mn shows only smeared antiferromagnetic ordering at about 5.0 K with no trace of ferromagnetic correlations up to the highest field studied.

ASSOCIATED CONTENT

Supporting Information

The Supporting Information is available free of charge at https://pubs.acs.org/doi/10.1021/acs.jpcc.2c04893.

Additional information regarding single-crystal XRD, method of calculating ΔS, selection rules and factor group analysis, description of magnetic properties for $MHyCoCl_3$ and $MHyNiCl_3$, DSC traces, histograms representing M^{II}-NH_2 coordination bonds, comparison of the interatomic forces in $MHyMnCl_3$ in phase **I** and **II**, octahedra angle variance and bond length distortion as a function of ionic radius, powder XRD patterns before and after Pawley fitting, Raman and IR spectra, the wavenumber dependence of the MHy-cage mode for hybrid compounds, temperature-dependent IR and Raman spectra for $MHyMnCl_3$, position and width of the MHy-cage modes, CCN, CH_3, NH_2, and NH_2^+ modes as a function of temperature, absorption spectra, band gap energies, temperature-dependent emission spectra, and their intensity for $MHyNiCl_3$, CIE chromaticity diagram, activation energies, luminescence decay profiles, lattice parameters, cell volume, beta angle,

https://doi.org/10.1021/acs.jpcc.2c04893
J. Phys. Chem. C 2022, 126, 15809−15818

M^{II}−N distance, T_c, TF, δNH_2 band position, νNH_2 band position, dielectric permittivity, and the position of the MHy-cage mode as a function of Allen electronegativity, the variation of M^{II}−N distance, volume of octahedra, bond length distortion index, and bond angle variance in **I** and **II**, fragment of reciprocal space of $MHyNiCl_3$ measured at 100 K, change of the unit cell choice for **I** and **II**, magnetic properties of $MHyCoCl_3$ and $MHyCoCl_3$, experimental details of single crystal XRD, selected geometric parameters, HB parameters, assignment of IR and Raman bands (PDF)

Crystal structure of $MHyMnCl_3$ at 295 K (CIF)

Crystal structure of $MHyMnCl_3$ at 100 K (CIF)

Crystal structure of $MHyCoCl_3$ at 295 K (CIF)

Crystal structure of $MHyCoCl_3$ at 120 K (CIF)

Crystal structure of $MHyNiCl_3$ at 295 K (CIF)

Crystal structure of $MHyNiCl_3$ at 100 K (CIF)

AUTHOR INFORMATION

Corresponding Author

Jan A. Zienkiewicz − *Institute of Low Temperature and Structure Research, Polish Academy of Sciences, 50-422 Wroclaw, Poland;* orcid.org/0000-0002-4268-0177; Email: j.zienkiewicz@intibs.pl

Authors

Maciej Ptak − *Institute of Low Temperature and Structure Research, Polish Academy of Sciences, 50-422 Wroclaw, Poland*

Dawid Drozdowski − *Institute of Low Temperature and Structure Research, Polish Academy of Sciences, 50-422 Wroclaw, Poland;* orcid.org/0000-0001-5918-5503

Katarzyna Fedoruk − *Institute of Physics, Wrocław University of Science and Technology, 50-370 Wrocław, Poland;* orcid.org/0000-0001-7485-7144

Mariusz Stefanski − *Institute of Low Temperature and Structure Research, Polish Academy of Sciences, 50-422 Wroclaw, Poland;* orcid.org/0000-0001-7864-6002

Adam Pikul − *Institute of Low Temperature and Structure Research, Polish Academy of Sciences, 50-422 Wroclaw, Poland*

Complete contact information is available at: https://pubs.acs.org/10.1021/acs.jpcc.2c04893

Notes

The authors declare no competing financial interest.

ACKNOWLEDGMENTS

The authors would like to acknowledge M.Sc. E. Bukowska for performing XRD measurements and Dr. D. Kowalska for performing Pawley refinement of the obtained results.

REFERENCES

(1) Fu, A.; Yang, P. Lower Threshold for Nanowire Lasers. *Nat. Mater.* **2015**, *14* (6), 557−558.

(2) Maczka, M.; Ptak, M.; Gagor, A.; Stefańska, D.; Zareba, J. K.; Sieradzki, A. Methylhydrazinium Lead Bromide: Noncentrosymmetric Three-Dimensional Perovskite with Exceptionally Large Framework Distortion and Green Photoluminescence. *Chem. Mater.* **2020**, *32* (4), 1667−1673.

(3) Brenner, T. M.; Egger, D. A.; Kronik, L.; Hodes, G.; Cahen, D. Hybrid Organic-Inorganic Perovskites: Low-Cost Semiconductors with Intriguing Charge-Transport Properties. *Nat. Rev. Mater.* **2016**, *1*, 15007.

(4) Maczka, M.; Ptak, M.; Kojima, S. Brillouin Scattering Study of Ferroelectric Transition Mechanism in Multiferroic Metal-Organic Frameworks of $[NH_4][Mn(HCOO)_3]$ and $[NH_4][Zn(HCOO)_3]$. *Appl. Phys. Lett.* **2014**, *104* (22), 222903.

(5) Li, W.; Zhang, Z.; Bithell, E. G.; Batsanov, A. S.; Barton, P. T.; Saines, P. J.; Jain, P.; Howard, C. J.; Carpenter, M. A.; Cheetham, A. K. Ferroelasticity in a Metal-Organic Framework Perovskite; Towards a New Class of Multiferroics. *Acta Mater.* **2013**, *61* (13), 4928−4938.

(6) Wang, K.; Xiong, J. B.; Xia, B.; Wang, Q. L.; Tong, Y. Z.; Ma, Y.; Bu, X. H. Ferroelastic Phase Transition and Switchable Dielectric Constant in Heterometallic Niccolite Formate Frameworks. *Inorg. Chem.* **2018**, *57* (2), 537−540.

(7) Nagabhushana, G. P.; Shivaramaiah, R.; Navrotsky, A. Thermochemistry of Multiferroic Organic-Inorganic Hybrid Perovskites $[(CH_3)_2NH_2][M(HCOO)_3]$ (M = Mn, Co, Ni, and Zn). *J. Am. Chem. Soc.* **2015**, *137* (32), 10351−10356.

(8) Wojcik, N. A.; Kowalska, D. A.; Trzebiatowska, M.; Jach, E.; Ostrowski, A.; Bednarski, W.; Gusowski, M.; Staniorowski, P.; Cizman, A. Tunable Dielectric Switching of (Quinuclidinium)-$[MnCl_4]$ Hybrid Compounds. *J. Phys. Chem. C* **2021**, *125* (30), 16810−16818.

(9) Wang, Z.; Hu, K.; Gao, S.; Kobayashi, H. Formate-Based Magnetic Metal-Organic Frameworks Templated by Protonated Amines. *Adv. Mater.* **2010**, *22* (13), 1526−1533.

(10) Sun, X.; Li, P.; Liao, W.; Wang, Z.; Gao, J.; Ye, H.; Zhang, Y. Notable Broad Dielectric Relaxation and Highly Efficient Red Photoluminescence in a Perovskite-Type Compound: (N-Methylpyrrolidinium)$MnCl_3$. *Inorg. Chem.* **2017**, *56*, 12193−12198.

(11) Lou, F.; Gu, T.; Ji, J.; Feng, J.; Xiang, H. Tunable Spin Textures in Polar Antiferromagnetic Hybrid Organic - Inorganic Perovskites by Electric and Magnetic Fi Elds. *npj Comput. Mater.* **2017**, 1−9.

(12) Mączka, M.; Gagor, A.; Zareba, J. K.; Stefanska, D.; Drozd, M.; Balciunas, S.; Šimėnas, M.; Banys, J.; Sieradzki, A. Three-Dimensional Perovskite Methylhydrazinium Lead Chloride with Two Polar Phases and Unusual Second-Harmonic Generation Bistability above Room Temperature. *Chem. Mater.* **2020**, *32* (9), 4072−4082.

(13) Drozdowski, D.; Gagor, A.; Stefańska, D.; Zareba, J. K.; Fedoruk, K.; Maczka, M.; Sieradzki, A. Three-Dimensional Methylhydrazinium Lead Halide Perovskites: Structural Changes and Effects on Dielectric, Linear, and Nonlinear Optical Properties Entailed by the Halide Tuning. *J. Phys. Chem. C* **2022**, *126* (3), 1600−1610.

(14) Drozdowski, D.; Gagor, A.; Maczka, M. Methylhydrazinium Lead Iodide - One Dimensional Chain Phase with Excitonic Absorption and Large Energy Band Gap. *J. Mol. Struct.* **2022**, *1249*, 131660.

(15) Maczka, M.; Zareba, J. K.; Gagor, A.; Stefańska, D.; Ptak, M.; Roleder, K.; Kajewski, D.; Soszyński, A.; Fedoruk, K.; Sieradzki, A. $[Methylhydrazinium]_2PbBr_4$, a Ferroelectric Hybrid Organic-Inorganic Perovskite with Multiple Nonlinear Optical Outputs. *Chem. Mater.* **2021**, *33* (7), 2331−2342.

(16) Maczka, M.; Ptak, M.; Gagor, A.; Stefańska, D.; Sieradzki, A. Layered Lead Iodide of $[Methylhydrazinium]_2PbI_4$ with a Reduced Band Gap: Thermochromic Luminescence and Switchable Dielectric Properties Triggered by Structural Phase Transitions. *Chem. Mater.* **2019**, *31* (20), 8563−8575.

(17) Li, X.; Cuthriell, S. A.; Bergonzoni, A.; Dong, H.; Traore, B.; Stoumpos, C. C.; Guo, P.; Even, J.; Katan, C.; Schaller, R. D.; Kanatzidis, M. G. Expanding the Cage of 2D Bromide Perovskites by Large A-Site Cations. *Expanding the Cage of 2D Bromide Perovskites by Large A - Site Cations.* **2022**, *34*, 1132.

(18) Stoumpos, C. C.; Mao, L.; Malliakas, C. D.; Kanatzidis, M. G. Structure-Band Gap Relationships in Hexagonal Polytypes and Low-Dimensional Structures of Hybrid Tin Iodide Perovskites. *Inorg. Chem.* **2017**, *56* (1), 56−73.

(19) Li, X.; He, Y.; Kepenekian, M.; Guo, P.; Ke, W.; Even, J.; Katan, C.; Stoumpos, C. C.; Schaller, R. D.; Kanatzidis, M. G. Three-

Dimensional Lead Iodide Perovskitoid Hybrids with High X-Ray Photoresponse. *J. Am. Chem. Soc.* **2020**, *142* (14), 6625−6637.
(20) Sreenivasa Kumar, N. R.; Nethaji, M.; Patil, K. C. Synthesis, Characterization and Structure of $(N_2H_5)_3MnX_5$ (X = Cl and Br). *J. Coord. Chem.* **1991**, *24* (4), 333−337.
(21) Goedken, V. L.; Vallarino, L. M.; Quagliano, J. V. Cationic Ligands. Coordination of the 1,1,1-Trimethylhydrazinium Cation to Nickel (II). *Inorg. Chem.* **1971**, *10* (12), 2682−2685.
(22) Dolomanov, O. V.; Bourhis, L. J.; Gildea, R. J.; Howard, J. A. K.; Puschmann, H. OLEX2: A Complete Structure Solution, Refinement and Analysis Program. *J. Appl. Crystallogr.* **2009**, *42* (2), 339−341.
(23) Sheldrick, G. M. SHELXT - Integrated Space-Group and Crystal-Structure Determination. *Acta Crystallogr. Sect. A Found. Adv.* **2015**, *71* (1), 3−8.
(24) Ptak, M.; Sieradzki, A.; Simenas, M.; Maczka, M. Molecular Spectroscopy of Hybrid Organic - Inorganic Perovskites and Related Compounds. *Coord. Chem. Reviews* **2021**, *448*, 214180.
(25) Zhao, H.; Bodach, A.; Heine, M.; Krysiak, Y.; Glinnemann, J.; Alig, E.; Fink, L.; Schmidt, M. U. 4-Cyanopyridine, a Versatile Mono- and Bidentate Ligand. Crystal Structures of Related Coordination Polymers Determined by X-Ray Powder Diffraction. *CrystEngComm* **2017**, *19* (16), 2216−2228.
(26) Heine, M.; Fink, L.; Schmidt, M. U. Coordination Compounds Built up from $M^{II}Cl_2$ and 3-Cyanopyridine: Double Chains, Single Chains and Isolated Complexes. *CrystEngComm* **2019**, *21* (29), 4305−4318.
(27) Stucky, G. D. The Crystal Structure of $(CH_3)_4NNiCl_3$. *Acta Crystallogr.* **1967**, *B24*, 330−337.
(28) Caputo, R. E.; Roberts, S.; Willett, R. D.; Gerstein, B. C. Crystal Structure and Magnetic Susceptibility of $[(CH_3)_3NH]_3Mn_2Cl_7$. *Inorg. Chem.* **1976**, *15* (4), 820−823.
(29) Lee, T.; Straus, D. B.; Devlin, K. P.; Gui, X.; Louka, P.; Xie, W.; Cava, R. J. *Antiferromagnetic to Ferromagnetic Coupling Crossover in Hybrid Nickel Chain Perovskites.* **2022**, *61*, 10486.
(30) Paufler, P. *International Tables for Crystallography*; Hahn, T., Ed.; Kluwer Academic Publishers: Dordrecht, 2002; Vol. A. 5t..
(31) MacZka, M.; Ptak, M.; Vasconcelos, D. L. M.; Giriunas, L.; Freire, P. T. C.; Bertmer, M.; Banys, J.; Simenas, M. NMR and Raman Scattering Studies of Temperature-and Pressure-Driven Phase Transitions in $CH_3NH_2NH_2PbCl_3$ Perovskite. *J. Phys. Chem. C* **2020**, *124* (49), 26999−27008.
(32) Maczka, M.; Zienkiewicz, J. A.; Ptak, M. Comparative Studies of Phonon Properties of Three-Dimensional Hybrid Organic-Inorganic Perovskites Comprising Methylhydrazinium, Methylammonium, and Formamidinium Cations. *J. Phys. Chem. C* **2022**, *126* (8), 4048−4056.
(33) Maczka, M.; Gagor, A.; Pikul, A.; Stefańska, D. Novel Hypophosphite Hybrid Perovskites of $[CH_3NH_2NH_2][Mn(H_2POO)_3]$ and $[CH_3NH_2NH_2][Mn(H_2POO)_{2.83}(HCOO)_{0.17}]$ Exhibiting Antiferromagnetic Order and Red Photoluminescence. *RSC Adv.* **2020**, *10* (32), 19020−19026.
(34) Ciupa-Litwa, A.; Ptak, M.; Kucharska, E.; Hanuza, J.; Maczka, M. Vibrational Properties and DFT Calculations of Perovskite-Type Methylhydrazinium Manganese Hypophosphite. *Molecules* **2020**, *25* (21), 5215.
(35) Maczka, M.; Gagor, A.; Ptak, M.; Paraguassu, W.; Da Silva, T. A.; Sieradzki, A.; Pikul, A. Phase Transitions and Coexistence of Magnetic and Electric Orders in the Methylhydrazinium Metal Formate Frameworks. *Chem. Mater.* **2017**, *29* (5), 2264−2275.
(36) Sobczyk, L.; Obrzud, M.; Filarowski, A. H/D Isotope Effects in Hydrogen Bonded Systems. *Molecules* **2013**, *18*, 4467−4476.
(37) Wu, Y.; Binford, T.; Hill, J. A.; Cheetham, A. K.; Shaker, S. Hypophosphite Hybrid Perovskites : A Platform for Unconventional Tilts and Shifts. *Chem. Commun.* **2018**, *1* (c), 2−5.
(38) Mączka, M.; Gągor, A.; Macalik, B.; Pikul, A.; Ptak, M.; Hanuza, J. Order-Disorder Transition and Weak Ferromagnetism in the Perovskite Metal Formate Frameworks of $[(CH_3)_2NH_2][M(HCOO)_3]$ and $[(CH_3)_2ND_2][M(HCOO)_3]$ (M = Ni, Mn). *Inorganic Chemistry.* **2014**, *53*, 457−467.
(39) Li, M.; Smetana, V.; Wilk-Kozubek, M.; Mudryk, Y.; Alammar, T.; Pecharsky, V. K.; Mudring, A. V. Open-Framework Manganese(II) and Cobalt(II) Borophosphates with Helical Chains: Structures, Magnetic, and Luminescent Properties. *Inorg. Chem.* **2017**, *56* (18), 11104−11112.
(40) Hu, Y.; Zhang, H.; Chong, W. K.; Li, Y.; Ke, Y.; Ganguly, R.; Morris, S. A.; You, L.; Yu, T.; Sum, T. C.; Long, Y.; Fan, H. J. *Molecular Engineering toward Coexistence of Dielectric and Optical Switch Behavior in Hybrid Perovskite Phase Transition Material.* **2018**, *122*, 6416.
(41) White, W. B.; McCarthy, G. J.; Scheetz, B. E. Optical Spectra of Chromium, Nickel, and Cobalt-Containing Pyroxenes. *Am. Mineral.* **1971**, *56*, 72−89.
(42) Zannoni, E.; Cavalli, E.; Toncelli, A.; Tonelli, M.; Bettinelli, M. Optical Spectroscopy of $Ca_3Sc_2Ge_3O_{12}:Ni^{2+}$. *J. Phys. Chem. Solids* **1999**, *60* (4), 449−455.
(43) Wang, S. F.; Gu, F.; Lü, M. K.; Song, C. F.; Xu, D.; Yuan, D. R.; Liu, S. W. Photoluminescence of Sol-Gel Derived $ZnTiO_3:Ni^{2+}$ Nanocrystals. *Chem. Phys. Lett.* **2003**, *373* (1−2), 223−227.
(44) Shannon, R. D. Revised Effective Ionic Radii and Systematic Studies of Interatomie Distances in Halides and Chaleogenides. *Acta Crystallogr., Sect. A* **1976**, *32*, 751−767.
(45) Burger, S.; Ehrenreich, M.; Kieslich, G. Tolerance Factors of Hybrid Organic-Inorganic Perovskites: Recent Improvements and Current State of Research Received. *J. Mater. Chem. A* **2018**, *6*, 21785−21793.
(46) Krysiak, Y.; Fink, L.; Bernert, T.; Glinnemann, J.; Kapuscinski, M.; Zhao, H.; Alig, E.; Schmidt, M. U. Crystal Structures and Polymorphism of Nickel and Copper Coordination Polymers with Pyridine Ligands. *Zeitschrift fur Anorg. und Allg. Chemie* **2014**, *640* (15), 3190−3196.
(47) Alkorta, I.; Elguero, J. A Theoretical Study of Perovskites Related to $CH_3NH_3PbX_3$ (X = F, Cl, Br, I). *New J. Chem.* **2018**, *42* (16), 13889−13898.

https://doi.org/10.1021/acs.jpcc.2c04893
J. Phys. Chem. C 2022, 126, 15809−15818

Novel Hybrid Organic-Inorganic Crystals of [Methylhydrazinium]$M^{II}Cl_3$ (M^{II}=Co, Ni, Mn)

Jan. A. Zienkiewicz,[*,†] Maciej Ptak,[†] Dawid Drozdowski,[†] Katarzyna Fedoruk,[‡] Mariusz Stefanski,[†] and Adam Pikul[†]

[†]Institute of Low Temperature and Structure Research, Polish Academy of Sciences, Okólna 2, 50-422 Wroclaw, Poland

[‡]Institute of Physics, Wrocław University of Science and Technology, Wybrzeże Wyspiańskiego 27, 50-370 Wrocław, Poland

Table of Content

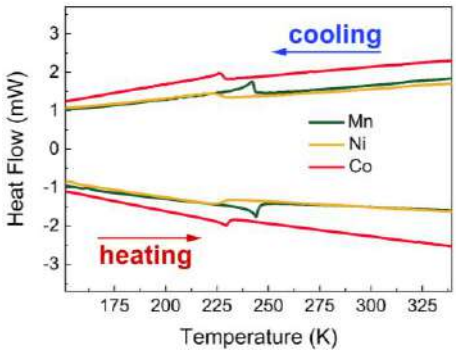

Figure S1. DSC traces for $MHyM^{II}Cl_3$ (M^{II}=Mn, Co, Ni)

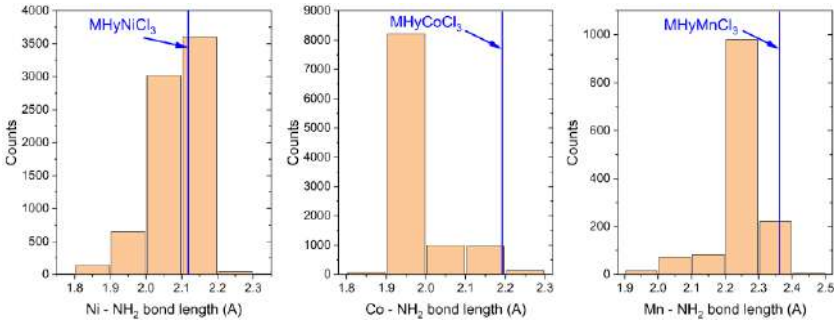

Figure S2. Histograms representing length of M^{II}-NH_2 coordination bonds in **I** based on the survey of CCDC 2020 (searched on 07.05.2021)

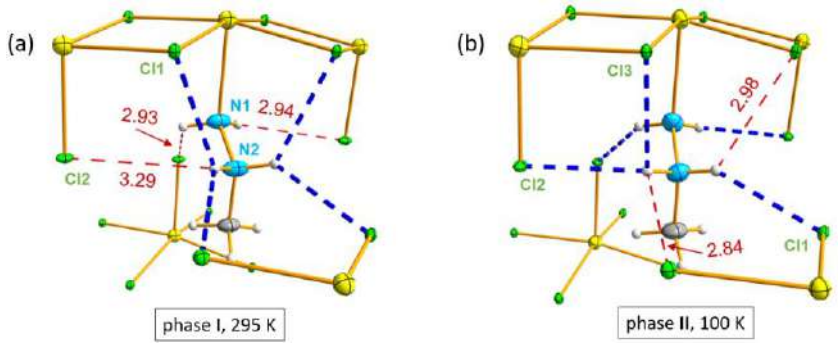

Figure S3. Comparison of the interatomic forces in $MHyMnCl_3$ in (a) phase **I** and (b) phase **II**. Dashed blue lines represent hydrogen bonding while red stand for long-range interactions. All distances are in Å

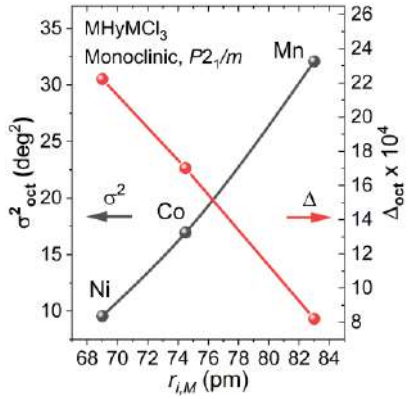

Figure S4. Octahedra angle variance (σ^2) and bond length distortion (Δd) versus M^{II} cation ionic radius ($r_{i,B}$)

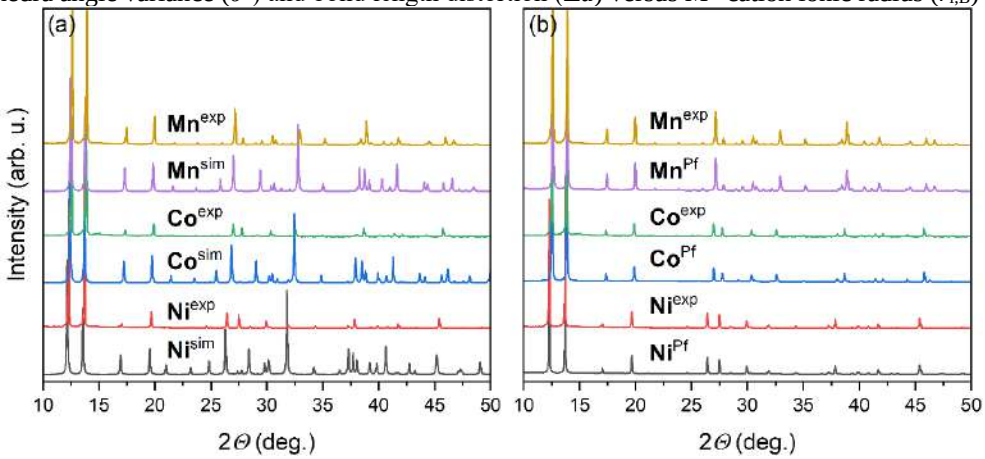

Figure S5. Comparison of experimental (exp) and simulated (sim) powder X-ray diffraction patterns for $MHyM^{II}Cl_3$ before (a) and after (b) Pawley fitting

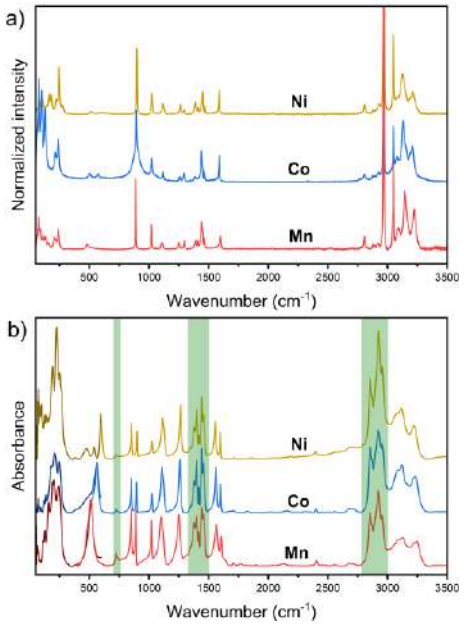

Figure S6. Raman (a) and IR (b) spectra measured for $MHyM^{II}Cl_3$. The green areas in (b) indicate the ranges, where bands of the sample and the medium used in the measurements (nujol) are overlapped

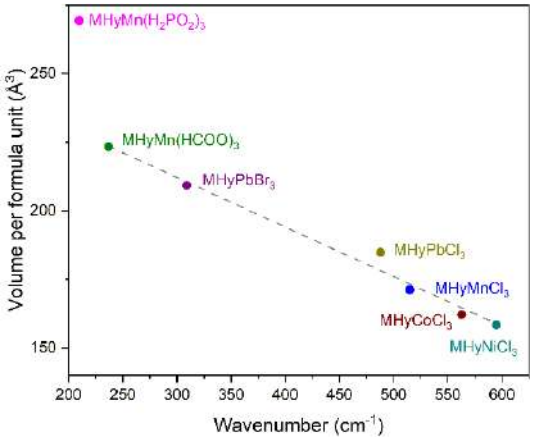

Figure S7. The correlation of the MHy^+-cage mode wavenumber and the volume per formula units in hybrid organic-inorganic compounds having the $AM^{II}X_3$ composition

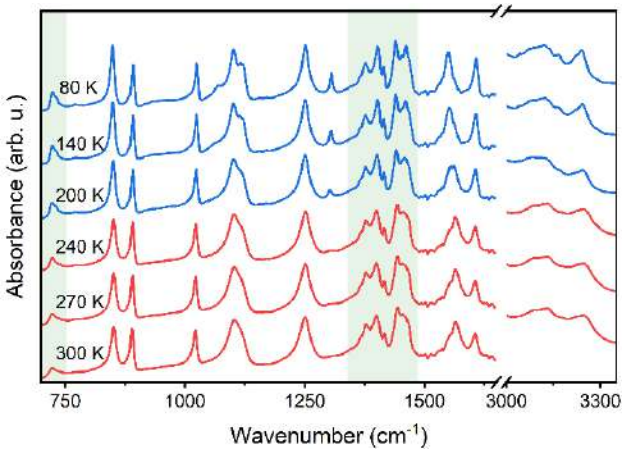

Figure S8. Temperature-dependent IR spectra measured for $MHyMnCl_3$. The green areas indicate the ranges, where bands of the sample and the medium used in the measurements (nujol) are overlapped

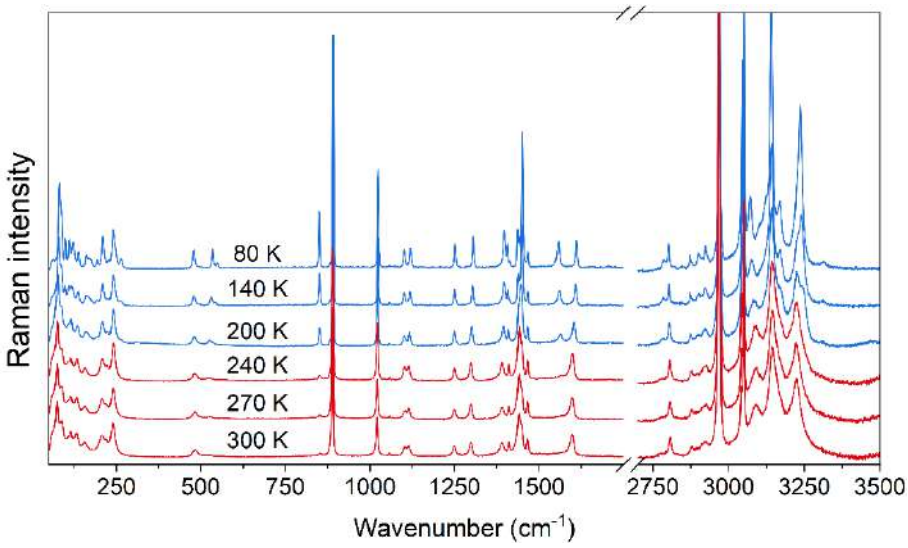

Figure S9. Temperature-dependent Raman spectra measured for $MHyMnCl_3$

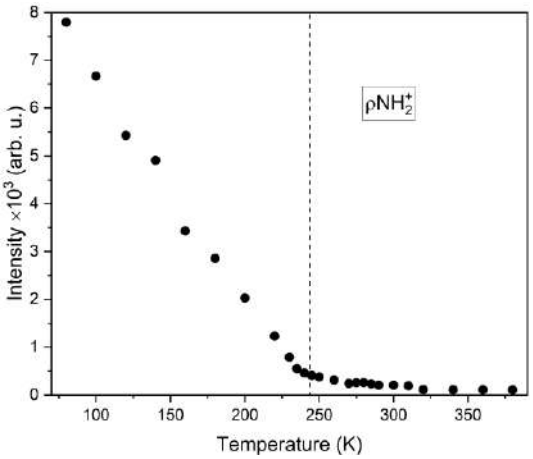

Figure S10. Temperature dependence of intensity of Raman band corresponding to ρNH_2^+ mode for $MHyMnCl_3$

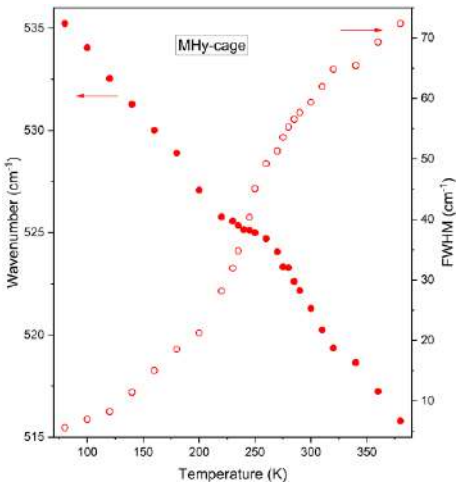

Figure S11. Thermal dependence of the MHy-cage Raman mode for $MHyMnCl_3$

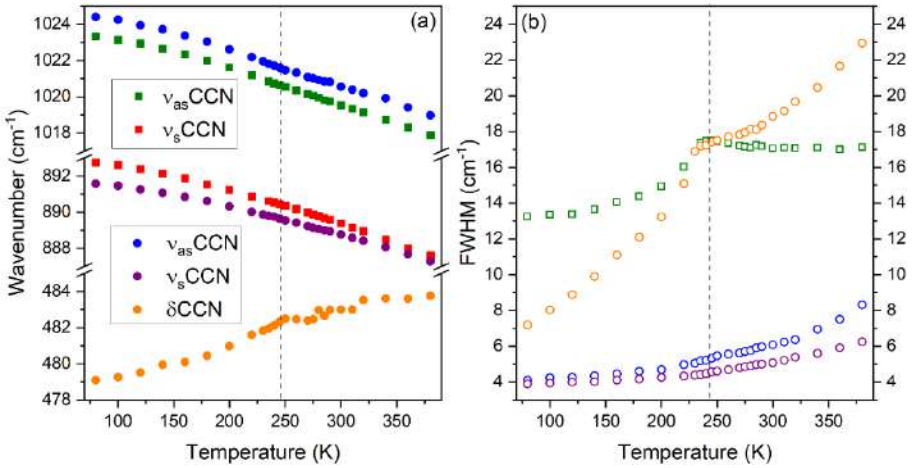

Figure S12. Thermal evolution of selected Raman (circles) and IR (squares) band positions (a) and FWHMs (b) corresponding to the vibrations of the CNN skeleton for $MHyMnCl_3$

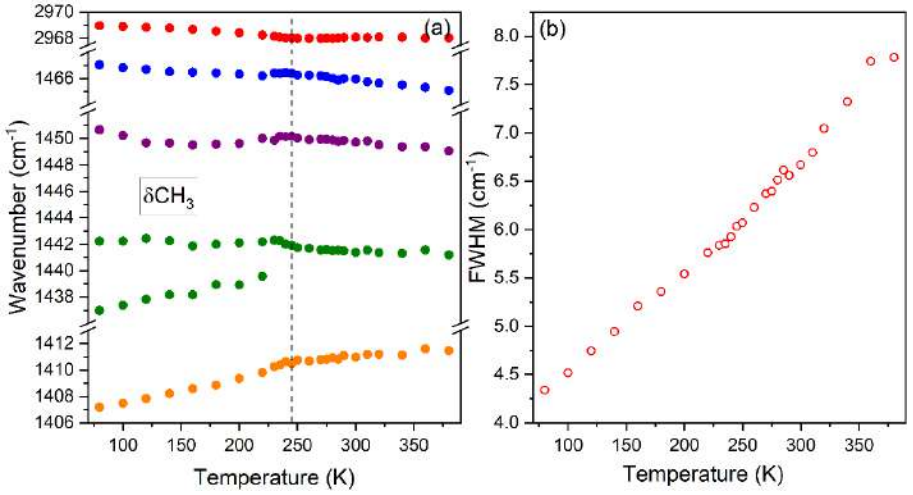

Figure S13. Temperature dependence of positions (a) and FWHM (b) of IR and Raman bands corresponding to internal modes of the methyl group for $MHyMnCl_3$

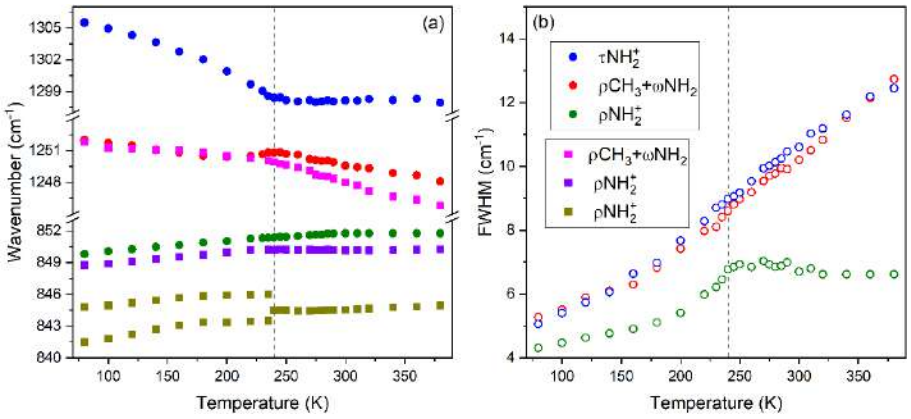

Figure S14. Temperature dependence of positions (a) and FWHMs (b) of IR and Raman bands corresponding to internal modes of the NH_2 and NH_2^+ groups for $MHyMnCl_3$

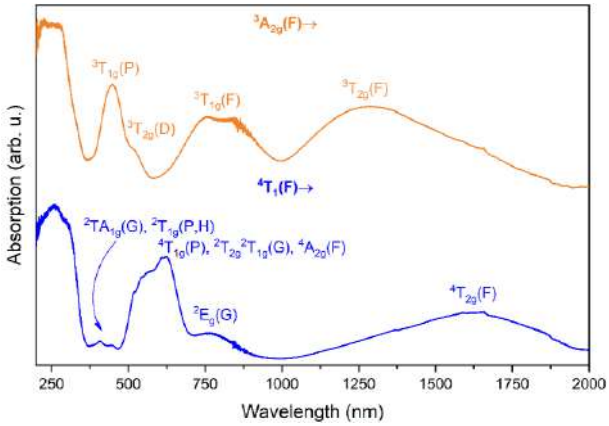

Figure S15. Absorption spectra measured for $MHyNiCl_3$ (orange) and $MHyCoCl_3$ (blue)

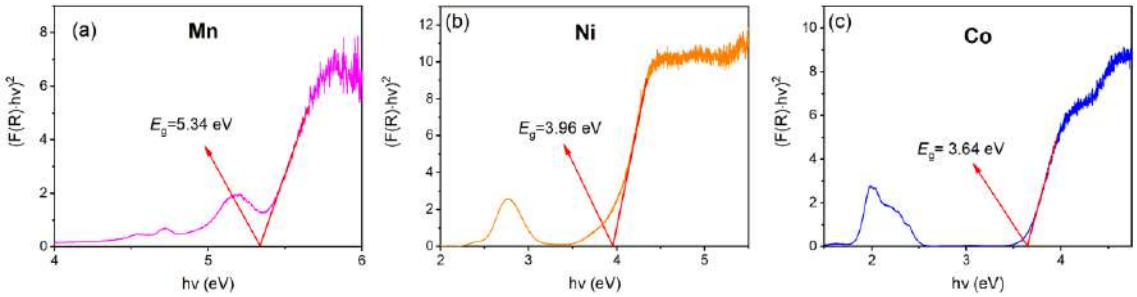

Figure S16. The energy band gap (E_g) calculation for $MHyM^{II}Cl_3$ crystals performed using the Kubelka-Munk theory

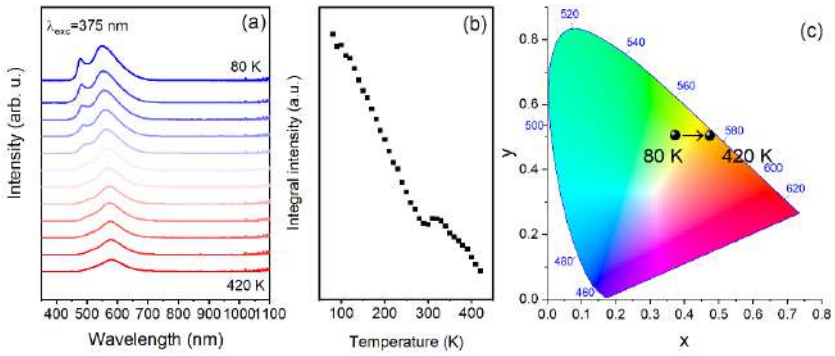

Figure S17. The temperature-dependent emission spectra (a) and the integral emission intensity (b) of the $MHyNiCl_3$ crystals registered under 375 nm excitation together with CIE chromaticity diagram (c)

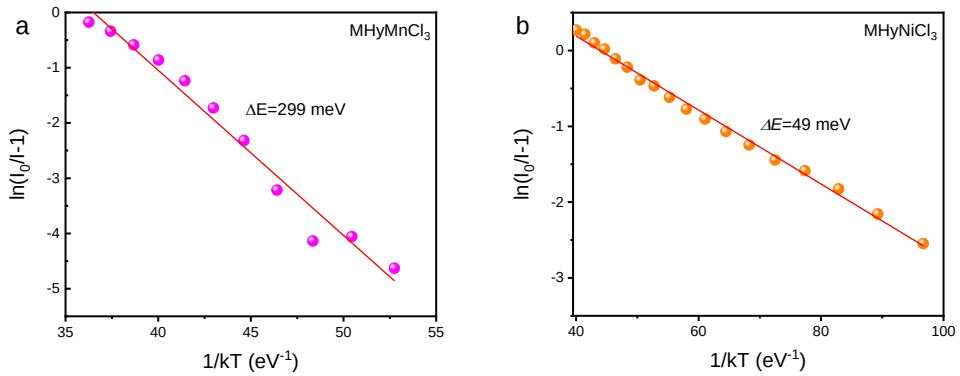

Figure S18. Activation energy of the thermal quenching for the $MHyMnCl_3$ (a) and $MHyNiCl_3$ (b) crystals

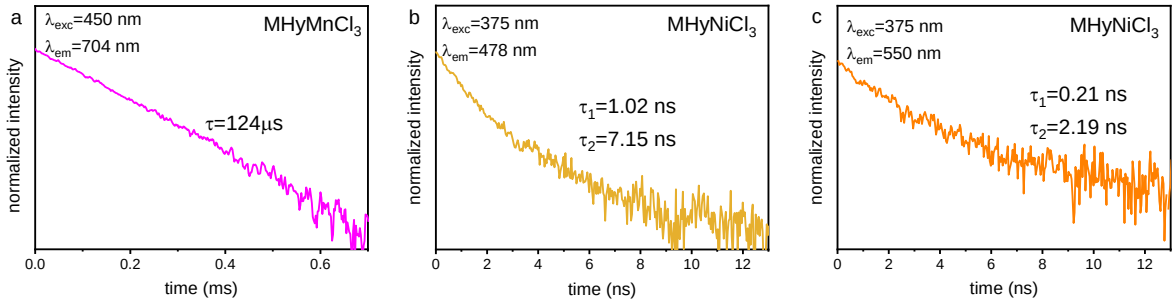

Figure S19. The luminescent decay profiles of the $MHyMnCl_3$ (a) and $MHyNiCl_3$ (b,c) crystals measured at 80 K

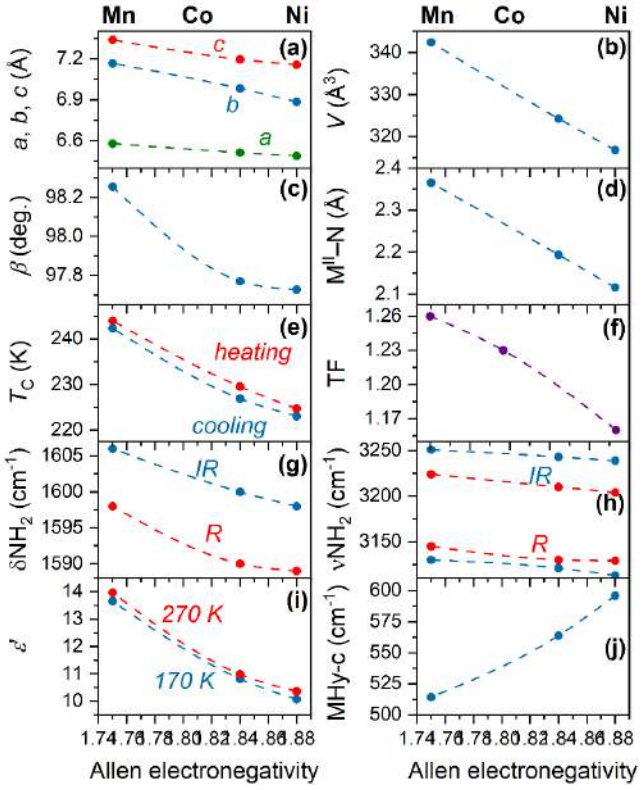

Figure S20. The unit cell parameters *a*, *b*, *c* (a), unit cell volume *V* (b), *β* angle (c) M^{II}-N bond length (d), temperature of PT T_c (e), tolerance factor TF (f), position of selected bands (g, h, j) and dielectric constant *ε*' (i) as a function of ionic radius and Allen electronegativity

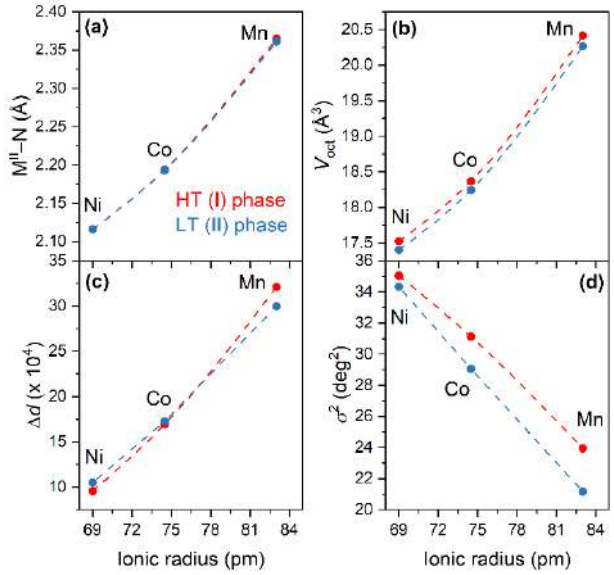

Figure S21. The variation of M^{II}-N distance (a), volume of octahedra (b), bond length distortion index (c), and bond angle variance (d) in phase **I** and **II** for $MHyM^{II}Cl_3$, where M^{II}=Mn, Co and Ni

Table S1. Experimental details of $MHyM^{II}Cl_3$ in phase **I**.

	$MHyNiCl_3$	**$MHyCoCl_3$**	**$MHyMnCl_3$**
Crystal data			
Chemical formula	$CH_7Cl_3N_2Ni$	$CH_7Cl_3CoN_2$	$CH_7Cl_3MnN_2$
Crystal system, space group	Monoclinic, $P2_1/m$		
Z	2		
M_r	212.15	212.37	208.38
Temperature (K)	295		
a, b, c (Å)	6.4891(5), 6.8847(4), 7.1564(4)	6.5135(2), 6.9823(2), 7.1963(2)	6.5795(2), 7.1655(2), 7.3384(2)
β (°)	97.728 (6)	97.771 (3)	98.255 (3)
V (Å^3)	316.81 (4)	324.28 (2)	342.39 (2)
μ (mm^{-1})	4.20	3.76	2.98
Crystal size (mm)	0.20 × 0.08 × 0.06	0.19 × 0.11 × 0.09	0.28 × 0.11 × 0.10
σ^2 (deg^2), $\Delta d \times 10^{-5}$	9.57, 222	17.0, 170	32.1, 82
Data collection			
T_{min}, T_{max}	0.835, 1.000	0.782, 1.000	0.811, 1.000
No. of measured, independent and observed [$I > 2\sigma(I)$] reflections	4046, 650, 593	7571, 665, 642	4679, 704, 683
R_{int}	0.022	0.023	0.021
$(\sin \theta/\lambda)_{max}$ (Å^{-1})	0.609	0.609	0.610
Refinement			
$R[F^2 > 2\sigma(F^2)]$, $wR(F^2)$, S	0.019, 0.044, 1.16	0.015, 0.035, 1.16	0.019, 0.051, 1.17
No. of reflections	650	665	704
$\Delta\rangle_{max}$, $\Delta\rangle_{min}$ (e Å^{-3})	0.31, -0.40	0.36, -0.33	0.38, -0.40

Table S2. Selected geometric parameters of phase **I** (Å, º).

MHyNiCl$_3$		**MHyCoCl$_3$**		**MHyMnCl$_3$**	
Ni1—Cl1^{i}	2.4233 (6)	Co1—Cl1^{i}	2.4646 (4)	Mn1—Cl1^{i}	2.5458 (5)
Ni1—Cl1^{ii}	2.4233 (6)	Co1—Cl1^{ii}	2.4646 (4)	Mn1—Cl1^{ii}	2.5458 (5)
Ni1—Cl1^{iii}	2.4137 (6)	Co1—Cl1	2.4562 (4)	Mn1—Cl1	2.5341 (5)
Ni1—Cl1	2.4137 (6)	Co1—Cl1^{iii}	2.4561 (4)	Mn1—Cl1^{iii}	2.5341 (5)
Ni1—Cl2	2.3967 (8)	Co1—Cl2	2.3901 (6)	Mn1—Cl2	2.4462 (8)
Ni1—N1	2.116 (3)	Co1—N1	2.194 (2)	Mn1—N1	2.365 (2)
N1—N2	1.406 (4)	N1—N2	1.401 (3)	N1—N2	1.399 (3)
N2—C1	1.471 (4)	N2—C1	1.475 (3)	N2—C1	1.474 (4)
Cl1—Ni1—Cl1^{iii}	91.02 (3)	Cl1^{iii}—Co1—Cl1	90.69 (2)	Cl1^{iii}—Mn1—Cl1	90.33 (2)
Cl1^{ii}—Ni1—Cl1^{i}	90.47 (3)	Cl1^{ii}—Co1—Cl1^{i}	90.08 (2)	Cl1^{ii}—Mn1—Cl1^{i}	89.09 (2)
Cl1^{iii}—Ni1—Cl1^{i}	173.010 (18)	Cl1—Co1—Cl1^{i}	88.830 (13)	Cl1—Mn1—Cl1^{i}	88.795 (15)
Cl1—Ni1—Cl1^{ii}	173.011 (18)	Cl1^{iii}—Co1—Cl1^{ii}	88.830 (13)	Cl1^{iii}—Mn1—Cl1^{ii}	88.795 (14)
Cl1—Ni1—Cl1^{i}	88.830 (18)	Cl1^{iii}—Co1—Cl1^{i}	170.505 (14)	Cl1^{iii}—Mn1—Cl1^{i}	166.863 (17)
Cl1^{iii}—Ni1—Cl1^{ii}	88.830 (18)	Cl1—Co1—Cl1^{ii}	170.505 (14)	Cl1—Mn1—Cl1^{ii}	166.863 (17)
Cl2—Ni1—Cl1^{ii}	94.29 (2)	Cl2—Co1—Cl1^{ii}	95.608 (17)	Cl2—Mn1—Cl1^{ii}	97.59 (2)
Cl2—Ni1—Cl1^{iii}	92.69 (2)	Cl2—Co1—Cl1	93.885 (17)	Cl2—Mn1—Cl1	95.54 (2)
Cl2—Ni1—Cl1^{i}	94.29 (2)	Cl2—Co1—Cl1^{i}	95.608 (17)	Cl2—Mn1—Cl1^{i}	97.59 (2)
Cl2—Ni1—Cl1	92.69 (2)	Cl2—Co1—Cl1^{iii}	93.885 (17)	Cl2—Mn1—Cl1^{iii}	95.54 (2)
N1—Ni1—Cl1^{i}	87.04 (5)	N1—Co1—Cl1^{i}	85.44 (4)	N1—Mn1—Cl1^{i}	83.17 (4)
N1—Ni1—Cl1^{iii}	85.98 (5)	N1—Co1—Cl1	85.07 (4)	N1—Mn1—Cl1	83.71 (4)
N1—Ni1—Cl1^{ii}	87.04 (5)	N1—Co1—Cl1^{ii}	85.44 (4)	N1—Mn1—Cl1^{ii}	83.17 (4)
N1—Ni1—Cl1	85.98 (5)	N1—Co1—Cl1^{iii}	85.07 (4)	N1—Mn1—Cl1^{iii}	83.71 (4)
N1—Ni1—Cl2	178.10 (8)	N1—Co1—Cl2	178.51 (6)	N1—Mn1—Cl2	178.92 (6)
Ni1—Cl1—Ni1^{i}	91.170 (18)	Co1—Cl1—Co1^{i}	91.170 (13)	Mn1—Cl1—Mn1^{i}	91.205 (15)
N2—N1—Ni1	119.6 (2)	N2—N1—Co1	119.95 (15)	N2—N1—Mn1	120.38 (17)
N1—N2—C1	116.8 (3)	N1—N2—C1	116.6 (2)	N1—N2—C1	117.2 (2)

Symmetry codes: (i) -*x*+1, -*y*+1, -*z*+1; (ii) -*x*+1, *y*+1/2, -*z*+1; (iii) *x*, -*y*+3/2, *z*.

Table S3. Experimental details of $MHyM^{II}Cl_3$ in phase **II**.

	$MHyNiCl_3$	**$MHyCoCl_3$**	**$MHyMnCl_3$**
Crystal data			
Chemical formula	$CH_7Cl_3N_2Ni$	$CH_7Cl_3CoN_2$	$CH_7Cl_3MnN_2$
Crystal system, space group	Monoclinic, $P2_1/n$		
Z	2		
M_r	212.15	212.37	208.38
Temperature (K)	100	120	100
a, b, c (Å)	8.9172(2), 6.8530(2), 10.2509(3)	8.9538(2), 6.9491(2), 10.3007(3)	9.0271(2), 7.1189(2), 10.4888(3)
β (°)	95.733 (2)	95.821 (2)	96.435 (2)
V (Å^3)	623.29 (3)	637.61 (3)	669.80 (3)
μ (mm^{-1})	4.27	3.83	3.05
Crystal size (mm)	0.20 × 0.08 × 0.06	0.19 × 0.11 × 0.09	0.28 × 0.11 × 0.10
σ^2 (deg^2), $\Delta d \times 10^{-5}$	10.5, 213	17.2, 156	30.0, 63
Data collection			
T_{min}, T_{max}	0.848, 1.000	0.754, 1.000	0.822, 1.000
No. of measured, independent and observed [$I > 2\sigma(I)$] reflections	7651, 1181, 1019	14345, 1210, 1140	8770, 1263, 1197
R_{int}	0.027	0.022	0.020
$(\sin \theta/\lambda)_{max}$ (Å^{-1})	0.610	0.610	0.610
Refinement			
$R[F^2 > 2\sigma(F^2)]$, $wR(F^2)$, S	0.018, 0.044, 1.09	0.015, 0.041, 0.96	0.014, 0.037, 1.12
No. of reflections	1181	1210	1263
No. of parameters	65	73	65
$\Delta\rangle_{max}$, $\Delta\rangle_{min}$ (e Å^{-3})	0.31, -0.38	0.21, -0.49	0.24, -0.37

Table S4. Selected geometric parameters of phase **II** (Å, º).

MHyNiCl$_3$		**MHyCoCl$_3$**		**MHyMnCl$_3$**	
Ni1—Cl1	2.4049 (6)	Co1—Cl1	2.4456 (4)	Mn1—Cl1^{i}	2.5429 (3)
Ni1—Cl1^{i}	2.4176 (6)	Co1—Cl1^{i}	2.4603 (4)	Mn1—Cl1	2.5229 (3)
Ni1—Cl3^{i}	2.4061 (6)	Co1—Cl3^{i}	2.4480 (4)	Mn1—Cl3^{i}	2.5219 (3)
Ni1—Cl3	2.4102 (6)	Co1—Cl3	2.4502 (4)	Mn1—Cl3	2.5230 (3)
Ni1—Cl2	2.3993 (6)	Co1—Cl2	2.3953 (4)	Mn1—Cl2	2.4569 (4)
Ni1—N1	2.1160 (18)	Co1—N1	2.1932 (14)	Mn1—N1	2.3614 (11)
N2—N1	1.443 (2)	N2—N1	1.4418 (19)	N2—N1	1.4458 (15)
N2—C1	1.486 (3)	N2—C1	1.485 (2)	N2—C1	1.4839 (17)
Cl1—Ni1—Cl1^{i}	173.458 (13)	Cl1—Co1—Cl1^{i}	171.083 (10)	Cl1—Mn1—Cl1^{i}	167.848 (9)
Cl1—Ni1—Cl3	89.077 (19)	Cl1—Co1—Cl3	89.155 (14)	Cl1—Mn1—Cl3	89.388 (11)
Cl1—Ni1—Cl3^{i}	90.836 (19)	Cl1—Co1—Cl3^{i}	90.476 (14)	Cl3^{i}—Mn1—Cl1	89.919 (11)
Cl3^{i}—Ni1—Cl1^{i}	88.876 (19)	Cl3^{i}—Co1—Cl1^{i}	88.867 (14)	Cl3^{i}—Mn1—Cl1^{i}	88.963 (11)
Cl3—Ni1—Cl1^{i}	90.463 (19)	Cl3—Co1—Cl1^{i}	90.115 (14)	Cl3—Mn1—Cl1^{i}	89.152 (11)
Cl3^{i}—Ni1—Cl3	173.444 (13)	Cl3^{i}—Co1—Cl3	171.063 (10)	Cl3^{i}—Mn1—Cl3	167.788 (9)
Cl2—Ni1—Cl1^{i}	94.02 (2)	Cl2—Co1—Cl1^{i}	95.205 (15)	Cl2—Mn1—Cl1	95.294 (12)
Cl2—Ni1—Cl1	92.52 (2)	Cl2—Co1—Cl1	93.711 (15)	Cl2—Mn1—Cl1^{i}	96.858 (12)
Cl2—Ni1—Cl3^{i}	92.472 (19)	Cl2—Co1—Cl3^{i}	93.473 (15)	Cl2—Mn1—Cl3^{i}	94.698 (11)
Cl2—Ni1—Cl3	94.08 (2)	Cl2—Co1—Cl3	95.462 (14)	Cl2—Mn1—Cl3	97.507 (11)
N1—Ni1—Cl1	88.70 (5)	N1—Co1—Cl1	87.92 (4)	N1—Mn1—Cl1	86.76 (3)
N1—Ni1—Cl1^{i}	84.77 (5)	N1—Co1—Cl1^{i}	83.17 (4)	N1—Mn1—Cl1^{i}	81.11 (3)
N1—Ni1—Cl3	89.62 (5)	N1—Co1—Cl3	88.21 (4)	N1—Mn1—Cl3	86.11 (3)
N1—Ni1—Cl3^{i}	83.82 (5)	N1—Co1—Cl3^{i}	82.85 (4)	N1—Mn1—Cl3^{i}	81.67 (3)
N1—Ni1—Cl2	176.12 (5)	N1—Co1—Cl2	175.99 (4)	N1—Mn1—Cl2	175.84 (3)
Ni1—Cl1—Ni1^{ii}	90.929 (18)	Co1—Cl1—Co1^{ii}	90.875 (13)	Mn1—Cl1—Mn1^{ii}	90.564 (10)
Ni1^{ii}—Cl3—Ni1	91.079 (18)	Co1^{ii}—Cl3—Co1	91.060 (13)	Mn1^{ii}—Cl3—Mn1	91.046 (10)
N1—N2—C1	113.98 (17)	N1—N2—C1	114.00 (12)	N1—N2—C1	114.50 (10)
N2—N1—Ni1	117.97 (13)	N2—N1—Co1	118.09 (9)	N2—N1—Mn1	118.24 (7)

Symmetry code(s): (i) -*x*+1/2, *y*-1/2, -*z*+1/2; (ii) -*x*+1/2, *y*+1/2, -*z*+1/2.

Table S5. Selected HB parameters of phase **I**.

D*—H···*A	***D*—H (Å)**	**H···*A* (Å)**	***D*···*A* (Å)**	***D*—H···*A* (°)**
$MHyNiCl_3$				
N1—H1···Cl2^{i}	0.89	2.80	3.4913 (5)	135.5
N1—H2···Cl2^{ii}	0.89	2.80	3.4913 (5)	135.5
N2—H3···Cl1^{iii}	0.89	2.64	3.323 (3)	133.9
N2—H3···Cl1^{i}	0.89	2.63	3.225 (2)	125.1
N2—H4···Cl1^{iv}	0.89	2.64	3.323 (3)	133.9
N2—H4···Cl1^{v}	0.89	2.63	3.225 (2)	125.1
$MHyCoCl_3$				
N2—H3···Cl1^{iii}	0.89	2.63	3.3191 (19)	134.5
N2—H3···Cl1^{i}	0.89	2.65	3.2537 (18)	125.5
N2—H4···Cl1^{iv}	0.89	2.63	3.3191 (19)	134.5
N2—H4···Cl1^{v}	0.89	2.65	3.2537 (18)	125.5
$MHyMnCl_3$				
N2—H3···Cl1^{iii}	0.89	2.63	3.327 (2)	135.8
N2—H3···Cl1^{i}	0.89	2.74	3.346 (2)	126.5
N2—H4···Cl1^{v}	0.89	2.74	3.346 (2)	126.5
N2—H4···Cl1^{iv}	0.89	2.63	3.327 (2)	135.8

Symmetry code(s): (i) -*x*+1, -*y*+1, -*z*+1; (ii) -*x*+1, -*y*+2, -*z*+1; (iii) *x*+1, *y*, *z*; (iv) *x*+1, -*y*+3/2, *z*; (v) -*x*+1, *y*+1/2, -*z*+1.

Table S6. Selected HB parameters of phase **II**.

D*—H···*A	***D*—H (Å)**	**H···*A* (Å)**	***D*···*A* (Å)**	***D*—H···*A* (°)**
$MHyNiCl_3$				
N2—H3···Cl3	0.89	2.62	3.1025 (18)	115.0
N2—H3···Cl3^{i}	0.89	2.82	3.2868 (19)	114.4
N2—H3···Cl2^{ii}	0.89	2.57	3.2747 (18)	137.2
N2—H4···Cl1^{iii}	0.89	2.81	3.3745 (19)	122.6
N2—H4···Cl1^{iv}	0.89	2.54	3.2951 (19)	142.7
N1—H1···Cl2^{v}	0.89	2.68	3.3902 (19)	138.1
N1—H2···Cl2^{iii}	0.89	2.58	3.4309 (18)	159.5
$MHyCoCl_3$				
N2—H3···Cl1^{vi}	0.89	2.53	3.2860 (14)	143.7
N2—H4···Cl3^{vi}	0.89	2.81	3.2873 (14)	115.0
N2—H4···Cl3^{vii}	0.89	2.63	3.1316 (14)	116.3
N2—H4···Cl2^{vii}	0.89	2.60	3.3093 (14)	136.8
N1—H1···Cl2^{viii}	0.85 (2)	2.66 (2)	3.4866 (15)	167.4 (18)
N1—H2···Cl2^{ix}	0.87 (2)	2.62 (2)	3.3857 (15)	147.1 (17)
$MHyMnCl_3$				
N2—H3···Cl3	0.89	2.71	3.2074 (11)	116.2
N2—H3···Cl2^{ii}	0.89	2.60	3.3233 (11)	139.6
N2—H4···Cl1^{iv}	0.89	2.51	3.2766 (11)	145.2
N1—H1···Cl2^{v}	0.89	2.60	3.3704 (11)	144.9
N1—H2···Cl2^{iii}	0.89	2.71	3.5790 (11)	165.0

Symmetry code(s): (i) -*x*+1, -*y*+1, -*z*+1; (ii) -*x*+1/2, *y*+1/2, -*z*+1/2; (iii) -*x*+1/2, *y*-1/2, -*z*+1/2; (iv) *x*+1/2, -*y*+1/2, *z*+1/2; (v) *x*-1/2, -*y*+1/2, *z*+1/2; (vi) *x*-1/2, -*y*+1/2, *z*-1/2; (vii) -*x*+1/2, *y*-1/2, -*z*+3/2; (viii) -*x*+1/2, *y*+1/2, -*z*+3/2; (ix) *x*+1/2, -*y*+1/2, *z*-1/2.

Table S7. Factor group analysis for $MHyM^{II}Cl_3$.

Ion	Vibrational mode	Free ion symmetry	Site symmetry I (II)	Factor group symmetry I (II)
MHy^+		$C_s=m$	$C_s=m$ ($C_1=1$)	$C_{2h}^2=2/m$ ($C_{2h}^5=2/m$)
	Internal modes			
	$\nu_sNH_2+\nu_sNH_2^+$	2A’	2A’ (2A)	$2A_g+2B_u$ ($2A_g+2A_u+2B_g+2B_u$)
	$\nu_{as}NH_2+\nu_{as}NH_2^+$	2A”	2A” (2A)	$2A_u+2B_g$ ($2A_g+2A_u+2B_g+2B_u$)
	$\delta NH_2+\delta NH_2^+$	2A’	2A’ (2A)	$2A_g+2B_u$ ($2A_g+2A_u+2B_g+2B_u$)
	$\rho NH_2+\rho NH_2^+$	2A”	2A” (2A)	$2A_u+2B_g$ ($2A_g+2A_u+2B_g+2B_u$)
	$\tau NH_2+\tau NH_2^+$	2A”	2A” (2A)	$2A_u+2B_g$ ($2A_g+2A_u+2B_g+2B_u$)
	$\omega NH_2+\omega NH_2^+$	2A’	2A’ (2A)	$2A_g+2B_u$ ($2A_g+2A_u+2B_g+2B_u$)
	ν_sCH_3	A’	A’ (A)	A_g+B_u ($A_g+A_u+B_g+B_u$)
	$\nu_{as}CH_3$	A’+A”	A’+A” (2A)	$A_g+A_u+B_g+B_u$ ($2A_g+2A_u+2B_g+2B_u$)
	δ_sCH_3	A’	A’ (A)	A_g+B_u ($A_g+A_u+B_g+B_u$)
	$\delta_{as}CH_3$	A’+A”	A’+A” (2A)	$A_g+A_u+B_g+B_u$ ($2A_g+2A_u+2B_g+2B_u$)
	ρCH_3	A’+A”	A’+A” (2A)	$A_g+A_u+B_g+B_u$ ($2A_g+2A_u+2B_g+2B_u$)
	τCH_3	A”	A’ (A)	A_g+B_u ($A_g+A_u+B_g+B_u$)
	$\nu_{as}CNN$	A’	A’ (A)	A_g+B_u ($A_g+A_u+B_g+B_u$)
	ν_sCNN	A’	A’ (A)	A_g+B_u ($A_g+A_u+B_g+B_u$)
	δCNN	A’	A’ (A)	A_g+B_u ($A_g+A_u+B_g+B_u$)
	External modes			
	T’	2A’+A”	2A’+A” (3A)	$2A_g+A_u+B_g+2B_u$ ($3A_g+3A_u+3B_g+3B_u$)
	L	A’+2A”	A’+2A” (3A)	$A_g+2A_u+2B_g+B_u$ ($3A_g+3A_u+3B_g+3B_u$)
Cl^-			$C_1=1$ | $C_s=m$ ($C_1=1$)	$C_{2h}^2=2/m$ ($C_{2h}^5=2/m$)
	T’		3A | 2A’+A” (3A)	$3A_g+3A_u+3B_g+3B_u$ | $2A_g+A_u+B_g+2B_u$ ($9A_g+9A_u+9B_g+9B_u$)
M^{II}			$C_s=m$ ($C_1=1$)	$C_{2h}^2=2/m$ ($C_{2h}^5=2/m$)
	T’		2A’+A” (3A)	$2A_g+A_u+B_g+2B_u$ ($3A_g+3A_u+3B_g+3B_u$)

Key: ν_s, symmetric stretching; ν_{as}, antisymmetric stretching; δ, bending; δ_s, symmetric bending; δ_{as}, antisymmetric bending; ρ, rocking; τ, twisting; ω, wagging; T’, translation; L, libration. Colors: green, IR- and Raman-active; blue, Raman-active; red, IR-active.

Table S8. Assignment of IR and Raman bands observed for $MHyM^{II}Cl_3$.

$MHyCoCl_3$		$MHyMnCl_3$		$MHyNiCl_3$		Assignments
IR	**Raman**	**IR**	**Raman**	**IR**	**Raman**	
3243m, 3210sh	3210w	3251m, 3222sh	3224m	3239m	3204w	$\nu_{as}NH_2$
3121s	3189sh, 3156sh, 3130w	3130m	3159sh, 3145w	3113m	3182vw, 3129w,b	$\nu_{s}NH_2$
3080s	3080w	3094sh	3088w,b	3065sh	3085vw	$\nu_{as}NH_2^+$
*	3050w	*	3050m, 3042w	*	3050m	$\nu_{s}NH_2^+ + \nu_{as}CH_3$
*	2969s, 2925vw	*	2968vs	*	2971s, 2932vw	$\nu_{s}CH_3$
*	2878vw,b, 2806vw,b	*	2919vw,b, 2879vw, 2807w	*	2921sh, 2896vw, 2878vw, 2808vw	νNH_2
1600s	1590w	1606m	1598w	1598m	1589w	δNH_2
1561m		1554m		1556m		δNH_2^+
*	1467vw, 1449sh, 1439sh	*	1466vw, 1450sh, 1441w	*	1469vw, 1450w, 1442sh	$\delta_{as}CH_3$
*		*	1411vw	*	1413vw	$\delta_{s}CH_3$
*	1386vw	*	1390w	*	1388vw	ωNH_2^+
1296vw	1293vw	1306vw	1298vw, 1295sh	1298vw	1295vw	τNH_2^+
1258vs	1258vw	1248s	1250vw	1265m	1264vw	$\rho CH_3 + \omega NH_2$
1120sh, 1107s	1116vw	1120sh, 1102s	1115vw, 1102w	1126sh	1224sh, 1115vw	$\rho NH_2 + \tau NH_2$
1025m	1023w	1019s	1020w	1025w	1024w	$\nu_{as}CNN$
896m	894m	889s	889m	900m	899m	$\nu_{s}CNN$
852m		850s, 844sh	852vw	853m	855vw	ρNH_2^+
563s	571vw	515vs	521vw,b	595m	603vw	MHy^+-cage
	502vw	492sh	483vw	541w, 475w	515vw	δCNN
250s, 209vs	240w, 214w	246vs, 199vs	271sh, 240w, 220vw, 207w	270sh, 251s, 226vs, 192s	278vw, 245w, 223vw, 206sh	ν($MnCl_5N$) +T'(MHy) +L(MHy)
176s, 135m, 120w	128m	157s, 127w, 110w	157vw,b, 132w, 115w, 112sh	144s, 125m	181w, 162w, 141vw, 109vw	δ($MnCl_5N$) +T'(MHy) +L(MHy)
	98m, 76m, 66sh, 60w	71vw, 60w	89w, 83w, 74w, 61sh	98m, 71m	81vw, 60vw	δ($MnCl_5N$) +T'(MHy) +L(MHy)

Key: ν, stretching; ν_s, symmetric stretching; ν_{as}, antisymmetric stretching; δ, bending; δ_s, symmetric bending; δ_{as}, antisymmetric bending; ρ, rocking; τ, twisting; ω, wagging; T', translation; L, libration; vs, very strong; s, strong; m, medium; w, weak; vw, very weak.

Appendix 1. Additional information regarding SC-XRD data

All the reported compounds were measured at 295 K for phase **I** ($P2_1/m$, Z=2). For the LT phase **II** ($P2_1/n$, Z=4) the measurements were performed at 100 K for Ni, Mn and at 120 K for Co. The selection of the unit cell of **II** requires a more detailed explanation. Basing on the coordinates of atoms, the PLATON software[1] suggests the unit cell of **I**. However, with this selection a large group of diffraction peaks remain unindexed (see example for $MHyNiCl_3$ in Figure S22). These additional peaks in **II** appear due to the loss of translational symmetry, with the atomic displacement unnoticeable for PLATON calculations. Hence, a doubled unit cell with Z=4 has to be chosen (Figure S23).

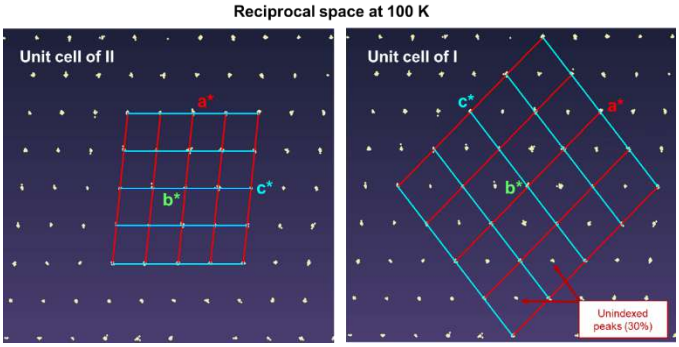

Figure S22. Fragment of reciprocal space of $MHyNiCl_3$ measured at 100 K. With implementation of the unit cell of phase **I** (suggested by PLATON software), ~30% of diffraction peaks remain unindexed

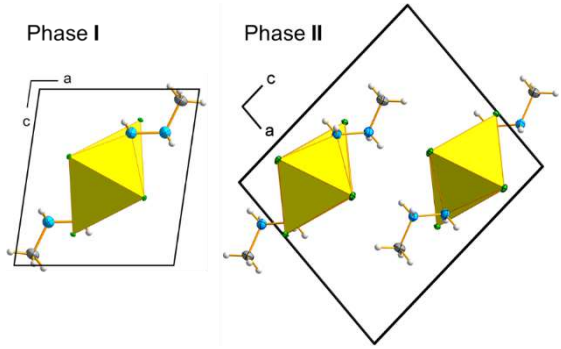

Figure S23. Change of the unit cell choice when going from RT phase **I** to LT phase **II**

Appendix 2. Method of calculating ΔS

The raw heat flow (HF) curve as a function of T was recalculated to C_p using a formula $C_p = \frac{60 \cdot HF \cdot M}{m \cdot R}$, where HF is heat flow (mW), M is molar mass ($gmol^{-1}$), m is a mass (mg), and R is temperature rate ($Kmin^{-1}$). Next, the excess heat capacity (ΔC_p), associated with PT, was evaluated by subtracting the baseline representing variation in the absence of PTs. The change of entropy (ΔS) was estimated using the dependence $\Delta S = \int_0^T \frac{\Delta C_p}{T} dT$.

Appendix 3. Pawley fitting

Table S9. Results of Pawley fitting for $MHyM^{II}Cl_3$ (M^{II}=Mn, Co, Ni)

	$MHyMnCl_3$	**$MHyCoCl_3$**	**$MHyNiCl_3$**
Structure and profile data			
Formula sum	$Mn_2Cl_6N_4H_{14}C_2$	$Co_2Cl_6N_4H_{14}C_2$	$Ni_2Cl_6N_4H_{14}C_2$
Formula mass/ g/mol	416.75	424.74	424.28
Density (calculated)/ g/cm^3	2.0224	2.1756	2.22.00
F(000)	206.00	210.00	212.00
Space group (No.)	P 1 $2_1/m$ 1 (11)	P 1 $2_1/m$ 1 (11)	P 1 $2_1/m$ 1 (11)
Lattice parameters			
a/ Å	7(179)	7(573)	6(454)
b/ Å	7(1044)	7(161)	7(61)
b/ Å	7(325)	7(291)	7(747)
alpha /°	90	90	90
beta /°	98(616)	98(684)	98(1357)
gamma /°	90	90	90
V/ 10^6 pm^3	342.14	324.14	316.61

[1] Spek, A. L. Single-crystal structure validation with the program PLATON. *J. Appl. Cryst.* **2003**, *36*, 7-13. DOI: 10.1107/S0021889802022112

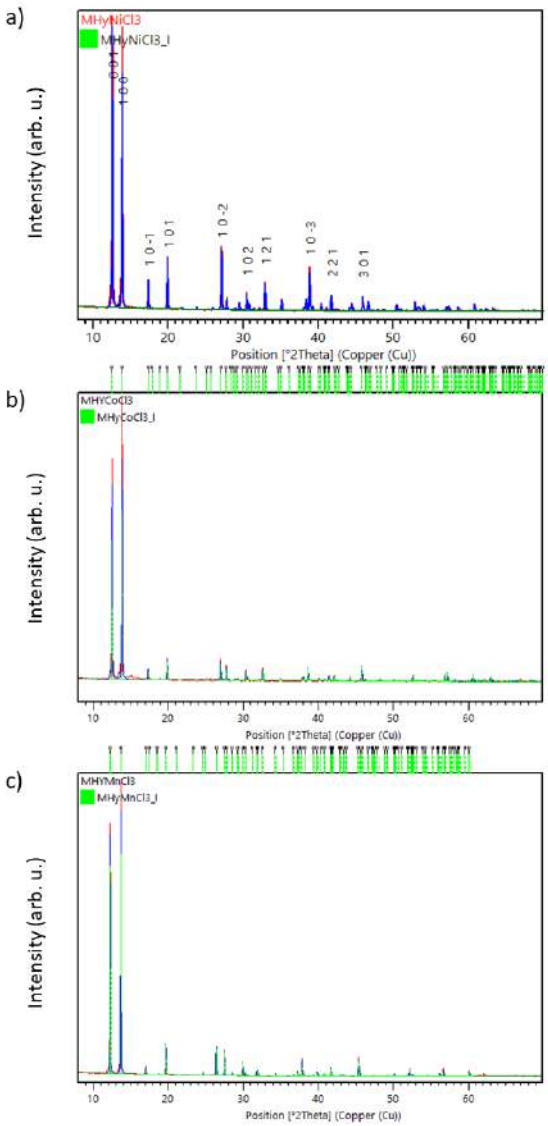

Figure S24. Results of Pawley fitting for $MHyM^{II}Cl_3$, M^{II}=Ni (a), Co (b), and Mn (c)

Appendix 4. Selection rules and factor group analysis

Free MHy^+ cation has 24 internal vibrations (14A'+10A"),[2] their detailed description is presented in Table S7. In phase **I**, the number of internal vibrations corresponding to MHy^+ increases to 48 ($15A_g+9A_u+9B_g+15B_u$). Remaining modes are distributed into 6 translations ($2A_g+A_u+B_g+2B_u$) and 6 librations ($A_g+2A_u+2B_g+B_u$) of MHy^+, 6 translations of M^{II} ($2A_g+A_u+B_g+2B_u$), and 18 modes of Cl^- ligands ($5A_g+4A_u+4B_g+5B_u$). During the **I→II** PT, resulting in a doubling of the primitive cell, the number of vibrational modes is also doubled. Specifically, the number of internal vibrations corresponding to MHy^+ raises to 96 ($24A_g+24A_u+24B_g+24B_u$), MHy^+ translations and librations to 12 ($3A_g+3A_u+3B_g+3B_u$ each), M^{II} translations to 12 ($3A_g+3A_u+3B_g+3B_u$), and Cl^- ligands to 36 ($9A_g+9A_u+9B_g+9B_u$).

[2] Ciupa-Litwa, A.; Ptak, M.; Kucharska, E.; Hanuza, J.; Mączka, M. Vibrational Properties and DFT Calculations of Perovskite-Type Methylhydrazinium Manganese Hypophosphite. Molecules 2020, 25, 5215. DOI: 10.3390/molecules25215215

Considering the above, the total number of modes in **I** and **II** phases equals to 84 ($26A_g+16A_u+16B_g+26B_u$) and 168 ($42A_g+42A_u+42B_g+42B_u$), respectively. Because A_u+2B_u describe acoustic modes in both phases, the remaining optical modes can be distributed into Raman- (g subscript) and IR-active (u subscript) modes in **I** (**II**), namely $26A_g+16B_g$ ($42A_g+42B_g$) and $15A_u+24B_u$ ($41A_u+40B_u$), respectively. It is worth noting that translations of M^{II} are Raman-active in both phases, but IR-active only in **II**.

Appendix 5. Magnetic properties of $MHyM^{II}Cl_3$ (M^{II}=Co, Ni)

MHyCoCl₃. Temperature dependence of χ^{-1}(T) of $MHyCoCl_3$ is shown in Figure S24a (left axis). The analysis of its linear part (i.e. of the experimental data collected above about 70 K) in terms of the Curie-Weiss law yielded the experimental values of C=3.43(2) emu mol^{-1}K and θ_p=-5.3(9) K (see the thick solid line in Figure S24a). The effective magnetic moment derived from C is equal to 5.24(1) μ_B, which is lower than the theoretical value of 6.63 μ_B calculated for a free Co^{2+} ion with the electron configuration $3d^7$ (S=3/2, L=3, J=9/2, g_J=1.33) and higher than 3.87 μ_B expected in the case of the orbital quenching (i.e. for S=3/2, L=0, J=3/2 and g_J=2), what indicates a significant orbital contribution to μ_{eff} of the cobalt ions in $MHyCoCl_3$. The negative value of θ_p points at presence of predominantly antiferromagnetic coupling between the magnetic moments of Co^{2+}, but weaker than in the system with Mn – $|\theta_p|$ is approximately two times lower in $MHyCoCl_3$ than in $MHyMnCl_3$.

As can be noticed in Figure S243a (right axis), χT of the compound with cobalt achieves at RT a value of about 3.33 emu mol^{-1}K (see Figure S24a, right axis), which lies between 5.49 emu mol^{-1}K and 1.87 emu mol^{-1}K expected for Co^{2+} in the absence and in the presence of the orbital quenching, respectively. At elevated temperature, χT(T) has a concave curvature, being in line with the fitted negative θ_p and pointing once more at presence of predominantly antiferromagnetic interactions in the system. However, the changes of χT in $MHyCoCl_3$ are much smaller than in $MHyMnCl_3$, what is in line with smaller $|\theta_p|$ in the former compound. Below about 50 K the curvature of χT(T) changes: χT quickly increases with decreasing temperature, goes through a high maximum and drops down well below the RT value, suggesting some evolution of the interactions between magnetic moments towards ferromagnetic ones.

Distinct cusp-like anomaly visible in χ(T) at low temperatures (Figure S24b) manifests an antiferromagnetic ordering of the $MHyCoCl_3$ system below the Néel temperature T_N=3.7 K, being in line with the negative sign of θ_p. Full overlap of the ZFC and FC curves also corroborates the antiferromagnetic character of the observed phase transition.

Figures S24c and S24d display field dependence of the magnetization of $MHyCoCl_3$ plotted in two different scales. As seen, M(H) is linear up to about 0.9 kOe and does not show any magnetic hysteresis, as expected for antiferromagnets. In higher fields the magnetization increases sharply from about 0.02 μ_B to almost 2 μ_B (i.e. by two orders of magnitude), and above about 10 kOe it exhibits clear tendency to saturation. Such a behavior manifests a metamagnetic transition from the antiferromagnetic arrangement of the moments to a field-induced ferromagnetism. The value of magnetization at the highest field applied (70 kOe) is equal to M_{sat}=2.3 μ_B, being not so far from the ordered magnetic moment of Co^{2+} in the presence of orbital quenching (i.e. μ_{ord}=3 μ_B).

MHyNiCl₃. As can be inferred from Figure S25a (left axis), χ^{-1}(T) of $MHyNiCl_3$ exhibits linear dependence above about 70 K, which can be described by the Curie-Weiss formula with the least-squares fitting parameters C=1.26(1) emu mol^{-1} K (yielding μ_{eff}=3.17(1) μ_B) and θ_p=17.8(4) K (see the thick solid line in Figure S25a). The obtained effective magnetic moment is lower than the theoretical μ_{eff}=5.59 μ_B calculated for a free Ni^{2+} ion ($3d^8$) within the Russel-Sunders approach (i.e. for S=1, L=3, J=4, g_J = 1.25) and higher than the spin-only value 2.83 μ_B (i.e. calculated for S=1, L=0, J=1, g_J=2), which suggests noticeable orbital contribution to the observed μ_{eff}. It is however very close to the average value observed in paramagnetic salts with Ni^{2+} (i.e. 3.12 μ_B). The positive value of θ_p points at the presence of predominantly ferromagnetic coupling between the magnetic moments of Ni^{2+}.

The value of χT at 300 K is of about 1.34 emu mol^{-1}K (see Figure S25a, right axis), which lies between the theoretical values of 3.91 emu mol^{-1}K and 1.00 emu mol^{-1}K, calculated for Ni^{2+} assuming full and spin-only magnetic moment, respectively, and it is very close to the averaged experimental value of C=1.22 emu mol^{-1}K reported for noninteracting Ni^{2+} ions. The postulated ferromagnetic character of the interactions between the magnetic moments of nickel can be also inferred from a convex shape of the χT(T) curve (clearly different from that in the compound with Co), which is well visible from room temperature down to a few Kelvin, where χT achieves a maximum followed by a sudden drop caused by a magnetic phase transition. Surprisingly, the character of that transition is clearly antiferromagnetic, and not ferromagnetic, as might be expected from the sign of θ_p and the curvature of χT(T). In particular, χ(T) exhibits a distinct anomaly with a cusp at T_N=3.7 K (see Figure S25b) and does not show any bifurcation of the ZFC/FC curves.

Results of the measurements of the field variation of the magnetization of $MHyNiCl_3$ shed more light on that discrepancy. As can be seen in Figures S25c and S25d, the magnetization of the compound increases linearly up to about 1 kOe and does not show any hysteresis upon increasing and decreasing the magnetic field, confirming the antiferromagnetic character of the evidenced magnetic ordering at 3.7 K. In higher fields the magnetization increases quickly, manifesting a metamagnetic transition to field-induced ferromagnetism with M_{sat}=2.1 μ_B, being very close to the ordered magnetic moment of Ni^{2+} ions with a spin-only magnetic moment (i.e. μ_{ord}=2 μ_B). Although this behavior looks similar to that observed in $MHyCoCl_3$, there is a

noticeable difference between *M*(H) of the compounds with Co and Ni. In particular, the initial slope of the linear part of *M*(H), associated with the antiferromagnetic ground states of the compounds, is much larger in $MHyNiCl_3$ than in $MHyCoCl_3$ (the linear dependence ends up at about 0.1 μB and 0.02 μB, respectively), which leads to less abrupt metamagnetic transition in the former system. It could mean, that the antiferromagnetic correlations are less predominant in the compound with nickel than with cobalt, which would explain differences between their θ_p's and the curvatures of χT(T).

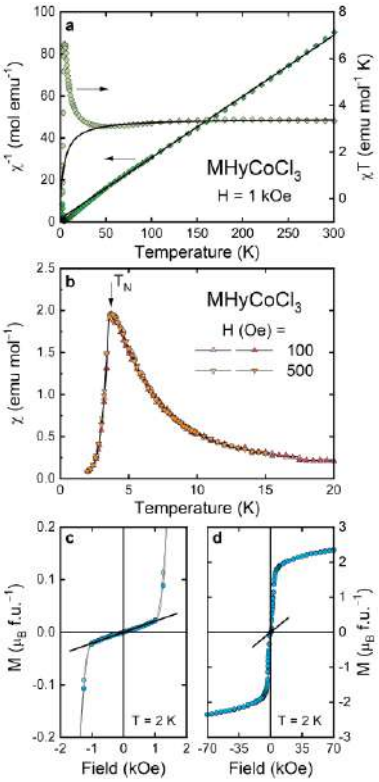

Figure S25. (a) χ^{-1}(T) (left axis) and χT(T) (right axis) of $MHyCoCl_3$ plotted together with the Curie-Weiss fit (solid lines). (b) Low-temperature χ(T) measured in various magnetic fields in the ZFC and FC regimes (bright and dark symbols, respectively); the arrow marks the Néel temperature T_N. (c,d) M(H) plotted in two different field ranges; solid lines indicate linear behavior of the magnetization in low fields

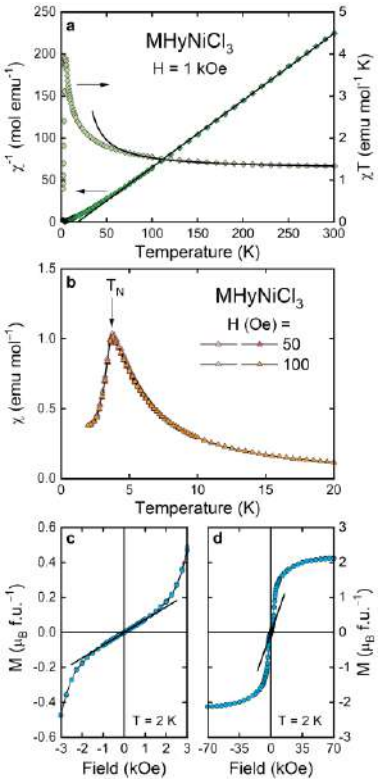

Figure S26. (a) Inverse magnetic susceptibility (left axis) and χT (right axis) of $MHyNiCl_3$ measured as a function of temperature; thick solid lines represent the Curie-Weiss fit (for details see the text). (b) Low-temperature part of χ(T) with the Néel temperature T_N marked by an arrow, measured in the ZFC and FC regimes (bright and dark symbols, respectively). (c,d) Magnetization measured as a function of increasing and decreasing field (bright and dark symbols, respectively) and plotted in two different field ranges; solid line show linear slope of *M*(H) in low fields

***Publikacja* [D4]**

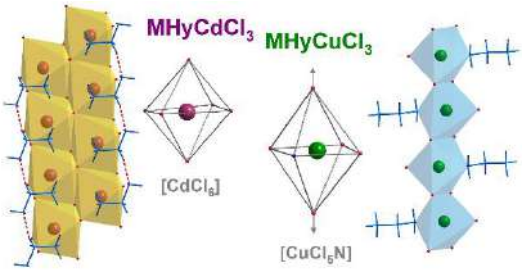

J.A. Zienkiewicz*, D.A. Kowalska, D. Drozdowski, A. Pikul, M. Ptak*

Hybrid chlorides with methylhydrazinium cation:$[CH_3NH_2NH_2]CdCl_3$ and Jahn-Teller distorted $[CH_3NH_2NH_2]CuCl_3$

Molecules **2023**, 28 (2), 473

doi: 10.3390/molecules28020473 IF = 4,927 140pkt.

Udział Doktoranta w powstanie pracy:

- Synteza monokryształów $[MHy]M^{II}Cl_3$ (M^{II} = Cu^{2+}, Cd^{2+}) metodą powolnego odparowywania z roztworu;
- Koncepcja badań oraz określenie metodologii;
- Wyznaczenie reguł wyboru oraz wykonanie analizy grupy faktorowej;
- Zaproponowanie przypisania pasm IR i Ramana;
- Pomiar widm Ramana oraz IR;
- Analiza widm rozproszonego odbicia;
- Dyskusja wpływu kationu M^{II} na właściwości strukturalne, cieplne oraz fononowe;
- Określenie przyczyn braku występowania przemian fazowych;
- Przygotowywanie manuskryptu, rysunków oraz tabel.

molecules

MDPI

Article

Hybrid Chlorides with Methylhydrazinium Cation: $[CH_3NH_2NH_2]CdCl_3$ and Jahn-Teller Distorted $[CH_3NH_2NH_2]CuCl_3$

Jan A. Zienkiewicz *, Dorota A. Kowalska, Dawid Drozdowski, Adam Pikul and Maciej Ptak *

Institute of Low Temperature and Structure Research, Polish Academy of Sciences, Okólna 2, 50-422 Wrocław, Poland

* Correspondence: j.zienkiewicz@intibs.pl (J.A.Z.); m.ptak@intibs.pl (M.P.)

Abstract: The synthesis, structural, phonon, optical, and magnetic properties of two hybrid organic-inorganic chlorides with monoprotonated methylhydrazinium cations ($CH_3NH_2NH_2^+$, MHy^+), $[CH_3NH_2NH_2]CdCl_3$ ($MHyCdCl_3$), and $[CH_3NH_2NH_2]CuCl_3$ ($MHyCuCl_3$), are reported. In contrast to previously reported $MHyM^{II}Cl_3$ (M^{II} = Mn^{2+}, Ni^{2+}, and Co^{2+}) analogues, neither compound undergoes phase transitions. The $MHyCuCl_3$ has a crystal structure familiar to previous crystals composed of edge-shared 1D chains of the $[CuCl_5N]$ octahedra. $MHyCuCl_3$ crystallizes in monoclinic $P2_1/c$ symmetry with MHy^+ cations directly linked to the Cu^{2+} ions. The $MHyCdCl_3$ analogue crystallizes in lower triclinic symmetry with zig-zag chains of the edge-shared $[CdCl_6]$ octahedra. The absence of phase transitions is investigated and discussed. It is connected with slightly stronger hydrogen bonding between cations and the copper–chloride chains in $MHyCuCl_3$ due to the strong Jahn–Teller effect causing the octahedra to elongate, resulting in a better fit of cations in the accessible space between chains. The absence of structural transformation in $MHyCdCl_3$ is due to intermolecular hydrogen bonding between two neighboring MHy^+ cations, which has never been reported for MHy^+-based hybrid halides. Optical investigations revealed that the bandgaps in Cu^{2+} and Cd^{2+} analogues are 2.62 and 5.57 eV, respectively. Magnetic tests indicated that $MHyCuCl_3$ has smeared antiferromagnetic ordering at 4.8 K.

Keywords: methylhydrazinium; organic-inorganic hybrid; chloride; phonon; crystal structure; Jahn–Teller effect

Citation: Zienkiewicz, J.A.; Kowalska, D.A.; Drozdowski, D.; Pikul, A.; Ptak, M. Hybrid Chlorides with Methylhydrazinium Cation: $[CH_3NH_2NH_2]CdCl_3$ and Jahn-Teller Distorted $[CH_3NH_2NH_2]CuCl_3$. *Molecules* **2023**, *28*, 473. https://doi.org/10.3390/molecules28020473

Academic Editor: Ahmad Mehdi

Received: 2 December 2022
Revised: 20 December 2022
Accepted: 21 December 2022
Published: 4 January 2023

1. Introduction

Hybrid organic–inorganic materials (mostly halides) have received a great deal of attention in recent years due to their enormous application potential in the field of high tech industry, particularly as materials for electronic and optoelectronic devices [1,2]. Many of them exhibit controllable optical [3], electric [4], ferroelectric [5–7], switchable dielectric [6], and magnetic [8] properties.

Hydrazine is an interesting small inorganic molecule capable of forming an onium or double onium cation that can be incorporated into crystal structures [9,10]. Compounds containing onium hydrazine cations (Hy^+) are well known and have been the focus of many investigations [9,10]. The degree of methylation of a hydrazine molecule affects its chemical properties and ability to bond in the crystal lattice. Simple organic methylhydrazinium cation (MHy^+) has just been recognized as an object of interest due to its small enough size to form a three-dimensional (3D) organic–inorganic perovskites [11–15]. Only four organic cations have so far matched the size and shape parameters required to form a 3D perovskite architecture with divalent metal ions. Next to MHy^+, these include the methylammonium (MA^+) [16–20], formamidinium (FA^+) [16,18,20–22], and aziridinium (AZ^+) [23] cations.

There is also a class of halogenide perovskites of larger monovalent metals (M^I = Na, K, Rb, Cs) that may form a 3D network with the general formula $AM^IX_3 \cdot 0.5H_2O$, where A

stands for bivalent organic cation. In such networks, the bigger dodecahedral gap accommodates larger organic cations, such as dabconium, methyldabconium, 3-aminopyrrolidinium, piperazinium, or methylpiperazinium cations [24–27].

Recent research has shown that MHy^+-containing hybrid coordination polymers may also form low-dimensional counterparts, such as layered (2D) [28] or chain (1D) [29,30] architectures. The most intriguing aspect is that the MHy^+ ligand may interact differently with inorganic metal–ligand subnetworks in the accessible space: (i) organic cation can simply fill the available space and connect with an inorganic network of metal–ligand octahedra $[M^{II}X_6]$ through N–H···X (X = oxygen, halide) hydrogen bonds (HBs), as reported in $[MHy]M^{II}(HCOO)_3$ (M^{II} = Mn^{2+}, Mg^{2+}, Fe^{2+}, Zn^{2+}) [13], $[MHy]Mn(H_2PO_2)_3$ [31], or in $MHyPbI_3$ [29]; (ii) organic cation can be strongly bound with the subnetwork of inorganic octahedra, resulting in additional short N···M^{II} contacts, as reported in $MHyPbX_3$ (X = Cl^-, Br^-) [14,15]; (iii) one of the N atoms can directly be in the first coordination sphere of the metal, forming non-uniform octahedra of the $[M^{II}X_5N]$ type, which has so far only been found for the $MHyM^{II}Cl_3$ (M^{II} = Mn^{2+}, Co^{2+}, Ni^{2+}) crystals [30]. The third type of rare coordination has also been found for hybrid coordination polymers with Hy^+, $(Hy)_3MnX_5$ (X = Cl^-, Br^-) [32], and 1,1,1-trimethylhydrazinium (Me_3Hy^+) [33] cations.

In this study, we synthesized new phases of the hybrid chlorides $MHyM^{II}Cl_3$ that include Cu^{2+} and Cd^{2+} ions. We undertook a comprehensive physicochemical examination to determine why the structural features, including coordination type and interactions of MHy^+ cations with the metal–chloride framework, of those two analogues vary from other known counterparts. The goal of this work is also to understand why Cu^{2+} and Cd^{2+} analogues do not exhibit phase transitions (PTs) when compared to other members of this family of chlorides.

2. Results and Discussion

2.1. Structural Properties

$MHyCuCl_3$ adopted monoclinic $P2_1/c$ symmetry. It is yet another example of hybrid $MHyM^{II}Cl_3$ compounds with M^{II} = Co^{2+}, Ni^{2+}, Mn^{2+} reported to date [30], in which the terminal N atom of MHy^+ is a co-creator of M^{II} first coordination sphere. In other words, $[CuCl_5N]$ octahedra were formed. The octahedra were arranged by edge-sharing, parallel chains propagating along the [010] direction (Figure 1a). The $P2_1/c$ phase was isostructural to the low temperature (measured at 100–120 K) phases of Co^{2+}, Ni^{2+}, and Mn^{2+} analogues [30]. All atoms occupied general positions of C_1 site symmetry. The Cu–Cl distances were 2.2691(10)–2.815(1) Å, while the Cu–N bond length was equal to 2.061(3) Å. The Cu–Cl distances had a much wider range (~0.55 Å) than their Co^{2+} (0.06 Å), Ni^{2+} (0.02 Å), and Mn^{2+} (0.07 Å) counterparts [30]. Indeed, an axial elongation of the octahedra was observed (Figure S1), pointing out the presence of the Jahn–Teller effect, characteristic of Cu^{2+} compounds with octahedral geometries [34]. The MHy^+ cations were positionally ordered and anchored in the structure by several N–H···Cl HBs (green dashed lines in Figure 1a,b). Both terminal and middle NH_2 groups interacted with chlorine ion acceptors from neighboring chains, stabilizing the crystal structure in [100] and [001] directions (with donor-acceptor (D···A) distances of 3.426(3) Å and 3.269(3) Å, respectively). The HBs within the chains were also present with D···A distances of 3.157(3)–3.631(3) Å. The intermolecular interactions lead to angular and (combined with Jahn–Teller effect) bond length distortion of the octahedra, as indicated by octahedral angle variance and bond length distortion values of σ^2 = 20.7 deg^2 and Δ = 0.1225, respectively. Both values were calculated using the VESTA program [35].

The second newly obtained compound reported herein, i.e., $MHyCdCl_3$, crystallized in triclinic, centrosymmetric $P\bar{1}$ symmetry. The motif of $MHyCdCl_3$ consisted of inorganic $[CdCl_3^-]_\infty$ double chains propagating along the [100] direction, separated by the MHy^+ cations. All atoms adopted C_1 site symmetry. The chains were composed of edge-sharing octahedra with Cd–Cl distances of 2.523(1)–2.712(1) Å. The MHy^+ cations were anchored via N–H···Cl (Figure 1c) and N–H···N (Figure 1d) HBs with D···A distances of

3.168(4)–3.384(4) and 2.975(5) Å, respectively. It is worth noting that both the N1 and N2 atoms of MHy^+ were engaged in creating a 3D network of HBs. An interplay between inorganic and organic constituents affected the octahedra symmetry, expressed in σ^2 and Δ values of 17.8 deg^2 and 0.021, respectively. Analogous atomic alignment, i.e., with 1D edge-sharing double chains, was reported for $MHyPbI_3$ [29]. Higher symmetry of $MHyPbI_3$ (monoclinic, $P2_1/c$) is associated with the presence of larger metal cations and halide anions, which leads to enlarged interatomic distances and, therefore, weaker HBs and less distorted octahedra (σ^2 = 6.32 deg^2). Analogous alignment was also reported for $[C_3H_7N_2S]CdCl_3$, where $C_3H_7N_2S^+$ is the 2-amino-4,5-dihydro-3*H*$^+$-1,3-thiazolium cation [36].

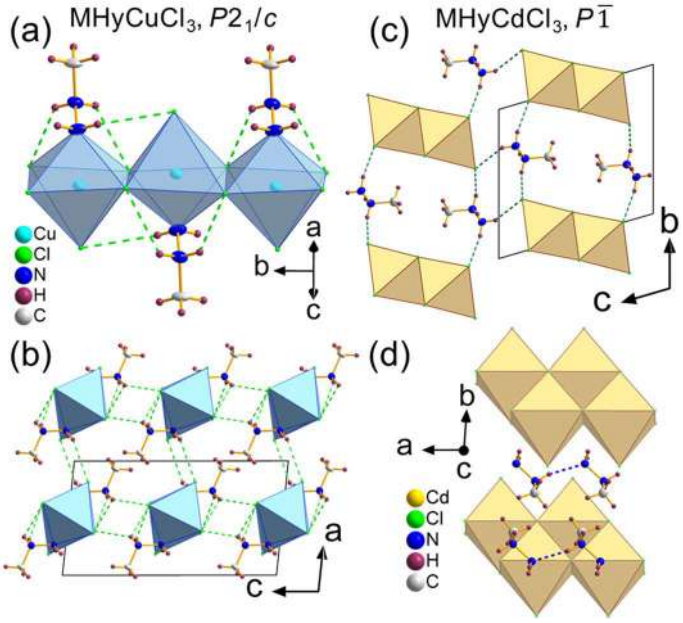

Figure 1. Crystal structures of (**a**,**b**) $MHyCuCl_3$ and (**c**,**d**) $MHyCdCl_3$; dashed lines represent hydrogen bonds: N–H···Cl (green) and N–H···N (blue).

The phase purity of the $MHyCdCl_3$ bulk sample was confirmed by a good match of its PXRD pattern (R_{exp} = 1.70, R_{prof} = 6.26, wR_{prof} = 11.22, *GOF* = 6.6) with the simulated one based on the single crystal structure (Figure 2). The measured PXRD pattern of the $MHyCuCl_3$ bulk sample was also in good agreement (R_{exp} = 1.52, R_{prof} = 5.44, wR_{prof} = 9.85, *GOF* = 6.5) with the calculated one based on the single-crystal data. The Pawley refinement method was used to obtain the fitted profiles. The PXRD analysis results also revealed the negligible presence of another phase ($CuCl_2 \cdot H_2O$) in an amount of about 2%; the peak from the additional phase is marked with an asterisk in Figure 2.

2.2. Phonon Properties

Table S1 defines and lists the 24 internal (13A′ + 11A″) and 6 external (3A′ + 3A″) vibrational modes of the free MHy^+ ion with C_s symmetry. The presence of two MHy^+ ions in the primitive cell doubles the number of modes corresponding to MHy^+ with the factor group symmetry C_i in the triclinic $MHyCdCl_3$ crystal with Z = 2. As a result, the internal and external modes are increased to 48 ($24A_g + 24A_u$) and 12 ($6A_g + 6A_u$), respectively. Since the number of modes corresponding to MHy^+ cations with the C_{2h} symmetry is increased by 4 times in the monoclinic $MHyCuCl_3$ crystal with Z = 4, the number of modes corresponding to MHy^+ cations with the C_{2h} symmetry is 96 ($24A_g + 24A_u + 24B_g + 24B_u$) and 24 ($6A_g + 6A_u + 6B_g + 6B_u$), respectively. Similar considerations apply to metal cations M^{II} and chloride ligands Cl^-, which have 6 ($3A_g + 3A_u$) and 18 ($9A_g + 9A_u$) modes in the triclinic $MHyCdCl_3$ crystal, respectively, and 12 ($3A_g + 3A_u + 3B_g + 3B_u$) and 36 ($9A_g + 9A_u + 9B_g + 9B_u$) modes in the monoclinic $MHyCuCl_3$ crystal.

To summarize, the total number of expected vibrational modes for $MHyCdCl_3$ is 84 ($42A_g + 42A_u$), which includes 81 optical ($42A_g + 39A_u$) and 3 acoustic ($3A_u$), and 168 ($42A_g + 42A_u + 42B_g + 42B_u$) for $MHyCuCl_3$, which includes 165 optical ($42A_g + 41A_u + 42B_g + 40B_u$) and 3 acoustic. Because *g*-type modes are only Raman-active and *u*-type modes are only IR (infrared)-active, the number of expected bands in the Raman (IR) spectrum of $MHyCdCl_3$ is 42 (39). These values are 84 and 81 for the $MHyCuCl_3$ analogue, respectively. The number of observed bands in the room-temperature (RT) spectra is lower than expected (Figure 3, Table S2). This effect is caused by the overlapping of closely spaced bands caused by the low factor group (Davydov) splitting.

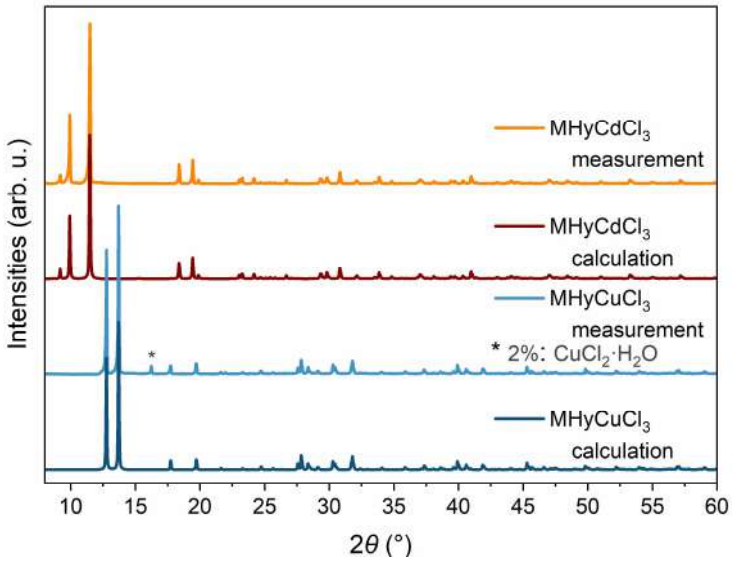

Figure 2. The comparison of the experimental and calculated using Pawley method PXRD patterns for $MHyCdCl_3$ and $MHyCuCl_3$ samples showing the quality of phase purity; * the additional phase is marked with an asterisk.

The proposed assignment, presented in Table S2, is based on a comparison with literature sources, including $MHyM^{II}Cl_3$ (M^{II} = Co^{2+}, Ni^{2+}, Mn^{2+}) [30], 3D and 2D lead halides comprising the MHy^+ cation [12,29,37], $MHyMn(H_2PO_2)_3$ [31], and $MHyM^{II}(HCOO)_3$ (M^{II} = Mg^{2+}, Fe^{2+}, Mn^{2+}, and Zn^{2+}) [13], as well as density functional calculations (DFT) calculations performed for the MHy^+ ion [31]. The majority of IR and Raman bands corresponding to the internal vibrations of MHy^+ are observed in typical ranges as reported in the literature.

The IR and Raman spectra of $MHyCuCl_3$ are qualitatively very similar to those of $MHyM^{II}Cl_3$ (M^{II} = Co^{2+}, Ni^{2+}, Mn^{2+}) [30]. The differences involving wavenumber up- or downshifts reaching a few cm^{-1} for $MHyCuCl_3$ are mainly due to the higher mass, different ionic radius, the strength of HBs, and Jahn–Teller effect activity of Cu^{2+} ions in an octahedral configuration. The most pronounced variations were observed for the so-called MHy^+-cage mode, which can be correlated with the parameter defined as the space available for cation per formula unit V_Z [30]. This mode was described as a torsional mode with a strong sensitivity to ligand type due to coupling with the inorganic cage via HBs bonds [37], which is similar to the behavior of the MA^+-cage mode, which has been initially reported for the $MAPbX_3$ (X = Br^-, I^-) hybrids [38]. In our previous paper concerning $MHyM^{II}Cl_3$ (M^{II} = Co^{2+}, Ni^{2+}, Mn^{2+}), the MHy^+-cage mode clearly correlates to the ionic radius of M^{II} and metal electronegativity, i.e., it was observed as an IR band at 515 cm^{-1} for $MHyMnCl_3$, 563 cm^{-1} for $MHyCoCl_3$, and at 595 cm^{-1} for $MHyNiCl_3$ [30]. Taking into account the IR and Raman spectra of $MHyCdCl_3$ and $MHyCuCl_3$, we assigned the MHy^+-cage mode to IR bands at 386 and 606 cm^{-1}, as well as Raman bands at 389 and 614 cm^{-1}, respectively (see Table S2). The correlation of these values with the ionic radius is higher for $MHyCuCl_3$ and much lower for $MHyCdCl_3$. This is not surprising considering

that MHy^+ is not a direct ligand for the metal cation in the $MHyM^{II}Cl_3$ series. As a result, the torsional vibrational energy is predicted to differ.

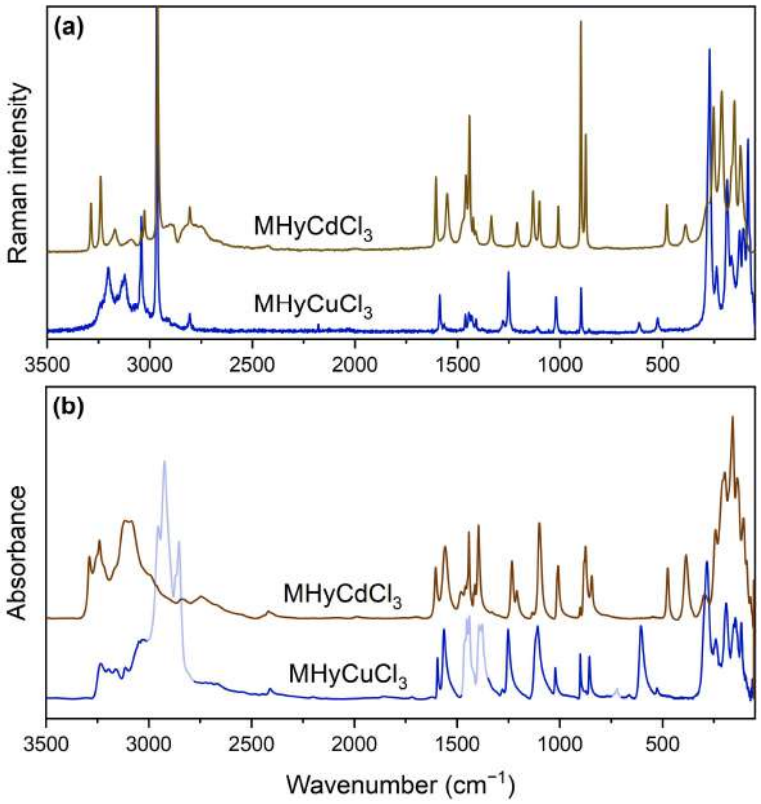

Figure 3. Raman (**a**) and IR (**b**) spectra of $MHyM^{II}Cl_3$ (M^{II} = Cd^{2+}, Cu^{2+}); transparent sections of the $MHyCuCl_3$ IR spectrum on panel (**b**) indicate the absorption ranges of the medium used (nujol).

Another interesting feature that can be analyzed using vibrational spectroscopy is the strength of HBs. The positions of IR and Raman bands corresponding to stretching vibrations of both NH_2 and NH_2^+ groups for the $MHyCuCl_3$ analogue have very similar energies in comparison to the previously studied $MHyM^{II}Cl_3$ (M^{II} = Co^{2+}, Ni^{2+}, Mn^{2+}) series. However, for $MHyCuCl_3$, most of the bands observed above 3000 cm^{-1} have the lowest positions among these four isostructural analogues. It proves our SCXRD analysis, showing that the $MHyCuCl_3$ analogue creates the shortest D···A contacts and thus forms the strongest hydrogen bonds.

As mentioned before, the vibrational spectra of $MHyCdCl_3$ differ most strongly in this region, suggesting that the HB network has different properties. Crystallographic data showed that the MHy^+ cations do not enter the first coordination sphere of Cd^{2+} ions, therefore, they have more freedom in the metal–chloride framework. This leads to the formation of direct, short, and strong N–H···N HBs between MHy^+ cations, which has never been reported for an MHy^+ cation so far. We think that these stronger contacts are responsible for the formation of the broad bands observed in spectra above 2750 cm^{-1}, which are absent for other representatives of the $MHyM^{II}Cl_3$ group.

2.3. Optical Properties

The diffuse reflectance spectra of $MHyM^{II}Cl_3$ (M^{II} = Cd^{2+}, Cu^{2+}) are shown in Figure 4. In the low-wavelength range, $MHyCdCl_3$ exhibits an intense absorption band with a maximum at 212 nm and a weaker band at 275 nm, similar to $FACd(H_2PO_2)_3$ (FA^+ = formamidinium) [39] and $[TPrA]Cd(dca)_3$ ($TPrA^+$ = tetrapropylammonium, dca^- = dicyanamide) [40]. $MHyCuCl_3$ has a much wider low-wavenumber band, with maxima at 249, 330, 379, and 410 nm previously assigned to the ligand-to-metal charge transfer from Cl^- ligand to Cu^{2+} centers for $(C_5H_{14}N_2)[CuCl_4]$ ($C_5H_{14}N_2^{2+}$ = diprotonated 1,4-diazacycloheptane), $(N(CH_3)_4)CdX_3$:Cu^{2+}

($N(CH_3)_4^+$ =tetramethylammonium, X = Cl^-, Br^-), and $MA_2CuCl_xBr_{4-x}$ (MA^+ = methylammonium) [41–43]. The diffuse reflectance spectrum of $MHyCuCl_3$ also has a very broad absorption band with a maximum of about 850 nm, which is caused by Cu^{2+} *d-d* transitions in the D_{4h} coordination centers [41,43,44]. The presence of this band for $MHyCuCl_3$, which is composed of $CuCl_6$ octahedra, indicates a strong Jahn–Teller effect causing octahedra elongation, as confirmed by SCXRD studies (see Figure S1).

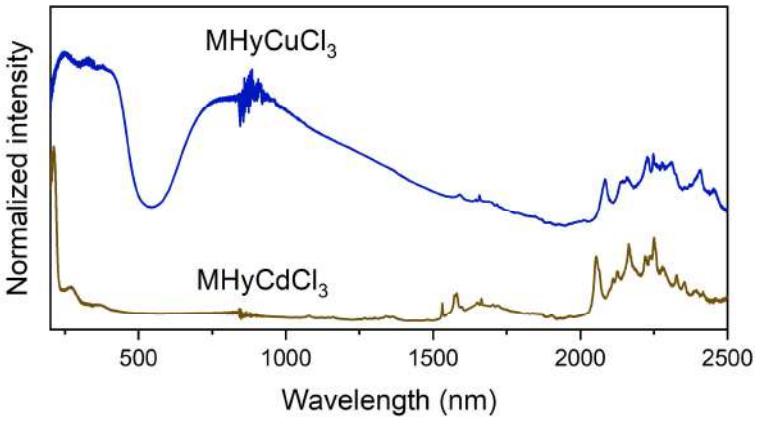

Figure 4. Diffuse reflectance spectra of $MHyM^{II}Cl_3$ (M^{II} = Cd^{2+}, Cu^{2+}).

Both spectra show the presence of several bands above 1500 nm that corresponds to MHy^+ overtones and combinations of vibrational modes.

The diffuse reflectance spectra of $MHyM^{II}Cl_3$ (M^{II} = Cd^{2+}, Cu^{2+}) were further recalculated to determine the bandgap energy using the Kubelka–Munk function $F(R) = (1 - R)^2/2R$, where R is the reflectance. The results are presented in Figure S2, and the obtained bandgap energies are 2.62 and 5.57 eV for $MHyCuCl_3$ and $MHyCdCl_3$, respectively. The obtained values are within the ranges reported previously for $(C_5H_{14}N_2)[CuCl_4]$ (2.56 eV) [41], $FACd(H_2PO_2)_3$ (5.42 eV) [39], and [TPrA]$Cd(dca)_3$ (5.02 eV) [40].

2.4. Magnetic Properties

Figure 5 summarizes the results of the magnetic property measurements carried out for $MHyCuCl_3$, which are very similar to those obtained for $MHyMnCl_3$ [30]. As can be inferred from panel (a), the compound with copper exhibited paramagnetic behavior in almost the entire temperature range studied, and its magnetic susceptibility $\chi(T)$ could be described by the Curie–Weiss law $\chi(T) = C/(T - \theta_p)$ down to a few kelvins with the least-squares fitting parameters C = 0.42(2) emu mol^{-1} K (Curie constant) and $\theta_p = -1.7(4)$ K (Curie–Weiss temperature); see the thick solid line in Figure 5a. The effective magnetic moment μ_{eff} derived from the Curie constant C was about 1.83(1) μ_B, which was lower than μ_{eff} = 3.55 μ_B expected for a free Cu^{2+} ion with the $3d^9$ electron configuration (i.e., for $S = 1/2$, $L = 2$, $J = 5/2$, $g_J = 1.2$) and only slightly higher than the spin-only magnetic moment of 1.73 μ_B (i.e., calculated for $S = 1/2$, $L = 0$, $J = 1/2$, $g_J = 2$), suggesting a non-negligible, yet still very small, orbital contribution to μ_{eff}. The estimated value of the magnetic moment was, in turn, very close to the averaged experimental value of μ_{eff} reported for paramagnetic salts containing non-interacting Cu^{2+} ions, i.e., 1.83 μ_B. Moreover, the fitted value of C was nearly the same as the RT value of the product χT, i.e., 0.41 emu mol^{-1} K, and the negative sign of θ_p, which indicated the presence of antiferromagnetic correlations in $MHyCuCl_3$, was in full agreement with the concave shape of the $\chi T(T)$ curve observed down to the lowest temperature studied (see Figure 5a, right axis).

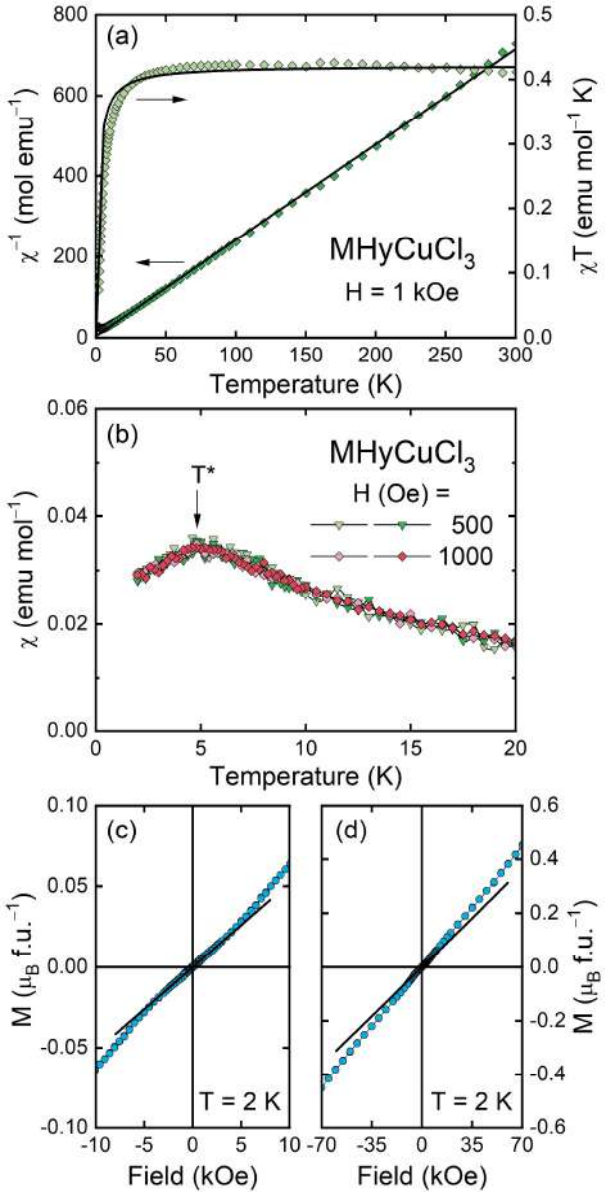

Figure 5. (**a**) $\chi^{-1}(T)$ and $\chi T(T)$ (left and right axis, respectively) of $MHyCuCl_3$ plotted with the fitted Curie–Weiss formula (solid curves). (**b**) $\chi(T)$ measured in the ZFC and FC regimes (bright and dark symbols, respectively); the arrow marks a characteristic temperature T^*. (**c**,**d**) M vs. H plotted in two different field ranges; solid lines show linear $M(H)$ dependence in low fields.

At low temperatures, $MHyCuCl_3$ exhibited a broad anomaly in the temperature variation of the magnetic susceptibility with a maximum at $T^* = 4.8$ K (Figure 5b), being very similar in shape to that found in its counterpart with Mn^{2+}, yet much smaller [30]. In addition, here, $\chi(T)$ was independent of the magnetic field H (at least in low fields) and showed no difference between the curves taken in the ZFC and FC regimes, which suggests antiferromagnetic ordering. The antiferromagnetic-like character of the observed anomaly was confirmed by the linear field dependence of the magnetization (Figure 5c,d), exhibiting only a small change in its slope of about 3 kOe. In the highest field applied (70 kOe), magnetization M is far from any saturation and achieves a value corresponding to only 0.45 μ_B, which is much smaller than $\mu_{ord} = 3$ μ_B and 1 μ_B expected for full and spin-only magnetic moment of Cu^{2+}, respectively.

2.5. Effect of Cd^{2+} and Cu^{2+} on the Properties

Cd^{2+} and Cu^{2+} coordination chemistry significantly differs from Ni^{2+}, Co^{2+}, and Mn^{2+}, which has a significant influence on the structures of $MHyCdCl_3$ and $MHyCuCl_3$ in comparison to previously described compounds. To begin, unlike the other metals discussed, Cd^{2+} has a d^{10} close-shell electronic configuration. Additionally, according to Shannon [45], the ionic radius of Cd^{2+} is greater (95 pm) than that of Ni^{2+}, Co^{2+}, Mn^{2+}, and Cu^{2+} (69–83 pm). Because of these features, the metal cation in $MHyCdCl_3$ is coordinated by six chloride anions, and the MHy^+ cation is excluded from the first coordination sphere. $MHyCdCl_3$ has a triclinic structure, with the MHy^+ cations occupying the voids in the metal–chloride framework. Furthermore, MHy^+ cations are stacked in chains that are linked by stronger intermolecular HB.

The distinct behavior of Cd^{2+} and Cu^{2+} analogues has previously been observed for other hybrids. Among the $AmM^{II}(HCOO)_3$ ($Am^+ = NH_4^+$; $M^{II} = Cd^{2+}$, Co^{2+}, Cu^{2+}, Fe^{2+}, Mg^{2+}, Mn^{2+}, Ni^{2+}, and Zn^{2+}) formates [46], only $AmCd(HCOO)_3$ and $AmCu(HCOO)_3$ members adopt the orthorhombic symmetry, which is lower compared to other hexagonal family members. Furthermore, as the sole representative, the $AmCd(HCOO)_3$ crystal exhibits no PT and adopts a perovskite-like topology [47] in contrast to other members, which have chiral-like crystal architecture.

A similar outcome effect has been observed for $[DMA]M^{II}(HCOO)_3$ (DMA^+ = dimethylammonium; $M^{II} = Cd^{2+}$, Co^{2+}, Cu^{2+}, Fe^{2+}, Mg^{2+}, Mn^{2+}, Ni^{2+}, and Zn^{2+}) formates [46], where only $[DMA]Cu(HCOO)_3$ and $[DMA]Cd(HCOO)_3$ do not undergo PTs. However, the structural symmetry of $[DMA]Cd(HCOO)_3$ is hexagonal in this example, as it is for all members except for $[DMA]Cu(HCOO)_3$, which crystallizes in the lower orthorhombic phase. In this case, the lack of PT has been attributed to the large size of the cavity occupied by DMA^+ and weak HB contacts between cations and the cadmium-formate framework [48].

To determine the reason for the absence of PTs in the $MHyCdCl_3$ and $MHyCuCl_3$, we compared the estimated structural parameters presented in Table 1. As one can see, the tolerance factor (TF) is insufficient to explain this phenomenon, as the values for $MHyCdCl_3$ and $MHyCuCl_3$ are comparable to those reported for $MHyM^{II}Cl_3$ ($M^{II} = Mn^{2+}$, Co^{2+}, Ni^{2+}) [30]. A detailed examination of σ^2 and Δ, which characterize the framework flexibility, reveals that the Jahn–Teller effect prevents the emergence of PT. This elongation also causes the shortest Cu–Cu distances between octahedral chains propagating along the [100] and [001] directions to be 6.988(1) and 6.505(1) Å, respectively. The M^{II}–M^{II} distances or $MHyM^{II}Cl_3$ ($M^{II} = Mn^{2+}$, Co^{2+}, Ni^{2+}) are comparable along the [001] direction (6.489(1)–6.580(1) Å) but much longer along the [100] direction (7.156(1)–7.338(1) Å) [30]. The closest Cu–Cu distances (3.601(1)–3.661(1) Å) along the chain are comparable or slightly higher than the M^{II}–M^{II} distances reported for $M^{II} = Mn^{2+}$, Co^{2+}, Ni^{2+}, which ranged from 3.455(1) to 3.630(1) Å [30]. Furthermore, among the other members, the Cu–N bond is the shortest (2.061(3) Å) and contributes the most covalent bonding (2.116(3), 2.194(2), and 2.365(2) Å for Ni^{2+}, Co^{2+}, and Mn^{2+}, respectively). The substantially elongated $[CuCl_5N]$ octahedra change the available space for MHy^+ cations and allow them to fit better in the accessible void, resulting in a slightly stronger network of HBs. This alignment in the metal-halide network might possibly be due to the ordered state of the MHy^+ cations, which has been reported for $MHyM^{II}Cl_3$ ($M^{II} = Mn^{2+}$, Co^{2+}, Ni^{2+}) in the low-temperature (LT) phase [30].

Table 1. Comparison of tolerance factors (TFs), octahedral angle variance σ^2, and bond length distortion Δ for $MHyM^{II}Cl_3$.

M^{II}	TF	Δ	σ^2 (deg^2)
Mn^{2+} [30]	1.16	0.0240	32.093
Co^{2+} [30]	1.23	0.0311	18.368
Ni^{2+} [30]	1.26	0.0350	9.569
Cu^{2+}	1.24	0.1225	20.661
Cd^{2+}	1.14	0.0210	17.839

The inability of Cd^{2+} ions to bind MHy^{+} also makes these cations better fit into the existing spaces in the network and can get close enough to form a HB between two adjacent cations. The existence of this unique contact, which is stronger than the HBs normally formed between organic cations and ligands, efficiently prevents cation disorder and allows the crystal to adopt lower triclinic symmetry with double edge-connected zig-zag octahedral chains, which is impossible for Ni^{2+}, Mn^{2+}, and Co^{2+} transition metal cations.

3. Materials and Methods

3.1. Synthesis

Methylhydrazine (98%, Sigma-Aldrich, Saint Louis, MS, USA), hydrochloric acid (35–38%, Avantor Performance Materials, Gliwice, Poland), cadmium(II) (98%, Sigma-Aldrich, Saint Louis, MS, USA), and copper(II) (98%, Sigma-Aldrich, Saint Louis, MS, USA) chlorides were obtained commercially and used without additional purification.

In order to grow $MHyM^{II}Cl_3$ (M^{II} = Cu^{2+}, Cd^{2+}) crystals, 1 mmol of $M^{II}Cl_2$ was digested in hydrochloric acid. The solution was then dropwise treated with methylhydrazine (1.5 mmol, 0.2 mL). The resulting mixture was left undisturbed at RT in order to slowly evaporate the solvent. After 7–30 days, the colorless and green crystals of $MHyCdCl_3$ and $MHyCuCl_3$, respectively, were harvested from the solution and air-dried.

3.2. Single-Crystal and Powder X-ray Diffraction

Single-crystal X-ray diffraction (SCXRD) experiments were carried out with MoKα radiation using an Xcalibur four-circle diffractometer (Oxford Diffraction, Abingdon, UK), an Atlas CCD detector, and graphite-monochromated MoKα radiation. Absorption was corrected by multi-scan methods using CrysAlis PRO 1.171.39.46 (Rigaku Oxford Diffraction, 2018, Tokyo, Japan). Empirical absorption correction using spherical harmonics, implemented in the SCALE3 ABSPACK scaling algorithm, was applied. Hydrogen atoms were initially placed based on the local geometry and refined using a riding model. The crystal structure was solved in Olex2 1.5 [49] using SHELXT-2014/4 [50] and refined with SHELXL-2018/3 [51]. The unit cell of $MHyCuCl_3$ (monoclinic, $P2_1/c$ with a = 6.9879(5) Å, b = 7.2032(5) Å, c = 13.0105(9) Å, β = 96.022(7)°, V = 651.3(1) Å^3, Z = 4) was chosen with respect to the analysis of diffraction pattern and systematic extinction rules (Figure S3). $MHyCdCl_3$ (triclinic, $P\bar{1}$ with a = 3.8660(1) Å, b = 9.3519(9) Å, c = 10.0790(3) Å, α = 106.146(6)°, β = 90.080(3)°, γ = 93.734(5)°, V = 349.21(4) Å^3, Z = 2) was treated as a two-domain non-merohedral twin with twin fraction (BASF) equal to 0.5358(11). Experimental details and selected geometric parameters are presented in Tables S3–S5. The main components of the crystal structures of both compounds are presented in Figure S4. The CIF files of reported structures can be found in the CCDC Database with deposition numbers 2047529 for $MHyCdCl_3$ and 2047531 for $MHyCuCl_3$.

Powder X-ray diffraction (PXRD) experiments were performed in the reflection mode on a PANalytical X'Pert diffractometer (Almelo, The Netherlands) equipped with a a PIXcel solid-state linear detector using Ni filtered CuKα radiation (λ = 1.54184 Å). The X-ray diffraction patterns were generated at 30 mA and 40 kV. For the processing of the PXRD data, the program X'Pert High Score Plus (PANalytical, Almelo, The Netherlands) was involved [52].

3.3. Spectroscopic Measurements

IR spectra in the range of 4000–400 cm^{-1} (mid-IR) were measured using a Nicolet iS50 infrared spectrometer (Waltham, MA, USA) using a KBr pellet for $MHyCdCl_3$ and a nujol suspension for $MHyCuCl_3$ due to the reactivity of the compound with KBr. The far-IR spectra in the 400–50 cm^{-1} were measured as a nujol suspension on the polyethylene plate for both compounds. The spectral resolution was set to 2 cm^{-1}.

Raman spectra in the 3500–50 cm^{-1} range with 2 cm^{-1} resolution were measured using a Bruker FT MultiRAM spectrometer (Billerica, MA, USA) equipped with the YAG:Nd laser operating at 1064 nm.

The absorption spectra in the back-scattering mode in the UV-VIS range were measured using an Agilent Cary 5000 spectrophotometer (Santa Clara, CA, USA) equipped with a PryingMantis™ diffuse reflectance accessory.

3.4. Magnetic Measurements

Magnetization of randomly oriented single crystals of $MHyCuCl_3$ was measured using a commercial Quantum Design MPMS XL magnetometer (San Diego, CA, USA) from RT down to 2 K and in applied magnetic fields up to 70 kOe. The diamagnetic background coming from a sample holder was found to be weak and negligible in comparison to the signal coming from the samples; hence its subtraction was omitted. Moreover, no diamagnetization corrections were made to the data reported here.

4. Conclusions

The $MHyM^{II}Cl_3$ (M^{II} = Cd^{2+}, Cu^{2+}) hybrid organic–inorganic compounds were synthesized using a conventional technique of crystallization from solution by gradual evaporation. The $MHyCuCl_3$ analogue crystallizes in the monoclinic $P2_1/c$ symmetry, according to the single-crystal X-ray diffraction measurement. The structure is similar to previously reported M^{II} = Mn^{2+}, Ni^{2+}, and Co^{2+} structures in that it is made up of edge-sharing 1D chains of the $[CuCl_5N]$ octahedra running in the [010] direction. MHy^+ cations in $MHyCuCl_3$ are effectively coordinated by metal ions, as in the three analogues mentioned. $MHyCuCl_3$, as a single representative, on the other hand, experiences no PT, and the MHy^+ cations are ordered at RT. The absence of PTs was attributed to the significant Jahn–Teller effect, which was supported by single-crystal X-ray diffraction and diffuse reflectance measurements. The elongation of the $[CuCl_5N]$ octahedra results in a better fit of organic cations in the accessible space as well as a considerably stronger network of HBs that prevent the disorder. Magnetic measurements revealed that $MHyCuCl_3$ exhibits only smeared antiferromagnetic ordering at roughly 4.8 K and no ferromagnetic correlations up to the highest field investigated. Optical studies confirmed a strong Jahn–Teller distortion and revealed a bandgap of 2.62 eV for this material.

The cadmium analogue differs significantly from the other representatives in the $MHyM^{II}Cl_3$ class of hybrids. The $MHyCdCl_3$ compound crystallizes in triclinic $P\bar{1}$ symmetry, and its crystals are comprised of double zig-zag chains that propagate along the [100] direction. The MHy^+ cations are ordered at RT, and the $MHyCdCl_3$ crystal, like $MHyCuCl_3$, does not experience PTs. In this case, the absence of structural transition was attributed to the presence of a unique HB contact between two neighboring MHy^+ cations, which inhibits cation disorder. This type of contact is possible because, uniquely in this case, the organic cations are not included in the first coordination sphere of the Cd^{2+} ion. According to optical investigations, $MHyCdCl_3$ has a bandgap energy of 5.57 eV.

Supplementary Materials: The following supporting information can be downloaded at: https://www.mdpi.com/article/10.3390/molecules28020473/s1, Figure S1: Single $[CuCl_5N]$ octahedron labeled with atoms and bond lengths in Å; elongated Pb-Cl distances (marked in red and bold) indicate the Jahn–Teller effect; Figure S2: The energy band gap estimation for $MHyM^{II}Cl_3$ (Cd, Cu) crystals using the Kubelka–Munk method; Figure S3: Reciprocal space reconstruction of (a) the *h*0*l* and (b) the *h*1*l* layers in $MHyCuCl_3$; Figure S4: The main components of the crystal structures of (a) $MHyCuCl_3$, and (b) $MHyCdCl_3$ with vibrational ellipsoids at the 50% probability level; Table S1: Factor group analysis for $MHyCdCl_3$ and $MHyCuCl_3$ crystals; Table S2: Assignment of IR and Raman bands for $MHyCdCl_3$ and $MHyCuCl_3$; Table S3: Experimental and refinement details of $MHyCdCl_3$ and $MHyCuCl_3$; Table S4: Selected geometric parameters of $MHyCdCl_3$ and $MHyCuCl_3$ (Å, °); Table S5: Selected hydrogen bond parameters of $MHyCdCl_3$ and $MHyCuCl_3$.

Author Contributions: Conceptualization, J.A.Z. and M.P.; methodology, J.A.Z.; validation, J.A.Z., D.D., D.A.K., A.P. and M.P.; investigation, J.A.Z., D.D., D.A.K. and A.P.; resources, J.A.Z.; data curation, M.P.; writing—original draft preparation, J.A.Z., D.D., D.A.K. and A.P.; writing—review and editing, J.A.Z. and M.P.; visualization, J.A.Z., D.D., D.A.K. and A.P.; supervision, M.P.; project administration, J.A.Z.; funding acquisition, J.A.Z. All authors have read and agreed to the published version of the manuscript.

Funding: This research was supported by the National Science Centre, Poland (Narodowe Centrum Nauki) under project no. 2020/37/N/ST5/02257.

Institutional Review Board Statement: Not applicable.

Informed Consent Statement: Not applicable.

Data Availability Statement: Data available on request.

Conflicts of Interest: The authors declare no conflict of interest.

Sample Availability: Samples of the compounds $MHyCdCl_3$ and $MHyCuCl_3$ are available from the authors.

References

1. Quan, L.N.; Rand, B.P.; Friend, R.H.; Mhaisalkar, S.G.; Lee, T.W.; Sargent, E.H. Perovskites for Next-Generation Optical Sources. *Chem. Rev.* **2019**, *119*, 7444–7477. [CrossRef] [PubMed]
2. Liu, H.; Zhang, H.; Xu, X.; Zhang, L. The Opto-Electronic Functional Devices Based on Three-Dimensional Lead Halide Perovskites. *Appl. Sci.* **2021**, *11*, 1453. [CrossRef]
3. Fu, A.; Yang, P. Lower Threshold for Nanowire Lasers. *Nat. Mater.* **2015**, *14*, 557–558. [CrossRef] [PubMed]
4. Brenner, T.M.; Egger, D.A.; Kronik, L.; Hodes, G.; Cahen, D. Hybrid Organic-Inorganic Perovskites: Low-Cost Semiconductors with Intriguing Charge-Transport Properties. *Nat. Rev. Mater.* **2016**, *1*, 15007. [CrossRef]
5. Li, W.; Zhang, Z.; Bithell, E.G.; Batsanov, A.S.; Barton, P.T.; Saines, P.J.; Jain, P.; Howard, C.J.; Carpenter, M.A.; Cheetham, A.K. Ferroelasticity in a Metal-Organic Framework Perovskite; towards a New Class of Multiferroics. *Acta Mater.* **2013**, *61*, 4928–4938. [CrossRef]
6. Wang, K.; Xiong, J.B.; Xia, B.; Wang, Q.L.; Tong, Y.Z.; Ma, Y.; Bu, X.H. Ferroelastic Phase Transition and Switchable Dielectric Constant in Heterometallic Niccolite Formate Frameworks. *Inorg. Chem.* **2018**, *57*, 537–540. [CrossRef]
7. Nagabhushana, G.P.; Shivaramaiah, R.; Navrotsky, A. Thermochemistry of Multiferroic Organic-Inorganic Hybrid Perovskites $[(CH_3)_2NH_2][M(HCOO)_3]$ (M = Mn, Co, Ni, and Zn). *J. Am. Chem. Soc.* **2015**, *137*, 10351–10356. [CrossRef]
8. Wang, Z.; Hu, K.; Gao, S.; Kobayashi, H. Formate-Based Magnetic Metal-Organic Frameworks Templated by Protonated Amines. *Adv. Mater.* **2010**, *22*, 1526–1533. [CrossRef]
9. Britvin, S.N.; Spiridonova, D.V.; Siidra, O.I.; Lotnyk, A.; Kienle, L.; Krivovichev, S.V.; Depmeier, W. Synthesis, Structure and Properties of Hydrazinium Germanate Pharmacosiderite, $(N_2H_5)_3Ge_7O_{15}(OH)\cdot 2.5H_2O$. *Microporous Mesoporous Mater.* **2010**, *131*, 282–288. [CrossRef]
10. Zhao, T.M.; Chen, S.; Shang, R.; Wang, B.W.; Wang, Z.M.; Gao, S. Perovskite-Like Polar Lanthanide Formate Frameworks of $[NH_2NH_3][Ln(HCOO)_4]$ (Ln=Tb-Lu and Y): Synthesis, Structures, Magnetism, and Anisotropic Thermal Expansion. *Inorg. Chem.* **2016**, *55*, 10075–10082. [CrossRef]
11. Mączka, M.; Sobczak, S.; Kryś, M.; Leite, F.F.; Paraguassu, W.; Katrusiak, A. Mechanism of Pressure-Induced Phase Transitions and Structure-Property Relations in Methylhydrazinium Manganese Hypophosphite Perovskites. *J. Phys. Chem. C* **2021**, *125*, 10121–10129. [CrossRef]
12. Mączka, M.; Ptak, M.; Vasconcelos, D.L.M.; Giriunas, L.; Freire, P.T.C.; Bertmer, M.; Banys, J.; Simenas, M. NMR and Raman Scattering Studies of Temperature-and Pressure-Driven Phase Transitions in $CH_3NH_2NH_2PbCl_3$ Perovskite. *J. Phys. Chem. C* **2020**, *124*, 26999–27008. [CrossRef]
13. Mączka, M.; Gągor, A.; Ptak, M.; Paraguassu, W.; Da Silva, T.A.; Sieradzki, A.; Pikul, A. Phase Transitions and Coexistence of Magnetic and Electric Orders in the Methylhydrazinium Metal Formate Frameworks. *Chem. Mater.* **2017**, *29*, 2264–2275. [CrossRef]
14. Mączka, M.; Gagor, A.; Zareba, J.K.; Stefanska, D.; Drozd, M.; Balciunas, S.; Šimenas, M.; Banys, J.; Sieradzki, A. Three-Dimensional Perovskite Methylhydrazinium Lead Chloride with Two Polar Phases and Unusual Second-Harmonic Generation Bistability above Room Temperature. *Chem. Mater.* **2020**, *32*, 4072–4082. [CrossRef]
15. Mączka, M.; Ptak, M.; Gągor, A.; Stefańska, D.; Zaręba, J.K.; Sieradzki, A. Methylhydrazinium Lead Bromide: Noncentrosymmetric Three-Dimensional Perovskite with Exceptionally Large Framework Distortion and Green Photoluminescence. *Chem. Mater.* **2020**, *32*, 1667–1673. [CrossRef]
16. Oku, T. Crystal Structures of Perovskite Halide Compounds Used for Solar Cells. *Rev. Adv. Mater. Sci.* **2020**, *59*, 264–305. [CrossRef]

17. Capitaine, A.; Sciacca, B. Monocrystalline Methylammonium Lead Halide Perovskite Materials for Photovoltaics. *Adv. Mater.* **2021**, *33*, 2102588. [CrossRef]
18. Rosales, B.A.; Hanrahan, M.P.; Boote, B.W.; Rossini, A.J.; Smith, E.A.; Vela, J. Lead Halide Perovskites: Challenges and Opportunities in Advanced Synthesis and Spectroscopy. *ACS Energy Lett.* **2017**, *2*, 906–914. [CrossRef]
19. Ünlü, F.; Jung, E.; Haddad, J.; Kulkarni, A.; Öz, S.; Choi, H.; Fischer, T.; Chakraborty, S.; Kirchartz, T.; Mathur, S. Understanding the Interplay of Stability and Efficiency in A-Site Engineered Lead Halide Perovskites. *APL Mater.* **2020**, *8*, 070901. [CrossRef]
20. Jena, A.K.; Kulkarni, A.; Miyasaka, T. Halide Perovskite Photovoltaics: Background, Status, and Future Prospects. *Chem. Rev.* **2019**, *119*, 3036–3103. [CrossRef]
21. Stoumpos, C.C.; Malliakas, C.D.; Kanatzidis, M.G. Semiconducting Tin and Lead Iodide Perovskites with Organic Cations: Phase Transitions, High Mobilities, and near-Infrared Photoluminescent Properties. *Inorg. Chem.* **2013**, *52*, 9019–9038. [CrossRef]
22. Raval, P.; Kennard, R.M.; Vasileiadou, E.S.; Dahlman, C.J.; Spanopoulos, I.; Chabinyc, M.L.; Kanatzidis, M.; Manjunatha Reddy, G.N. Understanding Instability in Formamidinium Lead Halide Perovskites: Kinetics of Transformative Reactions at Grain and Subgrain Boundaries. *ACS Energy Lett.* **2022**, *7*, 1534–1543. [CrossRef]
23. Petrosova, H.R.; Kucheriv, O.I.; Shova, S.; Gural'skiy, I.A. Aziridinium Cation Templating 3D Lead Halide Hybrid Perovskites. *Chem. Commun.* **2022**. [CrossRef] [PubMed]
24. Ferrandin, S.; Slawin, A.M.Z.; Harrison, W.T.A. Syntheses and Crystal Structures of a New Family of Hybrid Perovskites: $C_5H_{14}N_2{\cdot}ABr_3{\cdot}0.5H_2O$ (A = K, Rb, Cs). *Acta Crystallogr. Sect. E Crystallogr. Commun.* **2019**, *75*, 1243–1248. [CrossRef]
25. Paton, L.A.; Harrison, W.T.A. Structural Diversity in Non-Layered Hybrid Perovskites of the $RMCl_3$ Family. *Angew. Chemie Int. Ed.* **2010**, *49*, 7684–7687. [CrossRef]
26. Zhang, W.Y.; Tang, Y.Y.; Li, P.F.; Shi, P.P.; Liao, W.Q.; Fu, D.W.; Ye, H.Y.; Zhang, Y.; Xiong, R.G. Precise Molecular Design of High-T_c 3D Organic-Inorganic Perovskite Ferroelectric: [MeHdabco]RbI_3 (MeHdabco = *N*-Methyl-1,4-Diazoniabicyclo[2.2.2]Octane). *J. Am. Chem. Soc.* **2017**, *139*, 10897–10902. [CrossRef]
27. Chen, X.-G.; Gao, J.-X.; Hua, X.-N.; Liao, W.-Q. Three-Dimensional Organic-Inorganic Hybrid Sodium Halide Perovskite: $C_4H_{12}N_2{\cdot}NaI_3$ and a Hydrogen-Bonded Supramolecular Three-Dimensional Network in $3C_4H_{12}N_2{\cdot}NaI_4{\cdot}3I{\cdot}H_2O$. *Acta Crystallogr. Sect. C Struct. Chem.* **2018**, *74*, 728–733. [CrossRef]
28. Mączka, M.; Sobczak, S.; Ratajczyk, P.; Leite, F.F.; Paraguassu, W.; Dybała, F.; Herman, A.P.; Kudrawiec, R.; Katrusiak, A. Pressure-Driven Phase Transition in Two-Dimensional Perovskite MHy_2PbBr_4. *Chem. Mater.* **2022**, *34*, 7867–7877. [CrossRef]
29. Drozdowski, D.; Gągor, A.; Mączka, M. Methylhydrazinium Lead Iodide—One Dimensional Chain Phase with Excitonic Absorption and Large Energy Band Gap. *J. Mol. Struct.* **2022**, *1249*, 131660. [CrossRef]
30. Zienkiewicz, J.A.; Ptak, M.; Drozdowski, D.; Fedoruk, K.; Stefanski, M.; Pikul, A. Hybrid Organic-Inorganic Crystals of [Methylhydrazinium]$M^{II}Cl_3$. *J. Phys. Chem. C* **2022**, *3*, 15809–15818. [CrossRef]
31. Ciupa-Litwa, A.; Ptak, M.; Kucharska, E.; Hanuza, J.; Mączka, M. Vibrational Properties and DFT Calculations of Perovskite-Type Methylhydrazinium Manganese Hypophosphite. *Molecules* **2020**, *25*, 5215. [CrossRef] [PubMed]
32. 3Sreenivasa Kumar, N.R.; Nethaji, M.; Patil, K.C. Synthesis, Characterization and Structure of $(N_2H_5)_3MnX_5$ (X = Cl and Br). *J. Coord. Chem.* **1991**, *24*, 333–337. [CrossRef]
33. Goedken, V.L.; Vallarino, L.M.; Quagliano, J.V. Cationic Ligands. Coordination of the 1,1,1-Trimethylhydrazinium Cation to Nickel(II). *Inorg. Chem.* **1971**, *10*, 2682–2685. [CrossRef]
34. Burns, P.; Hawthorne, F. Static and Dynamic Jahn-Teller Effects in Cu^{2+} Oxysalt Minerals. *Can. Mineral.* **1996**, *34*, 1089–1105.
35. Momma, K.; Izumi, F. IUCr *VESTA 3* for Three-Dimensional Visualization of Crystal, Volumetric and Morphology Data. *J. Appl. Crystallogr.* **2011**, *44*, 1272–1276. [CrossRef]
36. Kubiak, M.; Głowiak, T.; Kozłowski, H. Structure of 2-Amino-4,5-Dihydro-3H^+-1,3-Thiazolium Trichlorocadmate(II), $C_3H_7N_2S^+$ $CdCl_3{}^-$. *Acta Crystallogr. Sect. C Cryst. Struct. Commun.* **1983**, *39*, 1637–1639. [CrossRef]
37. Mączka, M.; Zienkiewicz, J.A.; Ptak, M. Comparative Studies of Phonon Properties of Three-Dimensional Hybrid Organic-Inorganic Perovskites Comprising Methylhydrazinium, Methylammonium, and Formamidinium Cations. *J. Phys. Chem. C* **2022**, *2022*, 4056. [CrossRef]
38. Nakada, K.; Matsumoto, Y.; Shimoi, Y.; Yamada, K.; Furukawa, Y. Temperature-Dependent Evolution of Raman Spectra of Methylammonium Lead Halide Perovskites, $CH_3NH_3PbX_3$ (X=I, Br). *Molecules* **2019**, *24*, 626. [CrossRef]
39. Mączka, M.; Stefańska, D.; Ptak, M.; Gągor, A.; Pikul, A.; Sieradzki, A. Cadmium and Manganese Hypophosphite Perovskites Templated by Formamidinium Cations: Dielectric, Optical and Magnetic Properties. *Dalt. Trans.* **2021**. [CrossRef]
40. Mączka, M.; Stefańska, D.; Zaręba, J.K.; Nyk, M.; Sieradzki, A. Temperature-Dependent Luminescence and Second-Harmonic Generation of Perovskite-Type Manganese and Cadmium Dicyanamide Frameworks Templated by Tetrapropylammonium Cations. *J. Alloys Compd.* **2020**, *821*, 153464. [CrossRef]
41. Bourwina, M.; Msalmi, R.; Walha, S.; Turnbull, M.M.; Roisnel, T.; Costantino, F.; Mosconi, E.; Naïli, H. A New Lead-Free 1D Hybrid Copper Perovskite and Its Structural, Thermal, Vibrational, Optical and Magnetic Characterization. *J. Mater. Chem. C* **2021**, *9*, 5970–5976. [CrossRef]
42. Valiente, R.; de Lucas, M.C.M.; Rodriguez, F. Polarized Charge Transfer Spectroscopy of Cu^{2+} in Doped One-Dimensional $[N(CH_3)_4]CdCl_3$ and $[N(CH_3)_4]CdBr_3$ Crystals. *J. Phys. Condens. Matter* **1994**, *6*, 4527–4540. [CrossRef]
43. Cortecchia, D.; Dewi, H.A.; Yin, J.; Bruno, A.; Chen, S.; Baikie, T.; Boix, P.P.; Grätzel, M.; Mhaisalkar, S.; Soci, C.; et al. Lead-Free $MA_2CuCl_xBr_{4-x}$ Hybrid Perovskites. *Inorg. Chem.* **2016**, *55*, 1044–1052. [CrossRef] [PubMed]

44. Jaffe, A.; Lin, Y.; Mao, W.L.; Karunadasa, H.I. Pressure-Induced Conductivity and Yellow-to-Black Piezochromism in a Layered Cu–Cl Hybrid Perovskite. *J. Am. Chem. Soc.* **2015**, *137*, 1673–1678. [CrossRef]
45. Shannon, R.D. Revised Effective Ionic Radii and Systematic Studies of Interatomie Distances in Halides and Chaleogenides. *Acta Cryst. A* **1976**, *32*, 751–767. [CrossRef]
46. Ptak, M.; Sieradzki, A.; Šimėnas, M.; Maczka, M. Molecular Spectroscopy of Hybrid Organic-Inorganic Perovskites and Related Compounds. *Coord. Chem. Rev.* **2021**, *448*, 214180. [CrossRef]
47. Gómez-Aguirre, L.C.; Pato-Doldán, B.; Stroppa, A.; Yáñez-Vilar, S.; Bayarjargal, L.; Winkler, B.; Castro-García, S.; Mira, J.; Sánchez-Andújar, M.; Señarís-Rodríguez, M.A. Room-Temperature Polar Order in $[NH_4][Cd(HCOO)_3]$—A Hybrid Inorganic-Organic Compound with a Unique Perovskite Architecture. *Inorg. Chem.* **2015**, *54*, 2109–2116. [CrossRef]
48. Szymborska-Małek, K.; Trzebiatowska-Gusowska, M.; Maczka, M.; Gagor, A. Temperature-Dependent IR and Raman Studies of Metal-Organic Frameworks $[(CH_3)_2NH_2][M(HCOO)_3]$, M = Mg and Cd. *Spectrochim. Acta—Part A Mol. Biomol. Spectrosc.* **2016**, *159*, 35–41. [CrossRef]
49. Dolomanov, O.V.; Bourhis, L.J.; Gildea, R.J.; Howard, J.A.K.; Puschmann, H. OLEX2: A Complete Structure Solution, Refinement and Analysis Program. *J. Appl. Crystallogr.* **2009**, *42*, 339–341. [CrossRef]
50. Sheldrick, G.M. *SHELXT*—Integrated Space-Group and Crystal-Structure Determination. *Acta Crystallogr. Sect. A Found. Adv.* **2015**, *71*, 3–8. [CrossRef]
51. Sheldrick, G.M. Crystal Structure Refinement with SHELXL. *Acta Crystallogr. Sect. C Struct. Chem.* **2015**, *71*, 3–8. [CrossRef] [PubMed]
52. Degen, T.; Sadki, M.; Bron, E.; König, U.; Nénert, G. The HighScore Suite. *Powder Diffr.* **2014**, *29*, S13–S18. [CrossRef]

Supporting Information for

Hybrid chlorides with methylhydrazinium cation: $[CH_3NH_2NH_2]CdCl_3$ and Jahn-Teller distorted $[CH_3NH_2NH_2]CuCl_3$

J. A. Zienkiewicz,* D. A. Kowalska, D. Drozdowski, A. Pikul and M. Ptak*

Institute of Low Temperature and Structure Research, Polish Academy of Sciences, Okólna 2, 50-422 Wrocław, Poland

Correspondence: j.zienkiewicz@intibs.pl (J.A.Z.), m.ptak@intibs.pl (M.P.)

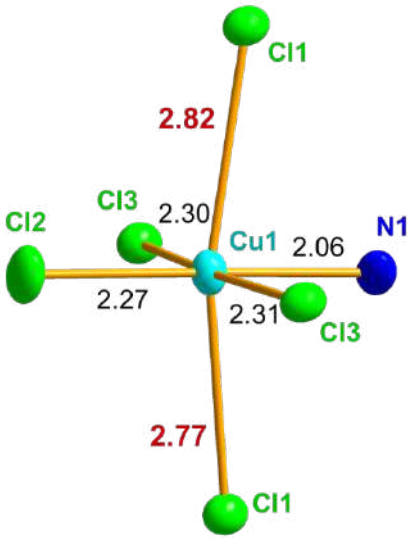

Figure S1. Single $[CuCl_5N]$ octahedron labeled with atoms and bond lengths in Å; elongated Cu–Cl distances (marked in red and bold) indicate the Jahn-Teller effect.

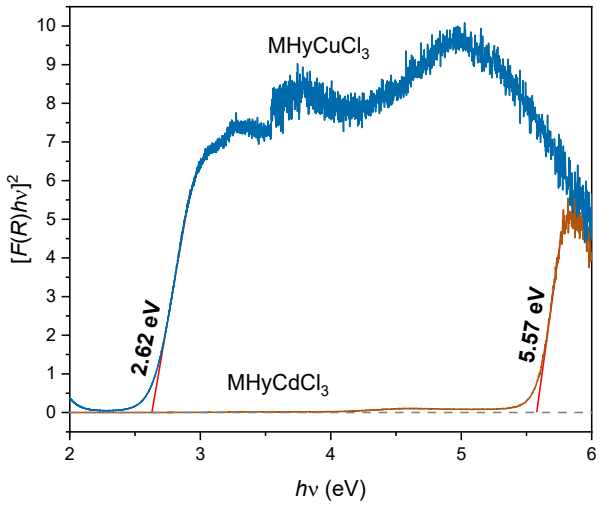

Figure S2. The energy band gap estimation for MHy$M^{II}Cl_3$ (M^{II}=Cd^{2+}, Cu^{2+}) crystals using the Kubelka-Munk method.

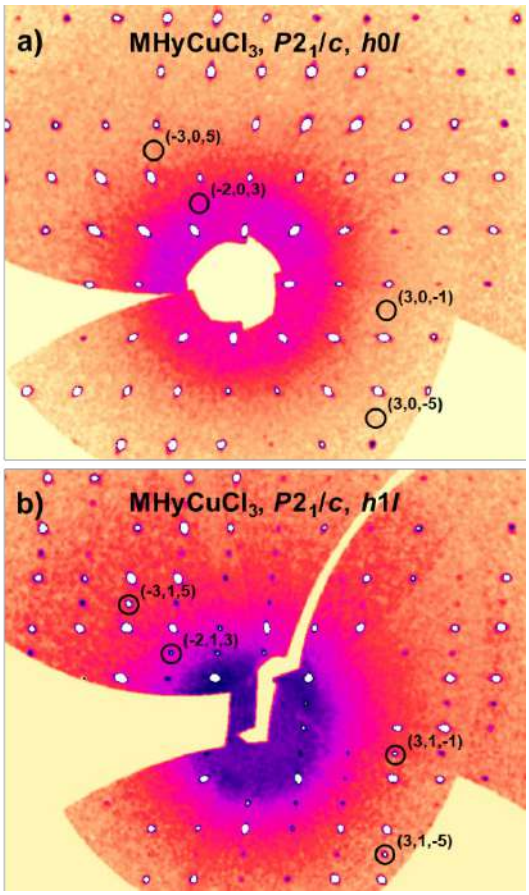

Figure S3. Reciprocal space reconstruction of (a) the *h*0*l* and (b) the *h*1*l* layers in $MHyCuCl_3$; (a) an extinction of reflexes with $l=2n+1$ points out to existence of a *c* glide plane perpendicular to the [010] direction; (b) the analogous reflexes are visible in the *h*1*l* layer. Thus, the unit cell of $P2_1/m$ symmetry and halved *c* axis, as suggested by PLATON software, cannot be chosen.

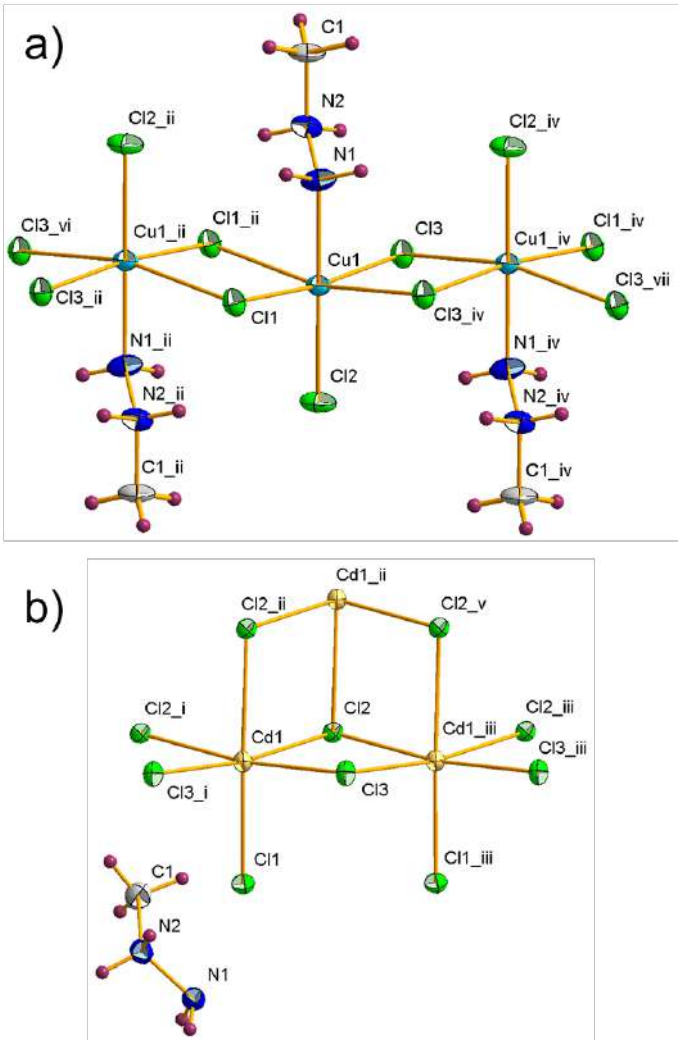

Figure S4. The main components of the crystal structures of a) $MHyCuCl_3$ and b) $MHyCdCl_3$ with vibrational ellipsoids at the 50% probability level. Roman numbers denote symmetry codes: (i) *x*+1, *y*, *z*; (ii) -*x*+1, -*y*+2, -*z*+1; (iii) *x*-1, *y*, *z*; (iv) -*x*+1, -*y*+1, -*z*+1; (v) -*x*, -*y*+2, -*z*+1; (vi) *x*, *y*+1, *z*; (vii) *x*, *y*-1, *z*.

Table S1. Factor group analysis for $MHyCdCl_3$ and $MHyCuCl_3$ crystals.

Ion	Vibrational mode	Free ion symmetry $C_s=m$	Site symmetry [a] $C_1=1$	Factor group symmetry $MHyCdCl_3$ $C_i=\bar{1}$	$MHyCuCl_3$ $C_{2h}=2/m$)
	Internal				
	$\nu_sNH_2+\nu_sNH_2^+$	2A′	2A	$2A_g+2A_u$	$2A_g+2B_g+2A_u+2B_u$
	$\nu_{as}NH_2+\nu_{as}NH_2^+$	2A″	2A	$2A_g+2A_u$	$2A_g+2B_g+2A_u+2B_u$
	$\delta NH_2+\delta NH_2^+$	2A′	2A	$2A_g+2A_u$	$2A_g+2B_g+2A_u+2B_u$
	$\varrho NH_2+\varrho NH_2^+$	2A″	2A	$2A_g+2A_u$	$2A_g+2B_g+2A_u+2B_u$
	$\tau NH_2+\tau NH_2^+$	2A″	2A	$2A_g+2A_u$	$2A_g+2B_g+2A_u+2B_u$
	$\omega NH_2+\omega NH_2^+$	2A′	2A	$2A_g+2A_u$	$2A_g+2B_g+2A_u+2B_u$
	ν_sCH_3	A′	A	A_g+A_u	$A_g+B_g+A_u+B_u$
	$\nu_{as}CH_3$	A′+A″	2A	$2A_g+2A_u$	$2A_g+2B_g+2A_u+2B_u$
MHy^+	δ_sCH_3	A′	A	A_g+A_u	$A_g+B_g+A_u+B_u$
	$\delta_{as}CH_3$	A′+A″	2A	$2A_g+2A_u$	$2A_g+2B_g+2A_u+2B_u$
	ϱCH_3	A′+A″	2A	$2A_g+2A_u$	$2A_g+2B_g+2A_u+2B_u$
	τCH_3	A″	A	A_g+A_u	$A_g+B_g+A_u+B_u$
	$\nu_{as}CNN$	A″	A	A_g+A_u	$A_g+B_g+A_u+B_u$
	δ_sCNN	A′	A	A_g+A_u	$A_g+B_g+A_u+B_u$
	δCNN	A′	A	A_g+A_u	$A_g+B_g+A_u+B_u$
	External				
	T′	2A′+A″	3A	$3A_g+3A_u$	$3A_g+3B_g+3A_u+3B_u$
	L	A′+2A″	3A	$3A_g+3A_u$	$3A_g+3B_g+3A_u+3B_u$
Cl^-	T′		3A	$9A_g+9A_u$	$9A_g+9B_g+9A_u+9B_u$
M^{II}	T′		3A	$3A_g+3A_u$	$3A_g+3B_g+3A_u+3B_u$

Key: [a] the same for both crystals; ν_s, symmetric stretching; ν_{as}, antisymmetric stretching; δ, bending; δ_s, symmetric bending; δ_{as}, antisymmetric bending; ϱ, rocking; τ, twisting; ω, wagging; T′, translation; L, libration; Colors: green, IR- and Raman-active; blue, Raman-active; red, IR-active.

Table S2. Assignment of IR and Raman bands for $MHyCdCl_3$ and $MHyCuCl_3$.

$MHyCdCl_3$		$MHyCuCl_3$		Assignments
Raman	**IR (KBr)**	**Raman**	**IR (nujol)**	
3288m	3290m			$\nu_{as}NH_2$
3240m	3255sh, 3241m, 3223sh	3238sh, 3202w	3236m, 3198m	$\nu_{as}NH_2$
3171w	3164sh	3122w	3161m, 3115m	$\nu_{s}NH_2$
3091vw	3117s, 3085s	3077vw		$\nu_{as}NH_2^+$
3043w, 3027m	3029sh	3048sh, 3041m	3049m, 3033m	$\nu_{s}NH_2^+ + \nu_{as}CH_3$
2962vs	2995sh, 2961sh	2967vs	*	$\nu_{s}CH_3$
2886w, 2806w, 2748w	2839vw, 2747w, 2673sh	2908vw, 2807w	*	νNH_2
1606m	1604m	1587w	1596m	δNH_2
1551m	1558m	1566vw	1564s	δNH_2^+
1477sh, 1460m, 1442s	1481w, 1459w, 1449sh, 1443m	1462vw, 1444vw	*	$\delta_{as}CH_3$
1424w, 1413vw	1420vw, 1414w	1431vw, 1410vw	*	$\delta_{s}CH_3$
	1396m		*	ωNH_2^+
1336w	1331vw		*	τNH_2^+
1210m	1233m, 1209w	1278vw, 1252m	1280vw, 1252s	$\rho CH_3 + \omega NH_2$
1133m, 1101m	1134vw, 1100m	1111w	116sh, 1109s	$\varrho NH_2 + \tau NH_2$
1010m	1011m	1020w	1022w	$\nu_{as}CNN$
900vs	901vw	899w	901m	$\nu_{s}CNN$
876s	883m, 875m, 845w	859vw	857m	ϱNH_2^+
389w	386m	614vw	606s	MHy^+-cage
480m	476m	525vw	528vw	δCNN
283m, 253s, 213s	295w, 243s, 209s, 197s	280sh, 271s, 237w	285vs, 241m	$\nu(M^{II}Cl_5N)/\nu(CdCl_6)+T'(MHy)+L(MHy)$
163sh, 150s, 121m	160vs, 135s	187m, 165m, 126m	192s, 146s, 117s	$\delta(CuCl_5N)/\delta(CdCl_6)+T'(MHy)+L(MHy)$
107sh, 87sh, 86vw	106s, 91m, 73m	107s, 85m, 77sh	95sh	$\delta(CuCl_5N)/\delta(CdCl_6)+T'(MHy)+L(MHy)$

Table S3. Experimental and refinement details of $MHyCdCl_3$ and $MHyCuCl_3$.

	$MHyCdCl_3$	**$MHyCuCl_3$**
Crystal data		
M_r	265.84	216.98
Crystal system, space group	Triclinic, $P\bar{1}$	Monoclinic, $P2_1/c$
Temperature (K)	265	295
a, b, c (Å)	3.8660 (1), 9.3519 (9), 10.0790 (3)	6.9879 (5), 7.2032 (5), 13.0105 (9)
α, β, γ (°)	106.15 (1), 90.08 (1), 93.73 (1)	90, 96.02 (1), 90
V (Å^3)	349.2 (1)	651.3 (1)
Z	2	4
μ (mm^{-1})	4.16	4.47
Crystal size (mm)	0.15 × 0.06 × 0.05	0.14 × 0.09 × 0.06
Data collection		
T_{min}, T_{max}	0.940, 1.000	0.930, 1.000
No. of measured, independent and observed [$I > 2\sigma(I)$] reflections	9262, 2226, 1954	2773, 1237, 979
R_{int}	-	0.023
$(\sin \theta/\lambda)_{max}$ (Å^{-1})	0.610	0.610
Refinement		
$R[F^2 > 2\sigma(F^2)]$, $wR(F^2)$, S	0.021, 0.062, 1.08	0.026, 0.064, 1.12
No. of reflections	2226	1237
No. of parameters	68	66
$\Delta\rho_{max}$, $\Delta\rho_{min}$ (e Å^{-3})	0.43, -0.48	0.37, -0.38

Table S4. Selected geometric parameters of $MHyCdCl_3$ and $MHyCuCl_3$ (Å, °).

$MHyCdCl_3$		**$MHyCuCl_3$**	
Cd1—Cl2^{i}	2.6953 (11)	Cu1—Cl1^{ii}	2.8149 (9)
Cd1—Cl2	2.7124 (11)	Cu1—Cl1	2.3141 (8)
Cd1—Cl2^{ii}	2.6978 (10)	Cu1—Cl3	2.2990 (8)
Cd1—Cl3	2.6259 (11)	Cu1—Cl3^{iv}	2.7692 (9)
Cd1—Cl3^{i}	2.6235 (11)	Cu1—Cl2	2.2691 (10)
Cd1—Cl1	2.5228 (10)	Cu1—N1	2.061 (3)
Cl2^{ii}—Cd1—Cl2	82.38 (3)	Cl1—Cu1—Cl1^{ii}	89.46 (3)
Cl2^{i}—Cd1—Cl2	91.27 (3)	Cl1—Cu1—Cl3^{iv}	88.95 (3)
Cl2^{i}—Cd1—Cl2^{ii}	84.13 (3)	Cl3—Cu1—Cl1	172.80 (3)
Cl3^{i}—Cd1—Cl2^{i}	86.71 (3)	Cl3—Cu1—Cl1^{ii}	90.03 (3)
Cl3^{i}—Cd1—Cl2^{ii}	90.56 (3)	Cl3^{iv}—Cu1—Cl1^{ii}	166.92 (3)
Cl3—Cd1—Cl2^{i}	172.71 (3)	Cl3—Cu1—Cl3^{iv}	89.93 (3)
Cl3^{i}—Cd1—Cl2	172.82 (3)	Cl2—Cu1—Cl1	92.98 (3)
Cl3—Cd1—Cl2	86.30 (3)	Cl2—Cu1—Cl1^{ii}	96.07 (3)
Cl3—Cd1—Cl2^{ii}	88.73 (3)	Cl2—Cu1—Cl3	94.21 (3)
Cl3^{i}—Cd1—Cl3	94.86 (3)	Cl2—Cu1—Cl3^{iv}	96.98 (3)
Cl1—Cd1—Cl2^{i}	93.53 (3)	N1—Cu1—Cl1	86.47 (8)
Cl1—Cd1—Cl2^{ii}	174.07 (3)	N1—Cu1—Cl1^{ii}	84.58 (8)
Cl1—Cd1—Cl2	92.25 (3)	N1—Cu1—Cl3^{iv}	82.36 (8)
Cl1—Cd1—Cl3^{i}	94.74 (4)	N1—Cu1—Cl3	86.33 (8)
Cl1—Cd1—Cl3	93.44 (3)	N1—Cu1—Cl2	179.15 (8)
Cd1^{iii}—Cl2—Cd1^{ii}	95.87 (3)	Cu1—Cl3—Cu1^{iv}	90.07 (3)
Cd1^{ii}—Cl2—Cd1	97.62 (3)		
Cd1^{iii}—Cl2—Cd1	91.27 (3)		
Cd1^{iii}—Cl3—Cd1	94.86 (3)		

Symmetry code(s): (i) *x*+1, *y*, *z*; (ii) -*x*+1, -*y*+2, -*z*+1; (iii) *x*-1, *y*, *z*; (iv) -*x*+1, -*y*+1, -*z*+1.

Table S5. Selected hydrogen bond parameters of $MHyCdCl_3$ and $MHyCuCl_3$.

D—H···*A*	*D*—H (Å)	H···*A* (Å)	*D*···*A* (Å)	*D*—H···*A* (°)
$MHyCdCl_3$				
N2—H2A···Cl1	0.89	2.46	3.168 (4)	137.4
N2—H2B···N1^{i}	0.89	2.10	2.975 (5)	166.6
N1—H1A···Cl3^{ii}	0.89	2.59	3.404 (4)	151.7
N1—H1B···Cl1^{iii}	0.85	2.68	3.384 (4)	140 (4)
$MHyCuCl_3$				
N2—H2A···Cl1^{iv}	0.89	2.48	3.157 (3)	132.8
N2—H2B···Cl1^{v}	0.89	2.51	3.269 (3)	143.7
N2—H2B···Cl3	0.89	2.65	3.206 (3)	121.3
N1—H1A···Cl2^{i}	0.89	2.82	3.426 (3)	126.5
N1—H1B···Cl2^{vi}	0.89	2.80	3.631 (3)	155.2

Symmetry code(s): (i) *x*+1, *y*, *z*; (ii) *x*+1, *y*-1, *z*; (iii) -*x*+2, -*y*+1, -*z*; (iv) -*x*+1, -*y*+2, -*z*+1; (v) *x*, -*y*+3/2, *z*-1/2; (vi) -*x*+1, -*y*+1, -*z*+1.

***Publikacja* [D5]**

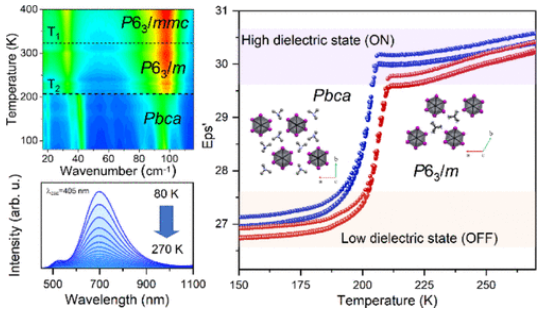

J.A. Zienkiewicz*, K. Kałduńska, K. Fedoruk, A.J. Barros dos Santos, M. Stefański, W. Paraguassu, T.M. Muzioł, M. Ptak

Luminescence and dielectric switchable properties of a 1D (1,1,1-trimethylhydrazinium)PbI_3 hybrid perovskitoid

Inorg. Chem. **2022**, 61 (51), 20886-20895

doi: 10.1021/acs.inorgchem.2c03287 IF = 5,436 140 pkt.

Udział Doktoranta w powstanie pracy:

- Synteza monokryształów $[Me_3Hy]PbI_3$ metodą przeciwrozpuszalnikową;
- Dyskusja wyników badań cieplnych, określenie mechanizmu termicznego rozkładu;
- Pomiar widm Ramana oraz IR;
- Analiza widm rozproszonego odbicia;
- Pomiar widm Ramana oraz IR, również w funkcji temperatury;
- Zaproponowanie przypisania pasm IR i Ramana;
- Analiza zachowania pasm IR i Ramana w funkcji temperatury, dekonwolucja widm oraz dopasowywanie krzywych Lorentza do danych eksperymentalnych;
- Analiza zachowania pasm Ramana w funkcji ciśnienia, obliczenie współczynników ciśnieniowych poszczególnych pasm;
- Dyskusja wyników;
- Określenie mechanizmów przemian fazowych pod wpływem temperatury i ciśnienia;
- Przygotowywanie manuskryptu, rysunków oraz tabel.

Inorganic Chemistry

pubs.acs.org/IC

Article

Luminescence and Dielectric Switchable Properties of a 1D (1,1,1-Trimethylhydrazinium)PbI_3 Hybrid Perovskitoid

Jan. A. Zienkiewicz,* Karolina Kałduńska, Katarzyna Fedoruk, Antonio J. Barros dos Santos, Mariusz Stefanski, Waldeci Paraguassu, Tadeusz M. Muzioł, and Maciej Ptak

Cite This: *Inorg. Chem.* 2022, 61, 20886−20895

Read Online

ACCESS | Metrics & More | Article Recommendations | Supporting Information

ABSTRACT: The synthesis and investigation of the physicochemical properties of a novel one-dimensional (1D) hybrid organic−inorganic perovskitoid templated by the 1,1,1-trimethylhydrazinium (Me_3Hy^+) cation are reported. $(Me_3Hy)[PbI_3]$ crystallizes in the hexagonal $P6_3/m$ symmetry and undergoes two phase transitions (PTs) during heating (cooling) at 322 (320) and 207 (202) K. X-ray diffraction data and temperature-dependent vibrational studies show that the second-order PT to the high-temperature hexagonal $P6_3/mmc$ phase is associated with a weak change in entropy and is related to weak structural changes and different confinement of cations in the available space. The second PT to the low-temperature orthorhombic *Pbca* phase that corresponds to the high change in entropy and dielectric switching is associated with an ordering of the trimethylhydrazinium cations, re-arrangement and strengthening of hydrogen bonds, and slightly shifted lead-iodide octahedral chains. The high-pressure Raman data revealed two additional PTs, one between 2.8 and 3.2 GPa, related to the symmetry decrease, ordering of the cations, and inorganic chain distortion, and the other in the 6.4−6.8 GPa range related to the partial and reversible amorphization. Optical studies revealed that $(Me_3Hy)[PbI_3]$ has a wide band gap (3.20 eV) and emits reddish-orange excitonic emission at low temperatures with an activation energy of 65 meV.

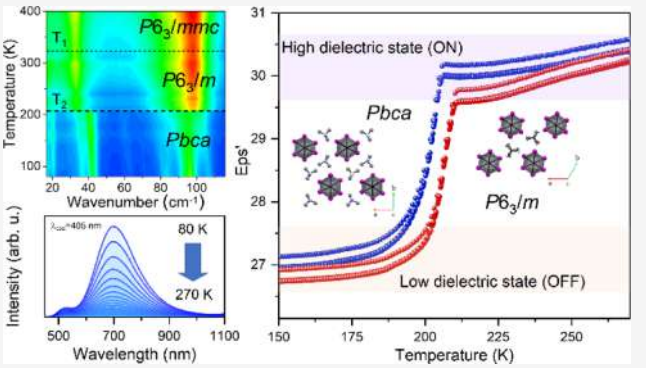

INTRODUCTION

Lead halides are one of the most well-known and researched groups of hybrid organic−inorganic perovskites, particularly for their photovoltaic applications.[1,2] They may exhibit interesting ferroelectric,[3−5] ferroelastic,[6,7] magnetic,[8] second harmonic generation,[9] switchable dielectric,[10] or luminescence[8,10,11] properties. While typical hybrid perovskites with a tolerance factor (TF) of 0.8 to 1 adopt a three-dimensional (3D) corner-sharing structure, compounds with higher TF are more likely to form one- or two-dimensional structures. Some of them have recently been called "perovskitoids."

Stoumpos et al. introduced this new term in materials science to describe compounds having ABX_3 stoichiometry and exclusively face-sharing connectivity between BX_6 octahedra.[12] The physicochemical properties of those hybrids (in oxide nomenclature termed 2H polytype) significantly differ from corner-sharing archetypical perovskites (3C polytype).[12] Later, the term "perovskitoid" was extended to include structures similar to perovskite but with connectivity other than corner-sharing, such as face- or edge-sharing.[13]

Similar to perovskites, perovskitoids also have interesting physicochemical properties that are important for optoelectronics.[12−14] One of them is the improvement of the application properties of perovskite solar cells (PSCs).[15−17] Despite many advantages of the commonly used $MAPbI_3$ and $FAPbI_3$ (MA^+ = methylammonium cation; FA^+ = formamidinium cation), such as low-production costs and high-power conversion efficiency, PSCs have relatively low intrinsic stability. One of the suggested ways to boost photovoltaic properties of PSCs is the passivation of the surface with other 1D perovskitoids templated by bulky ammonium cations, like diethyl-(2-chloroethyl)ammonium,[16] cyclohexylmethylammonium,[18] or methyl-1,3-propanediammonium.[15]

In recent years, hybrids templated by the hydrazinium cation[19] and its derivatives, such as methylhydrazinium[8−11,20] or 1,1-dimethylhydrazinium,[21,22] have received attention. Both cations were successfully employed to form 3D or two-dimensional (2D) perovskites in halide,[9−11] hypophosphite,[8] or formate frameworks.[21−23]

Despite the suggestions that partially substituting the MA^+ in $MAPbI_3$ with the 1,1,1-trimethylhydrazinium cation

Received: September 15, 2022
Published: December 15, 2022

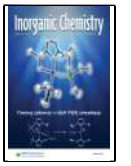

(Me_3Hy^+) would improve the photovoltaic properties and increase the intrinsic stability,[17] there is no published structure and detailed physicochemical characterization of $(Me_3Hy)[PbI_3]$. As a result, we have decided to undertake methodological research on this perovskitoid in order to define the observed phase transitions (PTs), clarify their mechanisms in detail, and to characterize the optical and phonon properties of each phase. We have also performed high-pressure Raman measurements of the low-wavenumber mode region, which is believed to be particularly sensitive even to very subtle structural changes, in order to assess the stability and flexibility of $(Me_3Hy)[PbI_3]$.

EXPERIMENTAL SECTION

Materials and Synthesis. Commercially available lead(II) iodide (99%, Sigma-Aldrich, US), 1,1,1-trimethylhydrazinium iodide (97%, Sigma-Aldrich, US), *N*,*N*-dimethylformamide (DMF) (99.8%, Sigma-Aldrich, US), dimethylsulfoxide (DMSO) (99.9%, Merck), and methyl acetate (99.5%, Sigma-Aldrich, US) were employed without additional purification.

The antisolvent method was used to synthesize $(Me_3Hy)[PbI_3]$. Lead(II) iodide and 1,1,1-trimethylhydrazinium iodide were dissolved in a mixture of DMF and DMSO (5:1). This solution was placed in a glass vial with a loose top, which was then placed in a bigger vial containing methyl acetate (antisolvent). After 5 days, yellow crystals were extracted, filtered from the mother solution, and dried at room temperature in air. The phase purity of crystals was validated by the good agreement of the powder X-ray diffraction (PXRD) pattern with the simulated one based on the single-crystal data (Figure S1).

X-ray Diffraction. All of the data for $(Me_3Hy)[PbI_3]$ were collected using an XtaLAB Synergy-S (Rigaku—Oxford Diffraction) four circle diffractometer with monochromatic and microfocus Mo$K\alpha$ (λ = 0.71073 Å) radiation. Experiments were carried out for a single yellow crystal with dimensions 0.139 × 0.112 × 0.083 mm, at 215, 230, 260, 290, 310, 330, 350, and 375 K temperatures. The complete data sets were collected at 230 and 375 K. For other temperatures, the strategy implemented in CrysAlis was applied. The data sets were obtained and processed with CrysAlisPro software (CrysAlisPRO (ver. 41_64.104a), Oxford Diffraction/Agilent Technologies UK Ltd, Yarnton, England). Absorption correction was also taken into account in CrysAlisPro software. The structures were solved using SHELX2014 program packages by direct methods and refined with the full-matrix least-squares method on F^2.[24] Nonhydrogen atoms in all phases were refined anisotropically, and the positions of hydrogen atoms were idealized with geometry and constrained during refinement with an implemented model in SHELX. The final refinement cycles were performed with the EXTI command due to the very high absorption coefficient reaching ca. 20 mm^{-1}. In the final model of the structure at 375 K, two hydrogen atoms from theNH_2 group are missing. The figures of $(Me_3Hy)[PbI_3]$ were prepared using Mercury 4.0 software.[25]

The powder data for low-temperature (LT) phase were collected using a Rigaku XtaLAB Synergy-S system and Cu$K\alpha$ radiation (λ = 1.54056 Å). The data were reduced first in CrysAlisPro and then in EXPO2014. The cell parameters were found using the McMaille routine, and then the space group was determined. The structure was solved by direct methods followed by a resolution bias modification procedure, and the chain was identified. Fourier recycling resulted in the location of the organic cation. Hydrogen atoms were assigned to calculated positions. To keep the reasonable geometry of the Me_3Hy^+ cation, several restraints for bond lengths and valence angles were applied. In the final model, two nitrogen atoms from the NH_2 group were missing.

The structural data have been deposited at the Cambridge Crystallographic Data Centre [2159778 for the room-temperature (RT) phase and 2159781 for the high-temperature (HT) phase].

Thermal Properties. Heat capacity was measured using a Mettler Toledo DSC-1 calorimeter (DSC, differential scanning calorimetry) with a high resolution of 0.4 μW. Nitrogen was used as a purging gas, and the heating and cooling rate was 5 K min^{-1}. The mass of the measured sample was 16.46 mg. The excess heat capacity associated with the PT was calculated by subtracting from the data a baseline representing the system variation in the absence of PTs.

Thermogravimetric analysis (TGA) was performed in the temperature range of 303−973 K using a PerkinElmer TGA 4000. The sample weighed 28.80 mg, and a 5 K min^{-1} heating rate was used. The atmosphere was pure nitrogen gas.

Dielectric Properties. Dielectric measurements of the examined samples were carried out using a broad-band impedance Novocontrol Alpha analyzer. Since the obtained single crystals were not large enough to perform single-crystal dielectric measurements, a pellet was placed between two copper, flat electrodes of the capacitor with a gap of 0.5 mm. A sinusoidal voltage with an amplitude of 1 V and a frequency in the range of 1 Hz to 1 MHz was applied across the sample. The measurements were taken every 1 K in the temperature range of 140−360 K. The temperature stability of the samples was better than 0.1 K. The temperature was stabilized by means of nitrogen gas using the Novocontrol Quattro system.

Vibrational Properties. The Raman spectra (3500−75 cm^{-1} range) of a polycrystalline sample were recorded at RT using a Bruker FT 100/S spectrometer and YAG:Nd laser excitation at 1064 nm. Temperature-dependent (80−400 K) Raman spectra of randomly oriented single crystals in the 3500−50 cm^{-1} range were measured using a Renishaw inVia Raman spectrometer with a confocal DM2500 Leica optical microscope, a thermoelectrically cooled CCD detector, and an Ar^+ ion laser operating at 488 nm. A Linkam THMS600 stage was used to regulate the temperature.

A Labram Evolution spectrometer from Horiba equipped with a microscope was used to record the high-pressure Raman spectra. A solid-state 514.5 nm laser line was used for excitation. The spectral resolution was set to 2 cm^{-1}. A diamond anvil cell Diacell μScopeDAC-RT(G) from Almax easyLab with a diamond of 0.4 mm culets was used to achieve high pressures. The sample was put into a 100 μm hole drilled in a stainless-steel gasket with a thickness of 200 μm using an electric discharge machine from Almax easyLab. The pressure transmitting medium was Nujol (mineral oil). The values of pressure were calculated using the shifts of the ruby R_1 and R_2 fluorescence lines.

Mid-infrared (IR) (4000−400 cm^{-1}) and far-IR (500−50 cm^{-1}) transmittance spectra were measured in the KBr disc and Nujol mull in a polyethylene plate, respectively, using a Nicolet iS50 FT-IR spectrometer with a resolution of 2 cm^{-1}. The temperature-dependent IR spectra in the 4000−600 cm^{-1} range were collected using a Nicolet iN10 FTIR microscope and a Linkam THMS600 cryostat cell equipped with ZnSe windows.

Optical Properties. The absorption measurement was performed in the back-scattering mode using an Agilent Cary 5000 spectrophotometer. Temperature-dependent emission spectra were measured with the Hamamatsu photonic multichannel analyzer PMA-12 equipped with a BT-CCD linear image sensor. The laser diode operating at 405 nm was applied as an excitation source. The temperature of the samples during emission measurements was controlled by a Linkam THMS600 heating/freezing stage. The luminescence decay profiles were recorded using a femtosecond laser (Coherent Model Libra).

RESULTS AND DISCUSSION

Thermal Properties. The PT behavior of $(Me_3Hy)[PbI_3]$ was investigated before performing detailed crystal structure characterizations. The DSC curve demonstrates that $(Me_3Hy)[PbI_3]$ undergoes two PTs during heating (cooling) at T_1 = 322 (320) K and T_2 = 207 (202) K (Figure S2). The ΔC_p peaks associated with the PT at T_1 are asymmetric and do not show temperature hysteresis between heating and cooling cycles (Figure 1). The associated change in entropy (ΔS) varies continuously with temperature, indicating the second-

https://doi.org/10.1021/acs.inorgchem.2c03287
Inorg. Chem. 2022, 61, 20886−20895

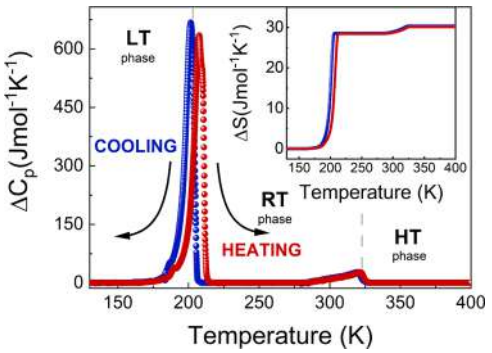

Figure 1. Temperature dependence of the excess heat capacity (ΔC_p) obtained for heating (red) and cooling (blue); the inset shows the corresponding change of entropy (ΔS).

order nature of PT at T_1. The heat capacity peaks associated with PT at T_2, on the other hand, are symmetrical, sharp, and with thermal hysteresis (5 K), indicating a first-order PT. This is further supported by the associated discontinuous change in ΔS (see Figure 1). The entropy changes were experimentally determined to be approximately 1.8 J mol^{-1} K^{-1} at T_1 and 28.5 J mol^{-1} K^{-1} at T_2.

According to X-ray diffraction (XRD) data (see further sections of this paper), the Me_3Hy^+ cations exhibit a sixfold disorder above T_2. Assuming that the LT phase III is completely ordered, the PT at T_2, separating the RT (II) and LT phases, according to the Boltzmann equation, would have a ratio of $N_{RT}/N_{LT} = 6$, where N_i is the number of accessible microstates in the ith phase and R is the gas constant. As a result, the predicted entropy change at T_2 would be around 15 J mol^{-1} K^{-1}. Nearly twice as low as the experimental value may imply that this PT is more complicated than a simple order−disorder model would predict.

The estimate of the ΔS is higher than expected, suggesting that the disorder may be caused by both the movement of the cations and the disturbance of the entire skeleton. A further increase in entropy after going from RT to the HT phase is associated with subtle changes in unit cell parameters (see further sections). Furthermore, the total change of ΔS in $(Me_3Hy)[PbI_3]$ is higher than recently reported for other known lead iodides, such as (methylhydrazinium)$_2$[PbI$_4$] (2D) (~2.88 J mol^{-1} K^{-1}), (*N*-methyldabconium)[PbI$_3$] (1D) (~4.3 J mol^{-1} K^{-1}), and (*R*-2-methylpiperidinium)[PbI$_3$] (1D) (~29.5 J mol^{-1} K^{-1}) analogues.[26−28]

Thermal stability has been used to evaluate the thermal stability of $(Me_3Hy)[PbI_3]$. The compound is stable up to roughly 573 K, according to the registered TGA curve shown in Figure S3. The $(Me_3Hy)[PbI_3]$ decomposes in three stages, with weight losses of around 4.7, 19.2, and 44.8% at inflection points at 595, 650, and 830 K, respectively. According to the literature data, the first step of trimethylhydriazine decomposition leads to *N*-methylmetanimine and the release of methylamine,[29] which is in good agreement with the registered weight loss. The residual *N*-methylmetaniminium lead iodide decomposes into *N*-methylmetanimine, PbI_2, and HI in the subsequent stage at 650 K.[30] The third stage involves the formation of HCN, CH_4, and the I_2 molecules, as well as residual of pure lead.[30]

Dielectric Properties. In order to characterize the dielectric response of $(Me_3Hy)[PbI_3]$, the complex dielectric permittivity as a function of frequency and temperature was investigated. Parts a and b of Figure 2 show the temperature dependences of the real ε' and imaginary ε'' parts of the

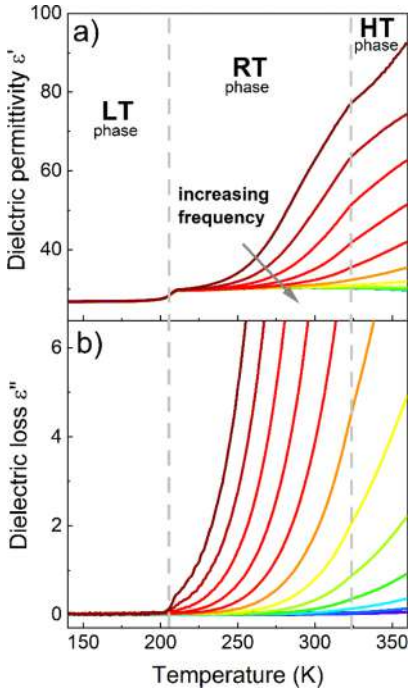

Figure 2. Temperature dependence of the dielectric permittivity (a) and dielectric loss (b) as a function of temperature measured for the pelletized $(Me_3Hy)[PbI_3]$ during heating. The dashed lines represent the PT temperatures determined by DSC measurements.

complex dielectric permittivity $\varepsilon^* = \varepsilon' - i\varepsilon''$. During heating, after the PT at T_2, ε' first shows a step-like rise from 26.5 to 30.4. Such a sharp increase in the dielectric response related to a first-order PT is a common example of the phenomenon called dielectric switching.[21,28,31,32] During continued heating, a high-frequency dispersion becomes dominant in the RT phase, which is most likely associated with ionic/electrical conductivity processes. Some hybrid perovskites, such as $(FA)M^{II}[H_2PO_2]_3$ (M^{II} = Cd, Mn), $(MHy)_2[PbI_4]$, $(MHy)[PbBr_3]$ (MHy^+ = methylhydrazinium cation), or $[(CH_3)_4N]_4Pb_3Cl_{10}$, already demonstrated similar behaviors.[10,11,33,34]

To better visualize the relaxation dynamics and exclude the contribution of electrode polarization, the frequency-dependent electric modulus ($M^* = 1/\varepsilon^*$) for several isotherms was analyzed for selected ones (Figure S4). The occurrence of the ionic/electrical conductivity process at HTs was revealed by isothermal complex electric modulus spectra with the characteristic bell (M'') and step (M') shapes. Additionally, the dielectric permittivity was measured as a function of temperature and time to confirm the phase stability during many switches between on/off states. The material was left at the specified temperatures for 20 min following the switching cycles, which involved temperature changes between 180 and 210 K at a rate of 2 K min^{-1} (Figure 3). These results indicate that the examined material, when subjected to repeated temperature changes, is reversible and stable.

Single-Crystal XRD. Depending on the temperature $(Me_3Hy)[PbI_3]$ crystal exists in three phases, namely HT phase I, RT phase II, and LT phase III. The crystal data and refinement details for I and II phases are gathered in Table S1.

https://doi.org/10.1021/acs.inorgchem.2c03287
Inorg. Chem. 2022, 61, 20886−20895

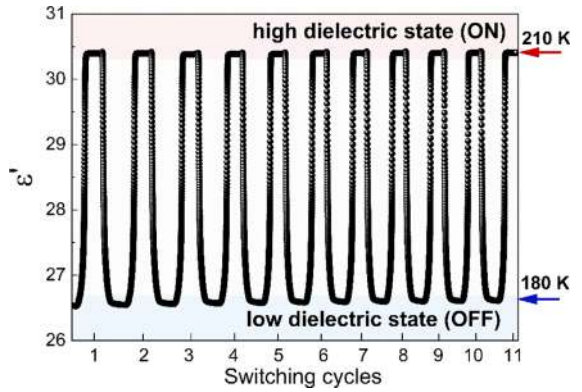

Figure 3. Several cycles of the temperature-induced dielectric switching of $(Me_3Hy)[PbI_3]$ at a frequency of 0.05 MHz.

Tables S2 and S3 list the geometric parameters for phases I and II, respectively. Crystals in the phase I adopt hexagonal $P6_3/mmc$ symmetry with unit cell volume V_{HT} = 658.44 Å^3. The PT to the phase II is associated with a symmetry lowering to $P6_3/m$ and a reduction in the unit cell volume to V_{RT} = 635.57 Å^3. The disappearance of c planes during PT at T_1 ($P6_3/mmc \rightarrow P6_3/m$) was confirmed by systematic absence analysis. Eventually, each structure-solving attempt with higher symmetry in phase II failed. In phase III, $(Me_3Hy)[PbI_3]$ crystal alters symmetry to the orthorhombic system with the *Pbca* space group.

It should be highlighted that structural and symmetry modifications justify DSC data showing a strong peak at T_2 and a weak one at T_1. In the former case, this strong peak, with a corresponding high change in entropy, represents considerable symmetry and unit cell volume change. In the latter case, both parameters change slightly, and the crystal structure is very similar. Furthermore, repeated cycle diffraction experiments in the 215−375 K range showed that crystal-to-crystal PT at T_1 is totally reversible and the crystal integrity is fully preserved. In contrast, the PT at T_2 leads to permanent crystal disintegration and multidomain diffraction pattern (see powder experiments).

In phases I and II, the inorganic part of the structure was built by two Pb^{2+} cations and six I^- ions. The face-sharing octahedral chain is created by $[PbI_6]^{4-}$ ions with three iodine atoms shared between every two octahedra (Figure 4).

The polymer chains are oriented along with the [001] direction, and the distance between the Pb atoms in the chain is $c/2$. The distance between adjacent lead atoms in the directions [100] and [010] defines the parameters a and b of the unit cell and is at 230 and 375 K, respectively, 9.620 and 9.774 Å. The organic part of the unit cell contains Me_3Hy^+, located in the voids of the framework. They fill the whole available volume, assuring dense packing. In I and II, cations show significant disorder due to rotation around sixfold inversion axes (N1 nitrogen atom is located at this axis and N2 in the m plane). The positions of the organic part are stabilized by a system of N−H···I and C−H···I hydrogen bonds. Due to the high symmetry, the intermolecular interactions are multiplied by symmetry operations, and the robust hydrogen bond network is created. Selected examples of contacts for II were presented in Table S4. For phase I, only C−H···I interactions were found (Table S5). No N−H···I interactions were found for the structure model in the HT phase, which is related to the high measurement temperature resulting in missing hydrogens in the amino group. The hydrogens from

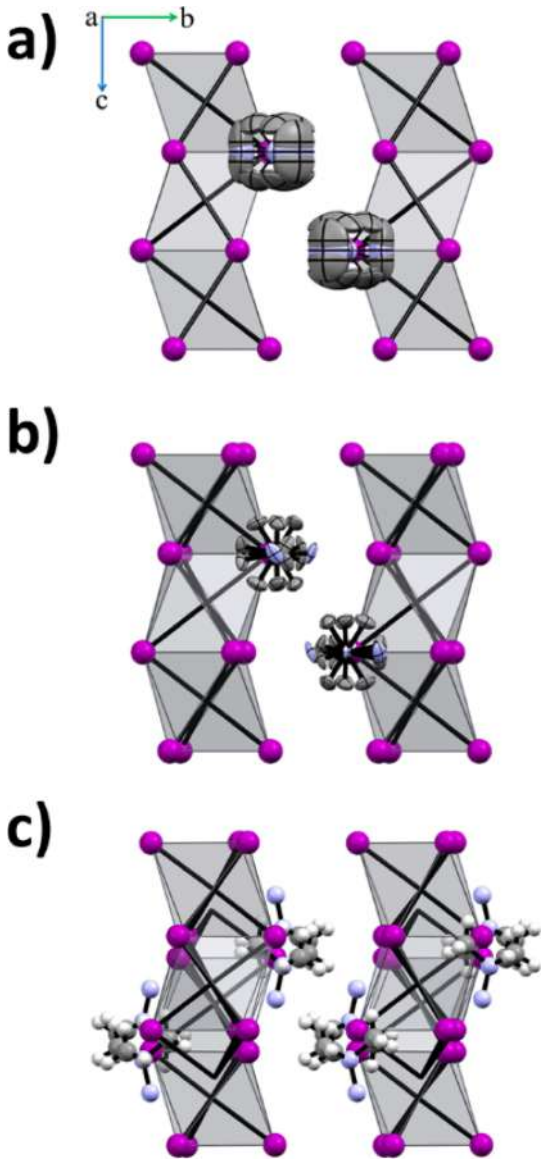

Figure 4. Packing of $(Me_3Hy)[PbI_3]$ at 375 K (I) (a) and at 230 K (II) (b) (with the thermal ellipsoids plotted at 30% probability) and at 190 K (III) (c) (structure solved from powder measurement); all structures are plotted along the [100] direction; hydrogen atoms are omitted for clarity.

the terminal NH_2 group cannot be observed from electron density because of higher thermal distortion parameters related to the elevated experiment temperature.

The PT at T_1 is connected with distortions in the organic part. The chain structure is composed of slightly distorted octahedra. It is rigid and remains unchanged with temperature and symmetry increase (Figure S5). The values of the I−Pb−I angles are practically identical for both polymorphs, being ca. 86 and 94°. Similarly, Pb−I distances are nearly identical—3.2361 and 3.2279 Å, in I and II, respectively. It is justified by subtle changes in cell parameters and cell volume. The c parameter shows some fluctuations (Figure 5), whereas for a, we observed a steady increase. The most linear increase was found for the cell volume, which showed an expansion of ca. 3.6% with a temperature increase from 215 to 375 K.

The single crystal studies for phase III (below 205 K) showed that single crystals crack into several domains related

https://doi.org/10.1021/acs.inorgchem.2c03287
Inorg. Chem. 2022, 61, 20886−20895

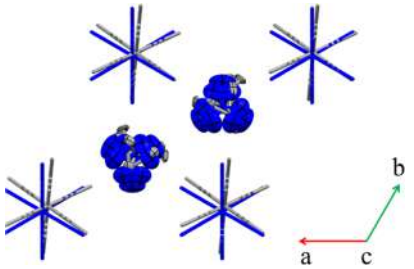

Figure 5. Superposition of $(Me_3Hy)[PbI_3]$ structures at 375 K (blue, phase I) and at 230 K (gray, phase II) with the thermal ellipsoids plotted at 30% probability (along the [001] direction); hydrogen atoms are omitted for clarity.

by rotation around the *c* axis (Figure S6). The treatment of them as domains of the twinned crystal failed. These experiments provided cell parameters, but the space group was incorrectly assigned and SHELXT[24] did not show a reasonable solution in the correct space group. Hence, the powder experiments were carried out (obtained data is in Table S6).

The cell parameters of the LT phase III showed that the volume expanded by approximately four times, and the *c* parameter remained retained. This parameter corresponds to the chain direction, forming the most robust part of the structure. Hence, we can assume that this topology might be preserved. The structure determination from powder data indicated a centrosymmetric *Pbca* space group. The structure clearly confirms that the chain composed of face-sharing PbI_6 octahedra is robust and did not undergo disruption despite the single crystal integrity being lost. The Pb−I distances range from 3.18 to 3.28 Å (d_{av} = 3.244 Å), which is comparable to the phases I and II (d_{av} being 3.228 and 3.236 Å for phases II and I, respectively). We conclude that there are subtle changes related to lowered symmetry of the $[PbI_6]^{4-}$ octahedron (Figure 4 and Table S7). It should be noted that adjacent chains are slightly shifted. It can be assessed by lead atom position—in I and II it is positioned in the (001) plane, whereas in III it is displaced by ca. 0.06 (in fractional coordinates) from this plane. The positions of $(Me_3Hy)^+$ cations in the unit cell show that they were slightly repositioned in the crystal framework (Figure S7), which should affect hydrogen bonds network. Moreover, PT results in reorientation of the cations in phase III, causing that the N−N bonds to be approximately parallel to the chain direction. It is conceivable that this change affects the hydrogen bond network. This effect cannot be fully discussed because in the final model, two hydrogen atoms from the NH_2 group are missing. Nevertheless, the organic cation is trapped in the crystal network by a robust network of C−H···I hydrogen bonds (Table S8). Summarizing, we can hypothesize that crystal cracking below T_2 and PT are related to the mutual shift of adjacent chains, the relocation of the cation and its reorientation in terms of the N−N bond position according to the chain propagation direction. All these factors can affect the N−H···I and C−H···I hydrogen bond network. These structural changes are much more severe than those between I and II phases and justify the big entropy change as well as distinct features observed in IR and Raman spectra (see Temperature-Dependent Raman and IR Studies).

Vibrational Properties. *Molecular Vibrations of the $(Me_3Hy)^+$ Cation.* The free Me_3Hy^+ cation has 42 vibrational degrees of freedom, including 14 stretching (ν) and 28 deformational modes. The stretching modes can be described as $\nu_s NH_2$ (symmetric), $\nu_{as} NH_2$ (antisymmetric), 3× $\nu_s CH_3$, 6× $\nu_{as} CH_3$, νNN, ν_sCNC, and ν_{as}CNC, whereas the bending as δNH_2 (bending), ρNH_2 (rocking), τNH_2 (twisting), ωNH_2 (wagging), 3× $\delta_s CH_3$, 6× $\delta_{as} CH_3$, 6× ρCH_3, 3× τCH_3, 3× δCNN, and 3× δCNC.

Assignment of Bands. RT Raman and IR spectra are presented in Figure S8. The proposed assignment, presented in Table S9, was based on comparative analysis with literature sources, including papers describing IR and Raman spectra of 1,1,1-methylhydrazinium iodide,[35] coordination nickel(II) compound with 1,1,1-trimethylhydrazinium as ligand[36] and perovskite-like compounds templated by 1,1-dimethylhydrazinium[22] and methylhydrazinium[37,38] cations. Bands corresponding to internal vibrations of Me_3Hy^+ are observed in a characteristic ranges as reported in literature.

The strongest Raman band, which has a maximum at 105 cm^{-1} and an IR counterpart at 101 cm^{-1}, was assigned to Pb−I stretching modes, while the weaker Raman band, which has a maximum at 60 cm^{-1}, was attributed to bending I−Pb−I vibrations as well as librational motions of the entire PbI_6 units.

Temperature-Dependent Raman and IR Studies. In order to understand the mechanisms of PTs, IR and Raman spectra were measured upon heating as a function of temperature in the range of 80−400 K (see Figures S9−S13). As may be seen, IR and Raman spectra evolve with noticeable changes at T_2 and very minor changes at T_1. This is consistent with the XRD measurements, which demonstrate an increase in symmetry from orthorhombic to hexagonal at T_2 and maintain hexagonal symmetry at T_1. Furthermore, it can be noticed that PT at T_2 causes strong splitting of the IR and Raman bands, which are due to symmetry change and the expected increased number of inequivalent Me_3Hy^+ cations in phase III. Furthermore, all the IR and Raman bands are very narrow in phase III, suggesting that the organic cations become fully ordered. The abrupt nature of the changes seen at T_2 demonstrates that organic cations completely order shortly below T_2 rather than gradually freeze upon cooling.

The Me_3Hy^+ cation is distinct among other hydrazine derivatives since only one amino group may create hydrogen bonding with the PbI_6 octahedra. The positions of bands corresponding to stretching vibrations of the NH_2 terminal group are a determinant of the strength of these interactions. Lorentz curves were used to fit spectra in order to identify shifts in band maxima and variations in full-width-at-half-maxima (fwhm) with temperature. Figures 6 and 7 show results obtained for stretching vibrations of the NH_2 terminal group. The positions of bands and fwhms hardly change during PT at T_1. In contrast, at T_2, a majority of bands are downshifted in phase III. The most pronounced shifts, by 16.4 and 15.8 cm^{-1}, were noticed for the Raman band at 3313 cm^{-1} and the IR band at 3314 cm^{-1}, respectively (see Figure 6). Additionally, while changes in fwhms at T_1 are undetectable, shifts at T_2 are accompanied by a considerable strong narrowing of bands, decreased most by 17.7 cm^{-1} for the Raman band at 3313 cm^{-1} (Figure 7). These findings suggest that the HB network is irrelevant to the mechanism of PT at T_1, while it is reorganized and strengthened during PT at T_2, which is driven by the ordering of the Me_3Hy^+ cations. This implies that phase III is stabilized by stronger HBs, which prevent further disorder of the cations and cause their lock-in. The same results are achieved by observing other characteristic

https://doi.org/10.1021/acs.inorgchem.2c03287
Inorg. Chem. 2022, 61, 20886−20895

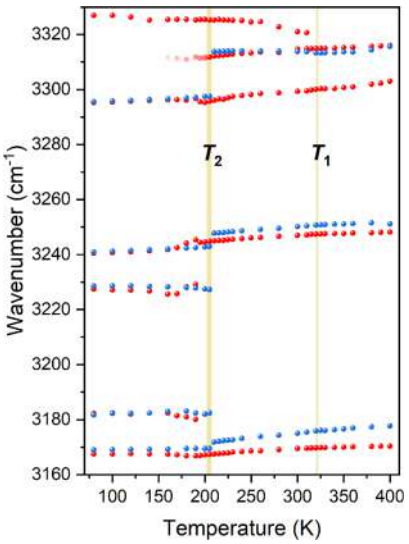

Figure 6. Thermal evolution of positions of the Raman (blue) and IR (red) bands corresponding to stretching vibrations of the amino group; vertical lines correspond to temperatures of PTs determined from DSC.

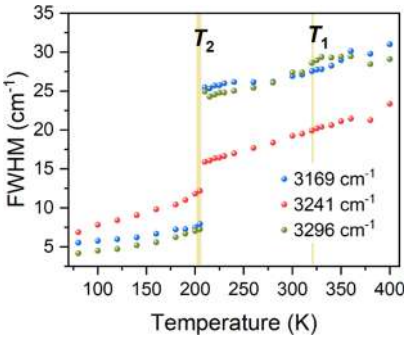

Figure 7. Thermal evolution of fwhms of the Raman bands corresponding to stretching vibrations of the amino group; vertical lines correspond to temperatures of PTs determined from DSC.

vibrations related to the amino group (Figure S14). In addition, the δNH_2 and ρNH_2 vibrations are more sensitive to PT, exhibiting modest inflections at T_1.

The thermal behavior of vibrational modes corresponding to the skeleton of Me_3Hy^+ cations (without H atoms) is depicted in Figure S15. Changes at T_1 are, as predicted, within the fitting error, but they are apparent at T_2. However, the changes at T_2 are minor, implying that the geometry of the skeleton is only marginally changed during this PT.

The positions of bands corresponding to stretching and bending vibrations of methyl groups shift during PT at T_2 (see Figure S16), which supports the dynamic character of this PT. The variations at T_1 are less pronounced because they are likely related to confinement changes induced by changes in cell volume.

The significant splitting and narrowing of low-wavenumber Raman modes below T_2 demonstrate that the symmetry is reduced to orthorhombic (Figure S17). The splitting of the Raman band near 100 cm^{-1} into three narrow components also demonstrates the presence of unequal Pb−I bonds in the LT phase. This kind of splitting needs to be connected with distortion of the lead-iodide chains. Moreover, the abrupt evolution of Raman spectra at T_2 confirmed the discontinuous nature of the transformation.

High-Pressure Raman Studies. In order to better understand the stability of $(Me_3Hy)[PbI_3]$, the low-wavenumber Raman spectra were measured as a function of pressure (Figure 8a). Figure 8b presents the pressure-dependent

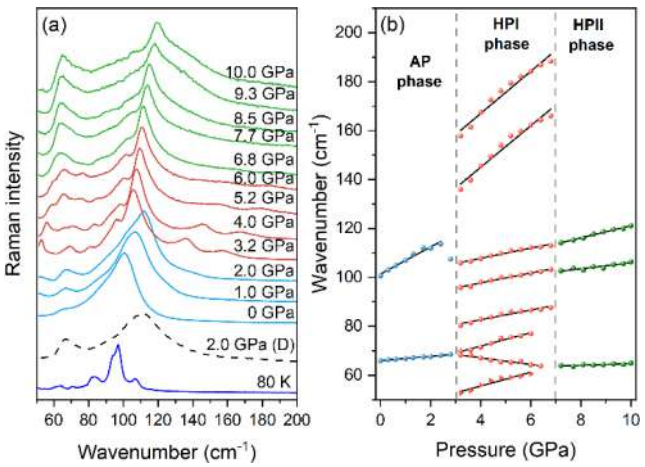

Figure 8. (a) Low-wavenumber Raman bands in the 0−10.0 GPa range during compression compared to a spectrum at 2.0 GPa measured during decompression (D, dashed line) and Raman spectrum obtained at ambient pressure at 80 K; (b) pressure evolution of Raman bands; the vertical dashed lines in (b) indicate the high-pressure PTs.

evolution for the observed modes. The values of pressure coefficients ($\alpha = d\omega/dP$) and wavenumber intercepts at zero pressure (ω_0) derived by fitting the experimental data with a linear function $\omega(P) = \omega_0 + \alpha P$ are shown in Table S10.

At first, the increase in pressure causes only minor changes. At 2.0 GPa, the components of the strongest band at 100 cm^{-1} start to experience intensity changes. At 3.2 GPa, the spectrum changes qualitatively, including the appearance of new bands, indicating a high-pressure PT (1st high-pressure phase, HPI) occurring between 2.8 and 3.2 GPa. The fact that there are more bands suggests that the HPI phase has lower symmetry than ambient-pressure (AP) phase. It is also possible that the symmetry of the HPI phase is orthorhombic based on the comparable number of bands observed at ambient pressure at 80 K (see Figure 8a). Strong narrowing of low-wavenumber modes also implies that the HPI phase may be ordered.

Furthermore, α coefficients change values, which confirms the PT between 2.8 and 3.2 GPa. Bands shift strongly toward higher wavenumber with increasing pressure in both the AP and HPI phases, indicating significant compression of the Pb−I bonds, similar to $MHyPbCl_3$.[39] A few Raman bands disappear when the pressure rises to 6.4−6.8 GPa, and the remaining bands broaden. This may simply be another PT to 2nd HP (HPII) or start of amorphization. The quality of the crystal remains unchanged up to 10 GPa and after decompression (see Figure S18). However, without more investigation, this is difficult to address. The process is entirely reversible, whether or not there is partial amorphization (see Figure 8a).

Optical Properties. The diffuse reflectance spectrum of $(Me_3Hy)[PbI_3]$ crystals recorded at RT is presented in Figure S19a. It consists of a broad band in the 200−500 nm range. On its edge (at 400 nm) one can observe an excitonic band characteristic for halide perovskites.[10,40] The recalculation of

https://doi.org/10.1021/acs.inorgchem.2c03287
Inorg. Chem. 2022, 61, 20886−20895

the data obtained from the absorption measurements made it possible to determine the energy band gap of the analyzed compound using the Kubelka–Munk function $F(R) = \frac{(1-R)^2}{2R}$, where R stands for reflectance.[41] The band gap energy (E_g) of the $(Me_3Hy)[PbI_3]$ crystals was calculated to be 3.20 eV (Figure S19b). The obtained value is similar to the size of the energy band gap of other 1D iodide hybrid perovskites (2.58–3.18 eV),[42] but higher compared to organic or inorganic 3D analogues such as $MAPbI_3$ (1.57 eV), $FAPbI_3$ (1.48 eV), or $CsPbI_3$ (1.73 eV).[43]

The temperature-dependent emission spectra of $(Me_3Hy)[PbI_3]$ crystals measured in the range of 80–270 K in 5 K steps at 405 nm is plotted in Figure 9a. It can be seen that the

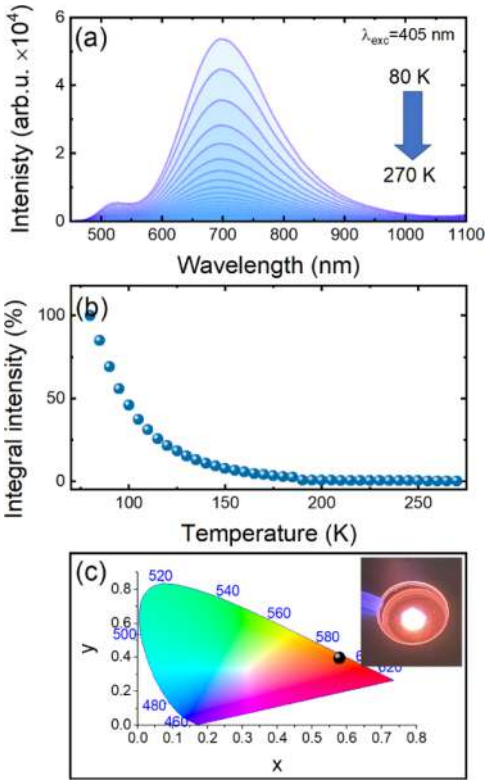

Figure 9. Temperature-dependence emission spectra (a), integral emission intensity (b) and the CIE chromaticity coordinates (c) of $(Me_3Hy)[PbI_3]$ crystals. Inset presents the photograph of the glowing sample.

emission bands cover a wide spectral region and exhibit two maxima, weaker and stronger, located at 520 and 700 nm, respectively. It was found that, the most intense luminescence was obtained at 80 K. Heating the sample causes a gradual decrease of its intensity until complete quenching at 190 K (Figure 9b) due to the thermally activated nonradiative decay channels.[44] The large Stokes shift between the excitonic absorption and the nearest emission band (120 nm) (Figure S20), the large fwhm of the main emission band (over 200 nm), and the strong temperature quenching of luminescence lead to the conclusion that the origin of the transition recorded in Figure 9a is associated with self-trapped excitons (STEs).[10,44−47] The presence of two bands indicates the existence of two kinds of defects with different depths. It is worth noting that excitation of the sample with the 405 nm line or with laser diodes of higher energy, that is, 266 and 375 nm, results in the absence of an emission band that could be assigned to FE (free exciton) and BE (bounded exciton), as shown in Figure S21. Since the position of the emission bands does not change with increasing temperature, the chromaticity coordinates were determined for the measurement performed at 80 K and presented on the CIE diagram (Figure 9c).

In order to study the thermal kinetics of $(Me_3Hy)[PbI_3]$ crystals, the following expression was used: $I = \frac{I_0}{1 + \frac{\Gamma_0}{\Gamma_v} e^{-E/kT}}$, where I is the intensity, I_0 is the initial intensity at LT, Γ_v denotes the radiative decay rate, Γ_0 is the attempt rate for thermal quenching, and ΔE is the activation energy for thermal quenching.[48] This equation has been recalculated as $\frac{\Delta E}{kT} = -\ln\left(\frac{I_0}{I} - 1\right) + \ln\left(\frac{\Gamma_0}{\Gamma_v}\right)$, in order to determine the activation energy of the investigated material (ΔE is the slope of $\ln\left(\frac{I_0}{I} - 1\right)$ as a function of $1/kT$ and $ln\left(\frac{\Gamma_0}{\Gamma_v}\right)$ is a constant). The calculated activation energy of $(Me_3Hy)[PbI_3]$ crystals was determined to be 65 meV (Figure S22).[49]

The luminescence decay profiles of $(Me_3Hy)[PbI_3]$ crystals recorded at the 405 nm excitation line, monitored at 520 and 700 nm at 80 K, corresponding to the two peaks observed in the emission spectrum, are presented in Figure S23. It was found that analyzed compound exhibits curves that can be fitted by a double exponential function regardless of the monitored wavelength using the following expression $I(t) = A_1 \exp\left(-\frac{t}{\tau_1}\right) + A_2 \exp\left(-\frac{t}{\tau_2}\right)$, where $I(t)$ is the emission intensity, A_1 and A_2 are fitting constants, and τ_1 and τ_2 are their corresponding lifetimes. The lifetimes determined for both emission peaks observed at 520 and 700 nm are $\tau_1 \approx 260$ ns and $\tau_2 \approx 725$ ns. Two components visible in the luminescence decays indicate the existence of non-radiation energy transfers in the $(Me_3Hy)[PbI_3]$ crystals. The obtained values are very similar for both bands, which proves the same nature of the defects.

CONCLUSIONS

We synthesized a new perovskitoid 1,1,1-trimethylhydrazinium lead iodide, composed of 1D face-shared chains of $[PbI_6]^{4-}$ octahedra along the [001] direction and disordered organic cations, to evaluate its structural, thermal, phonon, and emission properties using a variety of techniques. DSC measurement revealed the presence of two PTs at 322 (320) K and 207 (202) K upon cooling (heating), and the TGA measurement demonstrated that the material is stable up to 300 °C.

DSC, single-crystal XRD, and vibrational studies revealed that the transformation from the RT $P6_3/m$ phase to the HT $P6_3/mmc$ phase has a second-order nature and is associated with minor structural changes. In contrast, the PT to the LT orthorhombic ($Pbca$) phase has a first-order nature and is characterized by a significant change in entropy. It is associated with the ordering (locking) of the organic cations, rearrangement and strengthening of hydrogen bonds, deformation of the lead-iodide octahedral chains, and an increase in the number of inequivalent structural units. The abrupt character of this PT displays the desired switchable dielectric behavior between low (off) and high (on) dielectric states, designating it as a potentially switchable material.

https://doi.org/10.1021/acs.inorgchem.2c03287
Inorg. Chem. 2022, 61, 20886–20895

The high-pressure Raman data indicated the presence of two high-pressure PTs, in the 2.8−3.2 and 6.4−6.8 GPa ranges. The low-pressure PT is associated with the ordering of the organic cations, compression of PbI_6 octahedra, and distortion of the lead-iodide framework, while the second PT is most likely related to the partial and reversible amorphization.

The band gap energy of the crystals, as determined by optical measurements, is 3.20 eV. At LTs, they emit a reddish-orange broad-band emission that is related to STEs. The activation energy of the emission was found to be 65 meV.

■ ASSOCIATED CONTENT

Supporting Information

The Supporting Information is available free of charge at https://pubs.acs.org/doi/10.1021/acs.inorgchem.2c03287.

Powder XRD, DSC trace, frequency dependencies of the complex dielectric permittivity, complex electrical modules, packing diagrams for phases I, II, and III, RT and temperature-dependent Raman and IR spectra, IR spectrum, positions and bandwidths of selected IR and Raman bands as a function of temperature, pictures of crystals during HP Raman experiment, diffuse reflectance spectrum, emission spectra measured under 266 and 375 nm excitation, crystal data and structure refinement for I and II phases, selected geometric parameters for phases I and II, assignment of IR and Raman bands, Raman pressure intercepts and pressure coefficients (PDF), and crystal structure of $(Me_3Hy)[PbI_3]$ at 230 K (CIF) and 375 K (CIF) (PDF)

Accession Codes

CCDC 2159778 and 2159781 contain the supplementary crystallographic data for this paper. These data can be obtained free of charge via www.ccdc.cam.ac.uk/data_request/cif, or by emailing data_request@ccdc.cam.ac.uk, or by contacting The Cambridge Crystallographic Data Centre, 12 Union Road, Cambridge CB2 1EZ, UK; fax: +44 1223 336033.

■ AUTHOR INFORMATION

Corresponding Author

Jan. A. Zienkiewicz − *Institute of Low Temperature and Structure Research, Polish Academy of Sciences, 50-422 Wrocław, Poland;* orcid.org/0000-0002-4268-0177; Email: j.zienkiewicz@intibs.pl

Authors

Karolina Kałduńska − *Department of Biomedical and Polymer Chemistry, Faculty of Chemistry, Nicolaus Copernicus University in Toruń, 87-100 Toruń, Poland*

Katarzyna Fedoruk − *Institute of Physics, Wrocław University of Science and Technology, 50-370 Wrocław, Poland;* orcid.org/0000-0001-7485-7144

Antonio J. Barros dos Santos − *Department of Physics, Federal University of Pará, Belém 66075110 Pará, Brazil;* orcid.org/0000-0003-0739-7699

Mariusz Stefanski − *Institute of Low Temperature and Structure Research, Polish Academy of Sciences, 50-422 Wrocław, Poland;* orcid.org/0000-0001-7864-6002

Waldeci Paraguassu − *Department of Physics, Federal University of Pará, Belém 66075110 Pará, Brazil*

Tadeusz M. Muzioł − *Department of Inorganic and Coordination Chemistry, Faculty of Chemistry, Nicolaus Copernicus University in Toruń, 87-100 Toruń, Poland*

Maciej Ptak − *Institute of Low Temperature and Structure Research, Polish Academy of Sciences, 50-422 Wrocław, Poland*

Complete contact information is available at: https://pubs.acs.org/10.1021/acs.inorgchem.2c03287

Author Contributions

The manuscript was written through contributions of all authors. All authors have given approval to the final version of the manuscript.

Notes

The authors declare no competing financial interest.

■ ACKNOWLEDGMENTS

The authors would like to acknowledge Prof. Marek Drozd from the Institute of Low Temperature and Structure Research, PAS for performing TGA measurements and the National Science Centre, Poland, for financial support in the course of the realization of a project entitled, Synthesis and physicochemical characterization of novel layered and perovskite-like hybrid organic−inorganic lead halides with protonated alkyl derivatives of hydrazine" (no. UMO-2020/37/N/ST5/02257).

■ REFERENCES

(1) Yoo, J. J.; Seo, G.; Chua, M. R.; Park, T. G.; Lu, Y.; Rotermund, F.; Kim, Y.; Moon, C. S.; Jeon, N. J.; Correa-Baena, V.; Bulović, S. S.; Shin, M. G.; Bawendi, M. G.; Seo, J. Efficient Perovskite Solar Cells via Improved Carrier Management. *Nature* **2021**, *590*, 587−593.

(2) Kojima, A.; Teshima, K.; Shirai, Y.; Miyasaka, T. Organometal Halide Perovskites as Visible-Light Sensitizers for Photovoltaic Cells. *J. Am. Chem. Soc.* **2009**, *131*, 6050−6051.

(3) Liao, W.-Q.; Zhang, Y.; Hu, C.; Mao, J.; Ye, H.; Li, P.; Huang, S. D.; Xiong, R.-G. A Lead-Halide Perovskite Molecular Ferroelectric Semiconductor. *Nat. Commun.* **2015**, *6*, 7338.

(4) Shahrokhi, S.; Gao, W.; Wang, Y.; Anandan, P. R.; Rahaman, Z.; Singh, S.; Wang, D.; Cazorla, C.; Yuan, G.; Liu, J.; Wu, T. Emergence of Ferroelectricity in Halide Perovskites. *Small Methodas* **2020**, *4*, 2000149.

(5) Liu, S.; Zheng, F.; Koocher, N. Z.; Takenaka, H.; Wang, F.; Rappe, A. M. Ferroelectric Domain Wall Induced Band Gap Reduction and Charge Separation in Organometal Halide Perovskites. *J. Phys. Chem. Lett.* **2015**, *6*, 693−699.

(6) Xiao, X.; Li, W.; Fang, Y.; Liu, Y.; Shao, X.; Yang, R.; Zhao, J.; Dai, X.; Zia, R.; Huang, J. Benign Ferroelastic Twin Boundaries in Halide Perovskites for Charge Carrier Transport and Recombination. *Nat. Commun.* **2020**, *11*, 2215.

(7) Warwick, P. D.; Íñiguez, N. C.; Haynes, A. R.; Bristowe, I. First-Principles Study of Ferroelastic Twins in Halide Perovskites. *J. Phys. Chem. Lett.* **2019**, *10*, 1416.

(8) Mączka, M.; Gągor, A.; Pikul, A.; Stefańska, D. Novel Hypophosphite Hybrid Perovskites of $[CH_3NH_2NH_2][Mn(H_2POO)_3]$ and $[CH_3NH_2NH_2][Mn(H_2POO)_{2.83}(HCOO)_{0.17}]$ Exhibiting Antiferromagnetic Order and Red Photoluminescence. *RSC Adv.* **2020**, *10*, 19020−19026.

(9) Mączka, M.; Gagor, A.; Zaręba, J. K.; Stefanska, D.; Drozd, M.; Balciunas, S.; Šimėnas, M.; Banys, J.; Sieradzki, A. Three-Dimensional Perovskite Methylhydrazinium Lead Chloride with Two Polar Phases and Unusual Second-Harmonic Generation Bistability above Room Temperature. *Chem. Mater.* **2020**, *32*, 4072−4082.

(10) Mączka, M.; Ptak, M.; Gągor, A.; Stefańska, D.; Sieradzki, A. Layered Lead Iodide of [Methylhydrazinium]2PbI4 with a Reduced Band Gap: Thermochromic Luminescence and Switchable Dielectric Properties Triggered by Structural Phase Transitions. *Chem. Mater.* **2019**, *31*, 8563−8575.

(11) Mączka, M.; Ptak, M.; Gągor, A.; Stefańska, D.; Zaręba, J. K.; Sieradzki, A. Methylhydrazinium Lead Bromide: Noncentrosymmetric Three-Dimensional Perovskite with Exceptionally Large Framework Distortion and Green Photoluminescence. *Chem. Mater.* **2020**, *32*, 1667−1673.
(12) Stoumpos, C. C.; Mao, L.; Malliakas, C. D.; Kanatzidis, M. G. Structure-Band Gap Relationships in Hexagonal Polytypes and Low-Dimensional Structures of Hybrid Tin Iodide Perovskites. *Inorg. Chem.* **2017**, *56*, 56−73.
(13) Li, X.; He, Y.; Kepenekian, M.; Guo, P.; Ke, W.; Even, J.; Katan, C.; Stoumpos, C. C.; Schaller, R. D.; Kanatzidis, M. G. Three-Dimensional Lead Iodide Perovskitoid Hybrids with High X-Ray Photoresponse. *J. Am. Chem. Soc.* **2020**, *142*, 6625−6637.
(14) Sun, Q.; Xu, Y.; Zhang, H.; Xiao, B.; Liu, X.; Dong, J.; Cheng, Y.; Zhang, B.; Jie, W.; Kanatzidis, M. G. Optical and Electronic Anisotropies in Perovskitoid Crystals of $Cs_3Bi_2I_9$ Studies of Nuclear Radiation Detection. *J. Mater. Chem. A* **2018**, *6*, 23388−23395.
(15) Zhang, F.; Lu, H.; Larson, B. W.; Xiao, C.; Dunfield, S. P.; Reid, O. G.; Chen, X.; Yang, M.; Berry, J. J.; Beard, M. C.; Zhu, K. Surface Lattice Engineering through Three-Dimensional Lead Iodide Perovskitoid for High-Performance Perovskite Solar Cells. *Chem* **2021**, *7*, 774−785.
(16) Kong, T.; Xie, H.; Zhang, Y.; Song, J.; Li, Y.; Lim, E. L.; Hagfeldt, A.; Bi, D. Perovskitoid-Templated Formation of a 1D@3D Perovskite Structure toward Highly Efficient and Stable Perovskite Solar Cells. *Adv. Energy Mater.* **2021**, *11*, 2101018.
(17) Liu, G.; Xu, S.; Zheng, H.; Xu, X.; Xu, H.; Zhang, L.; Zhang, X.; Kong, F.; Pan, X. Boosting Photovoltaic Properties and Intrinsic Stability for MA-Based Perovskite Solar Cells by Incorporating 1,1,1-Trimethylhydrazinium Cation. *ACS Appl. Mater. Interfaces* **2019**, *11*, 38779−38788.
(18) Sun, W.; Zou, J.; Wang, X.; Wang, S.; Du, Y.; Cao, F.; Zhang, L.; Wu, J.; Gao, P. Enhanced Photovoltage and Stability of Perovskite Photovoltaics Enabled by a Cyclohexylmethylammonium Iodide-Based 2D Perovskite Passivation Layer. *Nanoscale* **2021**, *13*, 14915−14924.
(19) Chen, S.; Shang, R.; Hu, K. L.; Wang, Z. M.; Gao, S. $[NH_2NH_3][M(HCOO)_3]$ (M = Mn^{2+}, Zn^{2+}, Co^{2+} and Mg^{2+}): Structural Phase Transitions, Prominent Dielectric Anomalies and Negative Thermal Expansion, and Magnetic Ordering. *Inorg. Chem. Front.* **2014**, *1*, 83−98.
(20) Mączka, M.; Sobczak, S.; Kryś, M.; Leite, F. F.; Paraguassu, W.; Katrusiak, A. Mechanism of Pressure-Induced Phase Transitions and Structure-Property Relations in Methylhydrazinium Manganese Hypophosphite Perovskites. *J. Phys. Chem. C* **2021**, *125*, 10121−10129.
(21) Zienkiewicz, J. A.; Kowalska, D. A.; Fedoruk, K.; Stefanski, M.; Pikul, A.; Ptak, M. Unusual Isosymmetric Order-Disorder Phase Transition in the New Perovskite-Type Dimethylhydrazinium Manganese Formate Exhibiting Ferrimagnetic and Photoluminescent Properties. *J. Mater. Chem. C* **2021**, *9*, 6841−6851.
(22) Zienkiewicz, J. A.; Kucharska, E.; Ptak, M.Mechanism of Unusual Isosymmetric Order-Disorder Phase Transition in [Dimethylhydrazinium]$Mn(HCOO)_3$ Hybrid Perovskite Probed by Vibrational Spectroscopy. *Materials*. **2021**, *14* (). DOI: DOI: 10.3390/ma14143984.
(23) Mączka, M.; Gągor, A.; Ptak, M.; Paraguassu, W.; da Silva, T. A.; Sieradzki, A.; Pikul, A. Phase Transitions and Coexistence of Magnetic and Electric Orders in the Methylhydrazinium Metal Formate Frameworks. *Chem. Mater.* **2017**, *29*, 2264−2275.
(24) Sheldrick, G. M. Crystal Structure Refinement with SHELXL. *Acta Crystallogr., Sect. C: Struct. Chem.* **2015**, *71*, 3−8.
(25) Macrae, C. F.; Sovago, I.; Cottrell, S. J.; Galek, P. T. A.; McCabe, E.; Pidcock, M.; Platings, G. P.; Shields, J. S.; Stevens, M.; Towler, P. A.; Wood, P. A. Mercury 4.0: From Visualization to Analysis, Design and Prediction. *J. Appl. Crystallogr.* **2020**, *53*, 226−235.
(26) Mączka, M.; Zaręba, J. K.; Gągor, A.; Stefańska, D.; Ptak, M.; Roleder, K.; Kajewski, D.; Soszyński, A.; Fedoruk, K.; Sieradzki, A. [Methylhydrazinium]$_2PbBr_4$, a Ferroelectric Hybrid Organic-Inorganic Perovskite with Multiple Nonlinear Optical Outputs. *Chem. Mater.* **2021**, *33*, 2331−2342.
(27) Xue, C.; Yao, Z.-Y.; Zhang, J.; Liu, W.-L.; Liu, J.-L.; Ren, X.-M. Extra Thermo- and Water-Stable One-Dimensional Organic-Inorganic Hybrid Perovskite [N-Methyldabconium]PbI_3 Showing Switchable Dielectrics, Conductivity and Bright Yellow-Green Emission. *Chem. Commun.* **2018**, *54*, 4321−4324.
(28) Peng, H.; Liu, Y.; Huang, X.; Liu, Q.; Yu, Z.; Wang, Z.-X.; Liao, W.-Q. Homochiral One-Dimensional ABX3 Lead Halide Perovskites with High-Tc Quadratic Nonlinear Optical and Dielectric Switchings. *Mater. Chem. Front.* **2021**, *5*, 4756−4763.
(29) Gaber, A. A. M.; Wentrup, C. Pyrolysis of Hydrazine Derivatives and Related Compounds with N-N Single Bonds. *J. Anal. Appl. Pyrolysis* **2017**, *125*, 258−278.
(30) Fujiwara, H.; Egawa, T.; Konaka, S. Electron Diffraction Study of Thermal Decomposition Products of Trimethylamine: Molecular Structure of CH_3-N=CH_2. *J. Mol. Struct.* **1995**, *344*, 217−226.
(31) Trzebiatowska, M.; Mączka, A.; Gagor, A. Pyrrolidinium-Based Cyanides: Unusual Architecture and Dielectric Switchability Triggered by Order − Disorder Process. *Inorg. Chem.* **2020**, *59*, 8855.
(32) Mączka, M.; Nowok, A.; Zaręba, J. K.; Stefańska, D.; Gągor, A.; Trzebiatowska, M.; Sieradzki, A. Near-Infrared Phosphorescent Hybrid Organic − Inorganic Perovskite with High-Contrast Dielectric and Third-Order Nonlinear Optical Switching Functionalities. *ACS Appl. Mater. Interfaces* **2022**, *14*, 1460−1471.
(33) Mączka, M.; Stefańska, D.; Ptak, M.; Gągor, A.; Pikul, A.; Sieradzki, A. Cadmium and Manganese Hypophosphite Perovskites Templated by Formamidinium Cations: Dielectric, Optical and Magnetic Properties. *Dalton Trans.* **2021**, *50*, 2639−2647.
(34) Xue, C.; Wang, S.; Liu, W.-L.; Ren, X.-M. Two-Step Structure Phase Transition, Dielectric Anomalies and Thermochromic Luminescence Behavior in a Direct Bandgap 2D Corrugated Layer Lead Chloride Hybrid of $[(CH_3)_4N]_4Pb_3Cl_{10}$. *Chem.—Eur. J.* **2019**, *25*, 5280−5287.
(35) Kim, Y.; Son, G.; Na, T.; Choi, S. Synthesis and Physical and Chemical Properties of Hypergolic Chemicals Such as N,N,N-Trimethylhydrazinium and 1-Ethyl-4-Methyl-1,2,4-Triazolium Salts. *Appl. Sci.* **2015**, *5*, 1547−1559.
(36) Goedken, V. L.; Vallarino, L. M.; Quagliano, J. V. Cationic Ligands. Coordination of the 1,1,1-Trimethylhydrazinium Cation to Nickel(II). *Inorg. Chem.* **1971**, *10*, 2682−2685.
(37) Ciupa-Litwa, A.; Ptak, M.; Kucharska, E.; Hanuza, J.; Mączka, M. Vibrational Properties and DFT Calculations of Perovskite-Type Methylhydrazinium Manganese Hypophosphite. *Molecules* **2020**, *25*, 5215.
(38) Mączka, M.; Zienkiewicz, J. A.; Ptak, M. Comparative Studies of Phonon Properties of Three-Dimensional Hybrid Organic-Inorganic Perovskites Comprising Methylhydrazinium, Methylammonium, and Formamidinium Cations. *J. Phys. Chem. C* **2022**, *126*, 4048−4056.
(39) Mączka, M.; Ptak, M.; Vasconcelos, D. L. M.; Giriunas, L.; Freire, P. T. C.; Bertmer, M.; Banys, J.; Simenas, M. NMR and Raman Scattering Studies of Temperature-and Pressure-Driven Phase Transitions in $CH_3NH_2NH_2PbCl_3$ Perovskite. *J. Phys. Chem. C* **2020**, *124*, 26999−27008.
(40) Wu, K.; Bera, A.; Ma, C.; Du, Y.; Yang, Y.; Li, L.; Wu, T. Temperature-Dependent Excitonic Photoluminescence of Hybrid Organometal Halide Perovskite Films. *Phys. Chem. Chem. Phys.* **2014**, *16*, 22476−22481.
(41) Kubelka, P. New Contributions to the Optics of Intensely Light-Scattering Materials. Part I. *J. Opt. Soc. Am.* **1948**, *38*, 448−457.
(42) Qian, J.; Guo, Q.; Liu, L.; Xu, B.; Tian, W. A Theoretical Study of Hybrid Lead Iodide Perovskite Homologous Semiconductors with 0D, 1D, 2D and 3D Structures. *J. Mater. Chem. A* **2017**, *5*, 16786−16795.
(43) Eperon, G. E.; Stranks, S. D.; Menelaou, C.; Johnston, M. B.; Herz, L. M.; Snaith, H. J. Formamidinium Lead Trihalide: A Broadly

Tunable Perovskite for Efficient Planar Heterojunction Solar Cells. *Energy Environ. Sci.* **2014**, *7*, 982−988.
(44) Maqbool, S.; Sheikh, T.; Thekkayil, Z.; Deswal, S.; Boomishankar, R.; Nag, A.; Mandal, P. Third Harmonic Upconversion and Self-Trapped Excitonic Emission in 1D Pyridinium Lead Iodide. *J. Phys. Chem. C* **2021**, *125*, 22674.
(45) Nazarenko, O.; Kotyrba, M. R.; Yakunin, S.; Aebli, M.; Rainò, G.; Benin, B. M.; Wörle, M.; Kovalenko, M. V. Guanidinium-Formamidinium Lead Iodide: A Layered Perovskite- Related Compound with Red Luminescence at Room Temperature. *J. Am. Chem. Soc.* **2018**, *140*, 3850−3853.
(46) Nazarenko, O.; Kotyrba, M. R.; Wörle, M.; Cuervo-Reyes, E.; Yakunin, S.; Kovalenko, M. V. Luminescent and Photoconductive Layered Lead Halide Perovskite Compounds Comprising Mixtures of Cesium and Guanidinium Cations. *Inorg. Chem.* **2017**, *56*, 11552−11564.
(47) Adnan, M.; Rao, K. N.; Acharyya, J. N.; Kumar, D.; Dehury, K. M.; Prakash, G. V. Synthesis, Structural, Linear, and Nonlinear Optical Studies of Inorganic−Organic Hybrid Semiconductors ($R-C_6H_4CHCH_3NH_3)_2PbI_4$,(R=$CH_3$, Cl). *ACS Omega* **2019**, *4*, 19565−19572.
(48) Dorenbos, P. Thermal Quenching of Eu^{2+} 5d-4f Luminescence in Inorganic Compounds. *J. Phys.: Condens. Matter* **2005**, *17*, 8103−8111.
(49) Stefańska, D.; Bondzior, B.; Vu, T. H. Q.; Miniajluk-Gaweł, N.; Dereń, P. J. The Influence of Morphology and Eu^{3+} Concentration on Luminescence and Temperature Sensing Behavior of Ba_2MgWO_6 Double Perovskite as a Potential Optical Thermometer. *J. Alloys Compd.* **2020**, *842*, 155742.

https://doi.org/10.1021/acs.inorgchem.2c03287
Inorg. Chem. 2022, 61, 20886−20895

Luminescence and dielectric switchable properties of 1D (1,1,1-trimethylhydrazinium)PbI_3 hybrid perovskitoid

Jan. A. Zienkiewicz,[*,†] Karolina Kałduńska,[§] Katarzyna Fedoruk,[‡] Antonio J. Barros dos Santos[∂], Mariusz Stefanski,[†] Waldeci Paraguassu,[∂] Tadeusz M. Muzioł,[‖] and Maciej Ptak[†]

[†]Institute of Low Temperature and Structure Research, Polish Academy of Sciences, Okólna 2, 50-422 Wrocław, Poland

[‡]Institute of Physics, Wrocław University of Science and Technology, Wybrzeże Wyspiańskiego 27, 50-370 Wrocław, Poland

[§]Department of Biomedical and Polymer Chemistry, Faculty of Chemistry, Nicolaus Copernicus University in Toruń, Gagarina 7, 87-100 Toruń, Poland

[∂]Department of Physics, Federal University of Pará, Campus do Guamá, Rua Augusto Corrêa 01, 66075110 Belém, PA, Brazil

[‖]Department of Inorganic and Coordination Chemistry, Faculty of Chemistry, Nicolaus Copernicus University in Toruń, Gagarina 7, 87-100 Toruń, Poland

Figures

Tables

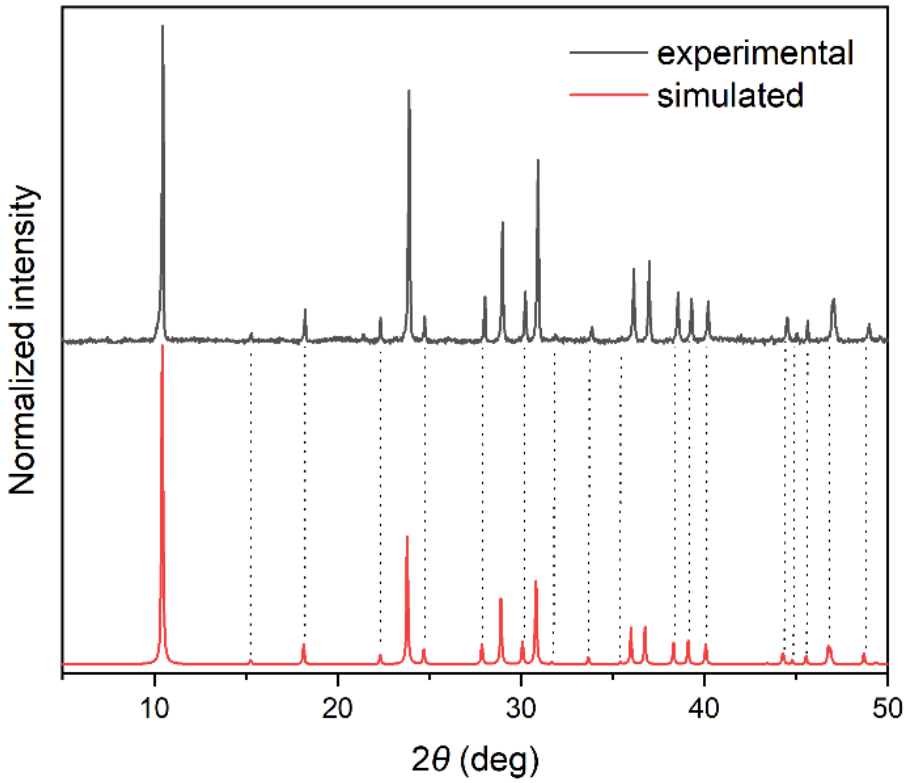

Figure S1. The comparison of an experimental room-temperature XRD pattern with a simulated one based on the single-crystal measurement at 230 K

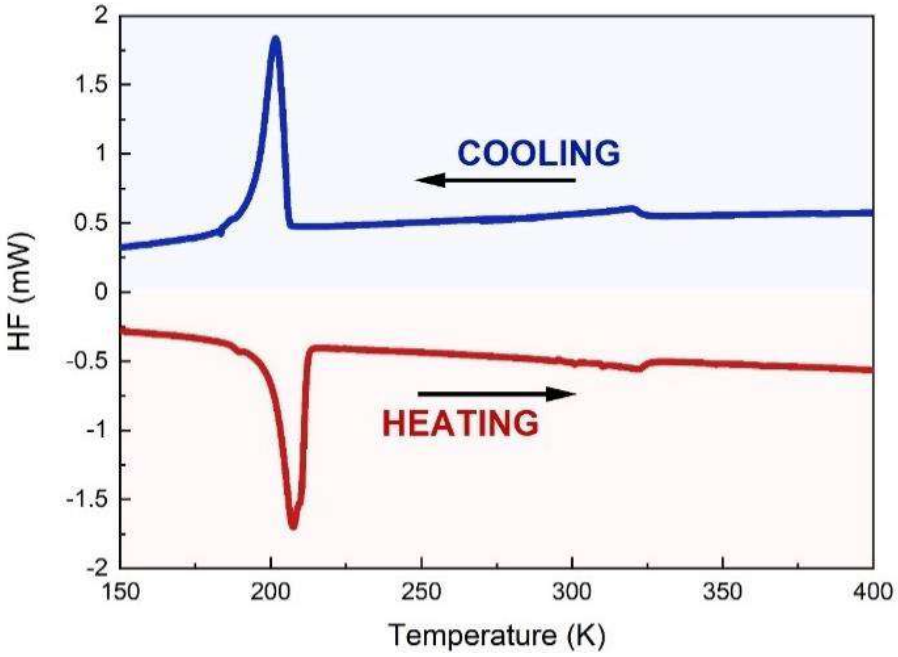

Figure S2. DSC trace for $(Me_3Hy)[PbI_3]$

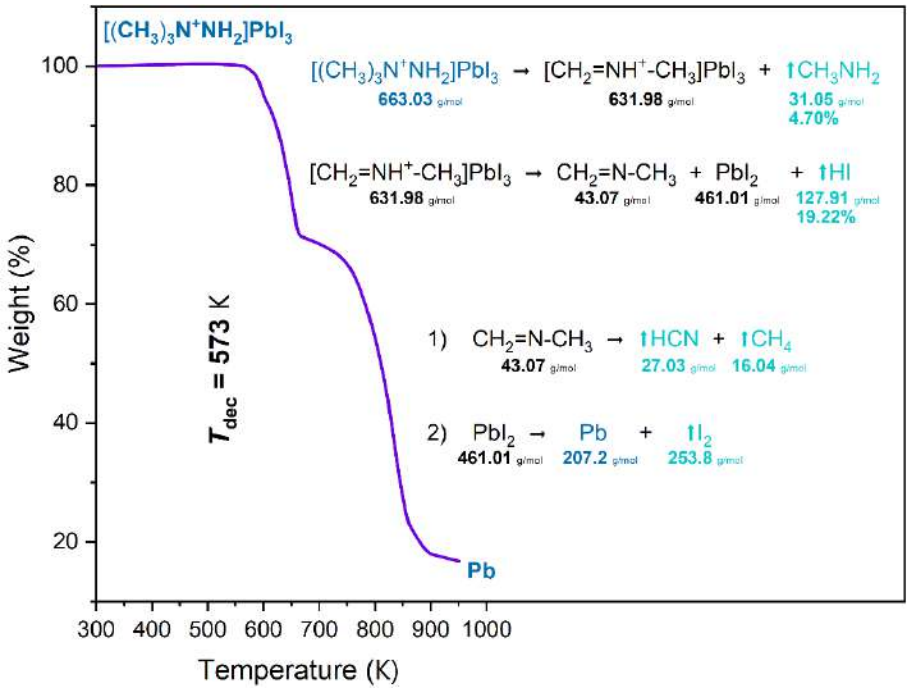

Figure S3. TGA curve for $(Me_3Hy)[PbI_3]$

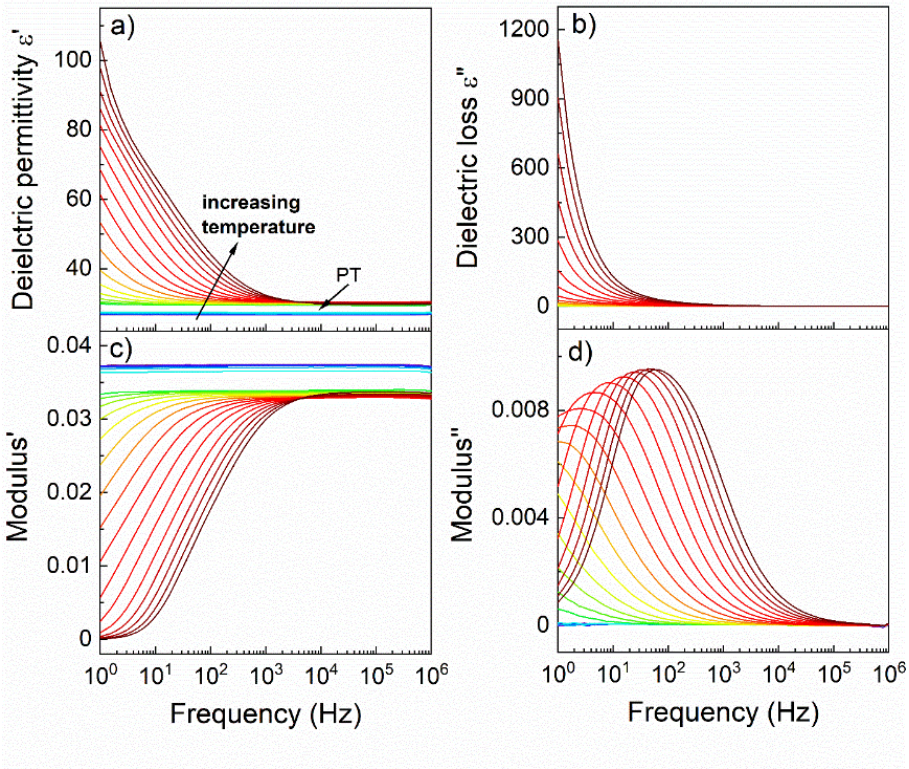

Figure S4. Frequency dependencies of the complex dielectric permittivity and the complex electrical modules

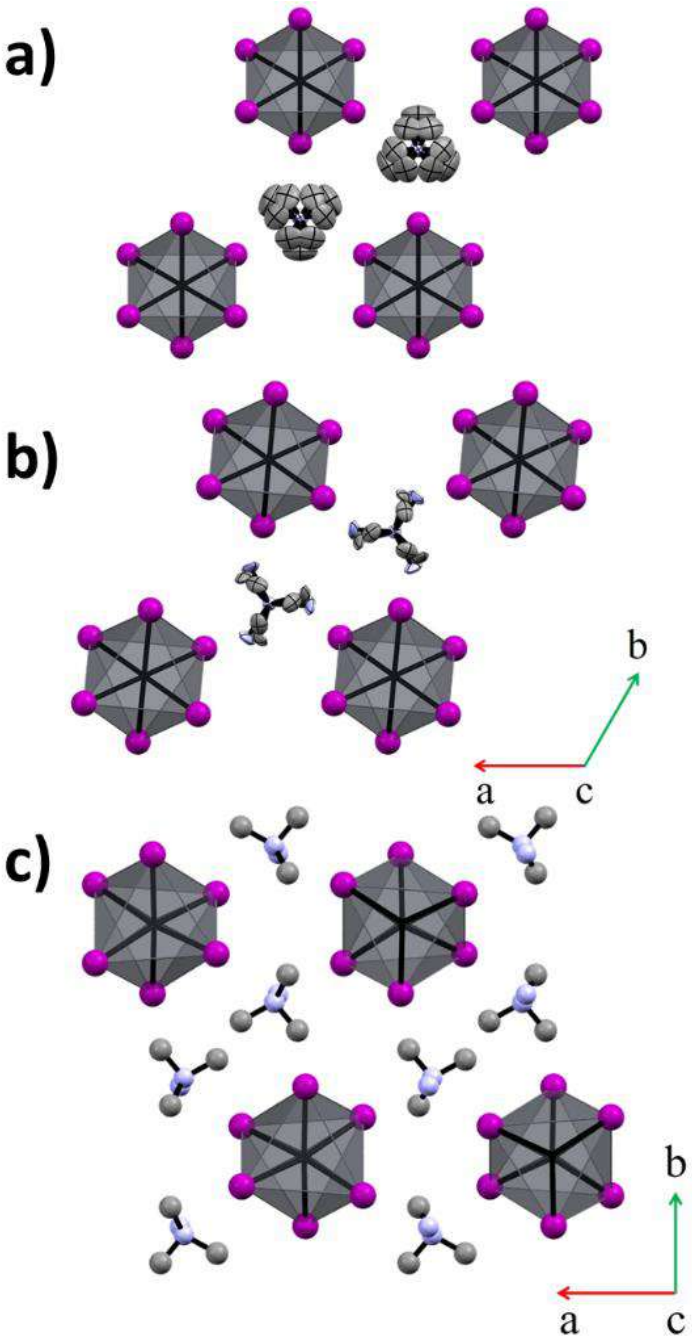

Figure S5. Packing of $(Me_3Hy)[PbI_3]$ at 375 K (phase I) (a) and at 230 K (phase II) (b) (with the thermal ellipsoids plotted at 30% probability) and 190 K (III) (c) (structure solved from powder measurement); all structures are plotted along the [001] direction; hydrogen atoms are omitted for clarity

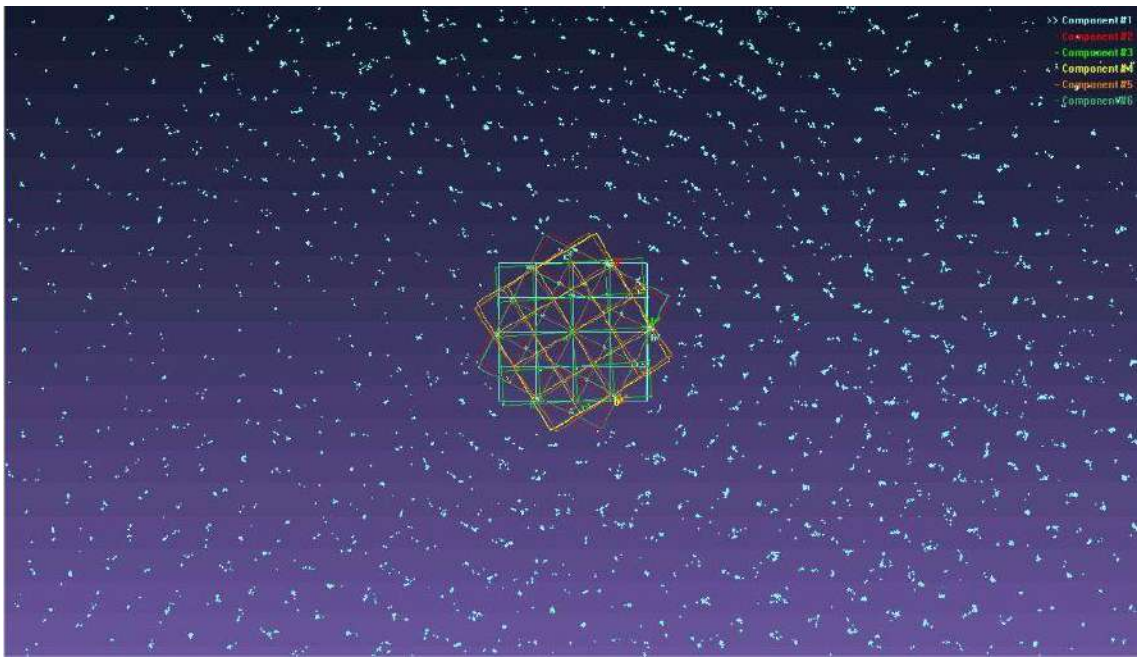

Figure S6. Ewald sphere for six domains detected in the cracked single crystal related by rotation around *c* axis. Their abundance is similar.

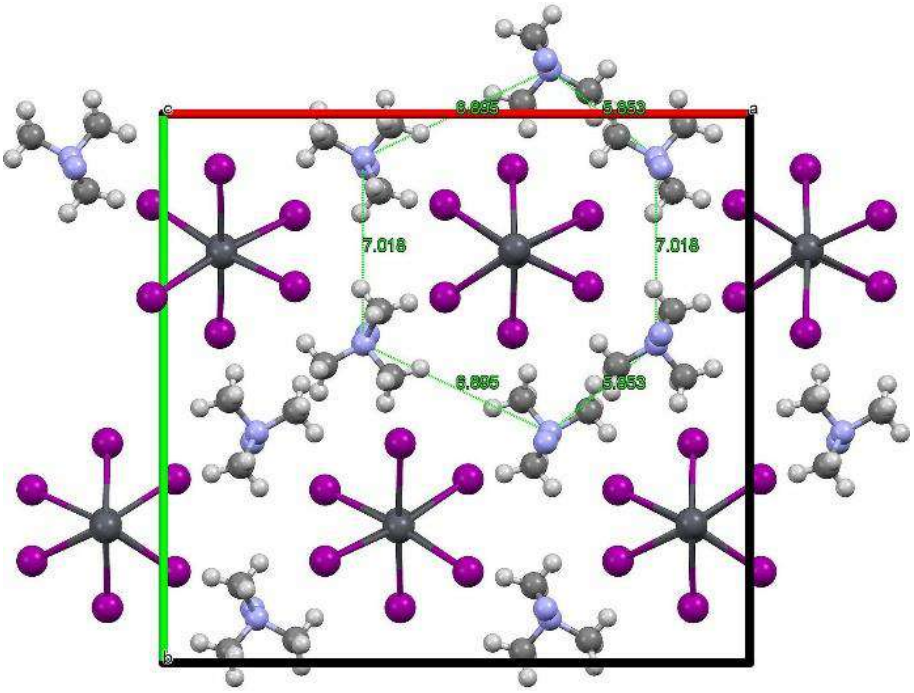

Figure S7. Packing along *c* axis in phase III. It shows maintained chain topology and altered positions of organic cations. Distances are given between central nitrogen atoms of the Me_3Hy^+ cations. Reorientation of the organic cations in terms of N-N bond direction according to chain propagation direction is also visible. In the final model two nitrogen atoms from NH_2 group are missing

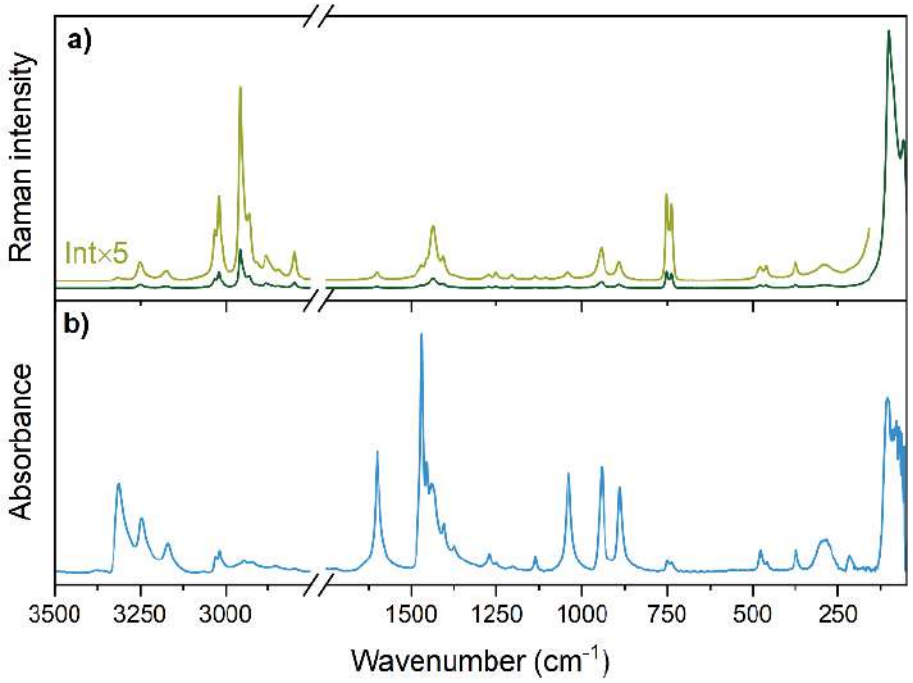

Figure S8. RT Raman (a) and IR (b) spectrum of $(Me_3Hy)[PbI_3]$

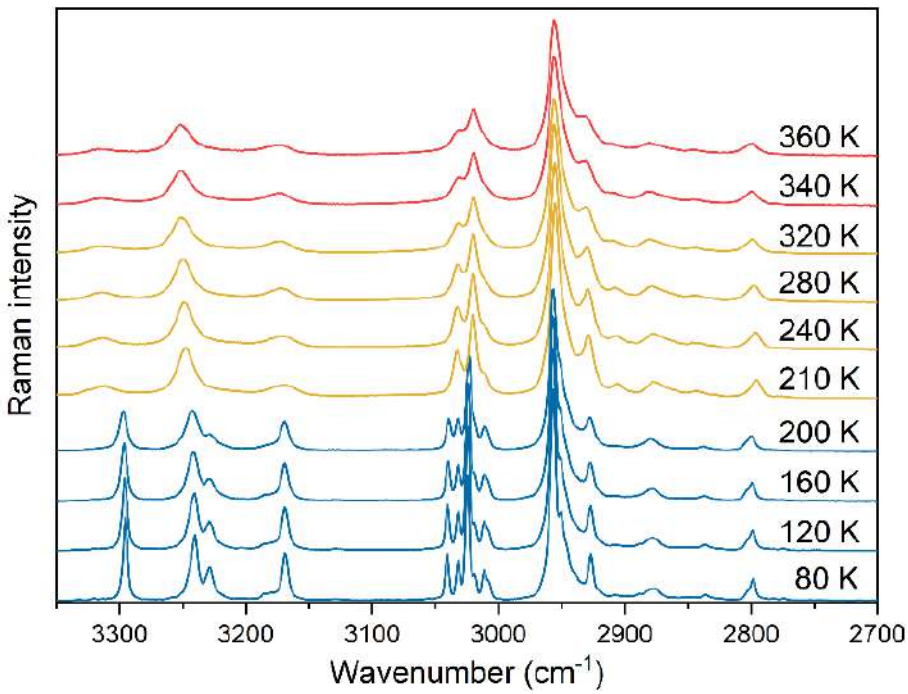

Figure S9. Temperature-dependent Raman spectra in the 3350-2700 cm^{-1} range

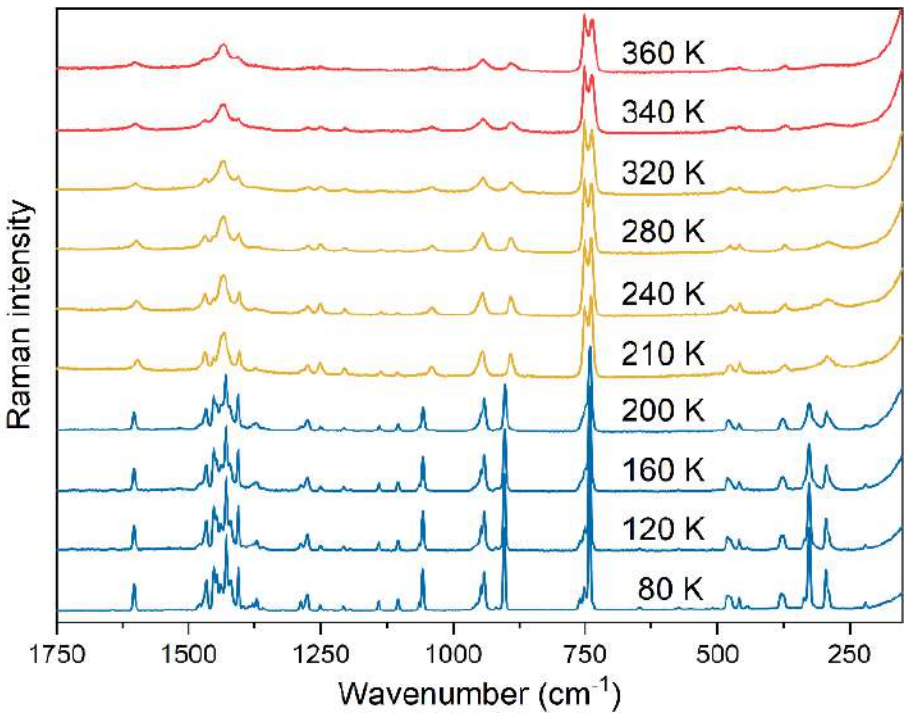

Figure S10. Temperature-dependent Raman spectra in the 1750-150 cm^{-1} range

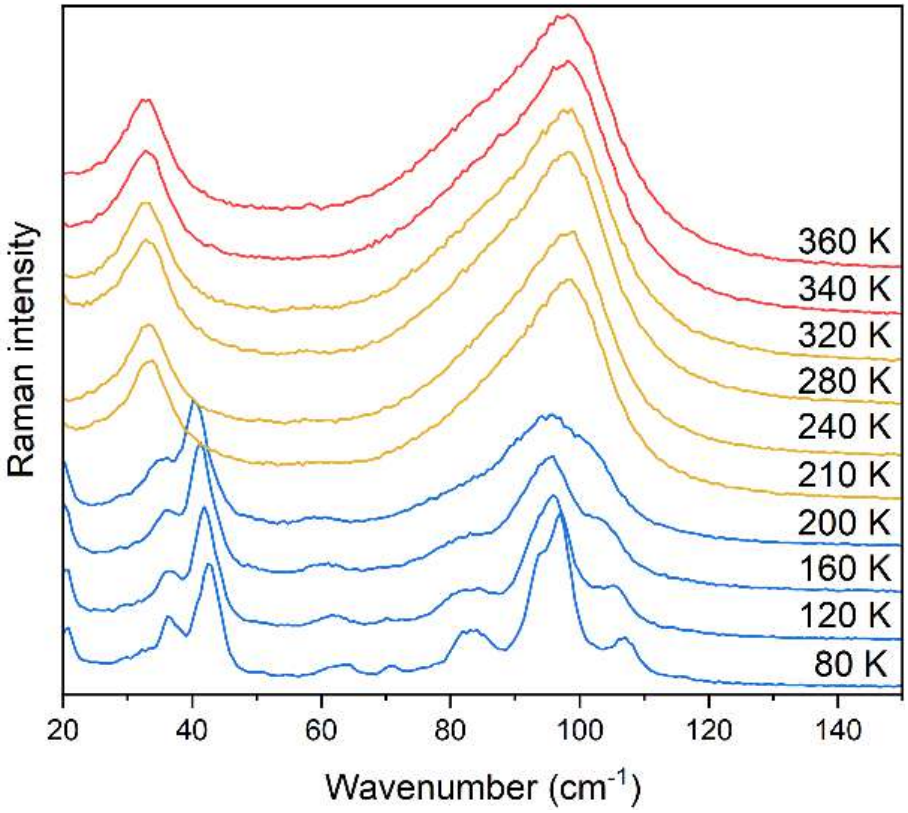

Figure S11. Temperature-dependent Raman spectra in the 150-20 cm^{-1} range

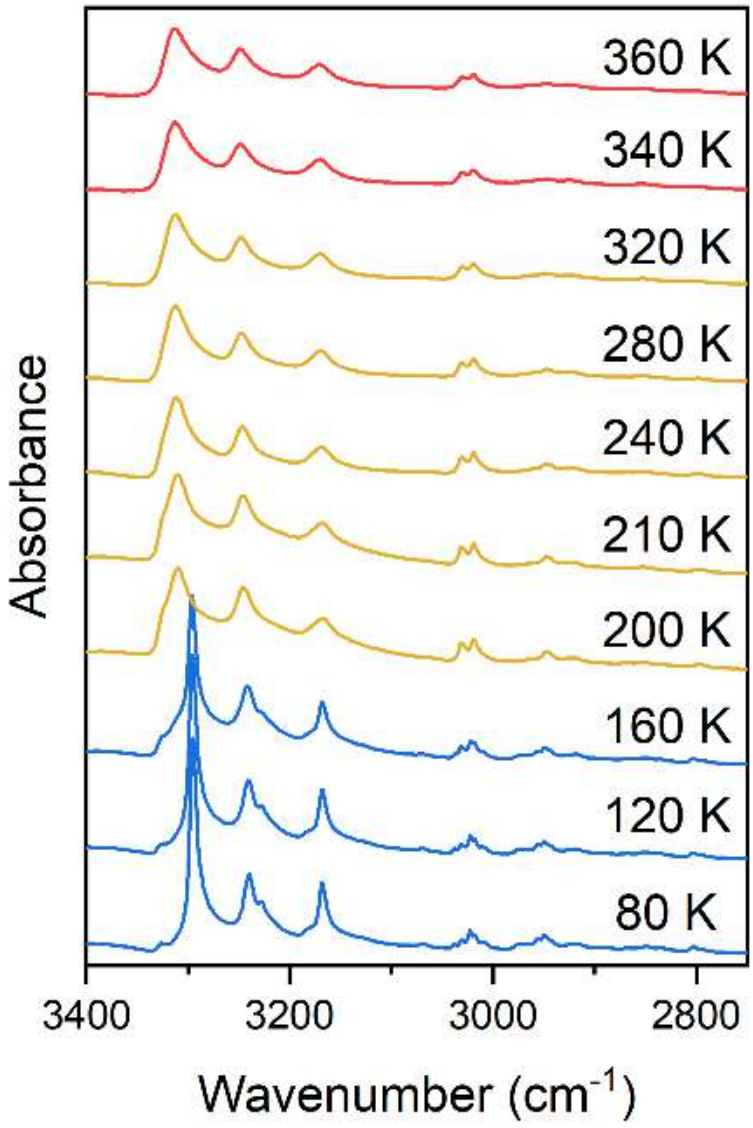

Figure S12. Temperature-dependent IR spectra in the 3400-2750 cm-[1] range

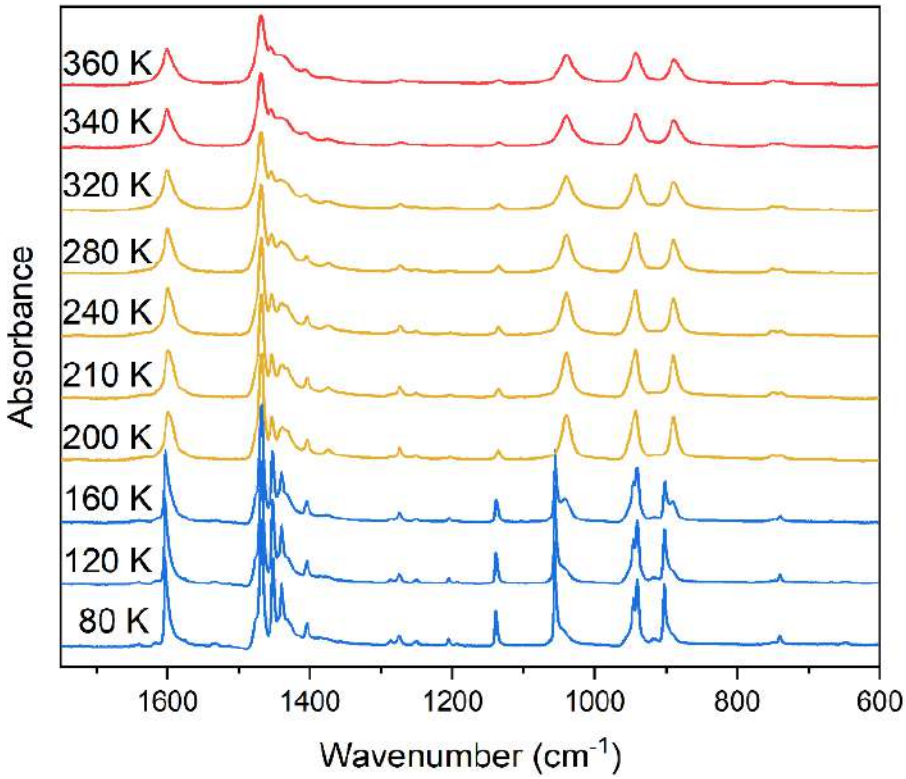

Figure S13. Temperature-dependent IR spectra in the 1750-600 cm-[1] range

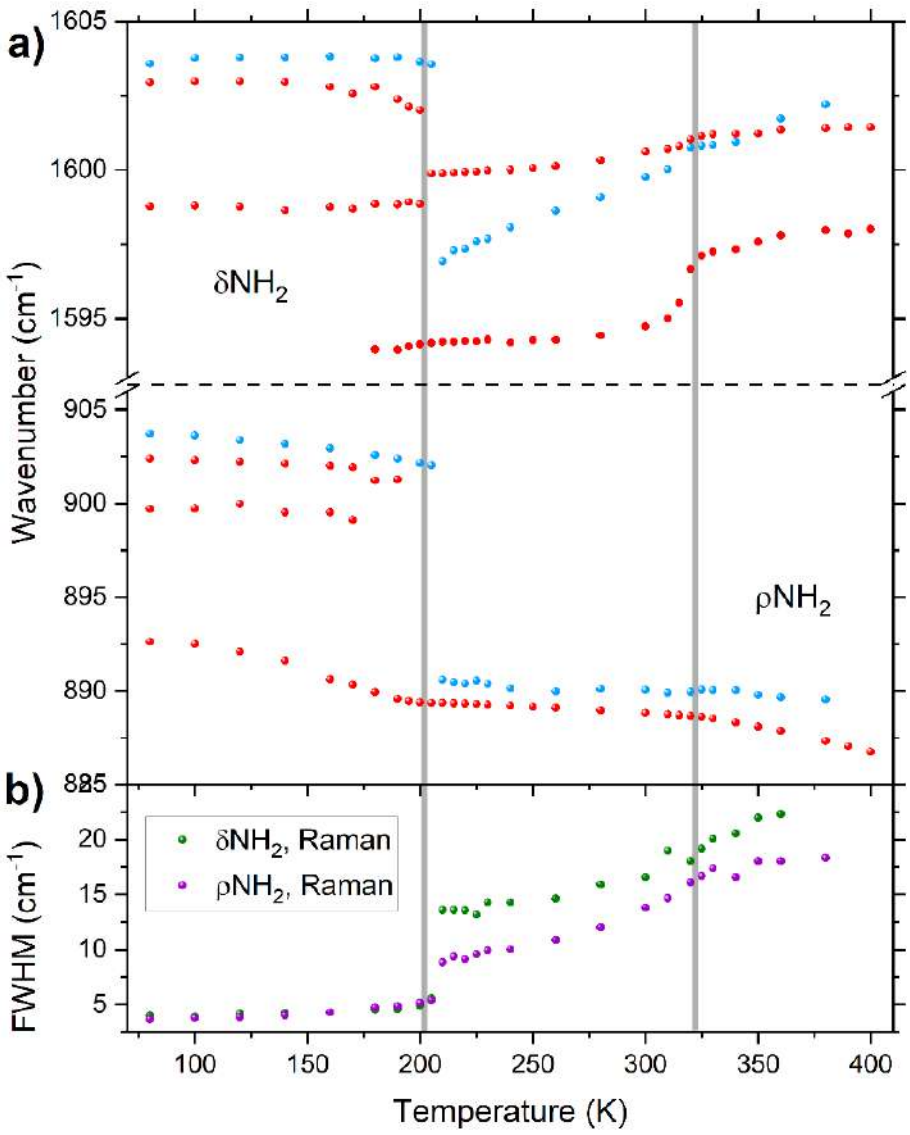

Figure S14. Thermal evolution of Raman (blue) and IR (red) band positions (a), as well as FWHMs of two Raman bands (b) corresponding to bending (δ) and rocking (ρ) vibrations of amino group; vertical lines correspond to temperatures of PTs determined from DSC

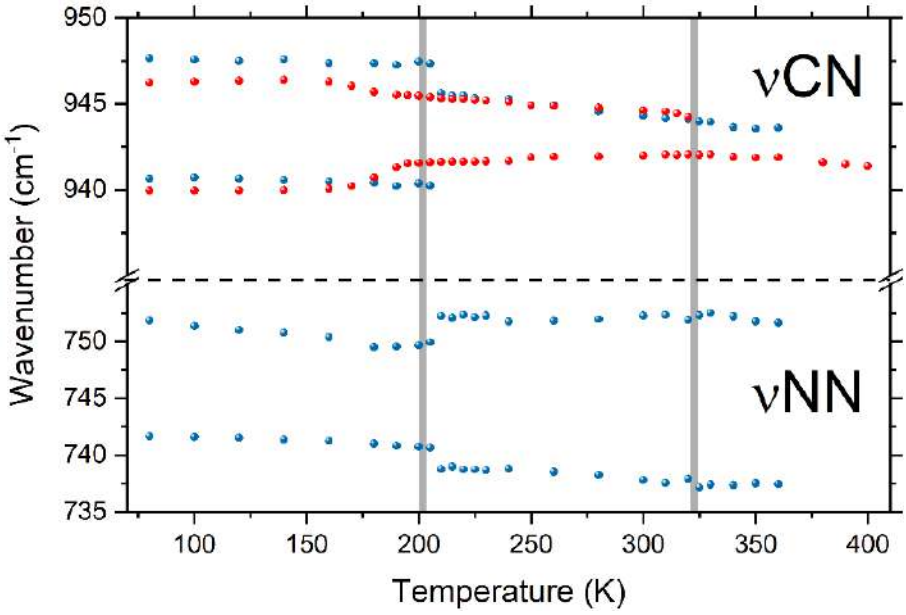

Figure S15. Thermal evolution of positions of the Raman (blue) and IR (red) bands stretching vibrations of CN and NN bonds; vertical lines correspond to temperatures of PTs determined from DSC

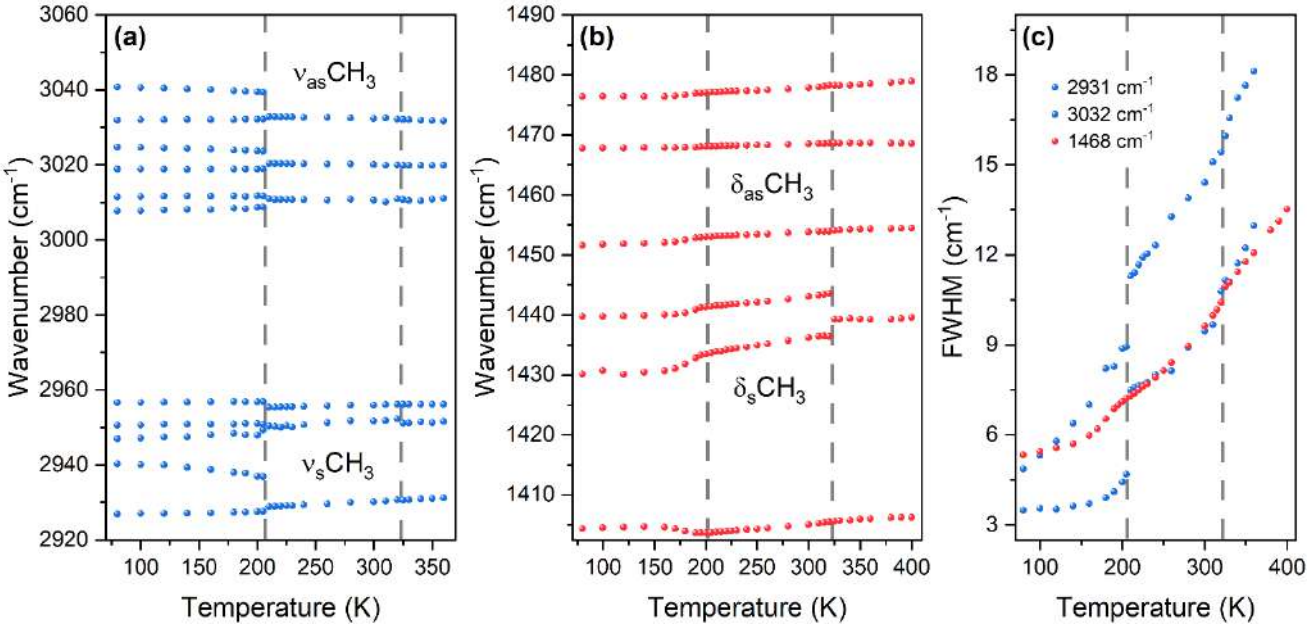

Figure S16. Thermal evolution of Raman (a) and IR (b) band positions corresponding to stretching (a) and bending (b) vibrations of methyl groups, and FWHMs of selected Raman and IR bands (c); vertical lines correspond temperatures of PTs determined from DSC.

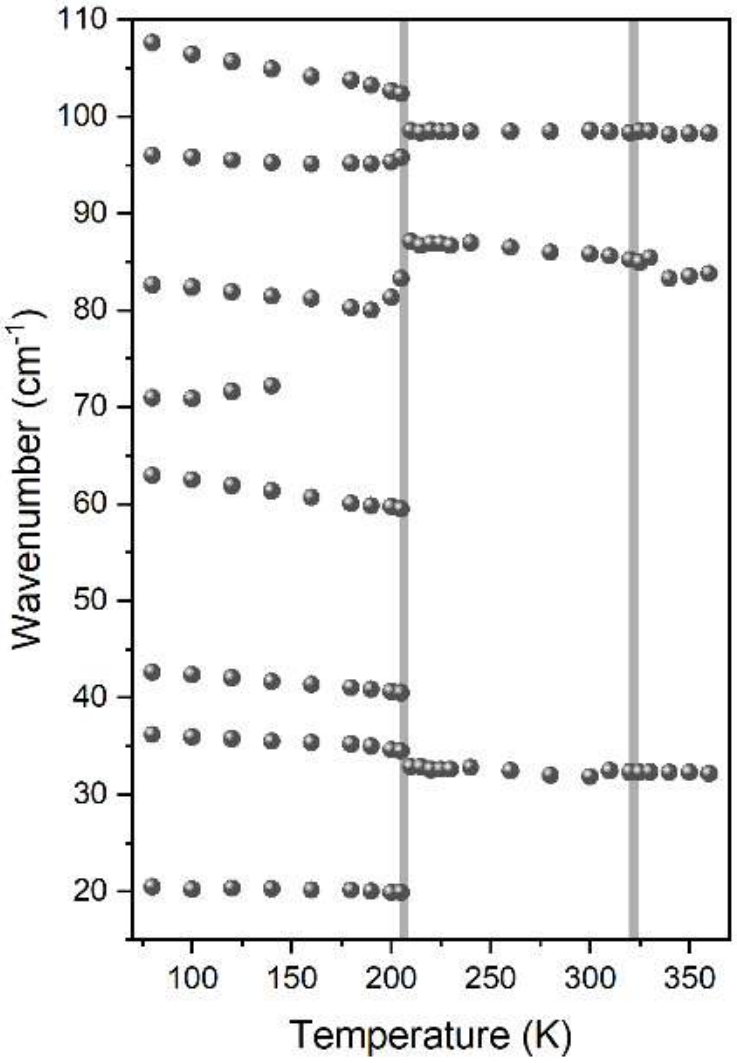

Figure S17. Thermal evolution of low-wavenumber Raman bands

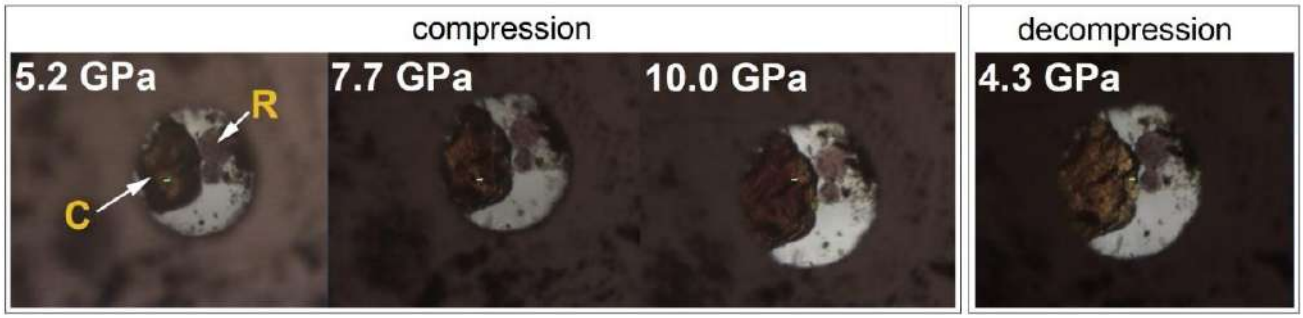

Figure S18. Changes of $(Me_3Hy)[PbI_3]$ crystal (C) loaded into a 100 μm hole in the stainless steel gasket, along with piece of ruby (R) at selected pressures during compression and after decompression to 4.3 GPa.

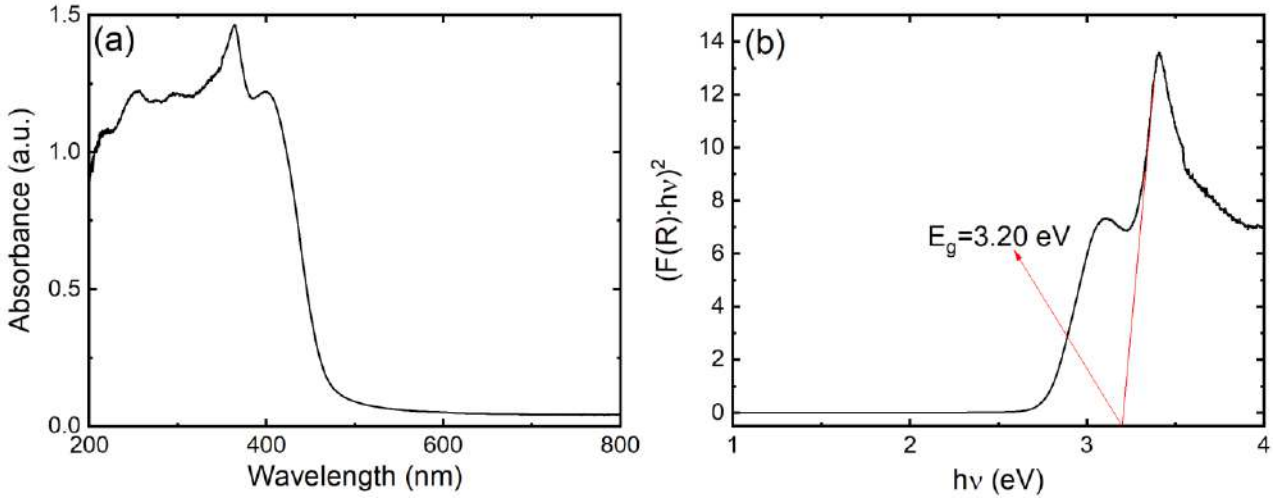

Figure S19. The diffuse reflectance spectrum of $(Me_3Hy)[PbI_3]$ crystals (a) and the calculation of its energy band gap by the Kubelka-Munk function (b)

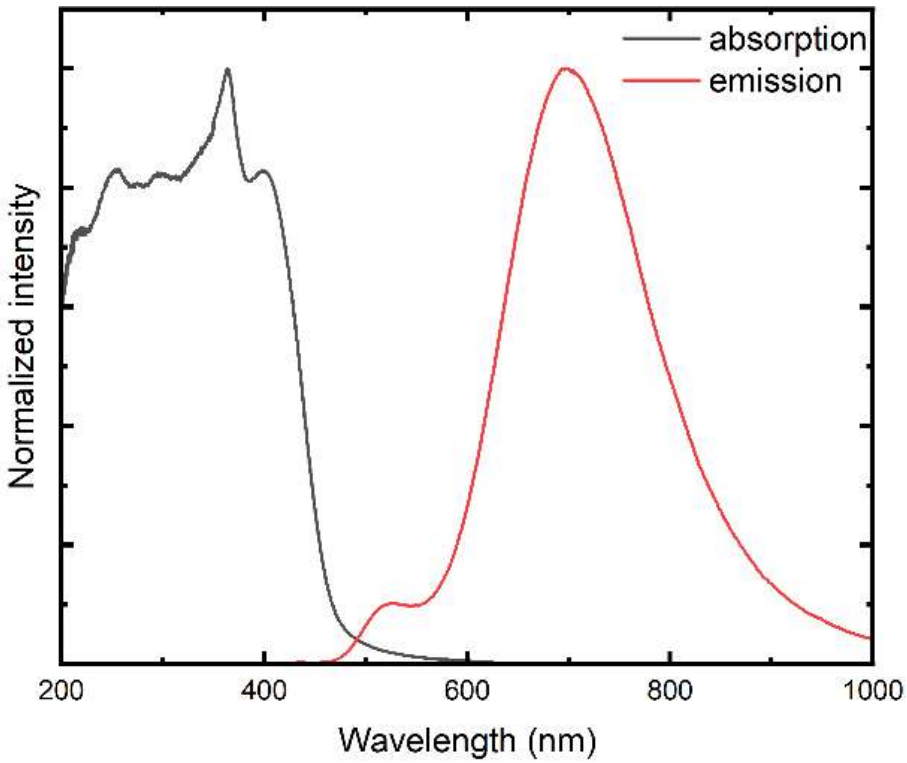

Figure S20. Diffuse reflectance at 300 K and emission spectra at 80 K of $(Me_3Hy)[PbI_3]$ crystals

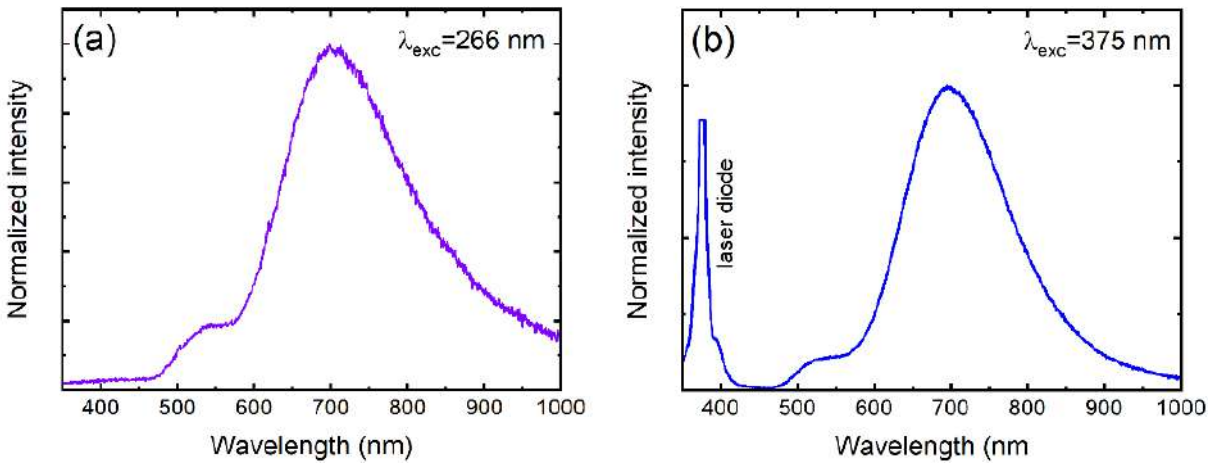

Figure S21. The emission spectra of $(Me_3Hy)[PbI_3]$ crystals measured under 266 (a) and 375 nm (b) excitation

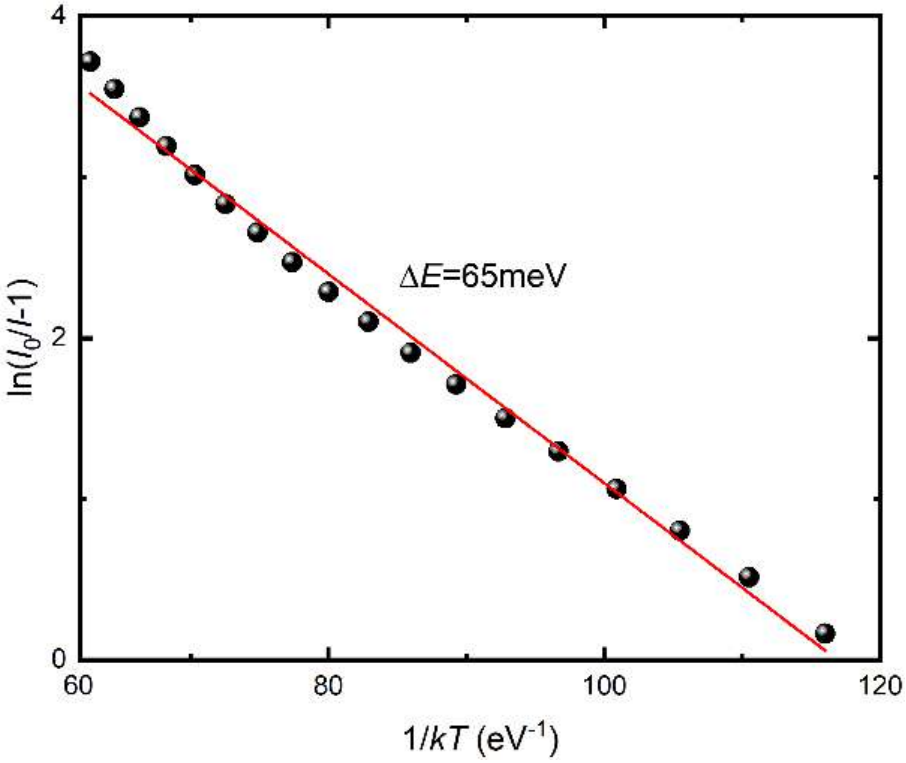

Figure S22. The activation energy of the thermal quenching of emission bands of $(Me_3Hy)[PbI_3]$

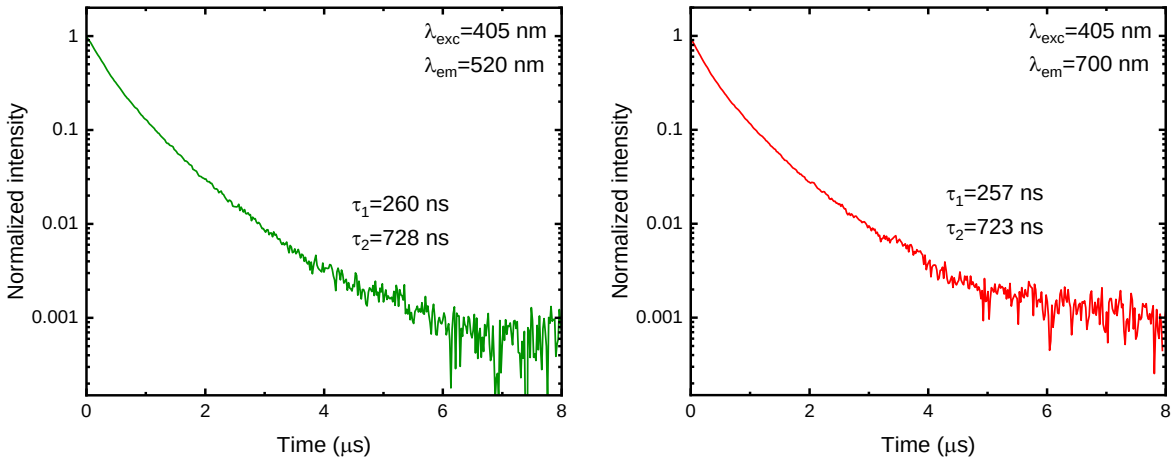

Figure S23. The luminescent decay profiles of $(Me_3Hy)[PbI_3]$ crystals measured at 80 K

Table S1. Crystal data and structure refinement for I and II phases of $(Me_3Hy)[PbI_3]$

	Phase II (230 K)	**Phase I (375 K)**
Crystal data		
Crystal system, space group	Hexagonal, *P*6$_3$/*m*	Hexagonal, *P*6$_3$/*mmc*
Temperature (K)	230(2)	375(2)
$a = b$, c (Å)	9.6202(3), 7.9298(2)	9.7735(5), 7.9594(3)
$\alpha = \beta$, γ(°)	90, 120	90, 120
V (Å^3)	635.57(4)	658.44(7)
Z / calculated density (g cm^{-3})	2 / 3.465	2 / 3.344
Absorption coefficient, μ (mm^{-1})	20.508	19.796
Index ranges	-11<=h<=12, -12<=k<=11, -9<=l<=9	-12<=h<=12, -12<=k<=12, -9<=l<=9
Data collection		
Theta range (°)	3.547 - 26.367	2.406° -26.301
No. of measured / independent reflections	4672 / 459	7706 / 283
R(int)	0.0275	0.0585
Completeness to theta = 25.242°	98.5 %	99.2 %
Refinement		
R [I > 2σ(I)], wR2 (I), S	0.0195, 0.0408, 1.129	0.0187, 0.0430, 1.147
Refinement method	Full-matrix least-squares on F^2	Full-matrix least-squares on F^2
Absorption correction	Gaussian	Gaussian
Data / restraints / parameters	459 / 6 / 32	283 / 9 / 26
Largest diff. peak and hole (e Å^{-3})	0.993, -0.727	0.384, -0.332
Extinction coefficient	0.0032(3)	0.0022(3)

For both phases M=663.03 g mol^{-1}; crystal size 0.139 x 0.112 x 0.083 mm.

Table S2. Geometric parameters (bond lengths (Å) and angles (°)) for phase I (HT) of $(Me_3Hy)[PbI_3]$

Pb1-I1#1	3.2361(6)	I1#2-Pb1-I1#5	93.850(12)
Pb1-I1#2	3.2361(6)	I1#3-Pb1-I1#5	86.150(12)
Pb1-I1#3	3.2361(6)	I1-Pb1-I1#5	86.150(12)
Pb1-I1	3.2361(6)	I1#4-Pb1-I1#5	180.0
Pb1-I1#4	3.2361(6)	Pb1-I1-Pb1#11	75.889(16)
Pb1-I1#5	3.2361(6)	N2#6-N1-N2#7	120.0
N1-N2#6	1.39(2)	N2#6-N1-N2	120.002(1)
N1-N2#7	1.39(2)	N2#7-N1-N2	120.002(1)
N1-N2	1.39(2)	N2#6-N1-C2#7	118.8(10)
N1-C2#8	1.47(2)	N2#7-N1-C2#7	16(6)
N1-C2#7	1.47(2)	N2-N1-C2#7	118.8(10)
N1-C2#9	1.47(2)	C2#8-N1-C2#7	122(2)
N1-C2#6	1.47(2)	N2#6-N1-C2#9	118.8(10)
N1-C2	1.47(2)	N2#7-N1-C2#9	16(6)
N1-C2#10	1.47(2)	N2-N1-C2#9	118.8(10)
N1-C1	1.50(3)	C2#8-N1-C2#9	113(5)
C2-H2A	0.9600	C2#7-N1-C2#9	32(10)
C2-H2B	0.9600	C2#8-N1-C2#6	32(10)
C2-H2C	0.9600	C2#7-N1-C2#6	113(5)
C1-H1A	0.9600	C2#9-N1-C2#6	122(2)
C1-H1B	0.9600	C2#8-N1-C2	122(2)
C1-H1C	0.9600	C2#7-N1-C2	113(5)
I1#1-Pb1-I1#2	86.151(12)	C2#9-N1-C2	122(2)
I1#1-Pb1-I1#3	93.849(12)	C2#6-N1-C2	113(5)
I1#2-Pb1-I1#3	180.00(2)	C2#8-N1-C2#10	113(5)
I1#1-Pb1-I1	180.0	C2#7-N1-C2#10	122(2)
I1#2-Pb1-I1	93.849(12)	C2#9-N1-C2#10	113(5)
I1#3-Pb1-I1	86.151(12)	C2#6-N1-C2#10	122(2)
I1#1-Pb1-I1#4	86.150(12)	C2-N1-C2#10	32(10)
I1#2-Pb1-I1#4	86.150(12)	N1-C2-H2A	109.5
I1#3-Pb1-I1#4	93.850(12)	N1-C2-H2B	109.5
I1-Pb1-I1#4	93.850(12)	H2A-C2-H2B	109.5
I1#1-Pb1-I1#5	93.850(12)	N1-C2-H2C	109.5
H2A-C2-H2C	109.5	H1B-C1-H1C	109.5
H2B-C2-H2C	109.5	N1-C1-H1A	109.5
N1-C1-H1A	109.5	N1-C1-H1B	109.5
N1-C1-H1B	109.5	H1A-C1-H1B	109.5
H1A-C1-H1B	109.5	N1-C1-H1C	109.5
N1-C1-H1C	109.5	H1A-C1-H1C	109.5
H1A-C1-H1C	109.5	H1B-C1-H1C	109.5

Symmetry transformations used to generate equivalent atoms:

#1 -x+2,-y,-z+1; #2 x-y,x-1,-z+1; #3 -x+y+2,-x+1,z; #4 y+1,-x+y+1,-z+1; #5 -y+1,x-y-1,z; #6 -x+y+1,-x+1,z; #7 -y+1,x-y,z; #8 -x+y+1,-x+1,-z+1/2; #9 -y+1,x-y,-z+1/2; #10 x,y,-z+1/2; #11 -x+2,-y,z-1/2

Table S3. Geometric parameters (bond lengths (Å) and angles (°)) for phase II (RT) of $(Me_3Hy)[PbI_3]$

Pb1-I1#1	3.2279(4)	I1-Pb1-I1#5	86.229(8)
Pb1-I1#2	3.2279(4)	I1#4-Pb1-I1#5	180.0
Pb1-I1#3	3.2280(4)	Pb1-I1-Pb1#8	75.780(11)
Pb1-I1	3.2280(4)	C1-N1-N2	54.9(9)
Pb1-I1#4	3.2280(4)	C1-N1-N2#6	104.0(16)
Pb1-I1#5	3.2280(4)	N2-N1-N2#6	120.002(1)
N1-C1	1.498(18)	C1-N1-N2#7	109.5(17)
N1-N2	1.56(7)	N2-N1-N2#7	120.000(19)
N1-N2#6	1.56(7)	N2#6-N1-N2#7	120.00(2)
N1-N2#7	1.56(7)	N2-N1-C2	20(5)
N1-C2	1.44(10)	N2#6-N1-C2	103(5)
C2-H2A	0.9700	N2#7-N1-C2	135(5)
C2-H2B	0.9700	N1-C2-H2A	109.5
C2-H2C	0.9700	N1-C2-H2B	109.5
N2-C1	1.41(4)	H2A-C2-H2B	109.5
N2-H4D	0.8572	N1-C2-H2C	109.5
N2-H4E	0.8867	H2A-C2-H2C	109.5
C1-H1A	0.9700	H2B-C2-H2C	109.5
C1-H1B	0.9700	C1-N2-N1	60(3)
C1-H1C	0.9700	N1-N2-H4D	112.3
I1#1-Pb1-I1#2	180.000(14)	N1-N2-H4E	94.3
I1#1-Pb1-I1#3	86.230(8)	H4D-N2-H4E	119.5
I1#2-Pb1-I1#3	93.770(8)	N2-C1-N1	65(3)
I1#1-Pb1-I1	93.771(8)	N2-C1-H1A	109.5
I1#2-Pb1-I1	86.229(8)	N1-C1-H1A	155.7
I1#3-Pb1-I1	180.0	N2-C1-H1B	109.5
I1#1-Pb1-I1#4	86.229(8)	N1-C1-H1B	55.7
I1#2-Pb1-I1#4	93.771(8)	H1A-C1-H1B	109.5
I1#3-Pb1-I1#4	86.229(8)	N2-C1-H1C	109.5
I1-Pb1-I1#4	93.771(8)	N1-C1-H1C	94.4
I1#1-Pb1-I1#5	93.771(8)	H1A-C1-H1C	109.5
I1#2-Pb1-I1#5	86.229(8)	H1B-C1-H1C	109.5
I1#3-Pb1-I1#5	93.771(8)		

Symmetry transformations used to generate equivalent atoms:

#1 x-y+1,x,-z+1; #2 -x+y+1,-x+2,z; #3 -x+2,-y+2,-z+1; #4 y,-x+y+1,-z+1; #5 -y+2,x-y+1,z; #6 -x+y+1,-x+1,z; #7 -y+1,x-y,z; #8 -x+2,-y+2,z-1/2

Table S4. Bond lengths (Å) of selected intermolecular contacts for phase II (RT) of $(Me_3Hy)[PbI_3]$

D - H···A	H···A (Å)	D···A [Å]	∠ D-H···A [°]
N(2) – H(4D) ···I(1) [-x+y,1-x,z]	3.260	3.494	98.63
C(1) – H(1A) ···I(1) [1-x,1-y,-1/2+z]	2.610	3.581	176.41
C(2) – H(2A) ···I(1)	3.190	3.808	122.95
N(2) – H(4D) ···I(1) [1-y,x-y,z]	3.210	3.883	137.19

Due to high symmetry, intermolecular interactions are multiplied by symmetry operations.

Table S5. Bond lengths (Å) of selected intermolecular contacts for phase I (HT) of $(Me_3Hy)[PbI_3]$

D - H···A	H···A (Å)	D···A [Å]	∠ D-H···A [°]
C(2) – H(2A) ···I(1) [x, x-y, 0.5-z]	2.947	3.809	150.15
C(2) – H(2B) ···I(1) [1-x+y, 1-x, z]	3.014	3.809	163.39

Due to high symmetry, intermolecular interactions are multiplied by symmetry operations.

Table S6. Crystal data obtained from PXRD experiment for phase III (LT) of $(Me_3Hy)[PbI_3]$

	Phase III (190 K) PXRD
Crystal system, space group	Orthorhombic, *Pbca*
Temperature (K)	190(2)
a , *b*, *c* (Å)	18.4083(3), 17.2246(4), 7.8215(2)
$\alpha = \beta, \gamma(^{\circ})$	90, 90, 90
V ($Å^3$)	2480.02(5)
Z / calculated density (g cm^{-3})	8, 3.541
Absorption coefficient, μ (mm^{-1})	84.34
Theta range (°)	2 - 45
R_p, R_{wp}	0.0500, 0.0747

For phase III M=663.03 g mol^{-1}

Table S7. Geometric parameters (bond lengths [Å] and angles [°]) for phase III (LT) of $(Me_3Hy)[PbI_3]$

Pb1-I1	3.184	I2-Pb1-I3#1	87.59
Pb1-I2	3.229	I2-Pb1-I1#1	94.23
Pb1-I3	3.282	I2-Pb1-I2#1	88.50
Pb1-I2#1	3.225	I2-Pb1-I3#1	175.54
Pb1-I3#1	3.261	I3-Pb1-I1#1	88.21
Pb1-I1#1	3.287	I3-Pb1-I3#1	96.23
I1-Pb1-I2	86.28	I3-Pb1-I2#1	171.58
I1-Pb1-I3	89.62	I1#1-Pb1-I3#1	88.20
I1-Pb1-I1#1	177.75	I1#1-Pb1-I2#1	84.65
I1-Pb1-I3#1	91.44	I3#1-Pb1-I2#1	88.01
I1-Pb1-I2#1	97.56		

#1 x, 1.5-y, -0.5+z

Table S8. Bond lengths (Å) of selected intermolecular contacts for phase III (LT) of (Me_3Hy)[PbI_3]

D-H···A	H···A [Å]	D···A [Å]	∠ D-H···A [°]
C(3)-H(3B)···I(1) [x, 1.5-y, 0.5+z]	2.977	3.547	118.75
C(6)-H(6B)···I(1) [-0.5+x, 1.5-y, 1-z]	3.110	4.072	171.30
C(6)-H(6A)···I(1) [0.5-x, -0.5+y, 1+z]	3.038	3,835	140.45

Table S9. Assignment of IR and Raman bands observed for $(Me_3Hy)[PbI_3]$

$(Me_3Hy)[PbI_3]$		Assignment
IR (cm^{-1})	**Raman (cm^{-1})**	
3311_m, 3247_m	3314_{vw}, 3251_{vw}	$\nu_{as}NH_2$
3169_w	3173_{vw}	ν_sNH_2
3030_w, 3019_w	3032_w, 3020_w, 3013_{sh}	$\nu_{as}CH_3$
2946_{vw}, 2923_{vw}, 2852_{vw}, 2798_{vw}	2956_w, 2931_w, 2909_{vw}, 2880_{vw}, 2846_{vw}, 2800_{vw}	ν_sCH_3
1600_m	1600_{vw}	δNH_2
1468_{vs}, 1454_m,	1470_{vw}, 1454_{sh}	$\delta_{as}CH_3$
1439_m, 1432_{sh}, 1405_w,	1436_w, 1407_{vw}	δ_sCH_3
1374_{vw}	1375_{vw}	ωNH_2
1273_w	1276_{vw}, 1251_{vw}	τNH_2
1251_{vw}, 1203_{vw}, 1178_{vw}, 1135_w, 1039_m	1206_{vw}, 1136_{vw}, 1106_{vw}, 1041_{vw}	ρCH_3
942_m	945_w	νCN
889_m	891_{vw}	ρNH_2
750_w, 737_w	753_w,739_w	νNN
475_w, 457_{vw}	476_{vw}, 459_{vw}	δCNC
373_w	375_{vw}	τCH_3
291_w, 216_w	291_{vw}	τCH_3
105_s, 80_s	101_{vs}, 93_{sh}	νPbI
	60_m	$\delta PbI+L(PbI_6)$

Key: ν, stretching (s, symmetric; as, antisymmetric); δ, bending (s, symmetric; as, antisymmetric); ρ, rocking; ω, wagging; τ, twisting; vs, very strong; s, strong; m, medium; w, weak; vw, very weak

Table S10. Raman pressure intercepts (ω_0) and coefficients (α) for three phases of $(Me_3Hy)[PbI_3]$ together with proposed assignment

Mode no	AP phase		HPI phase		HPII phase		Assignment
	ω_0 (cm^{-1})	$\alpha=d\omega/dP$ ($cm^{-1}GPa^{-1}$)	ω_0 (cm^{-1})	$\alpha=d\omega/dP$ ($cm^{-1}GPa^{-1}$)	ω_0 (cm^{-1})	$\alpha=d\omega/dP$ ($cm^{-1}GPa^{-1}$)	
1			132.6	8.61			νPbI
2			111.1	8.49			νPbI
3	101.4	5.52	99.5	2.08	96.2	2.49	νPbI
4			89.7	2.02	93.8	1.22	νPbI
5			74.8	1.98			δPbI+L(PbI_6)
6			72.6	-1.38			δPbI+L(PbI_6)
7	66.0	0.88	60.9	2.75	61.1	0.37	δPbI+L(PbI_6)
8			44.3	2.83			δPbI+L(PbI_6)

Key: ν, stretching; δ, bending; L, libration

6. Pozostałe osiągnięcia

6.1. Współautorstwo publikacji naukowych:

1. Paulina Sobierajska, Katarzyna Zawisza, Robert M. Kowalski, Guillaume Renaudin, Jean-Marie Nedelec, **Jan Zienkiewicz** and Rafal J. Wiglusz, „*Preparation of up-converting nano-biphasic calcium phosphate*" RSC Adv., **2017**, 7, 30086, doi: 10.1039/C7RA04809B.
2. **Jan A. Zienkiewicz**, Adam Strzep, Dawid Jedrzkiewicz, Nicole Nowak, Justyna Rewak-Soroczynska, Adam Watras, Jolanta Ejfler and Rafal J. Wiglusz, *„Preparation and Characterization of Self-Assembled Poly(l-Lactide) on the Surface of β-Tricalcium Diphosphate(V) for Bone Tissue Theranostics"* Nanomaterials, **2020**, 10, 331, doi: 10.3390/nano10020331.
3. Aneta Ciupa-Litwa, **Jan Albert Zienkiewicz**, Mariusz Stefanski, Maciej Ptak, Andrzej Majchrowski, Maciej Chrunik, „Vibrational and optical studies of a nonlinear optical crystal, $Cs_2Bi_2O(Ge_2O_7)$", Spectrochimica Acta Part A: Molecular and Biomolecular Spectroscopy, **2021**, 259, 119816, doi: 10.1016/j.saa.2021.119816.
4. **Jan Albert Zienkiewicz***, Dorota Anna Kowalska, Katarzyna Fedoruk, Mariusz Stefanski, Adam Pikul and Maciej Ptak, *„Unusual isosymmetric order–disorder phase transition in a new perovskite-type dimethylhydrazinium manganese formate exhibiting weak ferromagnetism and photoluminescence properties"*, J. Mater. Chem. C, **2021**,9, 6841-6851, doi: 10.1039/D1TC01014J.
5. **Jan A. Zienkiewicz**, Edyta Kucharska and Maciej Ptak, *"Mechanism of Unusual Isosymmetric Order-Disorder Phase Transition in [Dimethylhydrazinium]Mn(HCOO)$_3$ Hybrid Perovskite Probed by Vibrational Spectroscopy"*, Materials, **2021**, 14(14), 3984, doi: 10.3390/ma14143984.
6. Mirosław Mączka, **Jan A. Zienkiewicz***, Maciej Ptak*, *"Comparative Studies of Phonon Properties of Three-Dimensional Hybrid Organic–Inorganic Perovskites Comprising Methylhydrazinium, Methylammonium, and Formamidinium Cations"*, J. Phys. Chem. C, **2022**, 126, 8, 4048-4056, doi: 10.1021/acs.jpcc.1c09671.
7. **Jan A. Zienkiewicz***, Maciej Ptak, Dawid Drozdowski, Katarzyna Fedoruk, Mariusz Stefanski, and Adam Pikul, *„Hybrid Organic–Inorganic Crystals of [Methylhydrazinium]$M^{II}Cl_3$ (M^{II} = Co, Ni, Mn)"*, J. Phys. Chem. C, **2022**, 126, 37, 15809-15818, doi: 10.1021/acs.jpcc.2c04893.

8. **Jan. A. Zienkiewicz***, Karolina Kałduńska, Katarzyna Fedoruk, Antonio J. Barros dos Santos, Mariusz Stefanski, Waldeci Paraguassu, Tadeusz M. Muzioł, Maciej Ptak, *„Luminescence and dielectric switchable properties of 1D (1,1,1-trimethylhydrazinium)PbI_3 hybrid perovskitoid”*, Inorganic Chemistry, **2022**, 61, 51, 20886-20895, doi: 10.1021/acs.inorgchem.2c03287
9. **Jan. A. Zienkiewicz***, Dorota A. Kowalska, Dawid Drozdowski, Adam Pikul, Maciej Ptak*, *„Hybrid Chlorides with Methylhydrazinium Cation: $[CH_3NH_2NH_2]CdCl_3$ and Jahn-Teller Distorted $[CH_3NH_2NH_2]CuCl_3$”*, Molecules, 2023, 28, 2, 473, doi: 10.3390/molecules28020473

6.2. Wykłady na zaproszenie

1. Seria wykładów popularnonaukowych „Materiały wybuchowe w życiu człowieka” na zaproszenie Kół Naukowych z ośrodków akademickich z całej Polski:
   - Toruń, 16 listopada 2018, Studenckie Koło Naukowe Chemików Uniwersytetu Mikołaja Kopernika w Toruniu
   - Wrocław, 21 stycznia 2019, Koło Naukowe Chemików „Jeż”, Uniwersytet Wrocławski
   - Gdańsk, 22 marca 2019, Naukowe Koło Chemików Uniwersytety Gdańskiego
2. Seminarium Studenckiego Koła Naukowego Chemików UMK, *„O perowskitach, materiałach wybuchowych i spektroskopii, czyli czy wiedza ze studiów przydaje się w życiu?*, Toruń, 28.03.2022 (zdalnie)

6.3. Komunikaty konferencyjne

1. Referat, autor prezentujący, *„Selektywna synteza i charakterystyka spektroskopowa heksagonalnego i rombowego EuF_3 współdomieszkowanego jonami Yb^{3+}/Tb^{3+}, czyli o tym, że technika również ma znaczenie”*, L Ogólnopolska Szkoła Chemii „50 twarzy chemii”, Smardzewice 30.04.-4.05.2019 r.
2. Poster, autor prezentujący, *„Controlled synthesis and up-conversion characterization of Yb^{3+}/Tb^{3+} ions co-doped hexagonal and orthorhombic EuF_3 nanoparticles”*, 8th International Symposium on Optical Materials, Wrocław 9-14.06.2019 r. (konferencja międzynarodowa)
3. Referat, autor prezentujący, *„Biokompozyty oparte o β-diortofosforan triwapnia oraz polilaktyd, jako potencjalne materiały do teranostyki”*, II Ogólnopolska

Konferencja IMPLANTY 2019: Nowoczesna Implantologia – Dylematy i Nadzieje, Gdańsk 28-29.06.2019 r. (konferencja ogólnopolska).

4. Referat, autor prezentujący, *„Novel hybrid organic-inorganic perovskite with protonated unsymmetrical dimethylhydrazine – synthesis and physicochemical characterization”,* 64th International Conference for Students of Physics and Natural Sciences, Wilno (Litwa), 16-19.03.2021 r. (zdalnie);
5. Referat, autor prezentujący, *„Hybrydowe organiczno-nieorganiczne perowskity i perowskitoidy podstawione alkilowymi pochodnymi hydrazyny. Czym są i po co nam one?”*, II Międzynarodowa Multidyscyplinarna Konferencja Doktorantów Uniwersytetu Szczecińskiego (MKDUS 2.0), Szczecin, 22-24.06.2022 r. (zdalnie)
6. Poster, autor prezentujący, *„Application of Raman spectroscopy in studies on mechanisms of phase transitions in lead halide hybrid perovskitoids templated by hydrazinium derivatives”*, 27th International Conference on Raman Spectroscopy (ICORS), Long Beach, CA, USA, 14-19.08.2022 r.
7. Referat, autor prezentujący, *„Changes in the physicochemical behavior of (1,1,1-trimethylhydrazinium)PbI3 perovskitoid driven by temperature- and pressure-induced phase transitions”*, VI Konferencja Doktorantów PAN, Kraków, 21-23.10.2022 r.

6.4. Udział w grantach jako kierownik

1. NCN Preludum 19, UMO-2020/37/N/ST5/02257, *Synteza i charakterystyka fizykochemiczna nowych warstwowych i perowskitowych hybrydowych organiczno-nieorganicznych halogenków ołowiu z protonowanymi alkilopochodnymi hydrazyny*
   Przyznane środki: 139 980 PLN
   Czas trwania projektu: 1.02.2021 – 31.01.2023 r.

6.5. Upowszechnienie nauki

1. Prowadzenie zajęć w ramach tygodniowych warsztatów Niskie Łąki 2019 (INTiBS PAN)
2. Bałtycki Festiwal Nauki 2019, „Poznaj świat nauki od kuchni!”, Politechnika Gdańska, 22-25.05.2019 r.
3. XXII Dolnośląski Festiwal Nauki, edycja INTiBS PAN „Ciepło, zimno, jasno, ciemno – w nauce nie ma granic.”, 14-15.09.2019 r.

4. XXII Dolnośląski Festiwal Nauki, edycja INTiBS PAN „Doświadczenia z bliska”, 20-25.09.2019 r.
5. Piknik Naukowy z Wolfkem, 9-10.10.2022 r.

6.6. Działalność społeczna

1. Rada Samorządu Doktorantów INTiBS PAN
   - Przewodniczący, 01.01.2019-31.12.2020 r.
   - Wiceprzewodniczący, od 01.01.2021 r.

2. Krajowa Reprezentacja Doktorantów:
   - Obserwator w ramienia INTiBS PAN na XVIII Zjazd Delegatów Krajowej Reprezentacji Doktorantów, zdalnie, 10-11.12.2021 r.
   - Delegat INTiBS PAN na Zjazd Delegatów KRD zwołany w trybie nadzwyczajnym + III Otwarte Posiedzenie Zarządu, Gdańsk, 16-18.09.2022 r.
   - Członek Kapituły Konkursów PROPAN 2019. PRODOK 2020 i PRODOK 2021
   - Wiceprzewodniczący Kapituły Konkursu PROPAN 2022

6.7. Nagrody

1. I miejsce za najlepszą prezentację doktoranta na L Ogólnopolskiej Szkole Chemii za wygłoszenie referatu „*Selektywna synteza i charakterystyka spektroskopowa heksagonalnego i rombowego EuF_3 współdomieszkowanego jonami Yb^{3+}/Tb^{3+}, czyli o tym, że technika również ma znaczenie*”, Smardzewice 30.04.-4.05.2019 r.

7. Indeks rysunków i tabel

Rysunki

Tabele

8. Indeks skrótów stosowanych w pracy

AZ^+	kation azyrydyniowy
AZE^+	kation azetydyniowy
BA^+	kation butyloamoniowy
$BTBA^+$	kation benzylotributyloamoniowy
$BTEA^+$	kation benzylotrietyloamoniowy
$DABCO^+$	kation 1,4-diazabicyklo[2.2.2.]-oktaniowy
DFT	teoria funkcjonałów gęstości
DMA^+	kation dimetyloamoniowy
DMHy	dimetylohydrazyna
$DMHy^+$	kation dimetylohydrazyniowy
EA^+	kation etyloamoniowy
FA^+	kation formamidyniowy
FT	transformacja Fouriera
GUA^+	kation guanidyniowy
HOIP	hybrydowe organiczno-nieorganiczne perowskity
Hy^+	kation hydrazyniowy
IM^+	kation imidazoliowy
IR	podczerwień
LED	dioda emitująca światło
MA^+	kation metyloamoniowy
MD	metoda dyfuzyjna
Me_3Hy^+	kation trimetylohydrazyniowy
MHy^+	kation metylohydrazyniowy
MO	Metoda powolnego odparowywania roztworu
MOF	szkielety metalowo-organiczne
MP	metoda przeciwrozpuszczalnikowa
MS	metoda strąceniowa
NIR	bliska podczerwień
PED	dystrybucja energii potencjalnej
PIP^+	kation piperazyniowy
SHG	generacja drugiej harmonicznej
SPh_3^+	kation trifenylosulfoniowy
TF	parametr dopasowania
TGA	Analiza termograwimetryczna
TMA^+	kation tetrametyloamoniowy
$TrMA^+$	kation trimetyloamoniowy
UV	ultrafiolet
Vis	Zakres widzialny
XRD	dyfrakcja promieniowania rentgenowskiego
YAG	granat itrowo-aluminiowy

9. Referencje

[1] V.M. Goldschmidt, Die Gesetze der Krystallochemie, Naturwissenschaften. 14 (1926) 477–483. https://doi.org/10.1007/BF01507527.

[2] H. Megaw, Crystal Structure of Barium Titanate, Nature. 155 (1945) 484–485. https://doi.org/10.1038/155484b0.

[3] W. Li, Z. Wang, F. Deschler, S. Gao, R.H. Friend, A.K. Cheetham, Chemically diverse and multifunctional hybrid organic-inorganic perovskites, Nat. Rev. Mater. 2 (2017). https://doi.org/10.1038/natrevmats.2016.99.

[4] C. Zuo, L. Ding, Organic perovskites, J. Semicond. (2021) 040201. https://doi.org/10.1088/1674-4926/42/4/040201.

[5] R. Taheri-Ledari, F. Ganjali, S. Zarei-Shokat, M. Saeidirad, F. Ansari, M. Forouzandeh-Malati, F. Hassanzadeh-Afruzi, S.M. Hashemi, A. Maleki, a Review of Metal-Free Organic Halide Perovskite: Future Directions for the Next Generation of Solar Cells, Energy and Fuels. 36 (2022) 10702–10720. https://doi.org/10.1021/acs.energyfuels.2c01868.

[6] G. Kieslich, S. Sun, A.K. Cheetham, An extended Tolerance Factor approach for organic – inorganic perovskites, Chem. Sci. 6 (2015) 3430–3433. https://doi.org/10.1039/c5sc00961h.

[7] G. Kieslich, S. Sun, A.K. Cheetham, Solid-state principles applied to organic–inorganic perovskites: new tricks for an old dog, Chem. Sci. 5 (2014) 4712–4715. https://doi.org/10.1039/C4SC02211D.

[8] M. Ptak, A. Sieradzki, M. Simenas, M. Maczka, Molecular spectroscopy of hybrid organic – inorganic perovskites and related compounds q, Coord. Chem. Revievs. 448 (2021) 214180. https://doi.org/10.1016/j.ccr.2021.214180.

[9] H.L.B. Boström, M.S. Senn, A.L. Goodwin, Recipes for improper ferroelectricity in molecular perovskites, Nat. Commun. 9 (2018) 2380. https://doi.org/10.1038/s41467-018-04764-x.

[10] M. Trzebiatowska, Spectrochimica Acta Part A : Molecular and Biomolecular Spectroscopy The spectroscopic study of phase transitions in the series of cyanide perovskites, Spectrochim. Acta Part a Mol. Biomol. Spectrosc. 245 (2021) 118957. https://doi.org/10.1016/j.saa.2020.118957.

[11] Y. Wu, S. Shaker, F. Brivio, R. Murugavel, P.D. Bristowe, A.K. Cheetham, [Am]Mn($H_2POO)_3$: a New Family of Hybrid Perovskites Based on the Hypophosphite Ligand, J. Am. Chem. Soc. 139 (2017) 16999–17002. https://doi.org/10.1021/jacs.7b09417.

[12] M. Śanchez-Andújar, S. Presedo, S. Ýã Nez-Vilar, S. Castro-García, J. Shamir, M.A. Senaris-Rodriguez, Characterization of the order-disorder dielectric transition in the hybrid organic-inorganic perovskite-like formate $Mn(HCOO)_3[(CH_3)_2NH_2]$, Inorg. Chem. 49 (2010) 1510–1516. https://doi.org/10.1021/ic901872g.

[13] G.P. Nagabhushana, R. Shivaramaiah, A. Navrotsky, Thermochemistry of multiferroic organic-inorganic hybrid perovskites $[(CH_3)_2NH_2][M(HCOO)_3]$ (M = Mn, Co, Ni, and Zn), J. Am. Chem. Soc. 137 (2015) 10351–10356. https://doi.org/10.1021/jacs.5b06146.

[14] W. Li, A. Stroppa, Z. Wang, S. Gao, Hybrid Organic-Inorganic Perovskites, Wiley, 2020. https://doi.org/10.1002/9783527344338.

[15] M. Maczka, M. Ptak, S. Kojima, Brillouin scattering study of ferroelectric transition mechanism in multiferroic metal-organic frameworks of $[NH_4][Mn(HCOO)_3]$ and $[NH_4][Zn(HCOO)_3]$, Appl. Phys. Lett. 104 (2014). https://doi.org/10.1063/1.4880815.

[16] W. Li, A. Thirumurugan, P.T. Barton, Z. Lin, S. Henke, H.H. Yeung, M.T. Wharmby, E.G. Bithell, C.J. Howard, A.K. Cheetham, Mechanical Tunability via Hydrogen Bonding in Metal − Organic Frameworks with the Perovskite Architecture, J. Am. Chem. Soc. 136 (2014) 7801–7804. https://doi.org/10.1021/ja500618z.

[17] Z. Wang, K. Hu, S. Gao, H. Kobayashi, Formate-based magnetic metal-organic frameworks templated by protonated amines, Adv. Mater. 22 (2010) 1526–1533. https://doi.org/10.1002/adma.200904438.

[18] M. Maczka, B. Bondzior, P. Deren, A. Sieradzki, J. Trzmiel, A. Pietraszko, J. Hanuza, Synthesis and characterization of $[(CH_3)_2NH_2][Na_{0.5}Cr_{0.5}(HCOO)_3]$: a rare example of

luminescent metal–organic frameworks based on Cr(III) ions, Dalt. Trans. 44 (2015) 6871–6879. https://doi.org/10.1039/c5dt00060b.

[19] P. Jain, V. Ramachandran, R.J. Clark, D.Z. Hai, B.H. Toby, N.S. Dalal, H.W. Kroto, A.K. Cheetham, Multiferroic behavior associated with an order-disorder hydrogen bonding transition in metal-organic frameworks (MOFs) with the perovskite ABX_3 architecture, J. Am. Chem. Soc. 131 (2009) 13625–13627. https://doi.org/10.1021/ja904156s.

[20] K.I. Hadjiivanov, D.A. Panayotov, M.Y. Mihaylov, E.Z. Ivanova, K.K. Chakarova, S.M. Andonova, N.L. Drenchev, Power of Infrared and Raman Spectroscopies to Characterize Metal- Organic Frameworks and Investigate Their Interaction with Guest Molecules, Chem. Rev. 121 (2020) 1286–1424. https://doi.org/10.1021/acs.chemrev.0c00487.

[21] L. Jonathan, L.J. Diguna, O. Samy, M. Muqoyyanah, S.A. Bakar, M.D. Birowosuto, A. El Moutaouakil, Hybrid Organic – Inorganic Perovskite Halide Materials for Photovoltaics towards Their Commercialization, Polymers (Basel). 14 (2022) 1059. https://doi.org/10.3390/polym14051059.

[22] A. Kojima, K. Teshima, Y. Shirai, T. Miyasaka, Organometal Halide Perovskites as Visible-Light Sensitizers for Photovoltaic Cells, J. Am. Chem. Soc. 131 (2009) 6050–6051. https://doi.org/10.1021/ja809598r.

[23] M.P. Mamaeva, A.Y. Samsonova, A.O. Murzin, O.A. Lozhkina, A.A. Murashkina, N.I. Selivanov, Y. V Kapitonov, Ultrafast Random Lasing in $MAPbI_3$ Halide Perovskite Single Crystals, J. Phys. Chem. C. 126 (2022) 19816–19821. https://doi.org/10.1021/acs.jpcc.2c06114.

[24] L. Zi, W. Xu, R. Sun, Z. Li, J. Zhang, L. Liu, N. Wang, Y. Wang, N. Ding, J. Hu, S. Lu, H. Zhu, H. Song, Lanthanide-Doped $MAPbI_3$ Single Crystals : Fabrication , Optical and Electrical Properties , and Multi-mode Photodetection, Chem. Mater. 34 (2022) 7412–7423. https://doi.org/10.1021/acs.chemmater.2c01549.

[25] J. Luo, X. Zhang, N. Zhang, G. Fan, S. Ramakrishna, T. Ye, Small Molecule-Induced Modulation of Grain Crystallization and Ion Migration Leads to High-Performance $MAPbI_3$ Mini-Modules, ACS Appl. Energy Mater. 5 (2022) 9471–9478. https://doi.org/10.1021/acsaem.2c01036.

[26] Z. Xiong, L. Lan, Y. Wang, C. Lu, S. Qin, S. Chen, Multifunctional Polymer Framework Modified SnO2 Enablinga Photostable α-$FAPbI_3$ Perovskite Solar Cell with Efficiency Exceeding 23%, ACS Energy Lett. 6 (2021) 3824–3830. https://doi.org/10.1021/acsenergylett.1c01763.

[27] X. Chen, Y. Xia, Z. Zheng, X. Xiao, C. Ling, M. Xia, Y. Hu, A. Mei, R. Cheacharoen, Y. Rong, H. Han, In Situ Formation of δ - $FAPbI_3$ at the Perovskite / Carbon Interface for Enhanced Photovoltage of Printable Mesoscopic Perovskite Solar Cells, Chem. Mater. 34 (2022) 728–735. https://doi.org/10.1021/acs.chemmater.1c03505.

[28] Q. Zhang, G. Ma, K.A. Green, K. Gollinger, J. Moore, T. Demeritte, P.C. Ray, G.A. Hill, X. Gu, S.E. Morgan, M. Feng, S. Banerjee, Q. Dai, FAPbI 3 Perovskite Films Prepared by Solvent Self-Volatilization for Photovoltaic Applications, ACS Appl. Energy Mater. 5 (2022) 1487–1495. https://doi.org/10.1021/acsaem.1c02879.

[29] J. Yin, G. Teobaldi, L. Liu, Theoretical Insight into the δ-to-α Transition of $FAPbI_3$, J. Phys. Chem. Lett. 13 (2022) 3089–3095. https://doi.org/10.1021/acs.jpclett.2c00454.

[30] M.P.U. Haris, S. Kazim, S. Ahmad, Microstrain and Urbach Energy Relaxation in $FAPbI_3$ - Based Solar Cells through Powder Engineering and Perfluoroalkyl Phosphate Ionic Liquid Additives, ACS Appl. Mater. Interfaces. 14 (2022) 24546–24556. https://doi.org/10.1021/acsami.2c01960.

[31] M. Kinka, V. Klimavicius, S. Svirskas, V. Kalendra, M. Ptak, D. Szewczyk, A.P. Herman, R. Kudrawiec, A. Sieradzki, R. Grigalaitis, A. Walsh, Mixology of $MA_{1-x}EA_xPbI_3$ Hybrid Perovskites: Phase Transitions, Cation Dynamics, and Photoluminescence, Chem. Mater. 34 (2022) 10104–10112. https://doi.org/10.1021/acs.chemmater.2c02807.

[32] M. Mączka, M. Ptak, A. Gągor, D. Stefańska, J.K. Zaręba, A. Sieradzki, Methylhydrazinium Lead Bromide: Noncentrosymmetric Three-Dimensional Perovskite with Exceptionally Large Framework Distortion and Green Photoluminescence, Chem. Mater. 32 (2020) 1667–1673. https://doi.org/10.1021/acs.chemmater.9b05273.

[33] M. Mączka, A. Gagor, J.K. Zareba, D. Stefanska, M. Drozd, S. Balciunas, M. Šimenas, J. Banys, A. Sieradzki, M. Mączka, A. Gagor, J.K. Zaręba, D. Stefanska, M. Drozd, S. Balciunas, M. Šimėnas, J. Banys, A. Sieradzki, Three-Dimensional Perovskite Methylhydrazinium Lead Chloride with Two Polar Phases and Unusual Second-Harmonic Generation Bistability above Room Temperature, Chem. Mater. 32 (2020) 4072–4082. https://doi.org/10.1021/acs.chemmater.0c00973.

[34] H.R. Petrosova, O.I. Kucheriv, S. Shova, I.A. Guralskiy, Aziridinium cation templating 3D lead halide hybrid perovskites, Chem. Commun. (2022). https://doi.org/10.1039/d2cc01364a.

[35] D. Stefańska, M. Ptak, M. Mączka, Synthesis, Photoluminescence and Vibrational Properties of Aziridinium Lead Halide Perovskites, Molecules. 27 (2022) 7949. https://doi.org/10.3390/molecules27227949.

[36] C. Zheng, O. Rubel, Aziridinium Lead Iodide:A Stable, Low-Band-Gap Hybrid Halide Perovskite for Photovoltaics, J. Phys. Chem. Lett. 9 (2018) 874–880. https://doi.org/10.1021/acs.jpclett.7b03114.

[37] B. Dahal, W. Li, Configuration of Methylammonium Lead Iodide Perovskite Solar Cell and its Effect on the Device's Performance:A Review, Adv. Mater. Interfaces. 9 (2022) 2200042. https://doi.org/10.1002/admi.202200042.

[38] P. Schulz, E. Edri, S. Kirmayer, G. Hodes, D. Cahen, A. Kahn, Interface energetics in organo-metal halide perovskite-based photovoltaic cells, Energy Environ. Sci. 7 (2014) 1377–1381. https://doi.org/10.1039/c4ee00168k.

[39] G.E. Eperon, S.D. Stranks, C. Menelaou, M.B. Johnston, L.M. Herz, H.J. Snaith, Formamidinium lead trihalide:A broadly tunable perovskite for efficient planar heterojunction solar cells, Energy Environ. Sci. 7 (2014) 982–988. https://doi.org/10.1039/c3ee43822h.

[40] C. Zhou, H. Lin, Q. He, L. Xu, M. Worku, M. Chaaban, Materials Science & Engineering R Low dimensional metal halide perovskites and hybrids, Mater. Sci. Eng. R. 137 (2019) 38–65. https://doi.org/10.1016/j.mser.2018.12.001.

[41] M.D. Malouangou, Y. Yang, Y. Zhang, L. Bai, J.T. Matondo, M.T. Mbumba, M.W. Akram, M. Guli, Recent Progress in Perovskite Materials Using Diammonium Organic Cations Toward Stable and Ef fi cient Solar Cell Devices: Dion-Jacobson, Energy Technol. 10 (2022) 2101155. https://doi.org/10.1002/ente.202101155.

[42] C.C. Stoumpos, L. Mao, C.D. Malliakas, M.G. Kanatzidis, Structure-Band Gap Relationships in Hexagonal Polytypes and Low-Dimensional Structures of Hybrid Tin Iodide Perovskites, Inorg. Chem. 56 (2017) 56–73. https://doi.org/10.1021/acs.inorgchem.6b02764.

[43] X. Li, Y. He, M. Kepenekian, P. Guo, W. Ke, J. Even, C. Katan, C.C. Stoumpos, R.D. Schaller, M.G. Kanatzidis, Three-Dimensional Lead Iodide Perovskitoid Hybrids with High X-ray Photoresponse, J. Am. Chem. Soc. 142 (2020) 6625–6637. https://doi.org/10.1021/jacs.0c00101.

[44] Q. Sun, Y. Xu, H. Zhang, B. Xiao, X. Liu, J. Dong, Y. Cheng, B. Zhang, W. Jie, M.G. Kanatzidis, Optical and electronic anisotropies in perovskitoid crystals of $Cs_3Bi_2I_9$ studies of nuclear radiation detection, J. Mater. Chem. A. 6 (2018) 23388–23395. https://doi.org/10.1039/c8ta09525f.

[45] J.A. Zienkiewicz, E. Kucharska, M. Ptak, Mechanism of unusual isosymmetric order-disorder phase transition in [dimethylhydrazinium]$Mn(HCOO)_3$ hybrid perovskite probed by vibrational spectroscopy, Materials (Basel). 14 (2021). https://doi.org/10.3390/ma14143984.

[46] J.A. Zienkiewicz, K. Kałduńska, K. Fedoruk, A.J. Barros Dos Santos, M. Stefanski, W. Paraguassu, T.M. Muzioł, M. Ptak, Luminescence and Dielectric Switchable Properties ofa 1D (1,1,1-Trimethylhydrazinium)PbI_3Hybrid Perovskitoid, Inorg. Chem. (2022). https://doi.org/10.1021/acs.inorgchem.2c03287.

[47] M. Mączka, K. Pasińska, M. Ptak, W. Paraguassu, T.A. da Silva, A. Sieradzki, A. Pikul, Effect of solvent, temperature and pressure on the stability of chiral and perovskite metal formate frameworks of $[NH_2NH_3][M(HCOO)_3]$ (M = Mn, Fe, Zn) , Phys. Chem. Chem.

Phys. 18 (2016) 31653–31663. https://doi.org/10.1039/c6cp06648h.
[48] S. Chen, R. Shang, K.L. Hu, Z.M. Wang, S. Gao, $[NH_2NH_3][M(HCOO)_3]$ (M = Mn^{2+}, Zn^{2+}, Co^{2+} and Mg^{2+}): structural phase transitions, prominent dielectric anomalies and negative thermal expansion, and magnetic ordering, Inorg. Chem. Front. 1 (2014) 83–98. https://doi.org/10.1039/c3qi00034f.
[49] G. Kieslich, S. Kumagai, K.T. Butler, T. Okamura, C.H. Hendon, S. Sun, M. Yamashita, A. Walsh, A.K. Cheetham, Role of entropic effects in controlling the polymorphism in formate ABX_3 metal–organic frameworks, Chem. Commun. 51 (2015) 15538–15541. https://doi.org/10.1039/C5CC06190C.
[50] M. Mączka, A. Gągor, M. Ptak, W. Paraguassu, T.A. Da Silva, A. Sieradzki, A. Pikul, Phase Transitions and Coexistence of Magnetic and Electric Orders in the Methylhydrazinium Metal Formate Frameworks, Chem. Mater. 29 (2017) 2264–2275. https://doi.org/10.1021/acs.chemmater.6b05249.
[51] E. V Campbell, B. Dick, A.L. Rheingold, C. Zhang, X. Liu, Z. V Vardeny, J.S. Miller, Structures of a Complex Hydrazinium Lead Iodide, $(N_2H_5)_{15}Pb_3I_{21}$, Possessing $[Pb_2I_9]^{5-}$, $[PbI6]^{4-}$, and I^- Ions and α- and β-$(N_2H_5)PbI_3$, Chem. -A Eur. J. 24 (2018) 222–229. https://doi.org/10.1002/chem.201704356.
[52] W. Trawis, E.N.K. Glover, H. Bronstein, D.O. Scanlon, R.G. Palgrave, Chemical Science On the application of the tolerance factor to inorganic and hybrid halide perovskites: a revised system, Chem. Sci. 7 (2016) 4548–4556. https://doi.org/10.1039/c5sc04845a.
[53] D. Drozdowski, A. Gągor, M. Mączka, Methylhydrazinium lead iodide – one dimensional chain phase with excitonic absorption and large energy band gap, J. Mol. Struct. 1249 (2022). https://doi.org/10.1016/j.molstruc.2021.131660.
[54] D. Drozdowski, A. Gągor, D. Stefańska, J.K. Zaręba, K. Fedoruk, M. Mączka, A. Sieradzki, Three-Dimensional Methylhydrazinium Lead Halide Perovskites: Structural Changes and Effects on Dielectric, Linear, and Nonlinear Optical Properties Entailed by the Halide Tuning, J. Phys. Chem. C. 126 (2022) 1600–1610. https://doi.org/10.1021/acs.jpcc.1c07911.
[55] M. Mączka, M. Ptak, A. Gągor, D. Stefańska, A. Sieradzki, Layered Lead Iodide of $[Methylhydrazinium]_2PbI_4$ with a Reduced Band Gap: Thermochromic Luminescence and Switchable Dielectric Properties Triggered by Structural Phase Transitions, Chem. Mater. 31 (2019) 8563–8575. https://doi.org/10.1021/acs.chemmater.9b03775.
[56] M. Mączka, J.K. Zaręba, A. Gągor, D. Stefańska, M. Ptak, K. Roleder, D. Kajewski, A. Soszyński, K. Fedoruk, A. Sieradzki, $[Methylhydrazinium]_2PbBr_4$, a Ferroelectric Hybrid Organic-Inorganic Perovskite with Multiple Nonlinear Optical Outputs, Chem. Mater. 33 (2021) 2331–2342. https://doi.org/10.1021/acs.chemmater.0c04440.
[57] K. Fedoruk, D. Drozdowski, M. Maczka, J.K. Zareba, D. Stefan, A. Gagor, A. Sieradzki, $[Methylhydrazinium]_2PbCl_4$, a Two-Dimensional Perovskite with Polar and Modulated Phases, (2022). https://doi.org/10.1021/acs.inorgchem.2c02206.
[58] X. Li, S.A. Cuthriell, A. Bergonzoni, H. Dong, B. Traor, C.C. Stoumpos, P. Guo, J. Even, C. Katan, R.D. Schaller, M.G. Kanatzidis, Expanding the Cage of 2D Bromide Perovskites by LargeA - Site Cations, (2022). https://doi.org/10.1021/acs.chemmater.1c03605.
[59] G. Liu, S. Xu, H. Zheng, X. Xu, H. Xu, L. Zhang, X. Zhang, F. Kong, X. Pan, Boosting Photovoltaic Properties and Intrinsic Stability for MA-Based Perovskite Solar Cells by Incorporating 1,1,1-Trimethylhydrazinium Cation, ACS Appl. Mater. Interfaces. 11 (2019) 38779–38788. https://doi.org/10.1021/acsami.9b13701.
[60] M. Mączka, A. Gągor, A. Pikul, D. Stefańska, Novel hypophosphite hybrid perovskites of $[CH_3NH_2NH_2][Mn(H_2POO)_3]$ and $[CH_3NH_2NH_2][Mn(H_2POO)_{2.83}(HCOO)_{0.17}]$ exhibiting antiferromagnetic order and red photoluminescence, RSC Adv. 10 (2020) 19020–19026. https://doi.org/10.1039/d0ra03397a.
[61] A. Ciupa-Litwa, M. Ptak, E. Kucharska, J. Hanuza, M. Mączka, Vibrational Properties and DFT Calculations of Perovskite-Type Methylhydrazinium Manganese Hypophosphite, Molecules. 25 (2020). https://doi.org/10.3390/molecules25215215.
[62] J.A. Zienkiewicz, D.A. Kowalska, K. Fedoruk, M. Stefański, A. Pikul, M. Ptak, Unusual isosymmetric order-disorder phase transition in the new perovskite-type

dimethylhydrazinium manganese formate exhibiting ferrimagnetic and photoluminescent properties, J. Mater. Chem. C. 9 (2021) 6841–6851. https://doi.org/10.1039/D1TC01014J.
[63] A. Fu, P. Yang, Lower threshold for nanowire lasers, Nat. Mater. 14 (2015) 557–558. https://doi.org/10.1038/nmat4291.
[64] N.A. Wojcik, D.A. Kowalska, M. Trzebiatowska, E. Jach, A. Ostrowski, W. Bednarski, M. Gusowski, P. Staniorowski, A. Cizman, Tunable Dielectric Switching of (Quinuclidinium)[$MnCl_4$] Hybrid Compounds, J. Phys. Chem. C. 125 (2021) 16810–16818. https://doi.org/10.1021/acs.jpcc.1c04545.
[65] K. Wang, J.B. Xiong, B. Xia, Q.L. Wang, Y.Z. Tong, Y. Ma, X.H. Bu, Ferroelastic Phase Transition and Switchable Dielectric Constant in Heterometallic Niccolite Formate Frameworks, Inorg. Chem. 57 (2018) 537–540. https://doi.org/10.1021/acs.inorgchem.7b02386.
[66] M. Mączka, A. Gągor, K. Hermanowicz, A. Sieradzki, L. MacAlik, A. Pikul, Structural, magnetic and phonon properties of Cr(III)-doped perovskite metal formate framework [$(CH_3)_2NH_2$][$Mn(HCOO)_3$], J. Solid State Chem. 237 (2016) 150–158. https://doi.org/10.1016/j.jssc.2016.02.010.
[67] W. Li, Z. Zhang, E.G. Bithell, A.S. Batsanov, P.T. Barton, P.J. Saines, P. Jain, C.J. Howard, M.A. Carpenter, A.K. Cheetham, Ferroelasticity in a metal–organic framework perovskite; towards a new class of multiferroics, Acta Mater. 61 (2013) 4928–4938. https://doi.org/10.1016/j.actamat.2013.04.054.
[68] X. Xiao, W. Li, Y. Fang, Y. Liu, X. Dai, R. Zia, J. Huang, Benign ferroelastic twin boundaries in halide perovskites for charge carrier transport and recombination, Nat. Commun. 11 (2020) 2215. https://doi.org/10.1038/s41467-020-16075-1.
[69] P.D. Haynes, N.C. Bristowe, A.R. Warwick, I. Jorge, First-Principles Study of Ferroelastic Twins in Halide Perovskites, (2019). https://doi.org/10.1021/acs.jpclett.9b00202.
[70] W. Liao, Y. Zhang, C. Hu, J. Mao, H. Ye, P. Li,A lead-halide perovskite molecular ferroelectric semiconductor, Nat. Commun. (2015) 1–7. https://doi.org/10.1038/ncomms8338.
[71] S. Shahrokhi, W. Gao, Y. Wang, P.R. Anandan, Z. Rahaman, S. Singh, D. Wang, C. Cazorla, G. Yuan, J. Liu, T. Wu, Emergence of Ferroelectricity in Halide Perovskites, 2000149 (2020) 1–15. https://doi.org/10.1002/smtd.202000149.
[72] S. Liu, F. Zheng, N.Z. Koocher, H. Takenaka, F. Wang, A.M. Rappe, Ferroelectric domain wall induced band gap reduction and charge separation in organometal halide perovskites, J. Phys. Chem. Lett. 6 (2015) 693–699. https://doi.org/10.1021/jz502666j.
[73] R.I. Thomson, P. Jain, A.K. Cheetham, M.A. Carpenter, Elastic relaxation behavior, magnetoelastic coupling and order-disorder processes in multiferroic metal-organic frameworks, Phys. Rev. B. 214304 (2012) 1–7. https://doi.org/10.1103/PhysRevB.86.214304.
[74] L.N. Quan, B.P. Rand, R.H. Friend, S.G. Mhaisalkar, T. Lee, E.H. Sargent, Perovskites for Next-Generation Optical Sources, Chem. Rev. (2019). https://doi.org/10.1021/acs.chemrev.9b00107.
[75] H. Liu, H. Zhang, X. Xu, L. Zhang, The Opto-Electronic Functional Devices Based on Three-Dimensional Lead Halide Perovskites, Appl. Sci. 2021, Vol. 11, Page 1453. 11 (2021) 1453. https://doi.org/10.3390/APP11041453.
[76] K. Chondroudis, D.B. Mitzi, Electroluminescence from an Organic - Inorganic Perovskite Incorporating a Quaterthiophene Dye within Lead Halide Perovskite Layers, Chem. Mater. 11 (1999) 3028–3030. https://doi.org/10.1021/cm990561t.
[77] E. Yao, Z. Yang, L. Meng, P. Sun, S. Dong, Y. Yang, Y. Yang, High-Brightness Blue and White LEDs based on Inorganic Perovskite Nanocrystals and their Composites, Adv. Mater. 29 (2017) 1606859. https://doi.org/10.1002/adma.201606859.
[78] M. Yuan, L.N. Quan, R. Comin, G. Walters, R. Sabatini, O. Voznyy, S. Hoogland, Y. Zhao, E.M. Beauregard, P. Kanjanaboos, Z. Lu, D.H. Kim, E.H. Sargent, Perovskite energy funnels for efficient light-emitting diodes, Nat. Nanotechnol. 11 (2016) 872–877. https://doi.org/10.1038/nnano.2016.110.
[79] Z. Tan, R.S. Moghaddam, M.L. Lai, P. Docampo, R. Higler, F. Deschler, M. Price, A.

Sadhanala, L.M. Pazos, D. Credgington, F. Hanusch, T. Bein, H.J. Snaith, R.H. Friend, Bright light-emitting diodes based on organometal halide perovskite, Nat. Nanotechnol. 9 (2014) 687–962. https://doi.org/10.1038/nnano.2014.149.

[80] Y. Kim, S. Kim, A. Kakekhani, J. Park, J. Park, Y. Lee, H. Xu, S. Nagane, R.B. Wexler, D. Kim, S.H. Jo, L. Martínez-sarti, P. Tan, A. Sadhanala, G. Park, Y. Kim, B. Hu, H.J. Bolink, S. Yoo, R.H. Friend, A.M. Rappe, T. Lee, Comprehensive defect suppression in perovskite nanocrystals for high-efficiency light-emitting diodes, Nat. Photonics. 15 (2021) 148–155. https://doi.org/10.1038/s41566-020-00732-4.

[81] Y. Fang, J. Huang, Resolving Weak Light of Sub-picowatt per Square Centimeter by Hybrid Perovskite Photodetectors Enabled by Noise Reduction, Adv. Mater. 27 (2015) 2804–2810. https://doi.org/10.1002/adma.201500099.

[82] S. Shrestha, R. Fischer, G.J. Matt, P. Feldner, T. Michel, A. Osvet, I. Levchuk, B. Merle, S. Golkar, H. Chen, S.F. Tedde, O. Schmidt, R. Hock, M. Rührig, M. Göken, W. Heiss, G. Anton, C.J. Brabec, High-performance direct conversion X-ray detectors based on sintered hybrid lead triiodide perovskite wafers, Nat. Photonics. 11 (2017) 436–440. https://doi.org/10.1038/nphoton.2017.94.

[83] Y. Wang, Y. Zhang, Y. Lu, W. Xu, H. Mu, C. Chen, H. Qiao, Hybrid Graphene – Perovskite Phototransistors with Ultrahigh Responsivity and Gain, Adv. Opt. Mater. 3 (2015) 1389–1396. https://doi.org/10.1002/adom.201500150.

[84] C. Ma, Y. Shi, W. Hu, M. Chiu, Z. Liu, A. Bera, F. Li, H. Wang, L. Li, T. Wu, Heterostructured $WS_2/CH_3NH_3PbI_3$ Photoconductors with Suppressed Dark Current and Enhanced Photodetectivity, Adv. Mater. 28 (2016) 3683–3689. https://doi.org/10.1002/adma.201600069.

[85] S. Schünemann, S. Brittman, K. Chen, E.C. Garnett, H. Tüysüz, Halide Perovskite 3D Photonic Crystals for Distributed Feedback Lasers, ACS Photonics. 4 (2017) 2522–2528. https://doi.org/10.1021/acsphotonics.7b00780.

[86] F. Deschler, M. Price, S. Pathak, L. Klintberg, D. Dominik, R. Higler, S. Huettner, T. Leijtens, S.D. Stranks, H.J. Snaith, M. Atature, R.T. Phillips, R.H. Friend, High Photoluminescence Efficiency and Optically- Pumped Lasing in Solution-Processed Mixed Halide Perovskite Semiconductors, J. Phys. Chem. Lett. 5 (2014) 1421–1426. https://doi.org/10.1021/jz5005285.

[87] J.J. Yoo, G. Seo, M.R. Chua, T.G. Park, Y. Lu, F. Rotermund, Y. Kim, C.S. Moon, N.J. Jeon, V. Bulović, S.S. Shin, M.G. Bawendi, Efficient perovskite solar cells via improved carrier management, Nature. 590 (2021) 587–593. https://doi.org/10.1038/s41586-021-03285-w.

[88] H. Min, D.Y. Lee, J. Kim, G. Kim, K.S. Lee, J. Kim, M.J. Paik, Y.K. Kim, K.S. Kim, M.G. Kim, T.J. Shin, S. Il Seok, Perovskite solar cells with atomically coherent interlayers on SnO_2 electrodes, Nature. 598 (2021) 444–450. https://doi.org/10.1038/s41586-021-03964-8.

[89] G. Nazir, S. Lee, J. Lee, A. Rehman, J. Lee, S. Il Seok, S. Park, Stabilization of Perovskite Solar Cells : Recent Developments and Future Perspectives, Adv. Mater. 34 (2022) 2204380. https://doi.org/10.1002/adma.202204380.

[90] M. Trzebiatowska, M. Ptak, The mechanism of phase transitions in azide perovskites probed by vibrational spectroscopy, Spectrochim. Acta PartA Mol. Biomol. Spectrosc. 214 (2019) 184–191. https://doi.org/10.1016/j.saa.2019.02.027.

[91] M. Mączka, A. Pietraszko, B. Macalik, K. Hermanowicz, Structure, Phonon Properties, and Order − Disorder Transition in the Metal Formate Framework of $[NH_4][Mg(HCOO)_3]$, Inorg. Chem. 53 (2014) 787–794. https://doi.org/10.1021/ic4020702.

[92] R.X. da Silva, C.W. de Aruajo Paschoal, C.C. dos Santos, A.G. Fernandez, J. Salgado-Beceiro, M.A. Senaris-Rodriguez, M. Sanchez-Andujar, A.N.A. de Abreu Silva, Raman Spectroscopy Studies on the Barocaloric Hybrid Perovskite $[(CH_3)_4N][Cd(N_3)_3]$, Molecules. 25 (2020) 4754. https://doi.org/10.3390/molecules25204754.

[93] B. Dhanabalan, Y. Leng, G. Bi, M. Lin, P. Tan, I. Infante, L. Manna, M.P. Arciniegas, R. Krahne, Directional Anisotropy of the Vibrational Modes in 2D-Layered Perovskites, ACS Nano. 14 (2020) 4689–4697. https://doi.org/10.1021/acsnano.0c00435.

[94] K. Nakada, Y. Matsumoto, Y. Shimoi, K. Yamada, Y. Furukawa, Temperature-Dependent Evolution of Raman Spectra of Methylammonium Lead Halide Perovskites, $CH_3NH_3PbX_3$ (X = I, Br), Molecules. 24 (2019) 626. https://doi.org/10.3390/molecules24030626.
[95] Y. Guo, O. Yaffe, T.D. Hull, J.S. Owen, D.R. Reichman, L.E. Brus, Dynamic emission Stokes shift and liquid-like dielectric solvation of band edge carriers in lead-halide perovskites, Nat. Commun. 10 (2019) 1175. https://doi.org/10.1038/s41467-019-09057-5.
[96] R.X. Silva, R.R. Hora, A. Nonato, A. García-Fernández, J. Salgado-Beceiro, M.A. Señarís-Rodríguez, M.S. Andújar, A.P. Ayala, C.W.A. Paschoal, Order-disorder phase transition and molecular dynamics in the hybrid perovskite $[(CH_3)_3NH][Mn(N_3)_3]$, Spectrochim. Acta PartA Mol. Biomol. Spectrosc. 289 (2023) 122198. https://doi.org/10.1016/j.saa.2022.122198.
[97] M. Mączka, J.A. Zienkiewicz, M. Ptak, Comparative Studies of Phonon Properties of Three-Dimensional Hybrid Organic-Inorganic Perovskites Comprising Methylhydrazinium, Methylammonium, and Formamidinium Cations, J. Phys. Chem. C. 126 (2022) 4048–4056. https://doi.org/10.1021/acs.jpcc.1c09671.
[98] M. Mączka, M. Ptak, Lattice Dynamics and Structural Phase Transitions in Two-Dimensional Ferroelectric Methylhydrazinium Lead Bromide Investigated Using Raman and IR Spectroscopy, J. Phys. Chem. C. 126 (2022) 7991–7998. https://doi.org/10.1021/acs.jpcc.2c01731.
[99] M. MącZka, M. Ptak, D.L.M. Vasconcelos, L. Giriunas, P.T.C. Freire, M. Bertmer, J. Banys, M. Simenas, NMR and Raman Scattering Studies of Temperature-and Pressure-Driven Phase Transitions in $CH_3NH_2NH_2PbCl_3$ Perovskite, J. Phys. Chem. C. 124 (2020) 26999–27008. https://doi.org/10.1021/acs.jpcc.0c07886.
[100] L.A.T. Nguyen, D.N. Minh, Y. Yuan, S. Samanta, L. Wang, D. Zhang, N. Hirao, J. Kim, Y. Kang, Pressure-Induced Fluorescent Enhancement of $FA_\alpha PbBr_{2+\alpha}$ Composite Perovskites Received, Nanoscale. 11 (2019) 5868–5873. https://doi.org/10.1039/C8NR09780A.
[101] S. Sobczak, D. Linhares, P. Tarso, C. Freire, A. Katrusiak, Evidence of Pressure-Induced Phase Transitions and Negative Linear Compressibility in Formamidinium Manganese-Hypophosphite Hybrid Perovskite, J. Phys. Chem. C. 125 (2021) 26958–26966. https://doi.org/10.1021/acs.jpcc.1c08387.
[102] L. Wang, K. Wang, G. Xiao, Q. Zeng, B. Zou, Pressure-Induced Structural Evolution and Band Gap Shifts of Organometal Halide Perovskite-Based Methylammonium Lead Chloride, J. Phys. Chem. Lett. 7 (2016) 5273–5279. https://doi.org/10.1021/acs.jpclett.6b02420.
[103] L. Wang, T. Ou, K. Wang, G. Xiao, C. Gao, B. Zou, L. Wang, T. Ou, K. Wang, G. Xiao, C. Gao, B. Zou, Pressure-induced structural evolution, optical and electronic transitions of nontoxic organometal halide perovskite-based methylammonium tin chloride, Appl. Phys. Lett. 111 (2017) 233901. https://doi.org/10.1063/1.5004186.
[104] M. Li, T. Liu, Y. Wang, W. Yang, X. Lü, Pressure responses of halide perovskites with various compositions , dimensionalities , and morphologies Pressure responses of halide perovskites with various compositions , dimensionalities , and morphologies, Matter Radiat. Extrem. 5 (2020) 018201. https://doi.org/10.1063/1.5133653.
[105] D. Spirito, Y. Asensio, L.E. Hueso, B. Martín-García, Raman spectroscopy in layered hybrid organic- inorganic metal halide perovskites, J. Phys. Mater. 5 (2022) 034004. https://doi.org/10.1088/2515-7639/ac7977.
[106] M.J.. Frisch, G.W. Trucks, H.B. Schlegel, G.E. Scuseria, M.A. Robb, J.R. Cheeseman, J.A. Montgomery, T. Vreven, K.N. Kudin, J.C. Burant, E. Al., Gaussian 03, Revision A.1, (2003).
[107] A.D. Becke, Densityfunctional thermochemistry. IV.A new dynamical correlation functional and implications for exactexchange mixing functional and implications for exact-exchange mixing, J. Chem. Phys. 104 (1996) 1040. https://doi.org/10.1063/1.470829.
[108] C. Lee, W. Yang, R.G. Parr, Development of the Colic-Salvetti correlation-energy formula into a functional of the electron density, Phys. Rev. B. 37 (1988) 785–789. https://doi.org/10.1103/physrevb.37.785.
[109] R.G. Parr, Density Functional Theory of Atoms and Molecules, Springer, Dodrecht, The

Netherlands, 1989.
[110] A.D. Mclean, G.S. Chandler, Contracted Gaussian basis sets for molecular calculations. I. Second row atoms , Z=11-18, J. Chem. Phys. 72 (1980) 5639–5648. https://doi.org/10.1063/1.438980.
[111] R. Krishnan, J.S. Binkley, R. Seeger, J.A. Pople, Self-consistent molecular orbital methods. XX. a basis set for correlated wave functions, J. Chem. Phys. 650 (1980) 650–654. https://doi.org/10.1063/1.438955.
[112] H. Rostkowska, L. Lapinski, M.J. Nowak, Vibrational Spectroscopy Analysis of the normal modes of molecules with D_{3h} symmetry Infrared spectra of monomeric s-triazine and cyanuric acid, Vib. Spectrosc. 49 (2009) 43–51. https://doi.org/10.1016/j.vibspec.2008.04.012.
[113] G.A. Zhurko, D.A. Zhurko, Chemcraft Graphical Program of Visualization of Computed Results, Available online: http://chemcraftprog.com (Dostęp: 13.03.2023).